POLITECNICO DI MILANO

School of Industrial and Information Engineering

Department of Energy

Master of Science in Nuclear Engineering

A model for dynamical oscillations in magnetically confined fusion plasmas at the transition to high confinement

Advisor:
Prof. Matteo Passoni

Co-Advisor:
Dr. Peter Manz

Graduation Thesis of:
Federico Pesamosca
819246

Academic Year 2014-2015

A Franco Blanchini
che è stato discreto ma determinante
per questa mia scelta.

Contents

List of Figures

List of Tables

Abstract

Thermonuclear controlled fusion, that aims to exploit the energy produced in nuclear fusion reactions, is a promising solution explored for the fulfilment of the growing world energy demand. The candidate fuel, a mixture of deuterium and tritium, must be taken to extreme conditions in the plasma state in order to maintain the reaction. With this purpose, the tokamak reactor was developed. ITER, the reference experiment currently under construction, is an exemplar of this technological solution. ITER will operate in H-mode, a mode of operation of the plasma characterized by a high capability of energy confinement, which is reached from L-mode, less suited to maintain the reaction, following a certain amount of external heating power. The H-mode, however, features cyclic instabilities not yet fully understood, the Edge Localized Modes (ELMs) that, depending on the magnitude, could imply high energy losses.

Experimental studies in various tokamak allowed to characterized the L-H transition, not yet unequivocally explained, defining typical plasma oscillations, the Limit Cycle Oscillations (LCOs). Recent campaigns at ASDEX-Upgrade tokamak observed a gradual evolution of LCOs into ELMs during the L-H transition.

With the purpose to extend the knowledge of these phenomena, this thesis aims to provide a dynamical model, able to reproduce the observed transition from LCOs to ELMs during the I-phase, the intermediate phase between L- and H-mode.

It was therefore derived a reduced system of differential equations from fundamental physical models for the interested variables, that allows to include the typical parameters of the I-phase. A study of the nonlinear structure of the system was performed with the purpose to characterize analytically the possible solutions. In the end, a series of numerical simulations were performed, in order to define the possibility to describe the two phenomena, up to now treated separately, through the same physical mechanism and simulate the transition of LCOs into ELMs.

Sommario

La fusione termonucleare controllata, che si propone di sfruttare l'energia prodotta da reazioni di fusione nucleare, è una promettente soluzione esplorata per il soddisfacimento del crescente fabbisogno energetico mondiale. Il combustibile candidato, una miscela di deuterio e trizio, deve essere portato in condizioni estreme allo stato di plasma per mantenere la reazione. A tale scopo è stato sviluppato il reattore tokamak, di cui ITER, l'esperimento di riferimento in corso di costruzione, ne è un esemplare.

ITER opererà in H-mode, un modo di operazione del plasma che presenta un'elevata capacità di confinamento dell'energia, raggiunto a partire dall'L-mode, meno adatto a mantenere la reazione, a seguito di una sufficiente iniezione di potenza esterna. L'H-mode tuttavia presenta una serie di instabilità cicliche ancora non comprese completamente, le Edge Localized Modes (ELMs), che a seconda della gravità, possono comportare elevati rilasci di energia.

Studi sperimentali in vari tokamak hanno permesso di caratterizzare la transizione L-H, non ancora spiegata in modo univoco, definendo delle tipiche oscillazioni del plasma, le Limit Cycle Oscillations (LCOs). Recenti campagne del tokamak ASDEX-Upgrade hanno osservato una graduale evoluzione di LCOs in ELMs nel corso del passaggio dall' L- all'H-mode.

Con lo scopo di approfondire la comprensione di questi fenomeni, questa tesi si propone di fornire un modello dinamico che permetta di riprodurre la transizione osservata da LCOs ad ELMs durante l'I-phase, la fase intermedia tra L- ed H-mode.

Si è quindi derivato un sistema ridotto di equazioni differenziali da modelli fisici fondamentali del plasma per le variabili di interesse, che permettesse di includere i parametri tipici dell'I-phase. Uno studio della struttura nonlineare del sistema è stato effettuato con lo scopo di caratterizzarne analiticamente le possibili soluzioni. Si è infine proceduto con una serie di simulazioni numeriche, al fine di definire la possibilità di descrivere i due fenomeni, finora trattati separatamente, attraverso lo stesso meccanismo fisico e simulare la transizione di LCOs in ELMs.

Preface

In this thesis the evolution of the plasma edge in a tokamak, the candidate structure for the realization of thermonuclear controlled fusion, is studied. In particular, theoretical modeling and the numerical simulation of plasma dynamics is treated, aiming to reproduce and motivate recent experimental results at the ASDEX Upgrade tokamak. In [1], it is observed the evolution of plasma oscillations, called Limit Cycle Oscillations (LCOs), in instabilities able to degrade the energy confinement in the reactor, called Edge Localized Modes (ELMs), during the transition from L- to H-mode.

Nuclear fusion refers to the nuclear reaction by which two lighter nuclei merge to form a heavier element. For a series of elements, this implies an increase of binding energy per nucleon and therefore a release of energy. The possibility to exploit this reaction in order to rely on a long term clean and safe resource for electricity production in large base load power plants, the pacific use of thermonuclear fusion, is still a research topic. The ignition of the nuclear fusion reaction requires to maintain the reactants in a well-defined temperature and density range. In these conditions, the fuel is in the plasma state and the high temperatures required led to the necessity to properly confine the plasma, in order to avoid damages to the reactor. One of the most studied technological solutions for the scopes of thermonuclear controlled fusion is the tokamak, that allows to magnetically confine a plasma in a toroidal shape, through the interaction of this state of matter with external electromagnetic field and allowing to reach the desired conditions.

The H-mode is a state of magnetically confined plasma in a tokamak, characterized by improved energy confinement with reference to the L-mode. The transition to the high confinement state is reached overcoming an experimentally well defined threshold of the external heating power. The H-mode is the candidate regime for the realization of thermonuclear controlled fusion in ITER, the international pilot project currently under construction at CEA Cadarache (France), since it is considered to be

necessary to maintain the plasma in the required parameters range. The increase in confinement is essentially due to the reduction of the turbulence level, and therefore of transport, in the plasma. This phenomenon is limited to a reduced region by the external surface of the toroidal volume in which the plasma is confined. This fact motivates the interest in the context of thermonuclear controlled fusion for the plasma edge dynamics, which is consequently a current topic of research in plasma physics.

The comprehension of H-mode is nowadays not yet complete. A series of cyclic instabilities localized in the plasma edge, the Edge Localized Modes (ELMs), is observed to appear when the plasma reaches the high confinement state. These instabilities, depending on their magnitude, can cause high energy releases and undermine the advantages of the H-mode and are currently being studied.

Furthermore, the transition from L- to H- mode is not yet univocally explained. Experimental observations [2] allowed to characterize the I-phase, the intermediate phase between L- and H-mode, defining a series of plasma cyclic oscillations, the Limit Cycle oscillations (LCOs). These seem to agree with the solution of models that consider the formation of turbulence-driven macroscopic plasma flows, called Zonal Flows, able to reduce the turbulence and trigger the transition. Recent campaigns at ASDEX Upgrade tokamak [1] allowed to observe a gradual evolution of LCOs in ELMs, suggesting a common physical nature of the two phenomena.

The current dynamical models for the L-H transition or for ELMs are inherently simplified. This is due to the fact that no complete existing model was so far able to reproduce satisfactorily the interested phenomena. Consequently, reduced models are mostly not derived from fundamental equations and they often contain heuristic terms, not always formally justified, that make their falsification difficult. The role of these models is however fundamental in suggesting the direction for a further theoretical analysis or experimental research, proposing possible dynamics for the observed phenomena.

This work takes place in this context. The objective of this thesis is to propose a dynamical model able to reproduce the evolution of LCOs in ELMs during the I-phase observed in [1] in the electromagnetic oscillations of the ASDEX Upgrade plasma, and therefore sustain the hypothesis that the two mechanisms are generated from the same physical mechanism. This could allow to have access to a deeper understanding of the I-phase dynamics since no existing model, not even a reduced one, was able to reproduce the L-H transition. ELMs and LCOs phenomena were in fact treated separately up to now.

The model is derived analytically from Drift-Alfvén (DALF) equa-

tions, that describe low frequency phenomena in magnetically confined plasmas. These equations include the so-called magnetohydrodynamic (MHD) model, and are therefore in principle able to reproduce the MHD instabilities considered to be the responsible for ELMs, such as the interchange instability. The use of DALF model, that considers also the evolution of electromagnetic fluctuations, allows to have a direct comparison with experimental measurements. This approach allowed to derive the model from fundamental equations, avoiding a purely heuristic treatment.

The results of different experimental campaigns showed how both ELMs and the L-H transition, and therefore the evolution of LCOs into ELMs, feature a well defined dependence of frequency and amplitude with the external heating power and appear only over a well determined threshold of it. A minimal model, that considers a subset of the equations of the complete model, is able to summarize the dynamics of the complete system. The linear and nonlinear stability of the minimal model is analyzed, in order to determine the nature of the solution when variating the control parameter representing the external heating power.

The nonlinear structure of the equations implies that it is not possible to find an explicit analytical expression to study the temporal evolution of the interested variables. This led to rely on numerical integrations to simulate the expected behavior. Both the complete and the minimal model of ordinary differential equations are integrated through ODE solvers in Python, that allow to study the dynamics. The simulations of the reduced model confirms the analytical stability studies, while the simulations of the complete model are compared to the results of [1].

Chapter 1 is an introduction to fusion research, treated in its scientific and technological features in an historical context.

In Chapter 2, the main concepts relative to magnetically confined plasmas physics are introduced to explain the objective of this thesis.

In Chapter 3 a series of reduced models and the DALF equations, the theoretical instruments used for this thesis, are presented.

In Chapter 4, the interchange model for the plasma oscillations during the I-phase is derived from the the isothermal version of DALF.

In Chapter 5, a minimum model is isolated from the complete model, and is studied by means of nonlinear and numerical analysis. In the end, numerical simulations of the complete model are presented and described, comparing the predictions of the model with the results of [1].

Finally, in Chapter 6, the conclusions are summarized and a series of future issues are suggested.

The thesis is completed by a series of Appendixes on specific topics, whose reading is not required for an initial comprehension of the work.

This work was carried out during a seven months working period at Max-Planck-Institut für Plasmaphysik, Garching bei München (Germany), and the results were presented at the DPG-Frühjahrstagung 2016 at Hannover (Germany).

Estratto

In questa tesi viene studiata l'evoluzione del plasma di bordo (plasma edge) in un tokamak, una delle strutture candidate per la realizzazione della fusione termonucleare controllata come fonte energetica. In particolare, viene trattata la modellizzazione teorica e la simulazione numerica della dinamica del plasma, con l'obbiettivo di riprodurre e giustificare recenti risultati sperimentali del tokamak ASDEX Upgrade. In questi, viene osservata l'evoluzione di oscillazioni del plasma, chiamate Limit Cycle Oscillations (LCOs), in instabilità in grado di degradare il confinamento dell'energia nel reattore, chiamate Edge Localized Modes (ELMs), durante la transizione dall'L- all'H-mode.

La fusione nucleare si riferisce alla reazione nucleare per cui due nuclei leggeri si uniscono per formare un elemento più pesante. Per una serie di elementi, questo comporta un aumento dell'energia di legame per singolo nucleone e di conseguenza un rilascio di energia. La possibilità di sfruttare questo tipo di reazione per la produzione energetica in impianti di grandi dimensioni, ovvero l'utilizzo pacifico della fusione termonucleare controllata, è ancora argomento di ricerca. L'innesco della reazione di fusione nucleare richiede di mantenere i reagenti all'interno di un range di temperatura e densità ben definito. In queste condizioni, il combustibile si trova nello stato di plasma e le elevate temperature richieste rendono necessaria l'adozione di opportune strategie di confinamento per evitare danni al reattore. Una delle soluzioni tecnologiche più studiate per gli scopi della fusione termonucleare controllata è il tokamak, che permette di confinare magneticamente un plasma in una forma toroidale, sfruttando l'interazione questo stato della materia con campi elettromagnetici esterni e permettendo di raggiungere le condizioni desiderate.

L'H-mode è uno stato di un plasma confinato magneticamente in un tokamak, caratterizzato da migliori capacità di confinamento dell'energia rispetto all'L-mode. Questo stato ad elevato confinamento è raggiunto quando viene superata una soglia di potenza immessa nel reattore, sperimentalmente ben definita. L'H-mode è il regime candidato per la real-

izzazione della fusione termonucleare controllata in ITER, il progetto pilota internazionale attualmente in costruzione presso il CEA, Cadarache (Francia), in quanto si considera sia necessario per mantenere il plasma nel range di parametri richiesto. Il miglioramento della capacità di confinamento dell'H-mode è essenzialmente dovuto all'abbattimento del livello di turbolenza, e quindi del trasporto, nel plasma. Il fenomeno è ridotto ad una ristretta regione presso la superficie esterna del volume toroidale in cui il plasma è confinato. Questo fatto motiva l'interesse nel contesto della fusione termonucleare controllata per lo studio della dinamica del plasma di bordo, che è di conseguenza un argomento estremamente attuale nell'ambito ricerca sulla fisica dei plasmi.

La comprensione dell'H-mode è infatti tuttora incompleta. Una serie di instabilità cicliche localizzate nel plasma di bordo, le Edge Localized Modes (ELMs), appare quando il plasma si trova nello stato ad alto confinamento. Queste instabilità, che a seconda della gravità possono comportare un elevato rilascio di energia ed inficiare i benefici dell'H-mode, sono tuttora soggetto di studio. Inoltre, la transizione dall'L-mode all'H-mode non è ancora spiegata in modo univoco dal punto di vista fisico. Una serie di osservazioni sperimentali hanno permesso di caratterizzare l'I-phase [2], la fase intermedia tra L- ed H-mode, definendo delle oscillazioni caratteristiche del plasma, le Limit Cycle Oscillations (LCOs). Queste sembrano concordare con le soluzioni di modelli che prevedono la formazione di flussi macrosopici di plasma generati dalla turbolenza, detti Zonal Flows, in grado di abbattere quest'ultima e innescare la transizione. Recenti campagne sperimentali al tokamak ASDEX-Upgrade [1] hanno permesso di osservare una graduale evoluzione delle LCOs in ELMs, suggerendo una natura comune dei due fenomeni.

I modelli dinamici attualmente esistenti per la descrizione della transizione L-H o delle ELMs sono intrinsecamente semplificati. Ciò deriva innanzitutto dal fatto che nessun modello completo è stato finora in grado di riprodurre in maniera soddisfacente i fenomeni di interesse. Di conseguenza, i modelli ridotti spesso non sono derivati da equazioni fondamentali e contengono una serie di termini euristici che non sono sempre formalmente giustificati, rendendone difficoltosa una falsificazione sperimentale. Lo scopo di questi modelli è tuttavia fondamentale nell'indicare la direzione per una più approfondita analisi teorica o ricerca sperimentale, suggerendo possibili dinamiche per i fenomeni osservati.

In questo contesto si pone il lavoro sviluppato in questo manoscritto. L'obbiettivo di questa tesi è di proporre un modello dinamico il quale permetta di simulare l'evoluzione di LCOs in ELMs durante l'I-phase osservata in [1] nelle oscillazioni elettromagnetiche del plasma di ASDEX

Upgrade, e quindi sostenere l'ipotesi che i due fenomeni siano generati dallo stesso meccanismo fisico. Questo potrebbe dare accesso a una più profonda comprensione delle dinamiche dell'I-phase in quanto nessun modello esistente, neppure tra quelli ridotti, ha permesso di riprodurre la transizione interessata. I fenomeni di LCOs ed ELMs sono stati infatti finora trattati separatamente.

Il modello è derivato analiticamente dalle equazioni Drift-Alfvén (DALF), che descrivono fenomeni a bassa frequenza nei plasmi confinati magneticamente. Queste equazioni includono il modello magnetoidrodinamico (MHD), e sono dunque in principio in grado di riprodurre le instabilità MHD che sono considerate essere alla base delle ELMs. L'utilizzo del modello DALF, che considera anche l'evoluzione delle fluttuazioni elettromagnetiche, consente inoltre di avere un confronto diretto con le osservazioni sperimentali. Questo approccio ha permesso di costruire il modello sulla base di equazioni fondamentali, evitando una trattazione puramente euristica.

I risultati di diverse campagne sperimentali hanno mostrato che sia le ELMs che la transizione L-H, e quindi l'evoluzione da LCOs ad ELMs, presentano una ben definita dipendenza di frequenza e ampiezza al variare della potenza iniettata nel plasma dai sistemi di riscaldamento e appaiono solo oltre una determinata soglia di questa. Un modello minimo, costituito da un sottoinsieme delle equazioni del modello originale, è in grado di sintetizzare la dinamica complessiva del sistema completo. La stabilità lineare e nonlineare del sistema minimo è stata analizzata, in modo da determinare la natura delle soluzioni al variare di un parametro di controllo rappresentante la potenza iniettata dall'esterno del tokamak che raggiunga il plasma di bordo.

La struttura nonlineare delle equazioni del modello derivato implica che non sia possibile trovare una soluzione analitica esplicita per studiarne l'evoluzione temporale. Ciò ha condotto ad appoggiarsi alle integrazioni numeriche per la simulazione del comportamento previsto. Sia il modello completo che quello minimo, costituiti da equazioni differenziali ordinarie, sono stati integrati con l'uso di ODE solvers di Python, che hanno fatto in modo di poterne studiarne la dinamica. Le simulazioni del modello minimo hanno permesso di confermare i risultati analitici sulla stabilità, mentre le simulazioni del modello completo hanno permesso di avere un confronto con i risultati sperimentali di [1].

La tesi è divisa in tre parti. I primi due capitoli costituiscono una introduzione al tema trattato, presentando gli argomenti necessari per definire nello specifico gli obiettivi della tesi. Il terzo capitolo presenta gli strumenti teorici usati in seguito per la derivazione del modello dinamico,

in modo da enfatizzare i fondamenti su cui questo è basato. Il quarto e il quinto capitolo presentano i risultati di questo lavoro, includendo la derivazione e la simulazione del modello, assieme ai confronti con risultati sperimentali, e nel sesto capitolo sono contenute le conclusioni della tesi.

Il Capitolo 1 costituisce un'introduzione al tema della ricerca sulla fusione nucleare, trattata nei suoi aspetti scientifici e tecnologici in un contesto storico. Fin dagli inizi degli studi sulla fusione nucleare, introdotta per motivare la generazione di energia nelle stelle, l'interesse è stato diretto verso una possibile applicazione per la produzione energetica sulla Terra. Nonostante la prima applicazione tecnologica sia stata la bomba termonucleare, presto la ricerca si è spostata sullo sfruttamento pacifico di questa forma di energia. Nella trattazione viene chiarito come trattare la materia nello stato di plasma sia necessario per ricavare un guadagno energetico in un reattore. Il Criterio di Lawson, sviluppato dall'omonimo ingegnere inglese, è introdotto in quanto costituisce tuttora l'obbiettivo di parametri del plasma verso cui la ricerca è diretta per la realizzazione della fusione termonucleare. La competizione tra i due blocchi generata durante la Guerra Fredda ha portato allo sviluppo in Unione Sovietica del tokamak per il confinamento magnetico del plasma. Questa promettente soluzione tecnologica presenta tuttavia una serie di problematiche relative al trasporto di energia e instabilità del plasma, ancora oggi non pienamente risolte e trattate in questa tesi. La ricerca si è spostata sul piano di collaborazione internazionale, culminando nell'accordo tra le due superpotenze per la realizzazione di ITER, il cui scopo è dimostrare la fattibilità della fusione nucleare di deuterio e trizio per la produzione energetica. Un confronto tra ITER e ASDEX Upgrade, il tokamak presente al Max-Planck-Institut für Plasmaphysik, Garching bei München (Germania), è presentato a conclusione di questo capitolo.

Il Capitolo 2 vengono introdotti i principali concetti relativi alla fisica dei plasmi confinati magneticamente, necessari per trattare i fenomeni di plasma di bordo analizzati in questa tesi. Il capitolo inizia con la discussione del modello MHD, del modello a due fluidi e dei drift delle singole particelle cariche in un plasma magnetizzato. Differenti approcci per il trasporto nei plasmi sono analizzati, ponendo un enfasi particolare sul trasporto anomalo, in cui la turbolenza e i moti collettivi tipici dei plasmi hanno un ruolo dominante. L'origine microscopica della turbolenza è quindi trattata, mettendo in luce un'importante instabilità dei plasmi confinati magneticamente: l'instabilità interchange, in grado di generare un elevato trasporto anomalo. É in seguito introdotta la transizione L-H, soggetto specifico dell'analisi in questa tesi. Viene sottolineato come il miglior confinamento dell' energia durante l'H-mode sia

dovuto all'abbattimento del livello di turbolenza. Questo fenomeno è possibile grazie a flussi di plasma presenti nella regione di bordo originati dai ripidi profili di densità e temperatura del plasma caratteristici dell'H-mode. La transizione a partire dall'L-mode rimane soggetto di studio, per quanto alcune teorie sostengano un ruolo fondamentale dei Zonal Flows, la cui dinamica è spiegata nel capitolo. Le peculiarità dell'I-phase sono quindi illustrate, con particolare attenzione alla presenza di LCOs, che vengono presentate come oscillazioni del plasma attraverso i risultati di osservazioni sperimentali. Vengono poi introdotte le ELMs come instabilità cicliche del plasma in grado di incrementare il trasporto anomalo nella fase instabile e abbattere i gradienti di densità e temperatura del plasma di bordo, causando elevati rilasci di energia e particelle che vanno a sfogarsi sulla parete del reattore, in particolare nella regione del divertore. Al termine di questo capitolo vengono presentati i risultati di [1], i quali, osservando la transizione da LCOs ad ELMs, costituiscono la motivazione per questo lavoro. L'obiettivo di questa tesi è quindi discusso in dettaglio: la possibilità di riprodurre la transizione da LCOs ad ELMs con un modello di equazioni differenziali derivate da modelli fondamentali per suggerire un unico meccanismo fisico alla base dei due fenomeni.

Nel Capitolo 3 sono illustrati gli strumenti teorici utilizzati per lo sviluppo del modello per le oscillazioni del plasma derivato in questa tesi. Nella prima parte del capitolo sono introdotti una serie di modelli ridotti per la simulazione del plasma di bordo. Questi semplici modelli zerodimensionali (in cui l'unica variabile indipendente è il tempo) hanno permesso di orientare la semplificazione delle equazioni fondamentali per la derivazione del modello presentato in questa tesi. Questi infatti trattano sia la transizione L-H che le ELMs, seppure nessuno di essi le tratti contemporaneamente, né preveda l'evoluzione delle prime nelle seconde. Diverse caratteristiche sono comuni a tutti i modelli: il gradiente di pressione del plasma di bordo evolve e collassa a seguito dello sviluppo di un'instabilità pressure-driven. Un parametro di controllo rappresentante il flusso di energia/particelle verso il plasma di bordo agisce come parametro di controllo, definendo soluzioni stazionarie o cicliche. Le LCOs sono identificate a partire dalla dinamica dei Zonal Flows, se inclusa nel modello. Nella seconda parte del capitolo vengono presentate le equazioni DALF, introducendone le applicazioni nello studio della fisica dei plasmi e le ipotesi fondamentali per la loro validità. Queste equazioni, particolarmente adatte a descrivere i fenomeni di interesse, sono la base per la derivazione del modello di questa tesi.

Nel Capitolo 4 viene presentata la derivazione del modello completo. Il modello DALF3, la versione isoterma e adimensionale delle equazioni

DALF, viene introdotto con una serie di considerazioni preliminari. Sono quindi presentate le ipotesi usate per la riduzione del modello DALF3 a un modello zerodimensionale: la trattazione è fatta considerando una geometria semplificata (slab) e la dinamica è focalizzata sulla destabilizzazione di un singolo modo del plasma su una delle superfici razionali, le più instabili per i modi interchange, potendo così trascurare la dinamica parallela alle linee di campo magnetico del tokamak. Il modello interchange viene quindi derivato, ottenendo un'equazione per il gradiente di pressione al plasma di bordo, la descrizione dell'evoluzione accoppiata del modo MHD, la dinamica dei Zonal Flows e delle fluttuazioni magnetiche. Una serie di considerazioni energetiche permettono di giustificare un termine dissipativo legato alla turbolenza, necessario per un'evoluzione stabile del sistema.

Nel Capitolo 5, una serie di analisi e simulazioni sono effettuate con il supporto di Python e costituiscono i risultati del lavoro di tesi. Ciò risulta necessario per avere una comprensione della dinamica nonlineare del sistema. Il modello completo è derivato dalle equazioni DALF per riprodurre, sulla base di equazioni fondamentali, l'evoluzione delle variabili di interesse per la transizione interessata. E' tuttavia possibile osservare che la dinamica complessiva è dettata da un sottoinsieme di equazioni del modello originale, che non sono accoppiate alle rimanenti per le quali la dinamica è in questo senso passiva. Questo sottoinsieme di equazioni è isolato dal modello completo e costituisce un modello minimo. Nel capitolo, l'analisi nonlineare del modello minimo è effettuata per definire analiticamente la natura delle soluzioni: la destabilizzazione dei punti fissi comporta la presenza di una biforcazione supercritica di Hopf-Andronov. La natura di questo tipo di biforcazioni, che appaiono a seguito della variazione di un parametro rappresentante la potenza iniettata dall'esterno che raggiunga il plasma di bordo, implica la presenza di una soluzione periodica a cui il sistema tende a convergere. Le simulazioni numeriche del modello minimo sono usate per confermare lo studio analitico delle soluzioni e avere una comprensione della evoluzione temporale delle variabili. In seguito, attraverso una scelta opportuna dei valore dei parametri, il modello completo viene integrato numericamente per studiare l'evoluzione prevista durante l'I-phase. Una serie di confronti con i risultati sperimentali di [1] sono a questo punto possibili, sia a livello qualitativo che quantitativo.

Nel Capitolo 6 sono riassunte le conclusioni di questo lavoro e, evidenziando i limiti del modello, una serie di possibili sviluppi futuri sono suggeriti. Una completa rinormalizzazione del sistema è necessaria per un confronto quantitativo completo. Una simulazione della turbolenza può essere inserita considerando la presenza di più di un modo. Inoltre,

essendo derivato da equazioni fondamentali, il modello può essere implementato per considerare effetti derivanti dall'andamento spaziale delle variabili di interesse. Questo permetterebbe innanzitutto di includere nella descrizione la corrente di Bootstrap, la quale è ritenuta essere responsabile per la crescita instabile di modi current-driven. Di conseguenza, il modello potrebbe essere in grado di simulare in modo autoconsistente la destabilizzazione del modo peeling-ballooning, che è considerato a livello teorico essere il meccanismo fondamentale delle ELMs.

La trattazione è completata da una serie di appendici che trattano argomenti specifici, approfondimenti e integrazioni, i quali non sono essenziali per una prima lettura del lavoro di tesi. Nell'Appendice A, viene giustificata l'ipotesi di quasineutralità del plasma spesso considerata nel lavoro. Nell'Appendice B, vengono presentati il trasporto classico e neoclassico, trattati attraverso la teoria collisionale del random walk. Nell'appendice C è spiegata l'instabilità da driftwave, un'ulteriore instabilità oltre a quella interchange inclusa nel modello DALF e considerata anch'essa responsabile per la formazione dello stato turbolento nei plasmi. Nell'appendice D, ulteriori modelli ridotti per la descrizione del plasma di bordo sono inclusi per illustrare descrizioni alternative a quelle presentate nel capitolo 4. Nell'Appendice E, infine, la derivazione completa delle equazioni DALF a partire dal modello a due fluidi per il plasma è presentata.

Questa tesi è stata sviluppata in un periodo di sette mesi al Max-Planck-Institut für Plasmaphysik, Garching bei München (Germania), dove si trova il tokamak ASDEX Upgrade.

Chapter 1

A brief history of fusion research

> "A star is drawing on some vast reservoir of [...] sub-atomic energy which, it is known, exists abundantly in all matter; we sometimes dream that man will one day learn how to release it and use it for his service."
>
> — Arthur Eddington

Nuclear fusion refers to the nuclear reaction by which two lighter nuclei merge to form a heavier element. The study of this topic started from basic questions about the source of energy in the stars, developed sharply during the golden age of nuclear physics and was eventually integrated in the research for energy production from nuclear fusion reactions. Intense studies from the '50s focused on the peaceful exploitation of this form of energy, in order to rely on a long term clean and safe resource for electricity production in large base load power plants. This required to design machines able to handle the plasma state of matter, the necessary environment for nuclear fusion reactions sustained by high kinetic energy of the particles involved. However, as will be introduced in this chapter, theoretical and technical challenges to overcome turned out to be harsh and up to present days no fusion reactor was built.

The aim of this chapter is to go through milestones and difficulties of this quest for a new energy source from the origin to present time, while introducing basic concepts used in this thesis. This will be done by means of a review of the scientific and technological basis framed in a historical background, in order to enlighten the deep ties between science, technique and society.

1.1 Scientific roots of nuclear fusion

By the end of the XIX Century, Physics seemed to reach a universal comprehension of Nature. In particular, the deep connections between thermodynamics and kinetic theory were considered to give a satisfying explanation of macro- and microscopic phenomena; however, a series of issues had still to be cleared up. One of the fields of friction was geology. William Thomson, Lord Kelvin convinced the geologists that Earth could not have existed for an infinite length of time and tried to estimate the years that it would have required to cool down to its current state. His figure of 20-40 million years, though, was not only refused by geologists, but also not sufficient for Charles Darwin to comply with his evolution theory. In another field, astronomy, Hermann von Helmholtz evaluated that any chemical energy was inadequate as a source for the Sun radiation. Furthermore, a gravitational contraction would have accounted for only 20 million years of energy output.

The reason for both the seemingly far incoherences was into the axiom of the atom immutability. In 1896 Antoine Henri Becquerel discovered the natural radioactivity of Uranium, breaking this paradigm. The equivalence of mass and energy, introduced shortly after by Albert Einstein during the Annus Mirabilis 1905, allowed to consider a new form of subatomic energy, released during Uranium decay. This energy source could justify Earth temperature and therefore physics, geology and biology agreed on the age of Earth to be around the billion years.

The Sun of course could not be younger than Earth. In 1920, Aston measured the mass defect in several isotopes and Arthur Eddington was the first to suggest the conversion of hydrogen into helium as the main energy source of the Sun. Few years later, in 1929 Atkinson and Houtermans invoked Gamow's quantum theory of barrier penetration introducing the concept of fusion to explain the conversion. At that time, the structure of nucleus was still unclear. The following discoveries in 1932 of the deuterium (^2H) by Urey and the neutron by Chadwick, followed by the 1934 theory of β decay by Fermi, and the related introduction of the weak interaction, were turning points of nuclear physics. In 1936, Atkinson was then able to suggest the beta decay, inside a nucleus, of a proton into a neutron, and the subsequent interaction with another proton to form deuterium, as the first step of the proton-proton chain [1]. The global reaction reads:

$$4p \rightarrow {}^4He + 2e^+ + 2\nu + \gamma + 26.7\,\text{MeV} \tag{1.1}$$

[1] energy produced in the reaction is expressed in MeV where $1\ eV = 1.602 \times 10^{-19} J$.

In 1938, von Weizsäcker defined the CNO cycle, introduced independently by Bethe, who was also able to compute the reaction rate of the two cycles. Finally, the following year, Bethe published a paper containing the complete theory of nuclear fusion, describing the merging of nuclei with the possibility to release large amount of energy from the mass defect, if the products are lighter than the total mass of the reactants.

These reactions are therefore considered to be responsible for the energy release in stars, where nuclear fuel is held together by gravity that reaches a balance with the pressure due to the emitted radiation. The bottleneck given by the reaction rate of the p-p chain is the main reason for their long life compared to Earth life [3]. Environment in stars allowing thermonuclear fusion, the uphold of nuclear fusion reactions due to high temperatures with a net release of energy, is characterized by physical parameters (i.e. temperature and density) such that matter exists in the so-called plasma state.

1.2 The foundation of plasma physics

After an initial period at the beginning of XX century, during which development of quantum, relativistic, atomic, nuclear and solid state physics got the mainstream attention of scientists, classical XIX century physics made a comeback when electromagnetism, fluid mechanics and kinetic theory were merged together to describe the behavior of the fourth state of matter. The word "Plasma" was first introduced by the chemist Irvin Langmuir in 1928, while describing the physical behavior of a gas discharge [4].

Plasma is a physical system formed of a macroscopic number of charged particles, characterized by high conductivity and globally neutral, but not locally. These qualities reflect the fact that a plasma is dominated by long-range electromagnetic collective effects rather than single particles interactions. In the same paper, Langmuir also introduced the fundamental concepts of the Debye Length and plasma frequency. The first is used to define the thickness of the layer over which electric field due to a single charge in a plasma is screened by a locally increased charge density of the opposite sign. The second is a crucial parameter for determining dynamic plasma properties, e.g. the response of a plasma to an external electromagnetic field. Both of them are an expression of the above mentioned collective behavior, and the most important theories to describe the physic of plasmas follow a Eulerian approach, rather than concentrating on single particle dynamics through a Lagrangian approach.

The description of a plasma, consequently, can be done not only through the study of its single components, but also by the means of a more general treatment based on statistical mechanics. This consists in a kinetic approach that considers an extension of the Boltzmann equation to include averaged self-consistent electromagnetic fields to describe a collisionless plasma. Such a way to compute an evolution equation for the distribution function was performed by Anatoly Vlasov, while Lev Landau derived in a formula for the collision term and studied the collisionless damping of waves in plasmas due to particles whose thermal velocity is near the phase velocity. Both physicists performed their works in the Soviet Union, in the years before, during and after the Second World War, between 1936 and 1946.

A prominent role in early plasma physics was played by astrophysicists: the topic for their field is of great interest since over 99% of the universe matter is in plasma state [5]. Swedish astrophysicist Hannes Alfvén, who already developed the concept of guiding-center orbits to describe the dynamics of single charged particles in Earth's magnetic field to explain polar light, described the astrophysical plasmas as conducting fluids. This approach, valid for appropriately large space and time scales, was published in the 1950 book *Cosmical Electrodynamics* and was named Magnetohydrodynamics (or MHD) to underline the leading role of magnetic forces on the dynamics compared to the electric ones. For this contribution he was awarded the Nobel price in 1970. A key figure emerging from this treatment is the so-called frozen-in magnetic field lines, directly connected to MHD or Alfvén waves. A related concept is the magnetic pressure, which can be able to compensate the kinetic pressure of the plasma leading to magnetic confinement, that is an equilibrium configuration which to persist needs to be stable.

In the same year in which Alfvén published his work, another astrophysicist, Arnulf Schlüter developed a two-fluid theory, in which plasma is separately described in its ion and electron components, each constituting a charged conducting continuum exchanging energy and momentum with the other. This approach was one of the crucial steps to reconcile single particle description and fluid description, since it can be considered an intermediate step between the two. Both MHD and two-fluids models can be derived from a kinetic approach, as will be pointed in Chapter 2.

Arnulf Schlüter was a member of the Max Planck Society, founded in 1948 to reform the Kaiser Wilhelm Society as the German association of research institutes after the Second World War. It was initially based in Göttingen (Germany), led by the German physicist Werner Heisenberg and named after the former honorary president of the KWS, Max Planck,

who died the year before [6]. In that period, Germany was not allowed to develop an autonomous nuclear program. The institute was anyway able to keep performing its studies, at a level of basic science but the Max-Planck-Institut für Plasmaphysik, the branch dedicated to nuclear fusion study and application, was founded only in 1960. These limitations of course derived from the tight controls of nuclear programs around the world following atomic bomb invention. Fission first technical application was a reactor: the Fermi pile of 1942, whose objective was to show the possibility of achieving criticality and releasing a controlled amount of power. Despite being only a step in the Manhattan project, whose aim was the A-bomb realization, it was the early foundation of nuclear power pacific exploitation for civil purposes. On the contrary, first artificial release of fusion energy on a large scale was integrally dedicated to military objectives: the first thermonuclear bomb from the USA was tested in 1952 on the Enewetak Atoll, soon followed in 1953 by the soviet equivalent developed by Sakharov and Kurchatov among the others, with a contribution from Landau also. In the first years of the Cold War, plasma physics research was switching its focus from the cosmic and gas discharge studies towards nuclear fusion research. Despite major applications, at least in the beginning, were warfare related and the funding was not comparable with the one spent for Manhattan Project [7], an organized effort began under the shroud of secrecy on the two sides of the Iron Curtain with the purpose of exploiting fusion energy for controlled power production.

1.3 Fusion reactor basis

The processes able to sustain a star energy balance through fusion reaction for billion years are utterly inadequate for Earth application. Despite the great quantity of energy released, the averaged power density in a star like the Sun is $0.27\,MW/m^3$. This value has to be compared, for example, to the equivalent parameter for an existing pressurized water reactor (PWR) nuclear power plant which is close to $100\,MW/m^3$. Just for purely economic reasons, related to the plant cost and dimension, a fusion reactor cannot be designed for such a low power density to be competitive with existing technology. Furthermore, the main mechanism by which a star is able to sustain the fusion reaction maintaining sufficiently high temperature and density is gravitational attraction and confinement. This is of course not reproducible on Earth due to the enormous quantity of

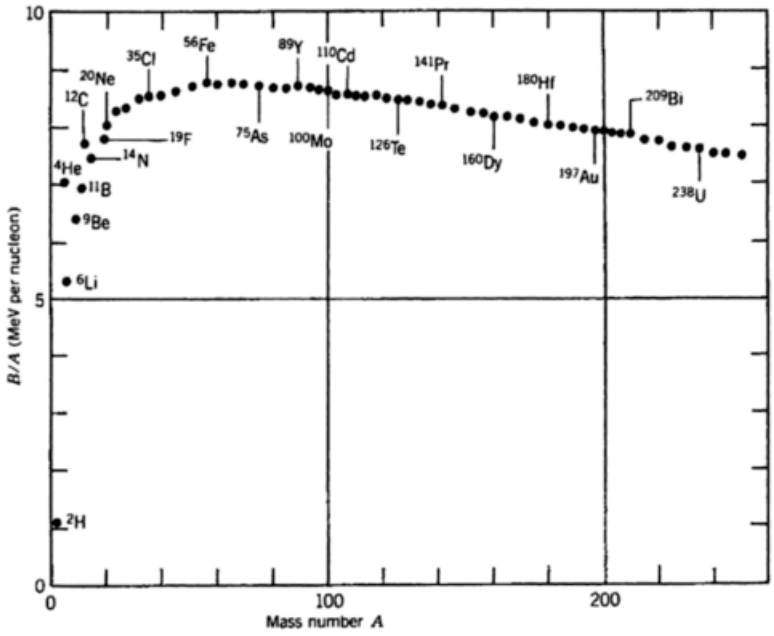

Figure 1.1: Binding energy per nucleon B/A as a function of the nuclear mass number A (fig. 3.16 [3])

matter involved[2]. Finally, charged particles accelerating are subjected to Bremsstrahlung, losing their kinetic energy in electromagnetic radiation. This mechanism is critical in a fusion reactor, being a constant and non avoidable energy loss pattern, since reabsorption mean free path exceeds any conceivable device. In stars, instead, this problem does not exist since the same mean free path is small compared to their characteristic dimension.

Exploitation of nuclear fusion as a peaceful energy source on Earth, therefore, is to be designed following a different scheme, but the main physical mechanism remains the same. Two positively charged nuclei need to be taken sufficiently close together in order to let the short range ($\approx 10^{-15}m$) nuclear force overcome the long range Coulomb repulsion between them. For the series of elements in which fusion increases the binding energy (see Fig. 1.1) between reactants and products, potential energy is released in the form of kinetic energy. Quantum tunnelling effect is involved in coping with the electrostatic barrier and consequently the event is inherently stochastic. The probability of any reaction to happen

[2]gravity, being the weakest of the known fundamental interaction, is largely negligible when considering reduced amounts of matter.

depends on the relative initial kinetic energy E of the colliding particles (reactants), and is quantified through the *cross-section* denoted by $\sigma(E)$, specific for the considered reaction. This quantity is measured in "barns" (b) where $1b = 10^{-24}cm^2$. The most common interpretation is that a target nucleus offers to the colliding one an effective area for the reaction on the reaction plane. In this picture, under the assumption of a particle flux ϕ impinging perpendicularly on a layer of target atoms with density n_t, the reaction rate per unit volume can be computed as

$$R = n_t \langle \sigma(v) n(v) v \rangle \, m^{-3} s^{-1} \tag{1.2}$$

Where the square brackets $\langle\rangle$ mean average over the whole velocity space, since one can consider the particles velocity v characterized by a distribution function and $\phi = \langle n(v)v \rangle$. The systematic investigation of nuclear reactions by means of particle accelerators developed during the first half of the century allowed to define quantitatively the fusion cross section dependence on energy for various elements. This was performed accelerating charged particles against conveniently prepared targets and measuring the effect of the impact on the flux. While the cross section for the p-p cycle main reaction $p + p \rightarrow D + e^- + 0.42\,\text{MeV}$ is too small to be measured experimentally and needs to be calculated from standard weak interaction theory [8], it was possible to identify a series of fusion reactions with promising characteristics for power production. Specifically, the desired qualities are high energy yield and cross section, both of which related to design a reactor with satisfying averaged power density. For these reasons, the most suitable elements are the lightest (low-Z) ones.

The considered reactions are:

$$\begin{gathered} D + D \rightarrow T + p + 4.0\,\text{MeV} \\ D + D \rightarrow {}^3He + n + 5.49\,\text{MeV} \\ D + T \rightarrow {}^4He + n + 17.6\,\text{MeV} \\ D + {}^3He \rightarrow {}^4He + p + 18.3\,\text{MeV} \end{gathered}$$

Here D is deuteron while T is triton, both nuclei of isotopes of hydrogen. The first is the nucleus of ${}^2H$ (deuterium) while the second of ${}^3H$ (tritium). Deuterium is a stable element, relatively abundant in nature, especially in ocean water. These properties, together with the low extraction cost, got the initial attention of fusion scientists and engineers towards the D-D reaction. Tritium instead is a radioactive element with

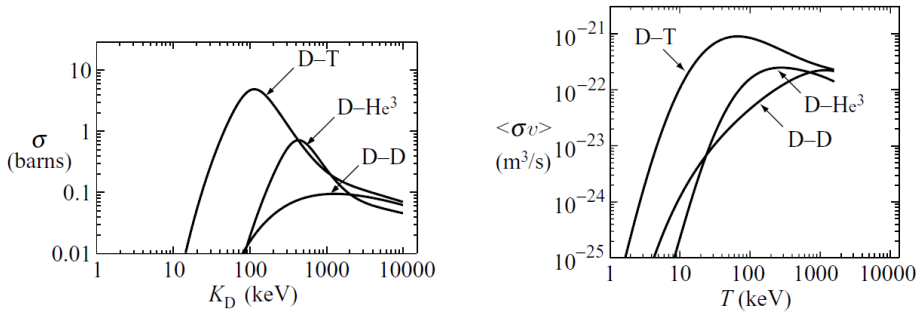

Figure 1.2: (a) Experimentally measured cross sections for the D-T,D-H_e^3 and D-D fusion reactions as a function of the deuteron energy $K_D = m_D v_D^2$ (fig. 3.10 [9]); (b) Velocity averaged cross section $< \sigma v >$ for D-T, D-^{3}He, D-D fusion reactions as function of temperature (fig. 3.11 [9]).

an half-life of 12 years and consequently needs to be produced artificially to be exploited since it is not present in nature. Despite this drawback, the D-T reaction was eventually preferred due to the higher cross section at low energies and the high energy yield. This is due to the fact that a product of the fusion reaction is an α particle (the nucleus of ^4He): being a nuclide with a double magic number of nucleons, its binding energy is especially high and a big amount of energy is released as byproduct of the reaction. As a consequence of momentum and energy conservation, kinetic energy is divided among the products: the neutron receives *14.1 MeV*, while the α particle the remaining *3.5 MeV*.

Accelerating a charged particle flux against a target allowed to experimentally study nuclear fusion cross sections, but it is not possible to apply this technique for a positive energy balance, as power generation for civil purposes requires. The accelerated particles, in fact, would transfer their energy to the target's electron and the energy gained from the few fusion reactions would not compensate the one needed to accelerate all the nuclei that would just slow down and stop in the target. Another scheme to reach fusion condition is to heat a designed quantity of fuel such that random collision between particles deriving from thermal agitation is sufficiently energetic to overcome Coulomb repulsion and let the strong nuclear force prevail for a sufficient number of impacts.

Consider the fuel as a mixture of deuterium and tritium at thermal equilibrium and assume a maxwellian velocity distribution. It can be seen from Fig. 1.2(b) how the curve peaks at a value around $15\,keV$,

around which the reaction rate at fixed density would be maximized. Way before reaching such conditions, the mixture of hydrogen isotopes becomes strongly ionized, since the ionization energy for a single hydrogen atom is $15\,eV$, over 1000 times inferior[3]. In such conditions, plasma state is reached, in which thermal energy allows the efficient production of nuclear reactions: a thermonuclear plasma.

Controlled thermonuclear fusion refers to a process able to maintain the reaction of nuclear fusion for a prolonged period of time, releasing a desired quantity of power.

Energy harvesting for civil power production can be performed together with tritium breeding outside the reaction chamber. In magnetic confinement designs the α particle remains in the plasma, helping the sustainment of high temperature, while the neutron is able to escape the magnetic cage. Lithium intentionally placed in the wall surrounding the plasma undergoes the neutron-induced reactions:

$$
\begin{aligned}
{}^{6}Li \; + \; n \; \rightarrow \; {}^{4}He \; + \; T + \; 4.8\,\mathrm{MeV}, \\
{}^{7}Li \; + \; n \; \rightarrow \; {}^{4}He + \; T \; + \; n \; - \; 2.5\,\mathrm{MeV}.
\end{aligned}
$$

Net energy produced in these reaction taking place in the solid blanket is able to be converted into heat by slowing down of reactions products and used in a thermodynamic cycle to drive a gas or steam turbine suitable for electricity production. Lithium, necessary for the mentioned step of the process, is not a resource bottleneck for the overall cycle since its abundance on Earth is 0.17 ppm (parts per million) in ocean water and widely available in salt deposits[4]. Furthermore, some 150 ppm of natural hydrogen is ${}^{2}H$. In this way, the amount of deuterium and lithium available in nature is able to support any foreseeable demand of fusion energy for centuries. The fist charge of Tritium, instead, can be obtained from present nuclear power plants, since this isotope of hydrogen is a low yield byproduct of several kind of fission reactors.

[3] due to the velocity distribution, there will always be ions with $E < 15eV$ and consequently able to neutralize, but the vast majority of constituents will be free ions and electrons

[4] Lithium is however widely used in modern technology (i.e. batteries) and this can limit the overall availability

1.4 Geneve 1958: Lawson criterion and Bohm diffusion

Suitable concepts had to be developed, in order to make the plasma reach sufficiently high temperatures and ignite nuclear fusion in a controlled way. In a simple arc during a gas discharge, the degree of ionization is low and ion temperature cannot rise sufficiently. Therefore, a series of innovative schemes and proposals were investigated during the '40s and the '50s. The majority of the effort was based on the concept of magnetic confinement, deriving from Alfvén MHD studies. The possibility to generate appropriate currents and therefore magnetic fields allowed to "pinch" a fully ionized plasma and isolate it from the wall, counterbalancing its tendency to expand due to pressure as

$$\nabla p = \mathbf{J} \times \mathbf{B}.$$

Small experiments, settling the base for magnetic configurations as linear pinch, toroidal pinch and magnetic mirror were initiated almost independently in US, USSR and UK. Some more elaborated concepts began to be developed, such as the tokamak, studied by Sakharov and Tamm in Soviet Union, and the stellerator under Lyman Spitzer's direction in the USA. In the tense atmosphere of the first decade of Cold War, all nuclear-related project were classified. Few information exchange was possible between East and West, and often also between members of the same side. At the 1955 "Atoms for Peace" [5] conference in Geneve, for the peaceful use of atomic energy, fusion was mentioned only in the opening address, and few or none discussion was developed on the theme. Despite the hope for a quick success suggested by early design of a complete power plant, as with fission, the main experiments of both sides led to unsatisfying results. It was soon discovered that pressure equilibrium could be unstable, leading to fast losses of the plasma as it moved and touched the wall breaking the confinement. Therefore, it was not possible to exceed energies of $\sim 100\,eV$, too low to start consistent nuclear fusion reactions.

Another parameter that could be experimentally measured is the confinement time for thermal energy that commonly defined as τ_E. Consider volume V with surface S containing plasma at an average pressure p. A specific energy flux S_k is defined as the rate at which a plasma with

[5] named after the speech delivered by U.S. President Dwight D. Eisenhower to the UN General Assembly in New York City on December 8, 1953.

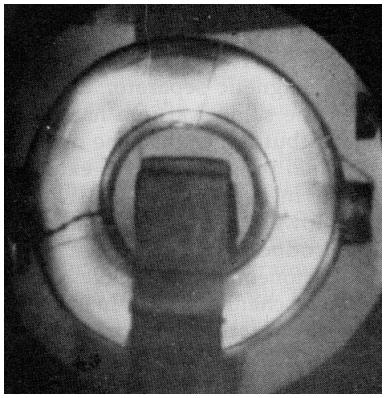

Figure 1.3: Photograph of an unstable toroidal pinch discharge in 1957 with current $1.3kA$ in a xenon plasma. The glass tube has a major radius of about $0.3m$. The instability is seen as a sinusoidal distortion of the plasma along the toroidal direction (fig. 1.8 [10])

internal energy $(3/2)p$ is released to the surrounding due to heat exchange

$$S_k = \frac{1}{V}\int \mathbf{q}\, d\mathbf{S} = \frac{3}{2}\frac{p}{\tau_E}. \tag{1.3}$$

The energy confinement time therefore describes the characteristic time that a plasma needs to reach thermodynamic equibrium with the environment. This is crucial to ignite fusion since the system needs to remain at sufficient high temperature for an extended period of time, as it will be derived.

Only in particular situations and due to single scientist's initiative, the secrecy was broken. On occasion of a Soviet state visit in Great Britain in 1956, Kurchatov, director of the Institute of Atomic Energy in Moscow, was allowed to hold a lecture in Harwell, the British center for nuclear related research. For the first time, there was the opportunity to express interest for an international collaboration, and he released a series of details on Soviet's progresses, making it clear how they were working on toroidal pinches. In that occasion, he presented also a series of critical points about plasma instabilities (see Fig. 1.3). Such a collaboration is even more remarkable, given the increasing tension of that time: just two years before the Hungarian revolution was crushed and two months later Khrushchev was to launch the Berlin ultimatum.

In the following years, both in public and in the scientific community, pressure towards declassification increased, and censorship on papers moving on the other side of the Iron Curtain was released. Finally, in September 1958, the international meeting for Peaceful use of Atomic En-

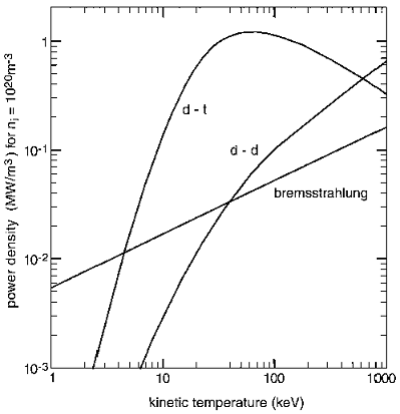

Figure 1.4: power density for the fusion reaction for a pure deuterium plasma and a 50% D and 50% T mixture as a function of plasma temperature compared with Bremsstrahlung (fig. 1.9 [10])

ergy again in Geneve led to an organized unveiling of important discoveries and inventions of both sides. For example Lyman Spitzer, that introduced the concept of rotational transform and derived the resistivity of plasma as a function of its temperature, presented there the Model C Stellarator: an evolution of the model A that he secretly designed already in 1951.

Scientists from both East and West were scared that on the opposite side problems had been already solved and their presentation would look obsolete. Eventually, the main discovery was that both sides went through the same difficulties in trying to study and realize thermonuclear fusion: plasma instabilities leading to reduced confinement time were unavoidable and no neutron deriving from fusion reaction in the experiments was detected. This experience started a basis for an enduring international collaboration.

An enlightening example of the situation was the overlapping of studies and discoveries. During a session of the IAU Symposium on Electromagnetic Phenomena in Cosmical Physics of Stockholm in 1956, Lev Artsimovich summarized a series of papers from *Atomnaya Energya*. He opened his paper with an introduction in which he derived a criterion for steady state power generation in a D-D reactor, based on specific relationship between n, T and τ_i where the last was the ion lifetime in a reacting plasma [10]. This was in essence the famous criterion derived the year before by John D. Lawson but secreted and declassified to be published only in 1957 [11].

A major concept derived from the work is an ignition condition for a self-sustaining burning plasma. Here a simple derivation is presented.

Consider a D-T plasma with equal number density of deuterium and tritium $n_D = n_T = n/2$ in thermodynamic equilibrium at temperature T. With these assumptions, the power density released by fusion reactions in plasma can be written as the product of reaction rate (reactions per volume unit per second from Eq (1.2)) and energy release per single fusion E_{DT}

$$S_f \;=\; \frac{n^2}{4}\langle\sigma v\rangle E_{DT} = \frac{1}{4}n^2\langle\sigma v\rangle\,(E_\alpha + E_n) \;=\; S_\alpha + S_n. \tag{1.4}$$

Where E_{DT} was split among the α particle and the neutron. Consider a simplified energy balance for the whole plasma in a reactor. The energy increase is due to fusion reactions $S_\alpha + S_n$ and external heating S_h. The energy reduction is due to loss from heat conduction S_k described in Eq (1.3) and from Bremsstrahlung radiation that evolves as as $S_B \sim n^2T^{1/2}$ and is extremely reduced only by the peak of S_f, as can be seen in Fig. 1.4. Considering a magnetic confinement design, where the α particle remains in the magnetic cage, the neutron escapes, causing an effective loss for plasma energy. In stationary state, when the neutron generated equal the lost, the balance reads:

$$S_h \;+\; S_\alpha \;+\; S_n \;=\; S_k \;+\; S_B \;+\; S_n. \tag{1.5}$$

The ignition condition, in which external heating is not needed to sustain the fusion reaction ($S_h = 0$), leads to a constraint on p and τ_E. This is expressed by an inequality that can be directly derived from Eq (1.5) when considering the power generated to be bigger than the lost

$$p\,\tau_E \geq K_I\,\frac{T^2}{\langle\sigma v\rangle}, \tag{1.6}$$

where K_I is a constant whose value depends from the unit of measurement considered. Note that the right hand side of the inequality is a function of the temperature only. This can be set at a minimum, since it depends inversely on the averaged product $\langle\sigma v\rangle$. Computing such a value, the optimal working point is obtained

$$\begin{aligned}(p\,\tau_E)_{min} &= 8.3\ atm\,s,\\ T_{min} &= 15\ keV.\end{aligned} \tag{1.7}$$

The Lawson criterion is able to reduce the complex and multiphysics process of thermonuclear fusion in an optimization of just three parameters. Since then, every experimental result was compared to this simple figure through Lawson diagrams. The charm of this approach is its global

nature that can be summarized in two points. First of all, such a general treatment is valid for any technological configuration used to reach ignition. Furthermore, it is able to relate τ_E to the transport due to particles or energy or even the pulse duration showing great flexibility.

In transport theory, movement and interaction of single microscopic particles (globally an inherently stochastic process), can be described as continuum diffusion of macroscopic variables such as a concentration profile. In this case, a crucial parameter is the so-called *diffusion coefficient* that characterizes the whole process, and therefore is an important step when modeling transport phenomena. In general, it is defied as

$$D = \frac{L^2}{\tau},$$

where L is a step length in a random walk model while τ is a time between two steps [12], both due to collisions between particles. Macroscopically, one can consider also Δx as the system dimension and τ equivalent to the characteristic confinement time already discussed in Eq (1.3). Consequently, when D is known, it is possible to derive τ by just inverting the above expression. This can be done not only for mass diffusion, but also for heat diffusivity, as will be shown in 2.2 For a theoretical motivation of the experimentally measured τ_E, it was initially linked to the "classical" resistive particle diffusion, considered the dominant loss mechanism in a thermonuclear plasma. Such phenomena would lead to a diffusion coefficient evolving as

$$D_{\perp B} = \frac{\eta p}{B^2}, \tag{1.8}$$

where η is the Spitzer plasma resistivity, p is the plasma pressure and B is magnetic field used for the confinement. In this way, the confinement time evolved as $\tau_E \sim B^2$. Therefore, one way to satisfy the Lawson criterion is to increase B sufficiently. However, measured losses were higher than expected and turned out to be linked to "anomalous" diffusion due to microscopic plasma turbulence (see Chapter 2.3). The measured plasma diffusion was much larger than the considered classical diffusion, closely resembling the so-called Bohm ion diffusion observed during electromagnetic uranium separation for enrichment during Manhattan Project. Bohm proposed a semi-empirical formula for the diffusion coefficient

$$D_{\perp B} = \frac{1}{16}\frac{k_B T}{eB},$$

where k_B is the Boltzmann constant and e the elementary charge. Therefore $\tau_E \sim B$ and the required magnetic field to obtain a sufficient confine-

ment time in order to reach ignition was way above the range of technical feasibility. Despite a deeper understanding of instabilities and the introduction of energy conservation method to predict plasma stability, anomalous transport plagued fusion research for the early '60s. As Braams and Stott perfectly summarized:

> Where Lawson had set the goal [...] Bohm had placed a seemingly insurmountable roadblock.

1.5 Novosibirsk 1968: unraveling the Tokamak

In Soviet Union, the foundation of thermonuclear controlled fusion research was based on the intuitions of Oleg Lavrentiev, a self-educated 19 years old soldier of the Red Army, and developed by the end of the '50s by Igor Tamm and Andrej Sakharov, responsibles for the soviet nuclear weapon program [10]. In 1951 the Council on Magnetic Thermonuclear Reactors was established. It was headed by Igor Kurchatov, director of the Institute of Atomic Energy that was to be named after him, while Lev Artsimovich was responsible for the experimental program.

Early work explored, like in the West, various configuration for magnetic confinement, among which toroidal pinches with strong stabilizing fields. The main difference between the Russian version of this kind of experiment and the classical pinch was the presence of a series of vertical magnetic coils around the plasma chamber. The torus 5 (see Fig. 1.5) was the first in 1959 to be defined *tokamak* (**to**roidal'naya **ka**mera - toroidal chamber - **ma**gnitnaya **ka**tushka - magnetic coils). Techniques for measurement and discharge control developed sharply since then and led to great experimental successes, expressed in 1968 Novosibirsk conference. Artsimovich presented astonishing results deriving from the T-3 tokamak: improved confinement with temperatures of $\sim 1keV$ and confinement times $> 30\tau_{Bohm}$. Bohm diffusion seemed not to be an obstacle anymore.

Such figures were by far better than any other equivalent device at that time, and questions raised about their validity. A reflexive skepticism was common among scientists at that time. This was deriving from former triumphant declaration in fusion research, regularly turning out to be embarrassing exaggerations of limited results [6], and more than ten years of frustrating experiments on various magnetic configuration.

[6] In 1951 an Austrian scientist in Argentina claimed to achieve thermonuclear con-

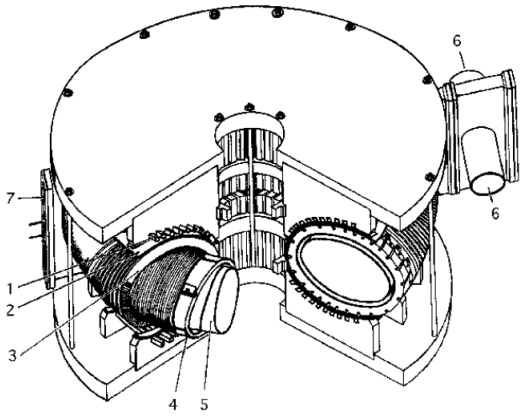

Figure 1.5: The Moscow Torus 5, later renamed Tokamak T-1. 1, coil for primary toroidal current; 2. screening copper shield; 3, longitudinal magnetic field coil; 4, stabilizing copper shield; 5. metal liner, 6, vacuum outlet; 7. port for diagnotic (fig.5.3 [10])

Artsimovich, who reported that data from the T-3 was "received with remarkable suspicion" [13], presented a suggestion. At Culham laboratories, the English scientists developed revolutionary techniques for detecting plasma temperatures: instead of probes in the plasma, non invasive laser beams could be directed into it. Scattering of particles is related to the temperature, and analysis of light spectrum escaping from a window allows more detailed measurement. Aware of that, Artsimovich invited a British team led by Sebastian Pease to Moscow, for what was to be the first experimental international collaboration in the field. The scientists were able to perform their studies and, in 1969, excellent tokamak performance was unequivocally confirmed.

Maintaining high temperature in order to achieve thermonuclear fusion requires a proper insulation of the plasma, that tokamak scheme, as other concepts, achieves through magnetic confinement. A particle of charge q moving in a magnetic field $\mathbf{B}$ with velocity $\mathbf{v}$ is subjected to the Lorenz force $\mathbf{F} = q\mathbf{v} \times \mathbf{B}$. Therefore, its trajectory in a uniform magnetic field is a spiral along the field line. A proper confinement for a plasma, composed of ions and electrons, is reached when the field lines are closed, such that particles keep rotating along them. The tokamak is an experimental machine characterized by a toroidally symmetric magnetic field, which can

trolled fusion, while in 1958 newspapers in Great Britain celebrated the "mighty Zeta" experiment as a successful attempt to access unlimited energy. Both results were soon disproved.

be decomposed in a toroidal component B_t and a poloidal component B_p.

B_t is the projection of $\mathbf{B}$ along the toroidal direction ξ of a toroidal reference frame and is produced by a current flowing in the poloidal direction θ through external coils, vertically belted along the torus. It is possible in principle to create a closed line configuration with B_t only, but in this case particles moving along the torus drift due to the non uniformity of the field. It is therefore necessary, in order to maintain an effective confinement, to add a B_p wrapping any poloidal section of the torus in the θ direction, which is mainly generated through another current, flowing in the plasma along ϕ. This current is induced in the plasma, acting as the secondary winding of a transformer due to its high conductivity, through a central solenoid. Consequently, since the current flowing in the primary coil cannot grow indefinitely, the process is inherently limited in time. Such a limit is a drawback when considering the tokamak as a candidate for a fusion reactor, since pulsed operation would require to include in the design expensive power smoothing mechanisms and the frequent heating and cooling of the components would lead to mechanical fatigue in the machine. In a tokamak, for stability purposes, $B_t \gg B_p$ and considering a the minor radius and R_0 the major radius of the torus such that $a \ll R_0$, an important parameter for stability of the equilibrium is the *safety factor* defined as

$$q = \frac{a}{R_0}\frac{B_t}{B_p} \sim 1.$$

A global treatment of the plasma as a fluid to study equilibrium configuration leads to consider magnetic surfaces characterized by constant pressure, along which plasma current flows. Unavoidable diffusion forces particles to move outwards from the hotter core plasma, such that insulation cannot be perfect. It is therefore useful to define the last closed flux surface (LCFS) of the plasma as the last surface characterized by closed magnetic field lines. When a particle moves outside of it into the scrape off layer (SOL), it ends onto a solid part of the tokamak following an open field line. Such component is crucial in the design of a tokamak. In fact, it is not only subjected to high heat and particle fluxes, but has also to avoid as much as possible impurity release, that would cool down the core plasma.

Two main configurations were used to control shape and position of the LCFS. The first, called Limiter, is characterized by a solid ring on the vessel surrounding the plasma, which magnetic field lines are forced to cross. The LCFS is defined at the border of this mechanical part facing the plasma. The second is characterized by a component, called divertor, and is named after it. In this case the profile of magnetic surfaces is more

complex: being shaped due to external currents, it presents one or more points in which $B_p = 0$. By these null or X-points the LCFS is defined. In divertor configuration, the boundary layer of a tokamak plasma is directed in side chambers and mainly impacts on the divertor plates where they can be pumped out. For an example of a cross section of a divertor tokamak, with the illustration of the mentioned geometric figures, see Fig. 1.6.

The tokamak fever spread, right at the time when oil crisis was to begin: from 1973 on, with increased funding for applied energetic R&D and a favorable notices in the mainstream press, several tokamaks were designed and built since the achievement of thermonuclear controlled fusion seemed closer than ever. Such devices were by far more expensive than former fusion experiments and got the benefit of increased budget. In Princeton, the C-Stellerator was converted into a tokamak in just six months and Americans were able to replicate the results of T-3. Worldwide, medium size (D-III, Alcator C, ASDEX) and large size tokamaks (JET, JT-60, TFTR, T-15) started to explore the possibilities offered by the promising configuration. By the early '80s there were nearly 300 fusion devices around the world, including seventy-three tokamaks.

New technological solutions were needed, especially for plasma heating: ohmic heating, related to the amount of current flowing in the plasma, became less effective at high temperature, since, as Spitzer derived already in 1956, the electrical resistivity scales as $\eta \sim T^{-3/2}$. Radiofrequency (RF) heating, based on waves generated outside the machine and able to transfer their energy to charged particles in the plasma edge, was developed already by the end of the '50s and was to be widely applied. Neutral Beam Injection (NBI) relies instead on particle accelerators: ions are first accelerated and neutralized, then directed towards the plasma. Having no charge, they easily penetrate the magnetic cage and are promptly ionized again. Eventually, they release their kinetic energy through a series of collision, increasing T and becoming a part of the plasma themselves. In 1976 at TFR in France and at ORMAK in the US, NBI heating exceeded finally Ohmic heating.

A fruitful competition boosted experimental results with always better parameters, albeit obtained mainly through a "brute force" approach based on applying more powerful heating methods and magnetic systems or by designing larger machines[7], such that next topical meetings were often defined as the "Plasma Olympics". Still, the τ_E associated to turbulent behaviour of thermal transport in a plasma was not sufficient and

[7] less then a decade after the results from T-3, there was a 10 fold increase in tokamak size and plasma currents [7]

major disruption following instabilities appeared, causing damages to the surrounding with energy release increasing with the machine size. Few years later, Harold Furth, director of the Princeton laboratories, declared:

> Sixteen years ago, the Kurchatov Institute handed us this present, the tokamak, but it was not possible physically to explain why it worked so well. Today is the same question. We don't understand physically why it works sometimes better than others.

1.6 Geneve 1985: ITER and beyond

Thermonuclear controlled fusion was always a step away. In 1979, for the first time, the minimum ion temperature to reach fusion was achieved at Princeton Large Torus (PLT, a T-3 scale experiment) in the US, but confinement time was observed to decrease as the heating power increased [14] as $\tau_E \sim I_P S_h^{-0.5}$. Scaling laws as the above mentioned were obtained through experiments performed both within individual machines, and by comparing results from different devices. Such laws depend on various parameters and were computed postulating that overall data could be empirically fit to the confinement time as

$$\tau_E = C\, B_t^{\alpha 1} I_p^{\alpha 2} n^{\alpha 3} a^{\alpha 4} R^{\alpha 5} \kappa^{\alpha 6} Z_i^{\alpha 7} S_h^{\alpha 8} \tag{1.9}$$

Where C and $\alpha 1 ... \alpha 8$ are simple numerical constants, Z_i is plasma ions atomic number and κ is enlongation of the poloidal cross section. A satisfying theoretical explanation for anomalous transport was not developed and a design purely based on scaling laws would have led to reactors with unreasonably large dimension [7]. A turning point was the discovery in 1982 at ASDEX, a divertor tokamak operating since 1980 in Germany, of a new state of a confined plasma, that was called H-mode (high confinement), in opposition to the L-mode (low confinement), as was described the previous mode of operation [15]. Such a state, that is more easily accessible in divertor configurations, is characterized by an increase of τ_E by a factor two at the L-H transition, reached when the heating power overcomes a threshold. Such results were quickly confirmed on other medium size tokamak around the world. Since theory could not explain this experimental success, the threshold value was studied by means of scaling laws with an approach analogous to the one for τ_E. Thanks to increased confinement, together with advances in theory such as the beta stability limit formulated by Troyon [16], and despite the budget cuts of the '80s it

was possible to design a second generation of optimized tokamaks (DIII-D, Alcator C-Mod, ASDEX Upgrade, JT-60U) to study improved plasma performance.

Finally, in 1985, at the first Summit Meeting between the American and Soviet leaders Reagan and Gorbachev in Geneve, the major step was decided. With a key role of the Kurchatov director Evgeniy Velihkov, able to get fusion on the meeting agenda, the idea of a collaboration to estabilish the feasibility of a fusion reactor was announced. This led to the 1987 signing of the ITER agreement between a series of nations in Reykjavik, in which it was decided to pursue a joint activity to design and realize the international fusion facility. ITER has a dual significance, being the Latin word for "the way" and an acronym for the "**I**nternational **T**hermonuclear **E**xperimental **R**eactor". Conceptual Design Activity (CDA) began in 1988 in Garching (Germany), while Engineering Design Activity was established from 1992 to 2001. The road to ITER was all but straightforward. This derived not only from the intrinsic difficulties deriving from the design of the largest fusion experiment ever built, but also from the enhanced complexity of the historical period: the fall of Berlin wall and the dissolution of the Soviet Union changed the world equilibria, deeply influencing ITER global collaboration. The mentioned period, which would move this analysis from history to current events, is not treated in its political aspects in the present chapter. The chosen site for ITER, after a series of proposals, was defined in 2005 to be Cadarache, in France, and construction began in 2013. During the design years, in 1991, another milestone was conquered: the Joint European Torus (JET) at Culham, in England, using a plasma of deuterium and tritium, achieved fusion conditions releasing a peak power from thermonuclear fusion of $\approx 1.7MW$. This was followed by the TFTR D-T campaign, that in 1994 released $\approx 10.7MW$ of fusion power, and by the current record release of $\approx 16MW$ again at JET in 1997.

ITER main objective is to prove the viability of fusion as a source of energy for a power plant. Furthermore, it will allow advanced studies on superconducting magnets, various plasma facing materials, large scale remote handling and tritium breeding. It will be the first magnetic fusion device to produce net energy. To clarify this concept, it is useful to introduce the figure of merit known as *physics gain factor* defined as

$$Q = \frac{\text{total thermal power out } - \text{ heating power in}}{\text{heating power in}} = \frac{S_f}{S_h}.$$

For example, the JET release of $\approx 16MW$ of fusion power was achieved with $\approx 22MW$ of injected power, leading to $Q = 0.65$. In the case of ignition, where no thermal power is required to maintain the reaction ($S_h = 0$, see 1.4), the power leaving the core is compensated by the generated power due to α particles. In this limit $Q \to \infty$. In the opposite case, in which no fusion reaction takes place and all the injected power in the plasma is released outside, obviously $Q = 0$. A condition of *burning plasma*, in which fusion power due to α particles equals the injected power, is achieved when $Q = 5$.

ITER [17] is designed to produce $500MW$ of fusion power out of $50MW$ of external heating, sustaining a D-T plasma. Therefore, with $Q = 10$, it will not reach ignition condition but can be considered an energy amplifier, without self-sustaining the reaction but relying on external power input. In this scenario, the plasma current induced by the central solenoid will reach $15\,MA$ and confinement is predicted to be $\tau_E = 1.2\,s$ with a pulse duration of $\tau = 400s$. Temperature will reach $11\,keV$ and $p\tau_E = 6.4atm\,s$. As mentioned above, these values do not satisfy the ignition condition (Eq (1.7)).

Besides Ohmic heating, external power input will be guaranteed by an RF system of $40MW$ and an NBI system able to reach $33MW$. Together with the bootstrap current, characteristic of a toroidal magnetically confined plasma, these two systems will also generate a non-inductive toroidal current. This in turn will be able to maintain the poloidal B_P of a plasma, leading to the possibility of exploring a steady-state operational regime. This second scenario, designed for $Q = 5$ will be characterized by a lower current of $9MA$ but a pulse of $\tau = 3000s$

A theory for anomalous transport does not exist yet, therefore many parameter of ITER design are extrapolated by scaling laws for the confinement time τ_E. This led to the choice of major radius $R_0 = 6.2m$ and minor radius $a = 2m$, for a volume of the plasma chamber of $V = 837m^3$. A toroidal magnetic field that can reach $B_t = 5.3T$ will be generated through Nb_3Sn superconducting coils. In order to allow the operation in superconducting state, a cryostat will keep the temperature at $T_{coils} = 4.5K$.

The chosen mode of operation is an ELMy H-mode, therefore a single-null divertor configuration with an enlongated poloidal cross section is chosen. Also the power threshold to reach H-mode is extrapolated from scaling laws.

The fusion reaction will be maintained in a vacuum chamber. Plasma facing components are studied with particular attention in order to support high heat and particle loads and avoid erosion that would contaminate the plasma and lead to premature cooling. The selected first wall

material will be Be while the divertor is designed in modular cassettes with separable high heat flux components, having a W structure.

ITER is not designed to be connected to the grid, therefore the produced fusion energy will not be transformed in electricity through a thermodynamic cycle but only released as heat. It will be an experimental device whose aim is to fill the gap between existing tokamak and a fusion power plant and allow the access to new plasma regimes. The first prototype for a commercial reactor is to be built in the future. Its name will be DEMO and will be a proper prototype for a complete power plant.

In order to have a better comprehension of ITER design, a comparison with ASDEX Upgrade is here performed. ASDEX Upgrade is a medium size tokamak operating at Max-Planck-Institut für Plasmaphysik at Garching bei München in Germany. Its name is an acronym for **A**xi**S**ymmetric **D**ivertor **EX**periment, deriving from the divertor geometry of its design. It succeeded ASDEX experiment, where H-mode was discovered, which operated since 1980 and was transferred in 1990 to SWIP at Leshan in China. ASDEX Upgrade became operational in 1991, with the overall goal to improve the scientific and technological base for ITER and DEMO [18]. This is performed through development of reactor-like conditions in term of plasma density, pressure and wall heat load. This experiment is not designed to treat a thermonuclear plasma but fusion reactions do happen at a very low rate between isotopes (mainly D) used for plasma discharges, releasing a maximum of 10^{19} neutrons per year. The activation of materials is so low and decay time so short, that the torus hall remain accessible out of operation times [19]. A major characteristic of the facility is the presence of an all-tungsten wall. The coating of the previous C wall started in 1999 and finished only in 2007, to evaluate gradually the consequences of W as plasma facing component, eventually revealing it to be ideally suited for studies of high performance plasmas. ASDEX Upgrade focuses on experiments on wall materials and divertor together with studies of plasma transport, turbulence and instabilities, therefore allowing to test various theoretical models. The tokamak has a major radius of $R_0 = 1.65m$ and a minor radius of $a = 0.5m$ for a volume of the plasma chamber of $V = 14m^3$. A toroidal magnetic field up to $B_t = 3.9T$ can be generated through a system of Cu coils [20], while a plasma current is up to $I_p = 1.4MA$ generates B_p. Confinement time is $\tau_E = 0.2s$ and every pulse or discharge lasts up to $\tau = 10s$. Plasma heating is provided by NBI and RF heating for a total 34 MW of installed power. In addition, a set of 16 internal B-coils, arranged in two rings above and below the midplane, can be used to generate resonant magnetic perturbations, used for ELM control. The table 1.1 summarizes the

parameters of the two machines, allowing an easy comparison.

		ITER	AUG
a	m	2	0.5
R_0	m	6.2	1.65
R_0/a		3.2	3.3
V_p	m^3	837	14
B_0	T	5.3	3.9
τ_E	s	1.2	0.2
τ	s	400	10
S_h	MW	73	34
I_p	MA	15	1.4
coils		$Nb_3Sn\,NbTi$	Cu

Table 1.1: Comparison between ITER Q=10 scenario and ASDEX Upgrade parameters. In S_h only NBI and RF heating are considered

Since 2014, ASDEX Upgrade is run in the framework of the MST (medium-size tokamaks) campaigns of EUROfusion consortium, enabling a research more integrated than ever with other institutions.

More paths were and are being explored in parallel to the tokamak design. Inertial fusion is a completely different solution, studied from the '70s and based on the possibility to ignite small pellets of solid D-T through the aid of laser pulses. It is nowadays explored thanks to large scale experiments such as the National Ignition Facility, built from 1997 to 2009 in the US, and Laser Mégajoule, whose construction in France finished in 2014. Furthermore, a renewed interest for the stellerator scheme and its long discharges is growing, in particular after the inauguration of Wendelstein 7-X at Greifswald (Germany) at the end of 2015, but the final aim remains the same. The road to fusion energy has started more than fifty years ago, evolving from a brand new topic for few specialists to a global collaboration between governments. It was first used to develop new weapons but now is studied to provide access to unlimited energy to the whole world. More challenges have to be faced and nothing can be taken for granted in the long term planning required, but the international collaboration that derived from the quest is the greatest resource. What Lev Artsimovich wrote in 1958 is still actual:

> The solution of the problem of thermonuclear fusion will require a maximum concentration of intellectual effort and the mobilization of very appreciable material facilities and complex

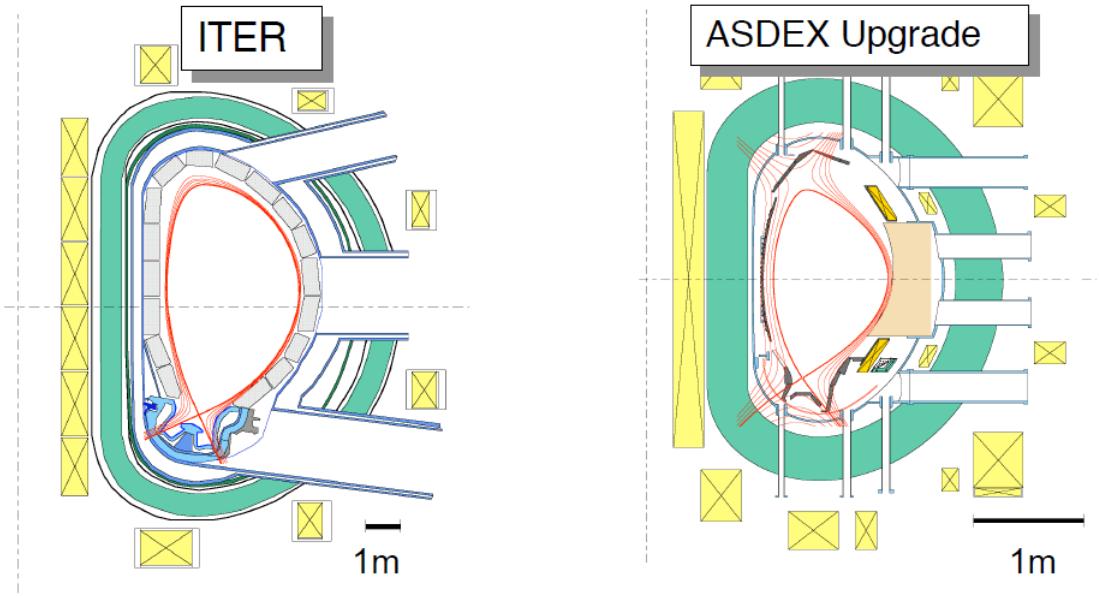

Figure 1.6: A comparison of the poloidal cross section of ITER and ASDEX Upgrade. It is possible to recognize from the inside the LCFS (in thick red), the magnetic surfaces in the SOL (in light red), the plasma facing components (in grey), ITER divertor cassette (in blue), the toroidal field coils (in green) the central solenoid and the corrective field coils (in yellow) and the channels for diagnostic and external heating (courtesy of Max-Planck-Institut für Plasmaphysik)

> apparatus. This problem seem to have been created especially for the purpose of developing close cooperation between the scientists and engineers of various countries.

The present challenges of controlled thermonuclear fusion, introduced in this chapter, are still open issues. In particular, the fields of transport and stability of a toroidally confined plasma are the main topics analyzed in this thesis, with a particular focus on the behavior of the plasma close to the LCFS: the plasma edge. In the following chapter, some of the main physics phenomena of plasma edge are introduced, in order to present the main goal of the thesis.

Chapter 2

Magnetically confined plasma physics and edge phenomena

The aim of present chapter is to introduce the plasma physics phenomena at the edge of a magnetically confined toroidal plasma necessary for the model developed in this thesis.

The MHD model is discussed in Sec. 2.1, with attention towards its derivation from the two-fluid model and the required assumptions.

Different approaches to describe energy and particle transport are analyzed in Sec. 2.2. Classical and neoclassical transport are initially studied and compared to experimental measurements. Eventually anomalous transport is introduced in order to underline the prominent role of turbulence in these phenomena.

Microscopic origin of turbulent transport is discussed in Sec. 2.3. The main microinstability considered in this thesis, the interchange instability, is then analyzed.

In Sec. 2.4 L-H transition in toroidal plasma is described, with focus on the edge phenomena. In particular, sheared flows among which turbulence driven zonal flows (ZFs) are discussed in order to provide the recent explanation for edge turbulence reduction and the onset of the L-H transition. In this section, limit cycle oscillations (LCOs) are delineated as a feature of the intermediate phase at the L-H transition, called I-phase.

In Sec. 2.5 edge localized modes (ELMs), violent instabilities present in H-mode, are described. A classification of the different type of ELMs is given and their role in thermonuclear fusion is explained.

In Sec. 2.6, recent experimental results are discussed, showing the transition of LCOs in type-III ELMs during the late I-phase, which is not yet explained. The modeling of this transition is the goal of this thesis, presented at the end of this chapter.

2.1 Magnetized Plasmas Description

The aim of this section is to introduce the resistive MHD model, presenting the main assumptions that need to be respected to reach a single-fluid like model for macroscopic phenomena in a magnetized plasma. The description of plasma requires to study the interaction of a macroscopic number of charged particles, where every particle moves according to Newton's law for a charge in an electromagnetic field, which is self-consistently generated according to the particles dynamics. An Eulerian approach is therefore required for a global description and this is obtained through a kinetic model of the plasma coupled with Maxwell's equations [21]. In this way, every population α of the plasma is described by a distribution function f_α evolving in time as a Boltzmann-like equation. By taking the appropriate moments, it is possible to move from an equation for function $f_\alpha(\mathbf{r}, \mathbf{u}, t)$, where $\mathbf{r}$ and $\mathbf{u}$ are the phase space coordinates, to an infinite set of equations in four variables $(\mathbf{r}, t)$ that conserve all the information contained in the original form. Consequently, a truncation is needed in order to close the system. Considering a plasma formed by only ions and electrons, with singly charged ions such that $q_i = -q_e = e$, the system describing the evolution of a plasma is a *two-fluid model*:

$$\frac{dn_\alpha}{dt} + n_\alpha \nabla \cdot \boldsymbol{v}_\alpha = 0, \tag{2.1}$$

$$n_\alpha m_\alpha \left(\frac{d\boldsymbol{v}_\alpha}{dt}\right) - q_\alpha n_\alpha (\boldsymbol{E} + \boldsymbol{v}_\alpha \times \boldsymbol{B}) + \nabla \cdot \mathbf{P}_\alpha = \boldsymbol{R}_\alpha, \tag{2.2}$$

$$\frac{3}{2} n_\alpha \left(\frac{dT_\alpha}{dt}\right) = \mathbf{P}_\alpha \colon \nabla \boldsymbol{v}_\alpha + \nabla \cdot \boldsymbol{h}_\alpha + Q_\alpha, \tag{2.3}$$

$$\nabla \times \boldsymbol{E} = -\frac{\partial \boldsymbol{B}}{\partial t}, \tag{2.4}$$

$$\nabla \times \boldsymbol{B} = \mu_0 e (n_i \boldsymbol{v}_i - n_e \boldsymbol{v}_e) + \frac{1}{c^2} \frac{\partial \boldsymbol{E}}{\partial t}, \tag{2.5}$$

$$\nabla \cdot \boldsymbol{E} = \frac{e}{\epsilon_0} (n_i - n_e), \tag{2.6}$$

$$\nabla \cdot \boldsymbol{B} = 0, \tag{2.7}$$

here $\alpha = e, i$ indicates the species. Eq (2.1) is the continuity equation for the species density n_α, Eq (2.2) the momentum equation for the fluid velocity $\boldsymbol{v}_\alpha$, Eq (2.3) is the energy evolution and Eq (2.4)-(2.7) are the coupled Maxwell equations. The system is not yet closed since there are still more unknowns than equations. Particular attention needs to be made upon the higher-order moments. Here $\mathbf{P}_\alpha = p_\alpha \mathbf{I} + \mathbf{\Pi}_\alpha$ is a full pressure tensor containing isotropic ($p_\alpha \mathbf{I}$) and anisotropic ($\mathbf{\Pi}_\alpha$) part, while $\boldsymbol{h}_\alpha$ is the heat flux . The other two moments are derived from the collisional term in the original kinetic equation. In particular $\boldsymbol{R}_\alpha$ represents the mean momentum transfer due to the friction of collisions and Q_α the heat generated by collision, both between unlike particles.

In order to simplify and close the model, different assumptions need to be introduced. A series of asymptotic expansions are inserted to eliminate high frequency, short wavelength information from the equations, since on a macroscopic scale these effects are uninteresting. For a typical fusion experiment, the characteristic space scale is the overall plasma dimension a (typically $\sim 1m$), then the timescale is $\tau = a/V_T$, where $V_{Ti} = \sqrt{2T_i/m_i}$ is the ion thermal speed. Assuming that the phenomena of interest have a frequency lower than plasma frequency $1/\tau \ll \omega_{pe} = \sqrt{n_0 e^2/m_e \epsilon_0}$ and a space scale longer than the plasma Debye length $a \gg \lambda_D = V_{T_e}/\omega_{pe}$ the following approximations are valid. The first approximation allows to neglect the displacement current and the net charge by letting $\epsilon_0 \to 0$. Considering only low frequencies phenomena, electrons have enough time to compensate any macroscopic charge separation, and maintain the plasma locally quasi neutral (see Appendix A). Therefore, neglecting this implies the *quasineutral approximation*

$$n_i = n_e = n.$$

A second approximation treats $m_e \to 0$, allowing the electron to respond infinitely fast to any perturbation. This allows to compute generalized Ohm's law from the momentum equation of the electrons.

To simplify the model, a series of single-fluid variables is introduced. For a complete derivation of the model, including all the assumptions required, see [21]. The consequences of the previous asymptotic approximations imply to consider a leading role of the ions in the definition of a single fluid plasma such that $\rho = \sum_\alpha m_\alpha n_\alpha = m_i n_i$ and $\boldsymbol{v} = \left(\sum_\alpha m_\alpha n_\alpha \boldsymbol{v}_\alpha\right) / \left(\sum_\alpha m_\alpha n_\alpha\right) = \boldsymbol{v}_i$. The final set of equations is the magnetohydrodynamic (MHD) model for a plasma:

$$\frac{\partial \rho}{\partial t} + \nabla \cdot \rho \boldsymbol{v} = 0, \tag{2.8}$$

$$\rho \frac{d\boldsymbol{v}}{dt} = \boldsymbol{J} \times \boldsymbol{B} - \nabla p, \tag{2.9}$$

$$\frac{3}{2}\frac{dp}{dt} = -p\nabla \cdot \boldsymbol{v} - \nabla \cdot \boldsymbol{q} + S, \tag{2.10}$$

$$\boldsymbol{E} + \boldsymbol{v} \times \boldsymbol{B} = \eta \boldsymbol{J}, \tag{2.11}$$

$$\nabla \times \boldsymbol{E} = -\frac{\partial \boldsymbol{B}}{\partial t}, \tag{2.12}$$

$$\nabla \times \boldsymbol{B} = \mu_0 \boldsymbol{J}, \tag{2.13}$$

$$\nabla \cdot \boldsymbol{B} = 0. \tag{2.14}$$

Here S is considered any known source of external heat. A model for heat conduction is inserted as $\boldsymbol{q} = -n\chi\nabla T$ and considering the kinetic pressure $p = nT = (\rho/m_i)T$ together with an isothermal assumption $T_e = T_i = T$. The knowledge of χ, the thermal conductivity, is of course required to close the system. This will be shown to be a severe problem in MHD when evaluating transport coefficients in section 2.1. Finally, $\eta\boldsymbol{J}$ describes the effects of small scale (i.e. within a Debye length) particles collisions[1]. Particles interact with each other through the generated low-range electromagnetic force, giving rise to a finite electrical resistivity

$$\eta = \frac{m_e \overline{\nu_{ei}}}{e^2 n_e}. \tag{2.15}$$

Here, $\overline{\nu_{ei}}$ is the net momentum collision frequency between ions and electrons, that can be evaluated analytically [9]

$$\overline{\nu_{ei}} = \sqrt{\frac{2}{\pi}} \frac{e^4 n_i}{12\pi\epsilon_0^2 m_e^{1/2} T^{3/2}} ln\Lambda, \tag{2.16}$$

where $ln\Lambda$ is the Coulomb logarithm. Usually $\nu_{ei} \ll \omega_{pe}$.

It is furthermore remarkable to underline how the collisionless MHD model [21], which makes predictions nearly identical to ideal MHD, can be derived from single particle motion in a collisionless plasma. In a plasma, every charged particle of a population α is subject to the Lorenz force, due to the presence of a magnetic field. Perpendicular to the field line, in absence of inhomogeneities or external fields, its trajectory is a gyro-motion whose frequency is $\omega_{c\alpha} = q_\alpha B_0/m_\alpha$, and whose amplitude is the Larmor

[1] in the ideal MHD model instead they are neglected

radius $r_{L\alpha} = V_{T\alpha}/\omega_{c\alpha}$. Here, the consequences of a single charged particle motion in an inhomogeneous magnetic field in presence of an electric field are presented. The dynamics, derived from approximated treatment of Newton equation, give rise to a series of so-called *drifts*, that together with the magnetization current generate a total current perpendicular to the magnetic field lines. Considering the guiding center approximation, the considered drifts[2] imply a perpendicular velocity for every particle

$$\mathbf{v}_{Dtot} = \mathbf{v}_E + \mathbf{v}_{\nabla B} + \mathbf{v}_\kappa + \mathbf{v}_P. \tag{2.17}$$

Here, $\mathbf{v}_E$ is the $\boldsymbol{E} \times \boldsymbol{B}$ drift

$$\mathbf{v}_E = \frac{\boldsymbol{E} \times \boldsymbol{B}}{B^2}, \tag{2.18}$$

$\mathbf{v}_{\nabla B}$ is the ∇B drift

$$\mathbf{v}_{\nabla B} = -\frac{\mu}{q}\frac{\nabla B \times \boldsymbol{B}}{B^2}, \tag{2.19}$$

$\mathbf{v}_\kappa$ is the curvature drift

$$\mathbf{v}_\kappa = -\frac{\mathrm{v}_\parallel^2}{\omega_c}\frac{\boldsymbol{\kappa} \times \boldsymbol{B}}{B}, \tag{2.20}$$

and $\mathbf{v}_P$ is the polarization drift

$$\mathbf{v}_P = -\frac{\boldsymbol{b}}{\omega_c} \times \frac{d}{dt}\left(\frac{\boldsymbol{E} \times \boldsymbol{B}}{B^2}\right). \tag{2.21}$$

In the previous equations $\kappa = \boldsymbol{b} \cdot \nabla \boldsymbol{B} = \boldsymbol{R}_C/R_C$ is the curvature of the magnetic field line, $\mathrm{v}_\parallel$ is the parallel component of the particle velocity with reference to the magnetic field line, μ is the magnetic moment of the particle and ω_c is the cyclotron frequency. It shall be considered that the $\boldsymbol{E} \times \boldsymbol{B}$ velocity is greater by r_{Li}/a than the other drifts, but it is identical for ions and electrons. Conversely, the other velocities are opposite in direction due to the presence of the charge in their expressions. Therefore, despite $\mathbf{v}_E$ is the main origin for perpendicular plasma velocity defined as

$$\boldsymbol{v}_\perp = \frac{1}{n}\int \mathbf{v}_{Dtot\,i}\; f_i(\mathbf{u})\; d\mathbf{u} \approx \frac{\boldsymbol{E} \times \boldsymbol{B}}{B^2} \equiv \boldsymbol{v}_E, \tag{2.22}$$

it does not contribute to the guiding centre current, namely the current deriving from drifts that flows perpendicular to the magnetic field lines.

$$\boldsymbol{J}_{D\perp} = e\int [\mathbf{v}_{Dtot\,i} f_i(\mathbf{u}) - \mathbf{v}_{Dtot\,e} f_e(\mathbf{u})]\; d\mathbf{u}. \tag{2.23}$$

[2]drift due to gravity is here neglected

The last quantity of interest introduced in this section is the magnetization current, deriving from the presence of gradient in the density of magnetic moments in a fluid description. It can be defined as

$$\boldsymbol{J}_{\boldsymbol{M}} = \boldsymbol{\nabla} \times \boldsymbol{M}, \tag{2.24}$$

$$\boldsymbol{M} = \frac{p}{B}\boldsymbol{b}. \tag{2.25}$$

Therefore, the total perpendicular current is given by

$$\boldsymbol{J}_{\perp} = \boldsymbol{J}_{D\perp} + \boldsymbol{J}_{M}. \tag{2.26}$$

2.2 Transport in magnetized plasmas

The aim of this section is to point the limits of a purely diffusive description of plasma transport and underline the role of turbulence in plasmas, that despite being the major responsible for transport is still not completely understood. The derivation follows those proposed in [9] and [22].

As a preliminary remark, the evolution of a scalar field $\varphi(\boldsymbol{x}, t)$ advecting with $\boldsymbol{v}(\boldsymbol{x}, t)$ can be described with a conservation law in a Eulerian approach reading

$$\frac{\partial \varphi}{\partial t} + \nabla \cdot (\varphi \boldsymbol{v}) = 0, \tag{2.27}$$

in absence of sources or sinks for φ. Fick's first and second law are used to model diffusive processes. This requires the assumption of local transport, namely that the scale of the process driving the diffusion mechanism and the scale of variation of the transported quantity are widely separated [23]. This means that widely separated regions of the considered system do not significantly interact with each other and fluxes can be modeled in terms of a diffusion coefficient D_{φ} which defines the flux $\boldsymbol{\Gamma}_{\varphi}$ as

$$\boldsymbol{\Gamma}_{\varphi} = \varphi \boldsymbol{v} = -D_{\varphi} \nabla \varphi. \tag{2.28}$$

In this way, the evolution in time of φ reads

$$\frac{\partial \varphi}{\partial t} = \nabla \cdot (D_{\varphi} \nabla \varphi), \tag{2.29}$$

where to evolve an initial $\varphi(\boldsymbol{x}, 0)$ it is not necessary to evaluate the evolution of the velocity field $\boldsymbol{v}(\boldsymbol{x}, t)$, but it is sufficient to model the diffusion coefficient.

2.2.1 Classical transport

The analysis starts from the presented resistive MHD model, which is used to compute classical diffusion coefficients in a 1D plasma cylinder, where all physical variables are functions of (r, t) only. Consider that the measured energy confinement time $\tau_E \sim 0.1{-}1s$ is large compared to MHD time scale $a/V_{Ti} \sim 1\mu s$. Therefore, it is allowed to neglect the inertial term in the momentum equation. The system evolves quasistatically through a sequence of MHD equilibria. Assume a magnetized plasma where the magnetic field has the following characteristics

$$\begin{gathered}\boldsymbol{B} = B_\theta \boldsymbol{e}_\theta + B_z \boldsymbol{e}_z, \\ B_z = B_0 + \delta B_z(r,t) \quad B_0 = const., \\ \frac{B_\theta(r,t)^2}{B_0^2} \sim \frac{\delta B_z(r,t)}{B_0} \ll 1 \quad \forall r, t\,,\end{gathered}$$

It is possible to analytically reduce the resistive MHD system. A key feature at this point is the possibility to eliminate the plasma velocity $v(r)$ from the system, obtaining a purely diffusive model for scalar fields. In this way, the remaining variables evolving in time can be written as a set of transport equations

$$\frac{\partial n}{\partial t} = \frac{1}{r}\frac{\partial}{\partial r}\left[r\left(\frac{2nT\eta_\perp}{B_0^2}\right)\left(\frac{\partial n}{\partial r} + \frac{n}{T}\frac{\partial T}{\partial r} + \frac{2\eta_\parallel}{\beta_p \eta_\perp}\frac{n}{rB_\theta}\frac{\partial r B_\theta}{\partial r}\right)\right], \tag{2.30}$$

$$3n\frac{\partial T}{\partial t} = \frac{1}{r}\frac{\partial}{\partial r}\left(rn\chi\frac{\partial T}{\partial r}\right) + S, \tag{2.31}$$

$$\frac{\partial r B_\theta}{\partial t} = r\frac{\partial}{\partial r}\left(\frac{\eta_\parallel}{\mu_0}\frac{1}{r}\frac{\partial r B_\theta}{\partial r}\right), \tag{2.32}$$

where $\beta_p = 4\mu_0 nT/B_\theta^2 \sim 1$ and the resistivity has been split among a parallel and a perpendicular component, relatively to the magnetic field lines as $\eta \boldsymbol{J} = \eta_\parallel \boldsymbol{J}_\parallel + \eta_\perp \boldsymbol{J}_\perp$. It is therefore possible to identify the diffusion coefficient for particles D_n and magnetic field D_B.

$$D_n = \frac{2nT\eta_\perp}{B_0^2}, \tag{2.33}$$

$$D_B = \frac{\eta_\parallel}{\mu_0}. \tag{2.34}$$

The diffusion proceeds in radial direction and the particle diffusion coefficient is exactly the one introduced in Eq (1.8). As for the original resistive

MHD model, in order to close the system χ is necessary[3]. This is a main limitation of such an approach, since it is not possible to estimate the confinement time for energy.

The derivation of transport coefficients can be performed at a different level considering the behavior of single particles. A simple treatment is based on the random walk model. The main advantage with reference to the previous approach is the possibility to estimate D_n and χ. A simplified analytical treatment can be found in Appendix B.1. In the analysis is fundamental to consider that, in a magnetized plasma, the charged particles after a Coulomb collision do not follow a straight trajectory as in a neutral gas but are bounded to their gyro-motion. This approach, developed in in Appendix B.2, is referred to as Classical Transport and interestingly leads to obtain the same expression for the particle diffusion coefficient D_n of Eq (2.33), but also provides an expression for χ.

A complete approach, based on the solution of a more fundamental kinetic model that includes non-Maxwellian corrections of the distribution function, allows to introduce the final correct coefficients. The thermal conductivity for classic transport reads

$$\chi = 10^{-21} \frac{n}{B_0^2 T^{1/2}} \frac{m^2}{s}, \tag{2.35}$$

An evaluation based on parameters for a simple designed fusion reactor $n = 1.5 \times 10^{20} m^{-3}$, $T = 15keV$ and $B_0 = 4.7T$ would lead to an excessively optimistic estimation of $\chi = 1.8 \times 10^{-3} m^2/s$, three orders of magnitude lower with respect to typical experimental values of $\chi = 1 m^2/s$. In conclusion, despite a rigorous analytical derivation, a classic transport theory is not able to correctly predict the diffusion coefficients.

2.2.2 Neoclassical transport

Neoclassical transport is a development of the previous classical theory that considers the main effect of a tokamak geometry in a magnetically confined plasma on particle and thermal diffusivity. One could expect that, in a large aspect ratio tokamak, the corrections to the previous results for cylindrical geometry would be in the order of $\epsilon = a/R_0$. Instead, the effects of the drifts generate an increase of nearly two orders of magnitude in the final result with reference to the diffusion coefficient obtained

[3]except for a simple adiabatic form for energy equation, that however would not lead to heat conduction

for the 1D cylindrically symmetric plasma column. The main result of neoclassical theory is the description of particles trapped in so-called *banana orbits* and their consequences for transport in plasma.

The combination of a longer step length and a shorter time between collisions in a random walk model, with reference to those considered for classical transport, implies an increase of diffusion coefficients. A treatment that motivates these features can be found in Appendix B.3.

The thermal diffusivity for neoclassical transport is obtained as

$$\chi^{NC} = 6.8 \times 10^{-22}\, q\, \epsilon^{-3/2}\, \frac{n}{B_0^2 T^{1/2}}\, \frac{m^2}{s}. \tag{2.36}$$

Neoclassical transport, despite the increase of two order of magnitude compared to classical transport, can estimate for a simple fusion reactor only $\chi^{NC} \sim 0.1 m^2/s$, still lower than the experimentally measured $\chi = 1 m^2/s$. This elegant derivation is anyhow useful to describe the minimum limit on energy transport, that was observed in portions of the plasma characterized by turbulence reduction [9]. In these modes of operation, transport barriers can be formed and ion transport can approach neoclassical values. A complete description of transport phenomena requires anyhow the introduction of turbulence in plasma that gives rise to the so-called anomalous transport.

2.2.3 Anomalous transport

The main reason for the limited predicting capability of neoclassical transport theory for the measured diffusion coefficient is the fact that transport in plasma is not dominated by Coulomb collisions, but by plasma turbulence driven by microinstabilities. Anomalous transport refers to the effects non predicted by neoclassical theory.

At present days, no complete theory predicting transport due to plasma turbulence exists. The effects of anomalous transport in ITER original design were evaluated with the aid of scaling laws, obtained from multi machine data interpolation. From these laws, it is possible to extrapolate the parameters of interest. Such empirical scaling relations are a great resource for the design of new experiments but there is no guarantee of their validity beyond the existing database. Therefore, a theoretical formulation for the turbulence in plasma could allow to access other ways to overcome the obstacle of the reduced confinement time instead of moving for bigger and more expensive machines, and would reduce the risks connected to data extrapolation.

Empirical scaling laws are based on the possibility to easily measure the confinement time. Consider the energy balance for a single fluid as in Eq (2.10), where convection and compressional work are neglected, due to their reduced transport role in the overall plasma for a fusion experiment.

$$\frac{3}{2}\frac{\partial p}{\partial t} = -\nabla \cdot \boldsymbol{q} + S. \tag{2.37}$$

In S ohmic and external heating are included, while Bremsstrahlung is neglected since is localized in the edge plasma region. Evaluating the balance for the whole plasma leads to define the total stored energy

$$W = \int \frac{3}{2} p \, d\mathbf{r}, \tag{2.38}$$

and to model the heat flux, introducing the confinement time τ_E, as

$$\frac{W}{\tau_E} \equiv \int \nabla \cdot \boldsymbol{q} \, d\mathbf{r}. \tag{2.39}$$

The assumption of a steady state operation leads to

$$\tau_E = \frac{W}{S_h}, \tag{2.40}$$

where S_h is the total external heating power ($S_h = \int S d\boldsymbol{r}$). The quantities on the right hand side of the equation are easily measured experimentally. This process allows to evaluate the experimental confinement time and build scaling laws as in Eq (1.9).

Theoretical modeling of anomalous transport requires to change the approach from the purely diffusive approximation. The presence of periodic fluctuations in the plasma influences the terms in conservation laws. Considering $\langle\,\rangle$ the average over a flux surface in a tokamak plasma, any quantity x can be described as a background value plus a fluctuating term as

$$x = \overline{x} + \widetilde{x},$$
$$\langle \overline{x} \rangle = \overline{x}, \; \langle \widetilde{x} \rangle = 0 \implies \langle x \rangle = \overline{x}.$$

For two different quantities x and y

$$\langle x\, y \rangle = \overline{x}\, \overline{y} + \langle \widetilde{x}\, \widetilde{y} \rangle \tag{2.41}$$

As an example, the continuity equation for density averaged on a flux surface reads

$$\frac{\partial \overline{n}}{\partial t} = -\nabla \cdot (\overline{\boldsymbol{v}}\, \overline{n}) - \nabla \cdot \langle \widetilde{\boldsymbol{v}}\, \widetilde{n} \rangle. \tag{2.42}$$

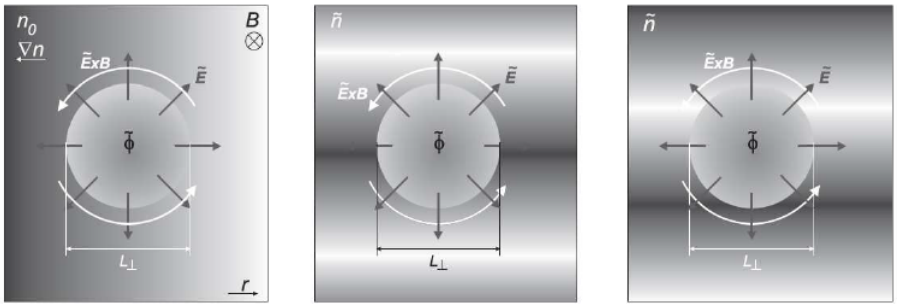

(a) (b) (c)

Figure 2.1: The mechanism of electrostatic transport. Darker shades of background grey indicate higher density and the poloidal coordinate is in vertical direction. (a) An eddy with unperturbed density. (b) Density and potential perturbations in phase. (c) Density and potential perturbations out of phase. (Fig. 1.9 [22]).

For a simplified analysis, assume that the fluctuations cannot be considered small perturbations, and therefore are not negligible just through linearization of the equation. Furthermore, assume that the fluctuations are periodic around the flux surface with a finite mode number m_θ such that a wavevector is associated to it as $k_\theta = 2\pi/\lambda = m_\theta/a$. Assume then that the plasma is strongly magnetized and the electric field perpendicular to $\boldsymbol{B}$ on a poloidal cross section is purely electrostatic such that it is generated only due to potential fluctuations

$$\widetilde{\boldsymbol{E}}_\perp = -\nabla_\perp \widetilde{\phi}. \tag{2.43}$$

Consequently, every potential perturbation results in an eddy or vortex due to the $E \times B$ drift. In the present picture, eddies are able to transport particles across their size.

The role of the cross phase between perturbation is now considered. A fluctuation in the potential only would lead to vortexes formation but no net transport is achieved. This can be seen both in the zero transport term that would result from averaging in equation Eq (2.42) and in Fig. 2.1(a), where despite the presence of a background density gradient the transport due to fluctuations vanishes. With an additional density fluctuation in phase with the potential fluctuation (Fig. 2.1(b)) still no transport is achieved. If density and potential are out of phase, more particles are transported outwards (lower part of the eddy) than inwards (higher part of the eddy) (Fig. 2.1(c)). Performing a Fourier transform of the interested quantities easily illustrates this concept, allowing a de-

scription in wavenumber space. The radial velocity due to $E \times B$ drift reads

$$\boldsymbol{v}_{Er} = -\partial_\theta \widetilde{\phi}/B \quad \overset{F}{\rightarrow} \quad -ik_\theta \, \widetilde{\phi}(k_\theta)\,/B, \tag{2.44}$$

and the part of the flux due to the fluctuations that leads to net transport is

$$\widetilde{\Gamma} = \langle \widetilde{v}_{Er} \, \widetilde{n} \rangle \tag{2.45}$$

$$= \frac{1}{2}\left(-i\frac{k_\theta}{B} \, \widetilde{n}(k_\theta) \, \widetilde{\phi}(k_\theta) \; + \; i\frac{k_\theta}{B} \, (\widetilde{n}(k_\theta) \, \widetilde{\phi}(k_\theta))^* \right) \tag{2.46}$$

$$= \frac{k_\theta}{B} |\widetilde{n}(k_\theta)||\widetilde{\phi}(k_\theta)| \sin \delta_{n,\phi}, \tag{2.47}$$

where $\delta_{n,\phi}$ is the cross-phase or space delay between density and potential fluctuation along the poloidal direction. It is straightforward to see that for $\delta_{n,\phi} = 0$ there is no transport, while for $\delta_{n,\phi} = \pi/2$ there is maximum transport.

Fluctuations in plasmas lead to enhanced transport, giving rise to a series of small and irregular structures able to advect the plasma. Turbulence in plasma consists of all these structures. In a magnetized plasma, the presence of different interacting fields (density, temperature, potential, magnetic field etc.) induces collective modes characterized by various spacial scales and generating net anomalous transport in an analogous fashion to the presented case. Consequently, this does not justify a purely diffusive description a priori for anomalous transport [24].

A mixing length model considers a dominant contribution from a single mode only, by modeling the anomalous transport flux as $\widetilde{\Gamma} = (L_c^2/t_c)\nabla n$, where L_c and t_c are respectively a characteristic length and time of the fluctuation. This is not a complete picture, since it only considers a single dominant structure and does not evaluate the effect of the crossphase. The transport related to fluctuations constitutes the major contribution to the overall transport and therefore modeling of turbulence is of paramount importance for the scope of thermonuclear fusion.

2.3 Turbulence

The aim of this section is to introduce the fundamental concepts for turbulent behavior in fluids, underlining both the difference and peculiarities of turbulence in plasma. Two fundamental microinstabilities will be presented and their role in turbulence seeding will be explained.

2.3.1 Turbulence in neutral fluids

Turbulence can be defined as

> [...] a state of spatio-temporal chaotic flow generally attainable for fluids with access to a sufficient source of free energy [25].

Its main consequence is an increased mixing of the fluid, through the formation of vortex structures that reduce the amount of free energy in the system. The vortices size spans from the system characteristic dimension to microscopic dissipative scales. Such a wide range is a major obstacle in modeling this phenomenon.

In the particular case of incompressible, divergence free and isothermal flow, the description of the velocity field can be reduced to the solution of the Navier-Stokes equations for non conducting fluids.

$$\left(\frac{\partial}{\partial t} + \boldsymbol{v}\cdot\nabla\right)\boldsymbol{v} = -\nabla P + \nu\Delta\boldsymbol{v}, \tag{2.48}$$

$$\nabla\cdot\boldsymbol{v} = 0, \tag{2.49}$$

where $P = p/\rho_0$ in which p is the scalar pressure field, and ν is the kinematic fluid viscosity. A crucial parameter for the characteristic of the fluid flow is the dimensionless Reynolds number Re, which expresses the ratio between inertial and viscous forces, or from another point of view, between the mean flow time scale and the dissipation time scale

$$Re = \frac{UD}{\nu}, \tag{2.50}$$

where U and D are a characteristic velocity and dimension of the system respectively. The character of the solution of Navier-Stokes equation is defined from the value of the Reynolds number that, being a dimensionless ratio, defines the dominating terms in the equation. At low Re viscosity dominates the solution and the flow results laminar. At high Re the nonlinear self advection of the velocity (the term $(\boldsymbol{v}\cdot\nabla)\boldsymbol{v}$) can drive the flow turbulent. From the point of view of a measured velocity field, the effect of turbulent eddies appears as an irregular fluctuating disturbance over the mean flow. In this sense, it is useful to introduce a scale separation to isolate the effect of eddies on the mean flow. The total flow can indeed be decomposed following the Reynolds decomposition

$$\boldsymbol{v} = \boldsymbol{V} + \widetilde{\boldsymbol{v}}. \tag{2.51}$$

A temporal average for this purpose is defined as $\langle \quad \rangle = (1/\Delta t) \int_t^{t+\Delta t} \quad d\,t$, in which Δt is chosen such that $\langle \boldsymbol{v} \rangle = \boldsymbol{V}$ while $\langle \widetilde{\boldsymbol{v}} \rangle = 0$. The application of this operator to Eq (2.49) allows to obtain the Reynolds averaged Navier-Stokes equation (RANS)

$$\left(\frac{\partial}{\partial t} + \boldsymbol{V} \cdot \nabla \right) \boldsymbol{V} = -\nabla P - \nabla \cdot \mathbf{R} + \nu \Delta \boldsymbol{V} \tag{2.52}$$

in which the structure is analogous to the original equation but with a new term $\nabla \cdot \mathbf{R}$ where $R_{ij} = \langle \widetilde{v}_i \widetilde{v}_j \rangle$, called *Reyolds Stress Tensor* and representing the effect of the eddies on the mean flow.

Some basic feature of turbulence are now introduced.

A strong enough gradient or shear in the velocity field is considered as a source of free energy for the turbulence onset. In this case, nonlinear self advection of the velocity leads to the formation of vortexes as a consequence of Kelvin-Helmoltz instability excitation [25].

Andrei Kolmogorov theorized in 1941 this form of evolution in a 3D system [26], such that the energy provided at a macroscopic scale I (*injection range*) is progressively transferred to smaller scales until it is dissipated at a molecular scale η (*dissipation range*) into internal energy. In this picture, nonlinear self advection and interaction of macroscopic modes create a series of smaller and smaller eddies, giving rise to the so-called direct cascade. Each eddy can be described by a characteristic linear dimension and therefore associated through Fourier transform to a wavevector $\boldsymbol{k}$. In steady state, the energy is distributed among the various harmonics. At high Reynolds number, the turbulence is considered isotropic and at high k the dissipation acts such that it is independent from the macroscopic scales, being only related to the viscosity. In this way, a dissipation rate[4] is evaluated as

$$\epsilon_0 = 2\nu \int_0^\infty k^2 E(k)\, dk, \tag{2.53}$$

where $E(k)$ represents the energy density per wave number. It is possible to define the characteristic dimension of the dissipation scale from dimensional analysis, as follows

$$\eta = \left(\frac{\nu^3}{\epsilon_0} \right)^{1/4}, \tag{2.54}$$

where ϵ_0 is the energy dissipation rate. In his theory Kolmogorov was able to define the energy spectrum as a function of k, such that in the *inertial*

[4]there is a conflict of notation due to the fact that ϵ_0 was defined in the Maxwell's equations as the vacuum permittivity

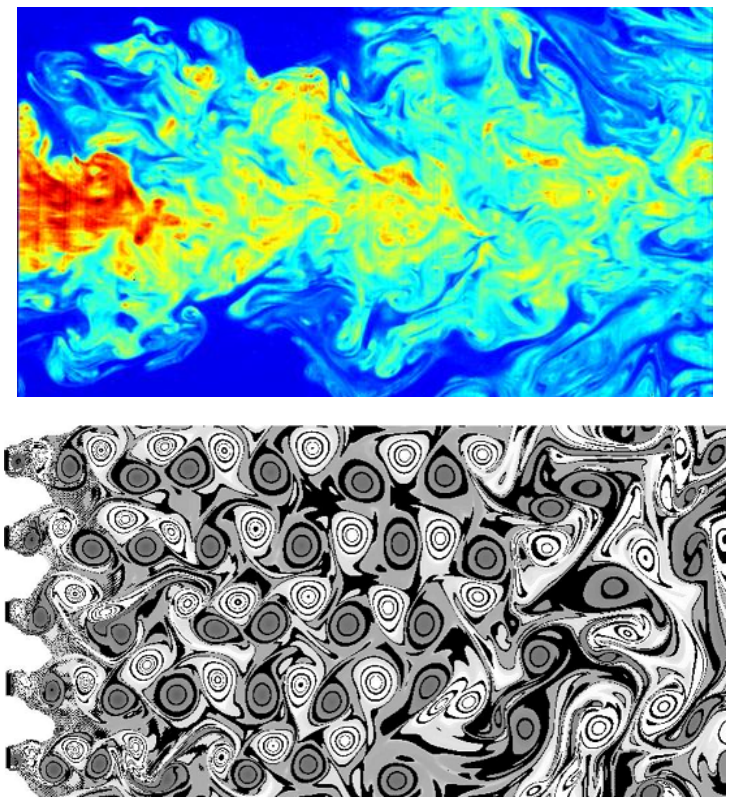

Figure 2.2: Turbulence in neutral fluids. (a) False-color visualization of a submerged turbulent jet by laser-induced fluorescence; the initial flow is soon spread in a series of smaller vortexes ([27])(b). Simulation of 2D flow by Lattice-Boltzmann code with visualization of the vorticity; the flow passing a grid is turbulent but gradually smaller eddies decay into larger structures in the far right of the picture (Fig. 3 [25]) .

range $I^{-1} \ll k \ll \eta^{-1}$ the energy of every single mode is given by

$$E(k) = C\epsilon_0^{2/3} k^{-5/3}, \tag{2.55}$$

where C is a constant value. This constitutes the energy spectrum that describes the energy distribution among the various modes and it is one milestone of turbulence.

When the dependence on one of the cartesian components can be negligible, the turbulence becomes quasi-two dimensional. Examples of such systems are soap films and geophysical flows. In order to underline the peculiarities of fluid behaviour in this limit, it is useful to introduce the *vorticity* as

$$\boldsymbol{\omega} = \nabla \times \boldsymbol{v}, \tag{2.56}$$

and taking the curl of the Navier-Stokes equation to obtain the vorticity equation

$$\left(\frac{\partial}{\partial t} + \boldsymbol{v}\cdot\nabla\right)\boldsymbol{\omega} = -\left(\boldsymbol{\omega}\cdot\nabla\right)\boldsymbol{v} + \nu\Delta\boldsymbol{\omega}. \tag{2.57}$$

In a 2D velocity field $\boldsymbol{v} = v_x\boldsymbol{e}_x + v_y\boldsymbol{e}_y$. Consequently $\boldsymbol{\omega} = (\partial_x v_y - \partial_y v_x)\boldsymbol{e}_z$ and the vortex stretching and twisting term $(\boldsymbol{\omega}\cdot\nabla)\boldsymbol{v} = 0$. Finally, for inviscid fluids ($\nu = 0$) the equation simply becomes $(\partial_t + \boldsymbol{v}\cdot\nabla)\boldsymbol{\omega} = 0$, that means that vorticity is constant along the fluid element, and it is possible to introduce the conservation of the total *enstrophy* $W = \int(1/2)|\boldsymbol{\omega}|^2 d\,\boldsymbol{x}$ in addition to the conservation of kinetic flow energy $E = \int(1/2)|\boldsymbol{v}|^2 d\,\boldsymbol{x}$. This peculiarity of 2D fluids gives rise to an inverse or backwards cascade [28] described by a $E(k) \sim k^{-5/3}$ spectrum for $k < I^{-1}$ from higher to lower wavenumber with zero-vorticity flow up to to the sysyem scale. The complementary part evolves as $E(k) \sim k^{-3}$ for $k > I^{-1}$ down to the viscous cutoff with a vorticity flow and a zero-energy flow. The inverse cascade can be simply visualized by the formation of macroscopic structures or flows from a self-organising process that involves the merging of smaller eddies into bigger structures. This is not observed in 3D systems, where only the direct cascade is present. In a 2D system further characterized by periodicity in one dimension, it is possible to observe also the formation of zonal structures with an effect of the turbulence giving rise to a sustained mean flow by the inverse cascade. An example of this phenomena for neutral fluids is observed in planetary atmospheres.

Examples of experimental observation of turbulence in 3D and simulations of the effect of inverse cascade in 2D systems are found in figure Fig. 2.2 that clearly visualizes the different behavior of the fluid.

2.3.2 Turbulence in magnetized plasmas

Plasmas, as conducting fluids, show a greatly increased complexity compared to neutral fluids due to their long range collective interaction. In plasmas a series of collective modes are generated due to the response to external electromagnetic fields or as the evolution of perturbations that are unavoidable in real experiments. Theory of collective modes in magnetically confined plasmas is divided in stability and transport studies. Stability treats large scale MHD modes to determine the conditions leading to macroscopically stable plasmas. In absence of MHD modes, transport is mainly caused by turbulence, which is a small scale instability. To be stable, a plasma would need to be in thermodynamic equilibrium (homogeneous in space and characterized by a Maxwellian distribution

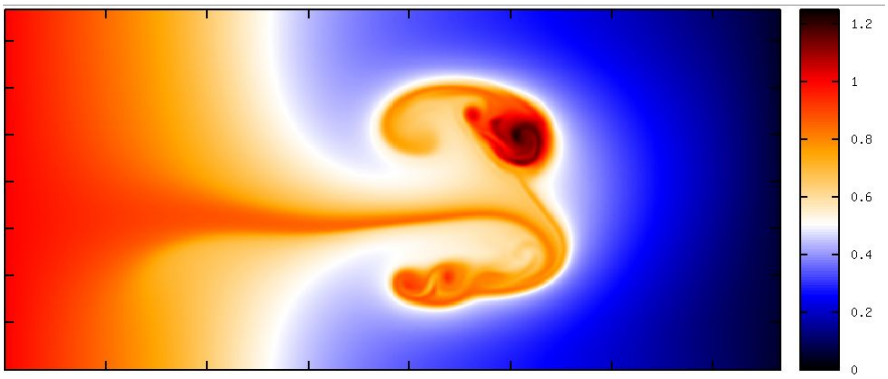

Figure 2.3: Single (seeded) blob computed with a full-f 2-D gyrofluid model. The K-H instability is clearly visible in the tails (Fig. 2 [30])

function). This is never the case in a magnetically confined plasma, which is characterized by various gradients, considered as source of free energy for the instabilities to develop. The linear growth of a plasma instability can be considered the origin of turbulence [29]. The nonlinear self advection of the plasma flow, following the unstable evolution of the perturbation amplitude, can lead to a fully developed turbulent state. To have an intuitive idea of this phenomena, in Fig. 2.3 a simulation of the evolution of a single blob in radial direction is represented. The high shear in radial velocity causes a Kelvin-Helmoltz instability to develop, with the formation of a series of eddies that characterize the turbulent state. The scales of unstable modes giving rise to plasma turbulence are different, such that a single injection range, as well as a single cascade, cannot be considered for turbulence in magnetized plasmas. It is straightforward to see the connection between deviation from thermodynamic equilibrium, linear instability and transport.

Focusing on a tokamak configuration, the strong toroidal magnetic field $\boldsymbol{B} \approx B_t \boldsymbol{e}_\phi$, together with the axisimmetric geometry, is able to order the dynamics such that the nonlinear part is essentially two dimensional. The fluid part of the dynamics occurs on the perpendicular plane with reference to the magnetic field, often referred to as drift plane, since here drift velocities and fluxes occur. The dynamics in the parallel direction is mainly related to the electrons, through their adiabatic response. As a consequence, turbulence in magnetized plasmas is quasi-two dimensional and exhibits a phenomena analogous to the dual cascade described in Sec. 2.3.1. The consequent formation of zonal structures is treated in more detail in Sec. 2.4.1. Different instabilities can lead to turbulence, among which the driftwave (see Appendex) or the interchange instability.

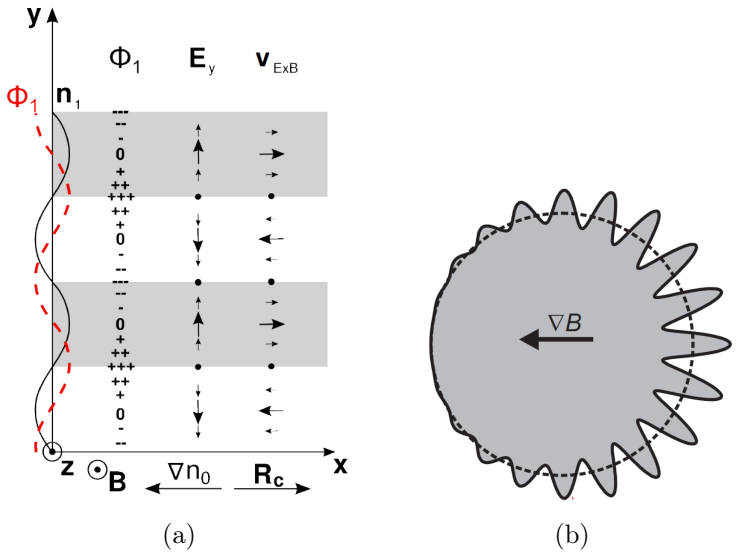

(a) (b)

Figure 2.4: (a) The mechanism of interchange instability. The black line indicates the density perturbation, the red dashed line the potential perturbation. The phase relationship is such that $E \times B$ velocity generates a large transport (b) Sketch of a ballooning mode in a tokamak. The relative direction of the density/temperature gradient and the curvature of the magnetic field determines the favorable or unfavorable curvature ([22]).

2.3.3 Interchange instability

The interchange instability in plasmas can be considered as the analogous of the Rayleigh-Taylor instability when a heavier neutral fluid lies on a lighter one. The density gradient corresponds to the pressure gradient in the plasma and the gravity has its parallel in the centrifugal force due to magnetic field curvature. The overall mechanism is more complicated than in a neutral fluid since in general, in a magnetically confined plasma, a force on particles generates a drift perpendicular to its direction. The basic picture of the interchange instability is here illustrated. The most unstable modes are those with $k_{\|} = 0$ (flute modes) since $k_{\|} \neq 0$ would bend the magnetic field lines along the toroidal direction, increasing the shear and therefore the magnetic energy with a stabilizing effect. Here, only flute modes will be considered. Contrarily to the driftwave case (see Appendix C), the dynamics is therefore purely two-dimensional. Consider a magnetized plasma, studied in a slab geometry but including the presence of a curvature of the magnetic field with radius $\boldsymbol{R_C} = R_C \boldsymbol{e}_x$. The

charged particles undergo a drift due to the presence of the curvature

$$\mathbf{v}_{\mathbf{D}\alpha} = \mathbf{v}_{\nabla B\alpha} + \mathbf{v}_{\kappa\alpha} = \frac{1}{\omega_{c\alpha}} \left(v_{\parallel}^2 + \frac{v_{\perp}^2}{2} \right)_{\alpha} \frac{\boldsymbol{e}_y}{R_C}. \tag{2.58}$$

The presence of $\omega_{c\alpha}$ in the velocity is such that particles with opposite charges undergo drifts in opposite directions. The effect of the curvature combined with an harmonic density perturbation $\widetilde{n} = n_0 exp[i(k_y y - \omega t)]$ induces a charge separation; with $k_{\parallel} = 0$, electrons are not able to short-circuit the charge separation due to the impeded dynamics along the magnetic field and a potential perturbation is maintained. Eventually, this leads to the formation of a cross phase of $\delta_{n,\phi} = \pi/2$. An electrostatic field is generated $\widetilde{\boldsymbol{E}} = -\nabla\widetilde{\phi}$, again directed along the y direction. In this case, the advection due to the $E \times B$ drift results maximum and directed in the positive x direction where the density perturbation peaks, therefore generating a strong transport (Fig. 2.4(a)). The growth of the initial perturbation can eventually become nonlinear and therefore perform a transition into turbulence.

In an MHD interpretation, the gradient tends to interchange flux tubes of different density when it is possible to generate a system with a lower potential energy, but an instability is actually able to develop only in regions of *unfavourable* or *bad curvature*. Here, the curvature radius of the magnetic field is parallel with the density and/or temperature gradient. Energy is minimized by taking a flux tube of high density down along the gradient. In regions of *favorable* or *good curvature*, i.e. where curvature and gradient are antiparallel, any perturbation is promptly damped due to the effect of a favorable $E \times B$ advection. The necessity for an average bad curvature is easily derived through the application of the energy principle [29]. In a tokamak, the interchange instability tends to evolve in so-called Ballooning modes, pressure driven instabilities. Fig. 2.4(b) clearly shows on the poloidal section the effect of good and bad curvature. In this sense, the poloidal field gives a stabilizing contribution to the overall dynamics, progressively carrying the particles from regions of bad curvature (the outside of the tokamak) to regions of good curvature (the inside) during their motion along the field lines.

2.4 L-H transition

The objective of this section is to introduce the main physical features of the so-called L-H transition, since the present thesis aims to model some

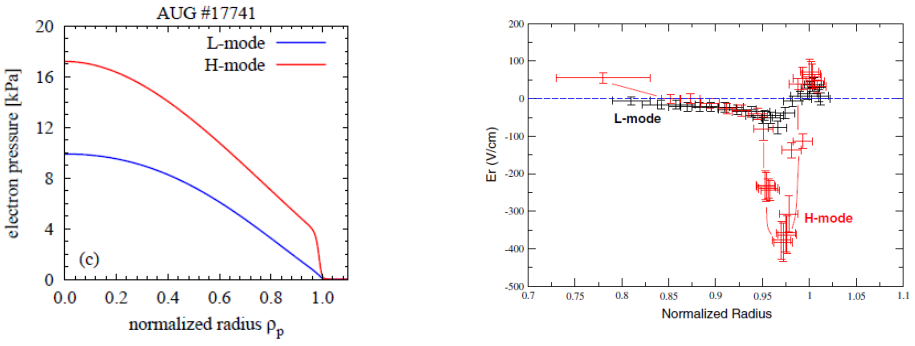

(a) (b)

Figure 2.5: Differences between L- and H-mode (a) Measured L- and H-mode pressure profiles in ASDEX Upgrade. The pedestal is evident in the outer region of the plasma, by $\rho_p = 1$ (Fig 1.2 [31]). (b) The measured radial electric field, generating the sheared $E \times B$ flow at the edge, by the well (Fig 7 [32])

of the aspects of this complex phenomenon that leads to an improved performance in a tokamak.

In a toroidally confined plasma there exist two mode of operation, named L-mode, from low confinement, and H-mode from high confinement. H-mode exhibits an increased value of the confinement time by a factor two, and therefore a raised energy content at constant heating power (see Eq (2.40)). Because of this great advantage, it is the chosen mode for operation in ITER, since it is evaluated that it will make the goals of fusion possible [9]. H-mode was discovered in 1982 at ASDEX [15] and soon reproduced on other experimental devices. This mode of operation is reached in a toroidally confined plasma when a sufficient amount of external heating power is provided and is more easily acquired in divertor geometries. A main feature of the H-mode is the sudden suppression of the plasma turbulence in a radially localized region in the proximity of the LCFS [33]. In this edge region, turbulent transport is sharply reduced and characteristic steep density and temperature gradients are established: a density and temperature *pedestal* is formed, above which the profile of the core plasma resembles that of L-mode but shifted to higher values (see Fig. 2.5(a)). The edge transport barrier inside the separatrix is what determines the increase in confinement time: with reduction of turbulent fluctuations, and consequent reduction of $\widetilde{\Gamma}$, the heat conductivity can go down to $\chi \approx \chi_i^{NC}$, as it was mentioned at the conclusion of Sec. 2.2.3.

Extended experimental studies allowed to characterize the L-H transition. The fluctuations present in the plasma edge in ASDEX were found

to be resistive ballooning and ion-temperature-gradient driven turbulence [34]. Scaling laws for the confinement time of L- and H- mode were evaluated and the threshold power required for the transition was estimated as

$$P_{LH} = 1.38 \times 10^{-20} n^{-0.77} B_0^{0.92} R_0^{1.23} a^{0.76} MW \tag{2.59}$$

A consistent physical description of the L-H transition is still missing. It is nowadays commonly accepted that the elementary process able to reduce the turbulence intensity and allow the consequent formation of the pedestal is the ability of $E \times B$ poloidal sheared flows to decorrelate the turbulent eddies [35] [36] (see Fig. 2.6(d)). This can be summarized in the following critical condition

$$\tau_S^{-1} > \gamma_{lin} \tag{2.60}$$

where τ_S^{-1} is the decorrelation rate of the turbulent eddies caused by the flow (the effect of sheared flows on eddies is introduced in Sec. 2.4.1) while γ_{lin} is the linear growth rate of the instability driving the turbulence.

These flows are macroscopic plasma flows, poloidally and toroidally homogeneous with finite radial wavenumber, deriving from $E \times B$ poloidal advection. Considering the magnetic geometry of a tokamak, the presence of the radial electric field plays therefore a key role in the development of the H-mode. Indeed, there is a sharp difference in the L- and H-mode E_r. In the former the profile is low and flat, while in the latter, a deep *well* is formed, which is localized inside the separatrix (see Fig. 2.5(b)). This is coherent with the fact that the critical transition is localized at the edge, with the formation of the edge transport barrier. Such a shape of the electric field is associated with a strong $E \times B$ shear flow localized at the edge, since in its radial range fluctuations are quenched, turbulence decreases and the steep gradients develop.

The steady-state radial electric field can be deduced from the radial force balance

$$E_r(r) = \frac{\nabla p_i}{Z\, e\, n_i} - v_\theta B_\phi + v_\phi B_\theta, \tag{2.61}$$

where the first term on the right is the diamagnetic contribution, often referred to as the neoclassical contribution E_r^{neo}, while the second and the third are the $v \times B$ components. The ∇p_i is in turn determined by the power and particle balance of the plasma, in which the heating power is considered, and depends also on the transport also. The diamagnetic contribution plays a key role after the L-H transition, since it is able to maintain the H-mode alone [33] by inducing an $E \times B$ flow that stabilizes the decorrelation condition Eq (2.60). Right at the L-H transition, instead,

the pressure gradient is found to lag behind the formation of the E_r [37]. Furthermore, the subtle mechanism of the transition implies a reduction of the turbulence whereas its driving force, the gradients in temperature and density, increase: in L-mode the gradients are smoother since the turbulence is higher, while in H-mode the gradients are steeper because the turbulence is lower since the gradient itself maintains the necessary $E \times B$ flow. In conclusion, the pressure gradient alone, despite locking the H-mode state when sufficiently steep, seems not to be able to primarily trigger the L-H transition. The seeding or initiation of the L-H transition requires therefore to consider further mechanisms, including $v \times B$ contributions to E_r which can be evaluated from toroidal and poloidal momentum equations. As an example, toroidal contribution can derive from NBI heating, while poloidal ones can have various origin. In particular, the role of zonal flows will be introduced in the following subsection.

2.4.1 Zonal Flows as collective phenomena

Zonal flows (ZFs) in a tokamak are defined as stationary ($\omega = 0$), toroidally symmetric ($k_\phi = 0$) $E \times B$ macroscopic flows, which are constant on a magnetic surface ($k_\theta = 0$) but vary in the radial direction ($k_r \neq 0$). In order to distinguish them from the background $E \times B$ flow, their definition has to include the fact that ZFs have to be driven exclusively by microturbulence. In toroidal machines, the existence of sheared flows at the edge region was found, the drive from microscopic turbulence was evidenced and an energy transfer study was performed [38]. In this way, a non-local energy transfer in wavevector space was recognized as the main mechanism for ZFs amplification. This means that energy is transferred between scales that are widely separated, i.e. from the microscopic eddies to the macroscopic zonal flow. The fact that ZFs cannot directly tap free energy from the background gradient implies that, if the underlying turbulent drive extinguishes, they vanish due to dissipative processes. In addition, since ZFs are driven by turbulent fluctuations, they constitute a sink for the turbulence energy and their role in the reduction of transport is intensively studied. The description of the overall mechanism of zonal flows formation requires a complete treatment of drift wave turbulence-ZFs nonlinear interaction through 3-wave coupling [39] which is beyond the scope of this thesis. Therefore, here only a basic introduction is presented that does not involve a rigorous deduction. This phenomenon is a classic example of self organization and structure formation in turbulent media, that is made possible by the fact that turbulence in plasma is essentially two-dimensional (see Sec. 2.3.1).

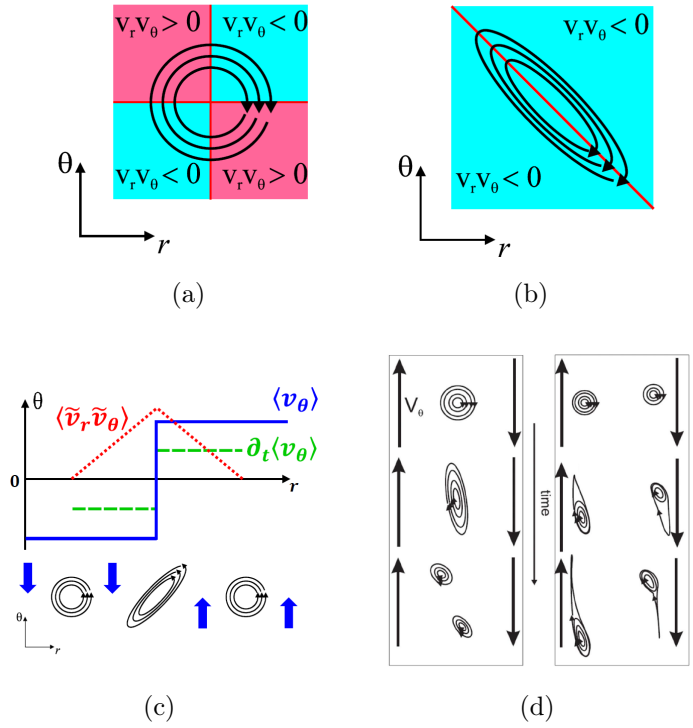

Figure 2.6: The mechanism of zonal flow generation. (a) A symmetric eddy generates no Reynolds stresses. (b) A tilted eddy and its net contribution. (c) Eddy tilting from sheared flow and generation of net poloidal flow. (d) Sketch of eddies decorrelation and straining out ((a)(b)(c)[40], (d)[38]).

The main difference with the already mentioned inverse cascade in fluids, i.e. where two smaller eddies of similar size merge together to form one of about twice the size, is the nonlocal energy transfer. This allows to consider a clear scale separation between turbulent eddies and ZF itself. Therefore, the evaluation of the zonal averaged poloidal momentum equation after a Reynolds decomposition leads to define the evolution equation of the ZFs

$$\frac{\partial \langle v_\theta \rangle}{\partial t} = -\frac{\partial \langle \widetilde{v}_\theta \widetilde{v}_r \rangle}{\partial r} - \mu \langle v_\theta \rangle, \tag{2.62}$$

where, respecting their definition, the ZFs drive derives only from microturbulence and here it is present as the divergence of the Reynolds stress tensor. The μ term represents the dissipation. Understanding the meaning of the Reynolds stress, beyond its role of radial transport of poloidal momentum, allows to comprehend the mechanism of ZFs gen-

eration. Consider a single symmetric eddy, as an example of isotropic turbulence: as can be easily observed in Fig. 2.6(a), this gives no contribution to Reynolds stress. A tilted eddy, instead, does (Fig. 2.6(b)). But in order to give rise to a net poloidal flow, a radial variation of the tilt is required. Since tilting can be caused by a sheared flow, this induces a bootstrap mechanism for an autonomous zonal flow amplification in presence of turbulence (Fig. 2.6(c)).

The nonlocal effect of sheared flows on eddies is described as a *straining out* process [40]. In this picture, eddies are tilted, elongated and finally curled up by the flow shear. Such a mechanism is inherently different from the classic decorrelation of eddies due to sheared flow, that resembles more a direct cascade, as can be observed in Fig. 2.6(d). Both of them are able to remove energy from the microturbulence, but only the first is able to drive a ZF.

2.4.2 I-phase and Limit Cycle Oscillations

The L-H transition is abrupt, in the sense that over the threshold value there is a sudden change in the plasma equilibrium state. The presence of a critical parameter as the heating power, determining the state change and depending on the system characteristics (Eq (2.59)), suggested that the L-H transition could be considered as an equilibria bifurcation and therefore treated through dynamical systems theory [41]. When the critical parameter is overcome, the new equilibrium is reached, but this is not mandatorily performed in a catastrophic way. If the transition happens at sufficiently low plasma density ($n < 5 \times 10^{-19} m^{-3}$) an oscillatory phase can be observed (see Fig. 2.7). This step was defined I-Phase in order to underline its intermediate character, sharing properties of both the L-mode and the H-mode [2]. The turbulence level, quantified through the measured Doppler reflectometry signal (A_D) from the E_r minimum at $\rho_p \sim 0.988$, moves from the constant L-mode level to a pulsating phase at around $2 - 4kHz$ and extends into the scrape-off layer. While the L-I transition is effectively sharp, with a well defined threshold at the critical heating power, the I-H transition appears to evolve smoothly in a fully developed H-mode. Furthermore, the I-phase can be maintained for a whole discharge (i.e. for $\tau \approx 10s$ at ASDEX Upgrade) when the heating power is chosen marginally close to te L-H power threshold. The I-phase is observed also in back-transition from the H-mode to the L-mode in the same conditions in which a forward transition can be observed when the external heating power is reduced. In this case an asymmetry is present: the fluctuation level is observed to be larger after the back-transition. This

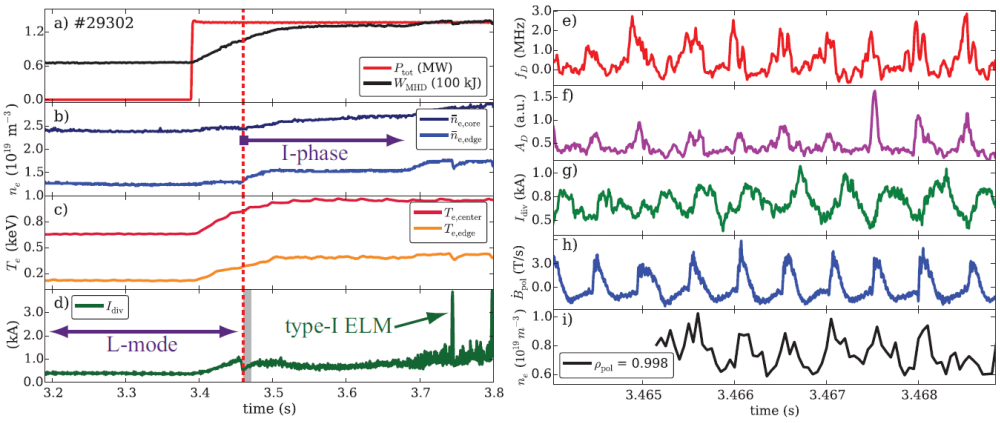

Figure 2.7: Typical L-H transition at low density in AUG. After switching on the auxiliary heating P_{tot}, the plasma energy content W_{MHD} (a) and the temperature (c) rise. The rise in linear averaged density (b) starts with a delay of about 50 ms and coincides with a drop of the divertor shunt current (d) and the start of the LCOs (dashed line). The time traces (e)-(i) show a short segment of the LCO and correspond to the shaded area in (d). The LCOs are visible in the doppler shift $f_D \sim u_\perp$ (where $u_\perp$ is the poloidal $E \times B$ flow)(e) and the backscattered amplitude of the Doppler reflectometry signal $A_D \sim \widetilde{n}^2$ (with $\widetilde{n}^2$ turbulence intensity)(f), as well in the divertor current (g), magnetic probe signal below the divertor (h), and the local density slightly inside the LCFS(i) (fig.1 [1])

can be explained by the fact that, while the direct transition occurs at L-mode conditions, the back-transition starts with the steeper gradients of the H-mode, thus a larger source for turbulence is available.

The characteristic pulsations of the I-phase are observed in various measurement timelines, where different signals are modulated with frequencies that existing models cannot predict quantitatively [1]. Due to their non-sinusoidal shape and characteristic phase lag between two pulsing quantities, for example density and poloidal velocity fluctuation, they are referred to as Limit Cycle Oscillations (LCOs) from dynamical systems theory. A basic definition for a limit cycle is that of a closed or periodic orbit, which is a solution of an initial value problem that exists for $0 \leq t < \infty$ such that $x(t) = x(t+T)$ for all t, thus extending the definition of a *fixed point* of a system [42]. A more rigorous approach is performed in Sec. 5.1, where the study of the stability of such orbits is introduced. This kind of solutions can appear after critical bifurcation at the variation of a parameter of a dynamical system and are therefore useful to study equilibria transitions.

Many dynamical models exist, that try to explain the observed oscillations during the I-phase. These are mainly based on a flow-turbulence interaction mediated by Reynolds stresses, often resulting in predator-prey type of equations that are able to reproduce the basic features of the LCOs. These will be reviewed in Sec. 3.1.

2.4.3 Conclusions on the L-H transition

While it is in general accepted that the final transition into H-mode is sustained by the neoclassical mean flow only (as specified in Sec. 2.4), the fundamental mechanism triggering the L-H transition is still unclear, despite there exist various ways to modify the background $E \times B$ flow. But when the background flow shear is strong enough, the self amplification of the zonal flow can be activated leading to stronger zonal flow and the necessary reduction of turbulence. In particular, the work described in [43] points in this direction, suggesting that the actual transition to the H-mode occurs when the shear due to zonal flows alone is sufficient to momentarily quench the turbulence, therefore allowing a rapid growth of the mean flow due to the gradient, which then locks the transition. The observation during the I-phase of pulsating predator-prey behavior of the flow-turbulence interaction at the onset of the transition [2] supports this theory. The ability of Reynolds stresses to effectively extract energy from the mean flow is actually supported experimentally [38]. However, other experimental results point in a different direction [44] [45], since the Reynolds-stress driven zonal flows were found to be too weak to justify the necessary $E \times B$ sheared flow for the initial turbulence quench. Furthermore, recent experiments at ASDEX Upgrade [46] indicated that the measured E_r can be explained solely by the E_r^{neo} predicted by the neoclassical theory, suggesting a negligible role of the zonal flows during the whole transition, with the poloidal $E \times B$ sheared flow reduced to the neoclassical flow only. In conclusion, the physics of L-H transition in toroidally confined fusion plasmas is still an open issue that requires a more satisfactory understanding with very important implications, mainly due to the impact of the confinement improvement that the H-mode guarantees.

2.5 Edge Localized Modes

In the present section, a phenomenological description of Edge Localized Modes (ELMs) is given, their role in nuclear fusion is presented and a classification is provided.

The H-mode state of a toroidally confined plasma, despite being characterized by a reduced level of edge turbulence is not a stationary equilibrium. A series of cyclic instabilities, located in the outer region of the plasma, causes the transport barrier to regularly collapse [47]. This is due to modes becoming unstable, therefore increasing the turbulence in a bursty fashion. These instabilities are called Edge Localized Modes (ELMs), and their role in nuclear fusion is of paramount importance. The ELM crash, the collapse of the pressure gradient, happens on a timescale $< ms$, while the repetition frequency, depending on the time needed to recover the pressure gradient, is in the order of $\approx 10Hz$ to $1kHz$. During the ELM crash, anomalous transport is strongly increased in the edge of the plasma and this is the reason why the steep gradient of the pedestal region cannot be sustained anymore. Particles and energy are thus expelled outwards of the LCFS. Once the gradient has collapsed, the free energy source for the turbulence is no more available, the confinement is restored and the edge pressure gradient can steepen again due to energy coming from the core, initiating a new cycle. During every ELM burst not only confinement is degraded, but also a high fraction of the energy stored in the plasma is expelled out of the LCFS, eventually impacting on the divertor target plates, which are therefore subjected to a high pulsed load of particles and energy (up to $20MW/m^2$ at ASDEX Upgrade). This can turn not sustainable both from a material and thermal hydraulic point of view in a fusion reactor, since could lead to a potential failure of the component as the energy release increases with the machine size [48]. However, ELMs also have an important advantage. Being able to expel particles, they can get rid of impurities and helium ash, allowing to experimentally control the particle inventory in a ELMy H-mode discharge . Despite their critical importance, there exist no complete theory about ELMs yet, and their description is still qualitative. Therefore, it is not possible to exactly predict the level of ELM activity in future experiments [9].

ELMs events are observed and measured through their signature in various diagnostics. For example, in Fig. 2.8 a timeline from a shot of ASDEX Upgrade is presented, showing two separated ELMs events. The divertor shunt current (a) is a measure of the particles impacting on the divertor, indicating the high transport period. It is strongly correlated to the D_α signal (d), indicating the presence of additional particles in the SOL following the enhanced transport out of the LCFS. Magnetic disturbances before and during an ELM event are measured through Mirnov coils disposed outside the plasma chamber, and show characteristic signatures, here in the radial magnetic field fluctuation (b). Furthermore, through the soft x-ray emission (c), it is possible to observe the gradual

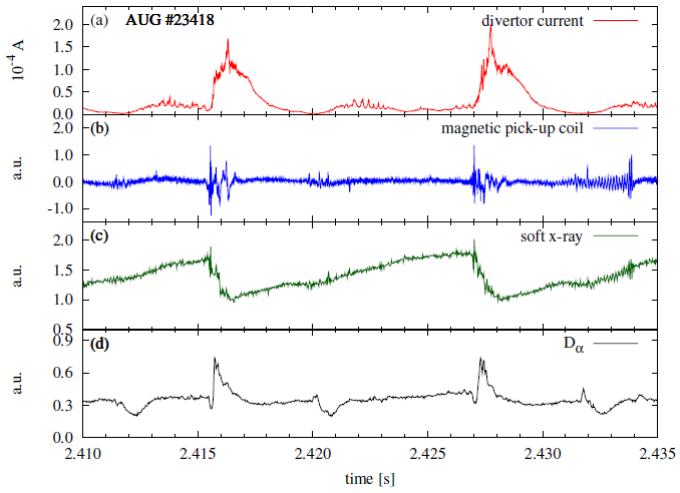

Figure 2.8: The signature of Type-I ELMs in different diagnostics. The burst like event is visible in (a) the divertor current (b), the magnetic pick-up coils (c), the soft x-ray radiation (d) and the D_α radiation. The gradual recovery between ELMs can be observed in the edge soft x-ray signal (d) (fig.2.9 [31])

recovery of the pedestal between the two ELMs events [31].

The high level of magnetic fluctuations during an ELM event suggests that ELMs can be explained as MHD events. The basic theoretical paradigm for ELMs is a coupled peeling-ballooning mode getting unstable [49]. As the edge pressure gradient increases, it approaches the ballooning limit: at the high field side, the pressure gradient has a destabilizing effect, counterbalanced by the energy required to bend the field lines. Right before the ELM crash, the bursty event, the gradient remains constant until an increasing bootstrap current can drive a kink instability, leading to the collapse of the edge transport barrier. This can be seen in Fig. 2.9(a), where the overall behavior is described as the evolution of two values: the pressure normalized to the ballooning pressure limit and the peak value of the parallel current in the pedestal region, normalized by the average pedestal parallel current.

2.5.1 Classification of Edge Localised Modes

Although some of the previous features are common to all ELMs events, the latter are classified on the basis of their relative differences, regarding the dependence on the heating power, the ELM frequency, the magnetic signature and the theoretical peeling-ballooning stability limit. Three main types of ELMs are classified accordingly [50]:

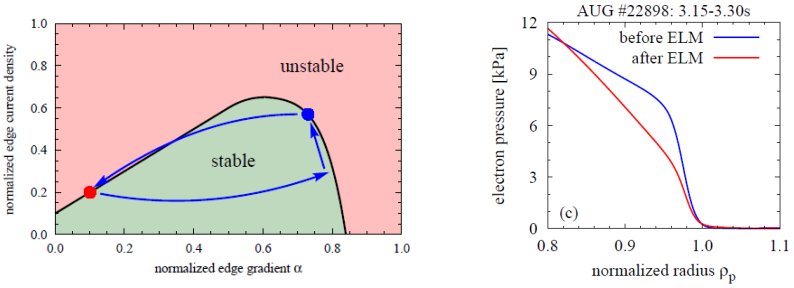

(a) (b)

Figure 2.9: (a) A sketch of an ELM cycle in the peeling ballooning theory adapted from [49]. At high pressure gradient and large current density (blue point) the ELM is triggered and causes the profile to relax (red point). From there the profile recovers until the next ELM can occur. (b) Pressure profile evolution during an ELM cycle. In red the profile right after the crash at the beginning of the cycle, in blue the profile right before the crash. (Fig 2.10 and 2.2c [31])

Type I-ELMs

Also defined large or giant ELMs, Type I-ELMs show the highest relative intensity (see Table 2.1) and were the first to be discovered. Due to their high energy losses and damage capabilities, Type-I ELMs cannot be tolerated in a fusion reactor. They appear as short, isolated bursts and they present a reduced magnetic activity. They are present only during a fully developed H-mode, at high edge temperature. Therefore, they are linked to ideal MHD instability and the pressure gradient achieves the ideal ballooning mode critical value before a kink mode is initiated. The frequency of the Type-I ELMs increases with increasing heating power but typically remains around $10 - 200 Hz$.

Type-II ELMs

This type of ELM event is characterized by a lower magnitude in the burst compared with the Type-I ELMs, while the frequency is relatively higher. Therefore, they are also referred to as *grassy* ELMs. Although Type-II ELMs show good performances for a fusion H-mode plasma, i.e. elevated confinement and low divertor heat load during the particle exhaust, it appears only in a narrow window of parameters characterized by high density and strong plasma enlongation.

Type-III ELMs

This type of ELM is mainly characterized by the presence of a *magnetic precursor* prior to the crash. This is a coherent magnetic mode that is measured in the radial magnetic field coils whose typical frequency range is $\approx 10-100\,kHz$, therefore faster than the crash itself. It is found to grow dramatically before the crash and to disappear right afterwards. In tokamaks where pick-up coils were disposed around the whole poloidal circumference, the precursor was observed as a mode propagating in the poloidal direction, while other devices such instruments are usually used to measure the radial magnetic fluctuation on the midplane only. The fact that Type-III ELMs are stabilized by high pedestal temperatures and that they appear well below the ideal ballooning limit, suggests that these modes are resistive MHD events. Their relative amplitude is much smaller than Type-I ELMs (see Table 2.1), but at the same time they appear with a higher frequency between 0.2 and $1kHz$. Furthermore, the frequency of this type of ELM decreases with increasing heating power.

	Type-I	Type-III
JET	$2-9$	
DIII-D	$1-7$	$1-5$
ASDEX Upgrade	$3-6$	$0.5-2$

Table 2.1: Experimental result for the fraction of energy lost during a single ELM crash, expressed as the percentage of the total plasma energy for Type-I and Type-III ELMs in different tokamaks. (Table 1 [51])

2.6 Thesis goal: LCOs into ELMs transition

In the previous chapters, the fundamental concepts for the background of this thesis were described and introduced. In this section, the motivation for this thesis is illustrated and consequently the its goal is presented.

The main motivation for this thesis derives from the experimental results of [1], whose most important conclusions will be summarized here. In [1], LCOs at the transition from L- to H-mode were investigated with the support of various diagnostics, showing LCOs frequency dependence on plasma density, temperature and current, and pointing to the same electromagnetic nature of LCOs and Type-III ELMs . A typical dis-

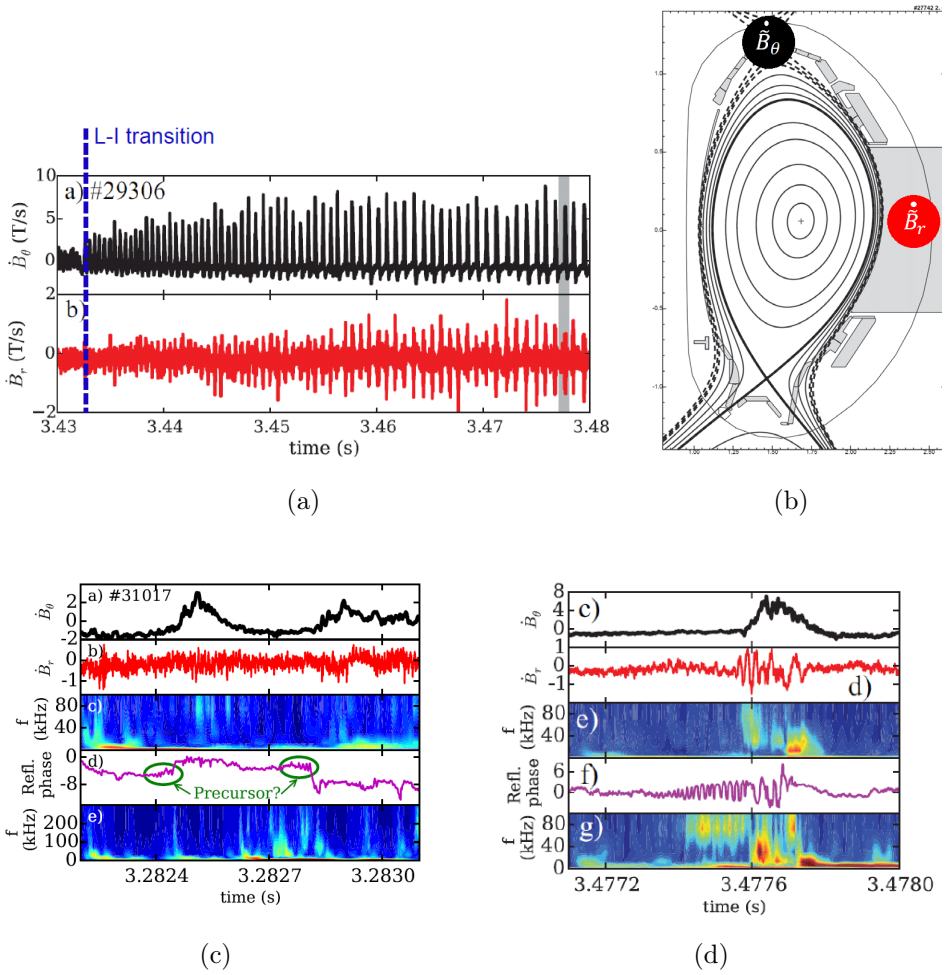

Figure 2.10: The observed transition of LCOs into ELMs during the I-phase. (a) Poloidal and radial magnetic field fluctuation. The L-I transition is evidenced. (b) The measurements are performed in different positions. (c) The very first two LCO pulses (early LCOs) after the L-I transition in the poloidal field. (d) A zoom in the late LCO phase (shaded area in (a)). Prior to the poloidal field perturbation, precursor activity is found in the raw signal of radial field perturbation ((a)(d) Fig 9, (c) Fig.10 [1]).

charge showing an L-H transition is illustrated in Fig. 2.7. When the NBI is switched on, plasma energy starts immediately to rise. Shortly after ($\approx 50ms$) when the density also starts to rise, the divertor shunt current drops. This is the moment at which LCOs become clearly visible in different signals as a $\sim 2\,kHz$ modulation. In particular, the $\dot{B}_\theta$ signal, measured with pick-up coils, allows to reveal in the most clear way

the oscillations. If the heating power value is chosen marginally close to that required for the L-H transition, LCOs can be maintained stable for a whole discharge. For slightly higher values, instead, the initial LCOs are observed to decrease steadily their frequency, while the amplitude of the oscillations constantly increases, until the first type-I ELM occurs, indicating a fully developed H-mode state. This evolution is visible in the magnetic field perturbation $\dot{B}_\theta$ in Fig. 2.10(a), in which the LCOs move smoothly from a very regular state to an intermittent state, characterized by single, isolated bursts.

At AUG, this magnetic activity is measured through a set of pick up coils. The ones for $\dot{B}_\theta$ are disposed poloidally around the torus. Among them, the stronger signal is measured in the ones below the divertor (coded 22 to 25). The coils for $\dot{B}_r$ are instead disposed on the midplane. The full diagnostic can be seen in Fig. 4.1(a) and Fig. 4.1(a). The position for the measurements of the signals reported in this section is sketched in Fig. 2.10(b).

A further zoom in the single peaks reveals then a clear difference between the magnetic signature of the two measurements. While the poloidal pick-up coils register modulated perturbation from the very beginning of the onset of LCOs ($\approx 5\,T/s$), the radial signal is much weaker, slightly above the noise level ($\approx 0.2\,T/s$) as can be seen in Fig. 2.10(c). In the late phase, instead, while the LCO turbulent pulse appears as a single peak in the $\dot{B}_\theta$ signal, $\dot{B}_r$ features a short oscillatory period at high frequency ($\sim 40 - 100kHz$) right before the $\dot{B}_\theta$ maximum (Fig. 2.10(d)). This is what can be defined as a *precursor* mode, that increases in amplitude and disappears when the LCOs is at its maximum.

This dynamics of the late oscillations during the I-phase fulfills the definition of Type-III ELMs.

Therefore, this smooth transition of oscillatory LCOs into higher isolated bursts with characteristic magnetic activity clearly points to identify the late LCOs with Type-III ELMs, suggesting a common nature of the two phenomena. This evolution of quasi-sinusoidal LCOs into a busty phase identified as type-III ELMs during slow L-H transitions was observed in various other devices [52] [53]. However, it is still an open question, whether the two pulsating phenomena originate from the same underlying physical mechanism. While most of the existing models for LCOs are able to reproduce the quasi-sinusoidal early phase, the transition into the intermittent phase with the presence of precursors is not covered. Furthermore, many existing models are derived from heuristic assumptions and therefore a falsification results difficult, due to the many parameters which can be adjusted to fit experimental observations.

The goal of this thesis is to develop a reduced model, derived from first principle equations for the plasma edge, able to provide a further step in the comprehension of the overall physics of the L-H transition, fundamental for ITER operation. In particular, the focus is on the possibility to present a minimal model able to reproduce the features of both LCOs and ELMs, with the evolution of the first in the second. This aims to sustain the hypothesis of a common nature of LCOs and ELMs during the I-phase. The typical features of this transition are related to the evolution in time of the plasma. A dynamical model is therefore implemented, studying the possibility to reproduce from a unique set of equations the transition over time of LCOs into ELMs. This will be performed with the aid of numerical simulations, since the expression of the equations is not enough to understand fully the features of the dynamics. Finally, the advantage of a reduced model is the possibility to isolate the most influencing terms and parameters from a more general plasma description, allowing to suggest a physical explanation for the observed phenomena.

A summary of selected existing models is presented in Chapter 3, in order to present the actual state of L-H transition modeling. The fundamental DALF (Drift-Alfvén) equations, used for the description of low frequency phenomena at the plasma edge are also introduced These will be the fundamental basis for the model presented in this thesis. In Chapter 4 the proposed model for LCOs into ELMs transition is derived from the DALF model. In Chapter 5 a minimum model is analyzed with a focus on the nonlinear stability, showing the presence of a stable limit cycle solution. In the following numerical simulation of the complete and minimum system are performed, proposing a comparison with experimental measurements from [1]. Finally, in Chapter 6, the final issues are discussed together with the conclusion.

Chapter 3

Physical models for tokamak plasma edge

The aim of this chapter is to introduce and describe a number of models adopted for the simulation of tokamak edge physics phenomena, in order to provide a state of the art for a direct comparison with the model provided in this thesis in Chapter 4.

In Sec. 3.1 a series of 0D and 1D heuristic models for the simulation of the physics of tokamak edge are introduced. In particular, the scope of this section is not to define a complete review of this topic but to describe the main ideas that influenced the equations derived in this thesis, and a possible comparison of the results with other theoretical models. Advantages and disadvantages of the various simplified approaches are analyzed and discussed, and the main results of their numerical integration are shown. These reduced dynamical models treat different aspects of the edge physics. Some of them try to reproduce the main features of the L-H transition, with a special focus on the LCOs and the final locking of the H-mode, trying to provide an explanation for the triggering. Others aim to include only the simulation of ELMs behavior. The models will be introduced in chronological order.

In Sec. 3.2 the DALF (Drift-Alfvén) model is introduced from the two-fluids description of a magnetically confined plasma. This model is widely applied in actual studies of tokamak edge behavior, and its main scope is the simulation of 3D plasma turbulence. In fact, this model constitutes an extension of MHD, considering also the adiabatic coupling phenomenon. Therefore, it is in principle able to consider both driftwave and interchange mechanisms, having a complete picture of the plasma edge turbulence. These equations also represent the starting point for the derivation of the model developed in the present thesis in Chapter 4.

3.1 Overview of reduced dynamical models for plasma edge physics

In the present section a selection of models for the plasma edge simulation is introduced, and their main results are presented. This is made in order to have a direct comparison with the model derived in Chapter 4.

Their inherent simplicity, i.e. the presence of heuristic terms or the lack of a derivation from basic plasma physics equation, is motivated by the fact that, at present, there is no complete theory for the L-H transition dynamics. Therefore, as suggested in [43]:

> [...] since no "first principles" simulation has ever successfully recovered the L-H transition, reduced models are the only option. Also, in the event that useful "first principle" simulations become available in the future, reduced models will still be necessary to extract the essence of the transition physics - i.e. to distill the lesson learned.

The models described here worked as a basis for the model derived in this thesis, by suggesting the direction for the simplification of the starting physical equations (introduced in 3.2), pointing the fundamental features that should be included and finally motivating the choice of a 0-D model, in which the only independent variable is the time. These models treat the plasma edge oscillations at the L-H transition or during the H-mode from the point of view of its evolution in time, therefore are mathematical models for dynamical systems. Often, the nonlinear structure of the coupled differential equations implies that there exist no explicit analytical solution, and therefore the numerical simulations are a necessary instrument to study the predicted behavior. The classification proposed in [51] identifies different classes for the various theoretical models of L-H transition and ELMs. The focus of the present analysis will be on the ones including limit cycle solution to dynamical equations, appearing when a parameter included in the system (usually the heating power) overcomes a threshold value. This agrees with the experimental observation that L-H transition happens only over a certain input heating power P_{LH}. Here, the three models that mostly influenced the present derivation are presented. Two further models for a comparison with different approaches for the description of the treated phenomena are included in Appendix D. At the end of this section, the main features of the presented models are summarized.

3.1.1 Lebedev et al.

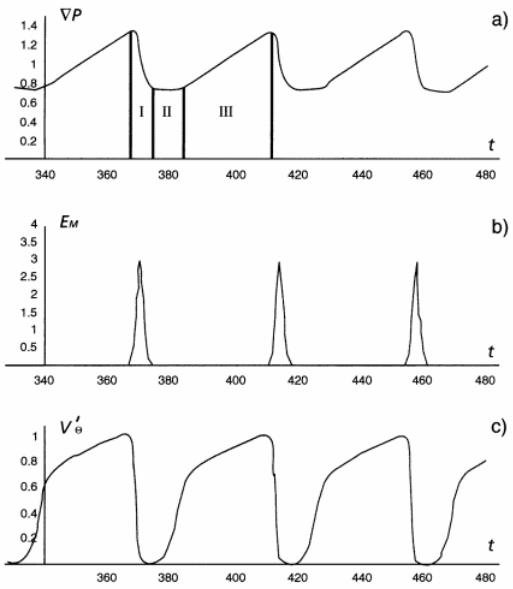

Figure 3.1: Time evolution with fixed Φ of (a) dimensionless pressure gradient; (b) dimensionless level of MHD fluctuations; and (c) dimensionless mean velocity shear(Fig. 5 [54])

The model proposed in [54] is a low dimensional model for ELMs that features a bifurcation of equilibria resembling the L-H transition. It includes a specific treatment for the tokamak edge, focusing on the excitation of a series of ballooning pressure driven modes that gradually reach a stable limit cycle behavior. This approach is quasilinear, in the sense that transport is evaluated through a mixing length approach, while nonlinear effect are neglected in the growth of the mode. The system is assumed to be at constant temperature, therefore changes in pressure are caused by variations of density only.

The ambient edge turbulence (i.e driftwave turbulence) is evaluated as a local intensity of density fluctuation $\mathcal{E}$ evolving as

$$\frac{\partial \mathcal{E}}{\partial t} = \gamma_0(P')\mathcal{E} - \alpha_1 \mathcal{E}^2 - \alpha_2 V_E'^2 \mathcal{E}, \tag{3.1}$$

with a linear growth due to the free energy available from the pressure gradient P', a nonlinear saturation term and the effect of the shear of $E \times B$ velocity V_E' able to suppress the turbulence. The shear of the $E \times B$ flow is evaluated from the equation of the radial electric field Eq

(2.61) as

$$V'_E = -c\frac{E'_r}{B_t} = v'_\theta - \frac{T}{eB}\frac{|P'|^2}{P^2}, \tag{3.2}$$

with the zonal flow shear v'_θ contribution and the diamagnetic contribution from the pressure gradient P', while neglecting toroidal flux terms. The MHD (i.e. ballooning) fluctuation intensity $\mathcal{E}_M$ is assumed to grow linearly once the pressure gradient overcomes the ballooning threshold, estimated as the standard limit for ballooning mode $P'_{cr} \approx 2B^2 s/8\pi q^2 R$.

$$\frac{\partial \mathcal{E}_M}{\partial t} = \lambda\,[\,(\,|P'| - P'_{cr}) + a v'^2_\theta - b V'^2_E\,]\,\mathcal{E}_M, \tag{3.3}$$

where an interesting feature is the evaluation of the stabilizing effect of the $E \times B$ shear but at the same time the effect of the centrifugal (therefore destabilizing, compare 2.3.3) force due to the poloidal motion v'_θ. From the averaged poloidal momentum balance, the evolution equation for the shear of poloidal flow Eq (2.62) is defined

$$\frac{\partial v'_\theta}{\partial t} = \alpha_3 V'_E \mathcal{E} - (\mu + \alpha_4 \mathcal{E}_M) v'_\theta, \tag{3.4}$$

in which the Reynolds stresses are induced by the total shear, while the damping is not only due to μ but also from a turbulent viscosity. Finally, the evolution of the edge pressure gradient is derived from the space derivative of the continuity equation for density at constant temperature. Since the analysis is limited to the edge, a particle source from the core plasma is assumed to be proportional to the total particle influx times a recycling factor. The actual transport is modeled through a coefficient of anomalous diffusion with a mixing length approach (compare 2.2.3). $D(\mathcal{E}, \mathcal{E}_M) \approx \widetilde{v}^2/\tau_c$ and therefore

$$\frac{\partial |P'|}{\partial t} = -\frac{D(\mathcal{E}, \mathcal{E}_M)}{L_I}\,|P'| + \Phi, \tag{3.5}$$

where Φ is a parameter representing the energy flux. All the previous equation form the dynamical model.

This system of equations can be studied analytically in two limits, in which the shear of the $E \times B$ flow is respectively due to v'_θ or $|P'|$ only. This allows to perform a complete nonlinear analysis of the system, isolating the control parameter Φ that defines the equilibrium of the system. An analogous approach is performed on the model provided in this thesis in 5.1. Here, only the first limit (i.e. $V'_E = v'_\theta$) is presented, since more relevant for the present treatment: the two limits, in fact, correspond respectively to a

heating power close to the L-H transition or much higher. For a low value of the heating power $\Phi < d\mu^2$ a stable state corresponding to L-mode is obtained, in which the fixed point has zero poloidal shear and the stable pressure gradient scales as $|P'|_0 \sim \sqrt{\Phi}$. For $\Phi > d\mu^2$ the L-mode fixed point becomes unstable as a consequence of a bifurcation, that correspond to an L-H transition. The new fixed point is said to correspond to a H-mode, due to the appearance of a finite $v'_{\theta 0}$ at the equilibrium, suggesting the formation of a transport barrier due to the shear. The stable pressure gradient now scales linearly with the heating power $|P'|_0 \sim \Phi$. Differently from the model from Itoh et al. (D.0.1), no dithering is observed at the border between L and H mode and the transition is analogous to a second-order phase transition, since all equilibrium variables remain continuous functions of the control parameter. ELM behavior appears after the L-H transition, when $\Phi > \mu[1 + (a - b)\mu]/[1 + (a - b)]$. In this case a Hopf bifurcation appears: the H-mode equilibrium becomes an unstable focus and a stable limit cycle appears, that is reached from any initial condition close to the unstable fixed point. For a more rigorous explanation of this bifurcation, see 5.1. The ELMs appear as a repeated cycle as in Fig. 3.1. A short burst of MHD activity discharges the pressure gradient (region I) and destroys the transport barrier by reducing V'_E. It follows a growth of $\mathcal{E}$ that allows v'_θ to increase again via Reynolds stresses and the transport barrier is restored. During this period of the cycle, the anomalous transport peaks, first due to $\mathcal{E}_M$ then due to $\mathcal{E}$ and $|P'|$ remains at a reduced level (region II). When the barrier is restored, the gradient steepens again until it overcomes P'_{cr} and a new cycle begins (region III).

The most interesting characteristic of this model are:

- The possibility to perform a complete nonlinear analysis, with the definition of L- and H- mode and the corresponding values of Φ.
- The behavior of the ELMs frequency ν with different Φ, identifying a continuous transition from Type-III ELMs ($\partial\nu/\partial\Phi < 0$) to Type-I ELMs ($\partial\nu/\partial\Phi > 0$).
- The evaluation of an MHD instability to describe ELMs.

But at the same time the drawbacks are:

- The heuristic coefficients derived from dimensional analysis only.
- The absence of LCOs at the smooth L-H transition and the appearance of ELMs only for $\Phi \gg \Phi_{LH}$.

3.1.2 Diamond et al. and Kim et al.

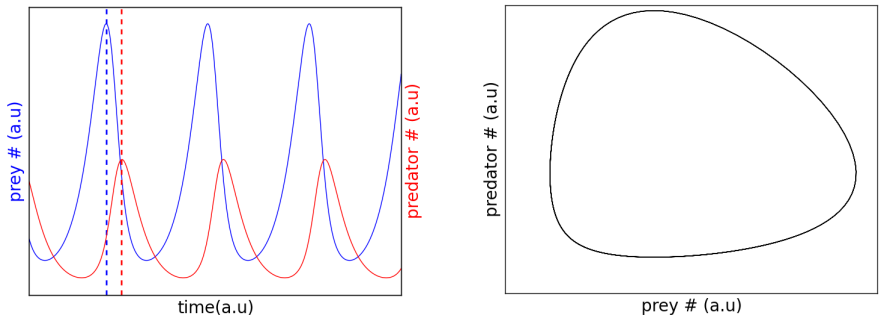

Figure 3.2: Numerical integration of the nonlinear predator-prey model. (a) The phase shift of $\pi/2$ of the nonsinusoidal cycle is easy to visualize in the extended phase space. (b) the limit cycle in the phase space

The model proposed in [55] is introduced and its integration in [56] is discussed. The main paradigm proposed in the first paper considers the zonal flows to explain the observed oscillations at the L-H transition.

Turbulent fluctuations in a tokamak plasma are able to drive a sheared flow (see 2.4.1), which acts back to its generating origin and annihilates the eddies. Once the fluctuation level is low, the zonal flow lacks its drive and it is damped due to dissipation. This leaves the turbulence free to develop again and another cycle can start, in a self-regulating fashion. The overall dynamics gives rise to a behavior which closely resembles the predator-prey cycle, a classic model of nonlinear dynamics [57]. The analogous model for flow-turbulence interaction in the tokamak edge considers the turbulence intensity and the zonal flow amplitude as the dependent variables of the system. Its general derivation simplifies the detailed treatments of various turbulence models. The fluctuation intensity becomes $\mathcal{E} = \langle \widetilde{n}_k^2 \rangle / n_0$, while the shear of zonal flow intensity is $U = \langle \partial_r v_\theta \rangle^2$. The linear drive of turbulence is given by γ_0, linked to the energy available from the edge gradient, while the damping is both due to the eddy decorrelation from sheared flows and a nonlinear coupling due to energy leakage to other helicities (the direct cascade). The evolution of zonal flows is instead obtained from Eq (2.62), derived along r and multiplied by $\langle v'_\theta \rangle$. The resulting coupled nonlinear 0D dynamical system is

$$\frac{1}{2}\partial_t \mathcal{E} = \gamma_0 \mathcal{E} - \alpha_1 \mathcal{E}^2 - \alpha_2 \mathcal{E} U, \tag{3.6}$$

$$\frac{1}{2}\partial_t U = \alpha_3 \mathcal{E}\, U - \mu U, \tag{3.7}$$

where the value of parameters derived from dimensional analysis is given in [55]. Note the analogy with Eq (3.1) and Eq (D.7). Neglecting the nonlinear term $\mathcal{E}^2$, the system is exactly a predator-prey model and a limit cycle solution is possible (Fig. 3.2). The result of numerical simulations shows a basic feature of the model: a fixed delay in the response of the zonal flow to the growth of turbulence, which is coherent with the measurement of fluctuations and flows during the I-phase [1].

The model is integrated in [56], where the shear of the total $E \times B$ flow is divided in two contributions, one from the Reynolds stress driven zonal flow shear, indicated as V_{ZF}, and one from the mean $E \times B$ flow shear, named V. The last is caused by E_r, which in this model is assumed to be originated from the ion pressure gradient only. The role of the two sheared flows in the L-H transition is different: the shearing due to ZFs is likely to dominate the one due to the mean flow before and during the L-H transition, until the shearing due to the mean flow becomes sufficiently large following a sudden profile steepening at the end of the transition and locks the H-mode. Furthermore, a characterizing feature of this model is the interplay between zonal and mean flow, namely, the inhibition of zonal flow growth by mean flow. Finally, the evolution of the background pressure gradient $\mathcal{N}$ is also evaluated, considering turbulent and neoclassical diffusion and its steepening from a input power Q that is the control parameter of the system. The 0D dynamical model reads

$$\partial_t \mathcal{E} = \mathcal{E}\mathcal{N} - a_1\mathcal{E}^2 - a_2 V^2 \mathcal{E} - a_3 V_{ZF}^2 \mathcal{E}, \tag{3.8}$$

$$\partial_t V_{ZF} = b_1 \frac{\mathcal{E} V_{ZF}}{1 + b_2 V^2} - b_3 V_{ZF}, \tag{3.9}$$

$$\partial_t \mathcal{N} = Q - c_1 \mathcal{E}\mathcal{N} - c_2 \mathcal{N}. \tag{3.10}$$

Comparing Eq (3.8) with Eq (3.6), the difference is in the split of the effect of the sheared flow on turbulence and the growth of $\mathcal{E}$ which is now driven by the pressure gradient. In Eq (3.9), the term with coefficient b_2, indicates the inhibition of the ZF shear by the mean flow shear. In Eq (3.10) Q is the heating power from the core, the second term is anomalous transport and the third is neoclassical transport. The shear due to the background flow is caused by the pressure gradient only, defining the last equation to close the system

$$V = d\mathcal{N}. \tag{3.11}$$

In the model equations a_i, b_i, c_i and d are parameters. The structure of the equation is such that the "prey" $\mathcal{N}$ feeds the first "predator" $\mathcal{E}$, which

in turn is a "prey" for V_{ZF}^2. The dynamics can be described in the following way. As the pressure gradient steepens, the higher available free energy allows the turbulence to increase, but only when the growth rate is sufficiently high to overcome the shear, due to zonal and mean flow, and the nonlinear saturation. As the turbulence peaks, the gradient drops due to the enhanced anomalous transport and so does the mean shear. The turbulence lacks its prey while its predator, the ZF, has now a strong drive. The dynamics of the system is complex and this case is related to specific values of the parameters only. The above described behavior is shown for increasing $Q = 0.01t$ in Fig. 3.3, that is the plot of the numerical integration in Python of the model described in [56] performed during this thesis. As the ZF are able to intervene, an oscillatory phase with characteristic phase shift of a predator-prey model is initiated, during which the shear due to ZFs limits the turbulence amplitude across the whole oscillating period. Meanwhile, the pressure gradient oscillates with an increasing average value over many oscillations, until it is able to suppress the turbulence alone. This initiates a phase free of turbulence due to mean shear and the zonal flows eventually damp to zero in lack of their drive. This dynamics is coherent with the experimentally observed oscillations of the I-phase and the locking of H-mode. The main effect of the mean shear on ZFs shear (b_2V^2) is to prolong the oscillatory phase, by limiting the ZFs amplitude that regulates the turbulence during the oscillatory phase. An interesting 1D (radial extension) integration of these equations is presented in [43], which is beyond the scope of this summary. In summary, the main features of the final model are:

- The initiation of an oscillatory phase with LCOs between L- and H-mode strongly resembling the I-phase behavior.
- Q as a control parameter for the behavior of the system.
- The separation of mean and zonal flow with different causes/effects.

While the drawbacks are:

- The absence of ELMs (only a quiescent H-mode is present).
- The fact that most of the parameters are heuristically included.
- The absence of MHD or magnetic activity in the description.
- The necessity to increase Q over time in order to observe the oscillatory phase, oppositely to the experimental observation (fixed S_h).

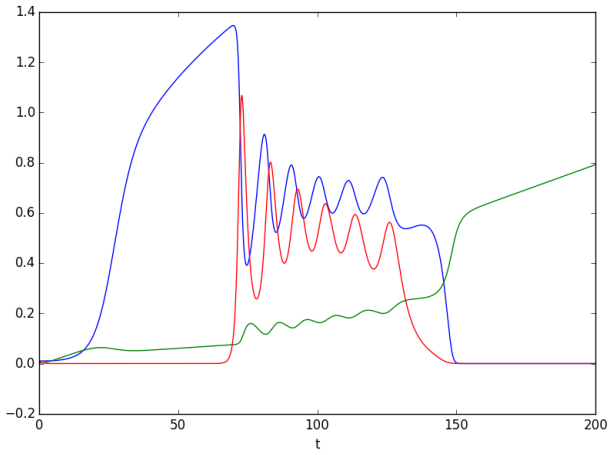

Figure 3.3: Simulation of the model described in [56]. Evolution of $\mathcal{E}$ (blue), V_{ZF} (red) and $\mathcal{N}/5$ (green) with input power $Q = 0.01 \times t$.
The onset of the LCOs ($t \approx 65$) coincides with a drop of the turbulence level and the pressure gradient starts to increase. As in Fig. 3.2 it is possible to observe the predator-prey behavior of the zonal flow shear and the turbulence, with a delay in the oscillations. The pressure gradient progressively steepens during the oscillatory phase until it is able to lock the H-mode by suppressing the turbulence ($t \approx 150$).

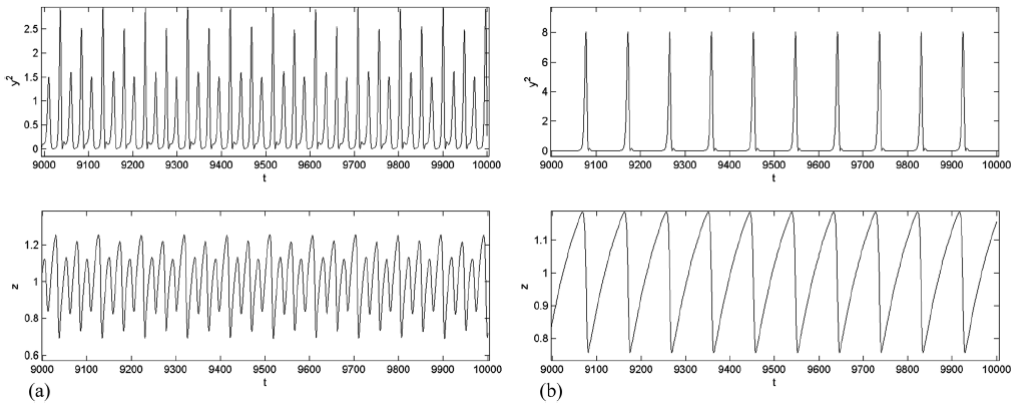

Figure 3.4: The functions $y^2(t)$ and $z(t)$ of the orbit starting at $(x_0, y_0, z_0) = (0, 1.7, 1.01)$ (a) with $(\delta, \eta) = (0.5, 0.07)$ (b) with $(\delta, \eta) = (0.5, 0.01)$ (Fig. 5 [58]).
Different behavior are possible for the model presented in [58]. Low amplitude, high frequency non-sinusoidal oscillations of (a) are analogous to the LCOs at the onset of the I-phase. High amplitude, low frequency spikes in (b) resemble ELM behavior. The model can in principle also show an (intermittent) chaotic regime, typical of the late I-phase.

3.1.3 Constantinescu et al.

The model presented in [58] describes plasma periodic nonlinear perturbations (e.g. ELMs) introducing a 0D model based on a relaxation and drive mechanisms of two equations. The first is related to the instability dynamics derived from MHD force balance, the second describes the edge pressure gradient dynamics.

The amplitude of a perturbation ξ is the characteristic variable defining the instability. A driving or restoring force is considered as a linear function of ξ, deriving from a Taylor expansion around an extremal point. This treatment leads to the standard linear MHD force balance used to evaluate the stability of a MHD equilibrium following a perturbation

$$\rho_{m0}\frac{d^2\boldsymbol{\xi}}{d^2t} = -\hat{K}\xi, \tag{3.12}$$

where $\hat{K}$ is a linear operator. It is assumed that ξ is a displacement in the magnetic field, in order to focus on the magnetic activity during ELM events. In this way, it is possible to introduce a dissipative term in which resistivity is the dissipation mechanism. Furthermore, the drive of the instability is assumed to be the pressure gradient p', coherently with the observation that during ELMs the instability develops as the edge pressure gradients steepens over a certain threshold. This leads to the first equation

$$\frac{d^2\xi}{d^2t} + \gamma_{mhd}(p')^2\xi + \delta^*\frac{d\xi}{dt} = 0, \tag{3.13}$$

where the second term is the drive/damping of the instability while the third is the resistive dissipation of the mode. The drive/damping term is assumed to be a linear function of p' only such that it is possible to find a critical value for the instability to develop by setting $\gamma_{mhd}(p')^2 = 0$. this defines the drive/damping coefficient as

$$\gamma_{mhd}(p')^2 = \gamma_0^2 + \left(\frac{d\gamma_{mhd}^2}{dp'}\right)p' = \gamma_0^2\left(1 - \frac{p'}{p'_{crit}}\right). \tag{3.14}$$

In this way, the dimensionless form of the equation for the drive/relaxation of the instability, indicating the amplitude of the magnetic perturbation, reads

$$\frac{d^2\xi_n}{d^2t_n} = -(1 - p'_n)\xi_n - \delta\frac{d\xi_n}{dt_n}. \tag{3.15}$$

Here ξ_n is the normalized perturbation amplitude,t_n is the normalized time and $p'_n = p'/p'_{crit}$. This is a typical *critical gradient model*, where

the instability develops once the gradient, following its coupled dynamics, overcomes a threshold value (compare Eq (3.3)). It is stressed that this critical parameter is heuristically inserted in the assumption of linear dependence of the drive term on the gradient. The equation for the evolution of the edge pressure gradient is evaluated from dimensional analysis. In its dimensionless form, it reads

$$\frac{dp'_n}{dt_n} = \eta \left(h - p'_n - p'_n \frac{\chi_{anom}}{\chi} \right) \tag{3.16}$$

where h is the dimensionless heating power, the second term in the RHS is the neoclassical transport and the third is the anomalous transport, described in a mixing legth approach. The full dimensionless system used to simulate the plasma edge oscillations is obtained defining the two dimensionless variables $y = (\sqrt{\chi_{anom}/\chi})\, \xi_n$ and $z = p'_n$ and splitting the second order time derivative of the instability equation.

$$\frac{dx}{dt} = (z-1)y - \delta x, \tag{3.17}$$

$$\frac{dy}{dt} = x, \tag{3.18}$$

$$\frac{dz}{dt} = \eta \left(h - z - y^2 z \right). \tag{3.19}$$

A complete nonlinear analysis of the system is presented in [59], showing the appearance of a limit cycle at $h = 1$. For specific values of δ and η, which are function of plasma parameters, it is also possible to start a chaotic behavior when $h > 1$. Furthermore, another feature not discussed here is the possibility to introduce in Eq (3.15) a term representative of pellet injection for ELM mitigation. The model shows therefore a series of different regimes that cover the typical phenomena observed in plasma edge: damped, periodic or intermittent behavior for the perturbation, while the pressure gradient slowly increases due to the heating power and rapidly collapses due to the high anomalous transport when the instability grows (see Fig. 3.4). In conclusion, this is a general model that aims to provide a minimum set of equations for generic plasma instability oscillations. The main features of the present model are:

- The possibility to assume both an oscillatory behavior, typical of the early I-phase, as much as a chaotic (intermittent) behavior, typical of ELMs in the late I-phase.
- The inclusion of magnetic fluctuation.

But at the same time the main drawbacks are:

- The anomalous transport driven by displacement in the magnetics, which is not considered the main responsible for this phenomenon.
- The lacking of sheared flows in the edge dynamics, useful to determine LCOs behavior.
- The arbitrary critical gradient, not specified from first principles.

3.1.4 Reduced models overview conclusions

The models introduced here, although derived with different approaches, try to simulate the same physics phenomena. The comparison with experimental results is often difficult, not only for the fact that many of these models are 0D (i.e. whose only independent variable is the time), but mostly because they contain heuristic parameters derived from dimensional analysis and therefore not explained in terms of fundamental equations. The objective of these descriptions is to justify the experimental observations by suggesting possible mechanisms for the underlying physics. The common features of the previous models are here summarized, also to underline their influence on the model derivation presented in the next chapter.

- Most of the models contain a term which describes a heating/particle flux coming from the core to the edge and acts as a control parameter, defining the typology of solution.
- An edge pressure gradient, regularly collapsing when transport increases, is included. This defines L and H-mode and the ELM crash.
- Fluctuation dynamics can describe turbulence, MHD activity or magnetic field perturbation, and identifies the instability.
- Stable oscillatory solutions are characteristic of these models, and they easily reproduce cyclic behavior as LCOs and ELMs.
- LCOs are identified with a typical shift of instability fluctuation and zonal flow.
- It is often possible to perform a nonlinear analysis of the model equations in order to define the value of the control parameter for the onset of the cyclic behavior.
- None of the models describes a transition of LCOs into ELMs.

3.2 Drift-Alfvén model

The aim of this section is to present the DALF model for the description of fluid drift plasma dynamics introduced in Sec. 3.2.1. The focus is on the required assumptions for spacial and temporal scales and their consequences on a treatment starting from the two-fluid equations to derive the fluid drift equations presented in Sec. 3.2.2. This is done in order to provide a justification for the equations used to derive the model in the next chapter. The choice of the DALF model in particular is also explained in Sec. 3.2.3. The complete derivation of fluid drift equations from the two fluids model is presented in Appendix E.

3.2.1 Fluid Drift Dynamics

The fundamental dynamics treated with the DALF model, the fluid drift dynamics of a magnetically confined plasma, is described. This requires a series of assumptions to be verified. In this section, coherently with the original derivation of the Drift-Alfvén model, the Gaussian unit system will be used.

Alfvén waves

When a plasma is confined with the aid of external magnetic fields as in a magnetized fusion plasma, its particles are subjected to the Lorenz force deriving from their motion in presence of the magnetic field. In a neutral plasma, the electric Lorenz force adds up to zero, while the magnetic part is the prominent. This force, in an MHD interpretation, is able to compensate the expansion force due to the kinetic pressure of the plasma as can be derived from Eq (2.9) evaluating an equilibrium condition

$$\nabla p = \frac{\boldsymbol{J} \times \boldsymbol{B}}{c}. \tag{3.20}$$

In a self-consistent treatment, the current in a plasma is given by the Ampére's law $\boldsymbol{J} = c/(4\pi)\,\nabla \times \boldsymbol{B}$, that, substituted in the above expression, expresses the two forces that a magnetic field exerts on a current-carrying plasma

$$\frac{\boldsymbol{J} \times \boldsymbol{B}}{c} = -\nabla_\perp \frac{B^2}{8\pi} - \frac{B^2}{4\pi R_c}\boldsymbol{n}, \tag{3.21}$$

where $\nabla_\perp$ considers only the gradient components perpendicular to the magnetic field while $\boldsymbol{n}$ is the curvature vector of the magnetic field. In a simple picture, magnetic field lines are interpreted as wires, that can

exhibit a *magnetic pressure* perpendicular to their orientation, compensating a gradient, as well as a *magnetic tension*, that is, a restoring force against the lines bending. The response to a perturbation, can therefore induce propagating waves due to these forces. Fluid plasma dynamics, in an MHD subset, admits Alfvén oscillations that propagate at Alfvén speed

$$c_A = \left(\frac{B^2}{4\pi n_i m_i} \right)^{1/2} \tag{3.22}$$

Magnetic pressure gives rise to compressional Alfvén waves, propagating longitudinally, perpendicular to the magnetic field. Magnetic tension, instead, results from shearing of the lines, giving rise waves that propagate transversely, along the magnetic field.

Spatial and temporal scales

As described in Chapter 2, what controls transport in a magnetized plasma are not collisions, but anomalous effects. Here a class of motion called fluid drift dynamics is considered, which is related to driftwave turbulence and has therefore a strong role in transport. Such motion, taking place perpendicularly to the magnetic field, is observed to be incompressible. The characteristic velocity of its motion is therefore below the sound speed in a plasma $c_s = (T_e/m_i)^{1/2}$, in which the contributions to the thermal energy from the electrons and to the inertia from the ions are analogous to the pressure and the mass density in a neutral fluid sound speed. Considering a perpendicular local scale of the inhomogeneities, $L_\perp$, the maximum considered frequency is

$$\omega \sim \frac{c_s}{L_\perp}. \tag{3.23}$$

It is furthermore defined a spacial scale, which have the same expression as a gyro (Larmor) radius and is called the *drift scale*

$$\rho_s = \frac{c_s}{\omega_{ci}} = \frac{c}{eB}(m_i T_e)^{1/2}. \tag{3.24}$$

It is noticeable that if $T_e = T_i$, then $\rho_s = r_{Li}$, but in many laboratory plasma, often $T_e \gg T_i$, that motivates this definition. It is in fact observed that turbulent flows have a spacial scale given by ρ_s and larger or proportional to r_{Li} [60].

Drift dynamics, which is the fundamental physics of the considered model, is valid if a particle undergoes many gyro orbits in the time the gyro center drifts over one gyro radius. This is satisfied if the highest

frequency of motion is small compared to any gyrofrequency, of which ω_{ci} is the lowest.

$$\frac{\omega}{\omega_{ci}} = \frac{c_s/L_\perp}{c_s/\rho_s} = \frac{\rho_s}{L_\perp} \equiv \delta \ll 1 \tag{3.25}$$

where δ is the *drift parameter*, and is treated as a smallness parameter. Note that this inequality, for high temperatures, is satisfied for magnetized plasmas.

Consider the dynamics of a long, thin plasma flux tube. The scales of the allowed disturbances (or fluctuations) have very disparate parallel and perpendicular values, with reference to the background magnetic field: the maximum allowed scale in the perpendicular section of the flux tube will remain smaller with reference to the parallel length. This can be described as

$$k_\perp \gg k_\parallel. \tag{3.26}$$

At low frequencies, the shear Alfvén dynamics can be considered the most important along the flux tube such that

$$\omega \sim k_\parallel c_A. \tag{3.27}$$

The two previous relations therefore imply

$$\omega \ll k_\perp c_A. \tag{3.28}$$

Consider now the condition for a low beta plasma, typical in current fusion experiments, in particular for β_e, in which only the electron contribution is considered

$$\beta_e = \frac{4\pi p_e}{B^2} = \frac{c_s^2}{c_A^2} \ll 1. \tag{3.29}$$

In this assumption, sound speed is negligible with reference to the Alfvén speed and allows to neglect the compressional waves in the perpendicular direction since

$$\omega \sim k_\perp c_s \ll k_\perp c_A, \tag{3.30}$$

and fluid drift dynamics is suitable to describe low frequency phenomena in low-β plasmas. The drift approximation consists in a formalism that allows to removes fast timescales from the governing equations, leaving only the dynamics of interest.

Perpendicular fluid drifts

The main consequence of the exclusion of fast timescales from the plasma perpendicular dynamics leads to consider a quasistatic evolution of the

force balance in the plane perpendicular to the magnetic field. In this sense, no dynamical oscillations (i.e. Alfvén compressional waves) are involved in its evolution. Consider the two-fluid model for a magnetically confined plasma. Due to $m_e \ll m_i$, the inertia of electrons is neglected and quasineutrality is assumed such that $n_i = n_e$. Furthermore, electron-ion collisions are retained only in the direction parallel to the magnetic field, indicated as $\boldsymbol{b} = \boldsymbol{B}/B$. The equations read

$$n_i m_i \frac{d\boldsymbol{v}_i}{dt} + \nabla \cdot \boldsymbol{\Pi}_i = -\nabla p_i + n_e e \left(\boldsymbol{E} + \frac{\boldsymbol{v}_i}{c} \times \boldsymbol{B} \right) - R_{ei} \boldsymbol{b}, \tag{3.31}$$

$$0 = -\nabla p_e - n_e e \left(\boldsymbol{E} + \frac{\boldsymbol{v}_e}{c} \times \boldsymbol{B} \right) + R_{ei} \boldsymbol{b}. \tag{3.32}$$

The perpendicular part of the electric field $\boldsymbol{E}_\perp$ is assumed *a priori* to be electrostatic. In this way, using the formalism of potential field approach, Faraday's law reads

$$\boldsymbol{E}_\perp = -\nabla_\perp \phi \qquad E_\parallel = -\frac{1}{c}\frac{\partial A_\parallel}{\partial t} - \nabla_\parallel \phi. \tag{3.33}$$

Finally, the left hand side (LHS) of Eq (3.31) is analyzed. The divergence of the anisotropic pressure tensor is considered to be of order δ with respect to the right hand side. This is coherent with the quasistatic evolution when a small departure from a Maxwellian distribution function is considered. Furthermore, when multiplying by $c/(B^2 e n_e)$ the LHS

$$\frac{1}{B}\frac{c m_i}{eB}\frac{d\boldsymbol{v}_i}{dt} \xrightarrow{F} \frac{1}{B}\frac{\omega}{\omega_{ci}}\boldsymbol{v}_i^{(0)} \sim O(\delta). \tag{3.34}$$

It is therefore possible to isolate the lowest order ($O(0)$) perpendicular flows, operating on the equation with $c\boldsymbol{B}/(B^2 e n_e)\times$ and deriving

$$\boldsymbol{v}_{\perp i}^{(0)} = \frac{c}{B^2}\boldsymbol{B} \times \nabla\phi \; + \; \frac{1}{e n_e}\frac{c}{B^2}\boldsymbol{B} \times \nabla p_i, \tag{3.35}$$

$$\boldsymbol{v}_{\perp e}^{(0)} = \frac{c}{B^2}\boldsymbol{B} \times \nabla\phi \; - \; \frac{1}{e n_e}\frac{c}{B^2}\boldsymbol{B} \times \nabla p_e. \tag{3.36}$$

Note that, with the same approach with the MHD model, only the $E \times B$ *drift* would appear (the first term on the RHS). The main difference is the consideration of the pressure gradient effects for the two fluid, giving rise to a *diamagnetic drift* (the second term on the RHS), which is opposite for ions and electrons assuming the same pressure profile. Both of them are actual *fluid* drifts (compare the particle drifts obtained with a guiding

center approximation for single charged particles in Sec. 2.1) and are defined as

$$\boldsymbol{v}_E = \frac{c}{B^2}\boldsymbol{B} \times \nabla\phi, \tag{3.37}$$

$$\boldsymbol{v}^*_\alpha = \frac{1}{n_e q_\alpha}\frac{c}{B^2}\boldsymbol{B} \times \nabla p_\alpha. \tag{3.38}$$

Note that, if considering a constant homogeneous magnetic field, ϕ and p_α act exactly as stream functions for the velocity field (compare 4.1.1). Consider now the evaluation of the $O(\delta)$ correction for the ion flow. This can be obtained inserting $\boldsymbol{v}^{(0)}_{\perp i}$ in the full Eq (3.31) and applying the same operator. An effect, called *diamagnetic cancellation* occurs, such that the anisotropic part of the pressure tensor cancels the advective part of the total time derivative due to diamagnetic flow. This effect will be shortly discussed later. Due to it, the O(δ) correction to the perpendicular velocity gives rise to the *polarization drift* for the ions

$$\boldsymbol{v}^{(1)}_{\perp i} = \boldsymbol{v}_{Pi} = \frac{cm_i}{eB^2}\boldsymbol{B} \times \frac{d_E}{dt}\boldsymbol{v}^{(0)}_{\perp i}, \tag{3.39}$$

where it was introduced the $E \times B$ *advective derivative*, that will be widely used in the remaining of the thesis, to underline that the only advection derives from the perpendicular $E \times B$ velocity. It is given by

$$\frac{d_E}{dt} = \frac{\partial}{\partial t} + \boldsymbol{v}_E \cdot \nabla. \tag{3.40}$$

A simplified picture of diamagnetic cancellation is now presented. In presence of an inhomogeneity (i.e gradient of density/temperature) in a magnetized plasma perpendicular to the magnetic field, the flux in term of $\boldsymbol{J_\alpha} = n_\alpha \boldsymbol{v}_\alpha$, crossing an area whose vector is perpendicular to both the inhomogeneity gradient and the magnetic field, is not null and directed in the direction of $\boldsymbol{v}^*_\alpha$. However, no gyro center is in motion. The presence of this flux is not evaluated in MHD, because ions and electron fluxes would cancel each other out since opposite in direction. Furthermore, this is exactly what implies the presence of a magnetization current (introduced as $\boldsymbol{J}_M$ in Sec. 2.1). The reconciliation with the presence of a flux but no gyro centers in motion from the point of view of the fluid equations comes from a subtle result, called diamagnetic cancellation. This is the fact that a series of terms in every conservation equation concur to cancel each other out. This result, illustrated in [61] and [62], can be simply summarized for the present study as follows: the only plasma advection,

at the lowest order in a fluid interpretation, comes from $E \times B$ velocity. This justifies the introduction of the $E \times B$ advective derivative.

While the polarization drift v_{Pi} is smaller by a factor δ compared to v_E and v_α^*, its divergence is not. This will have a deep influence in the subsequent analysis. Recall that the inhomogeneities scale with $L_\perp$ while the scale of motion is at minimum ρ_s. Therefore the advection term

$$\boldsymbol{v}_E \cdot \nabla n_e \sim \frac{c\,\phi}{B\rho_s}\frac{n_e}{L_\perp}, \tag{3.41}$$

and the divergence of the polarization drift times the density

$$n_e \nabla \cdot \boldsymbol{v}_{Pi} \sim n_e \frac{1}{\rho_s}\frac{c_s/L_\perp}{\omega_{ci}}\frac{c\,\phi}{B\rho_s} \sim n_e \frac{1}{L_\perp}\frac{c\,\phi}{B\rho_s}, \tag{3.42}$$

are comparable, since $\rho_s\omega_{ci} = c_s$ by definition. Polarization drift will be included only when appearing under divergence operator.

Drift Ordering

Some simple arguments are presented to justify the ordering of various terms, in order to support the simplification performed in the derivation of the model. The small scale disturbances involved in the dynamics at the perpendicular scale are coupled to the background gradient and are assumed to be strong enough to equilibrate it, therefore should satisfy (e.g. for the density)

$$\nabla_\perp \widetilde{n}_e \sim \nabla_\perp n_e \quad \Rightarrow \quad \frac{\widetilde{n}_e}{n_e} = \frac{\rho_s}{L_\perp} \ll 1. \tag{3.43}$$

The perpendicular advection of the background gradient as well as of the disturbances is responsible for the dynamics, and therefore

$$\frac{\partial}{\partial t} \sim \boldsymbol{v}_E \cdot \nabla \sim c_A \nabla_\parallel. \tag{3.44}$$

On the contrary, since the background gradients (e.g. ∇p) have small variations along the field lines, parallel advection is neglected such that

$$\nabla \cdot (n_i u_\parallel \boldsymbol{b}) = n_i \nabla \cdot (u_\parallel \boldsymbol{b}) + \boldsymbol{b} u_\parallel \cdot \nabla n_i = n_i \nabla \cdot (u_\parallel \boldsymbol{b}) + O(\delta), \tag{3.45}$$

where $u_\parallel = \boldsymbol{v}_i \cdot \boldsymbol{b}$. Finally the magnetic field is assumed to be characterized by small disturbances such that it is possible to neglect them in

the drift operator $(c/B^2)\boldsymbol{B}\times$. In conclusion, the relative amplitude of the disturbances scale together as

$$\frac{e\widetilde{\phi}}{T_e} \sim \frac{\widetilde{n_e}}{n_e} \sim \frac{u_\parallel}{c_s} \sim \frac{\widetilde{\boldsymbol{B}}_\perp}{B} \sim \delta \ll 1, \tag{3.46}$$

while the timescales are such that perpendicular Alfvén dynamics is neglected and

$$\frac{\partial}{\partial t} \sim \boldsymbol{v}_E \cdot \nabla \sim c_A \nabla_\parallel \sim \frac{c_s}{L_\perp} \ll \omega_{ci}. \tag{3.47}$$

These inequalities are known in literature as *drift ordering* or *gyrokinetic ordering* and fluid plasma dynamics under these restriction becomes fluid drift dynamics.

3.2.2 Fluid Drift Equations

The fluid plasma dynamics at low frequencies in an inhomogeneous background under drift approximation and quasineutrality is described by the following equations. The complete derivation from the two-fluids model can be found in Appendix E.

$$\frac{d_E\, n_e}{dt} = \frac{B}{e}\nabla_\parallel \frac{J_\parallel}{B} - n_e B \nabla_\parallel \frac{u_\parallel}{B} + \frac{1}{e}\mathcal{K}(p_e) + n_e \mathcal{K}(\phi), \tag{3.48}$$

$$\nabla \cdot \frac{n_i m_i c^2}{B^2}\frac{d_E}{dt}\left(\nabla_\perp \phi + \frac{\nabla_\perp p_i}{n_e e}\right) = B\nabla_\parallel \frac{J_\parallel}{B} + \mathcal{K}(p_e + p_i), \tag{3.49}$$

$$n_i m_i \frac{d_E}{dt} u_\parallel = -\nabla_\parallel p_i - B\nabla_\parallel(\Pi/B) + n_e e E_\parallel - R_{ei}, \tag{3.50}$$

$$\frac{n_e e}{c}\frac{\partial A_\parallel}{\partial t} + \frac{m_e}{e}\frac{d_E}{dt} J_\parallel = \nabla_\parallel p_e - n_e e \nabla_\parallel \phi - R_{ei}, \tag{3.51}$$

together with the energy equations Eq (E.18) and Eq (E.19) which are not presented here, since they will have no role in the isothermal dynamics of the DALF3 model. The dependent variables are $n_e, \phi, u_\parallel, A_\parallel, T_e$ and T_i, with the pressure given as $p_\alpha = n_\alpha T_\alpha$ and the parallel current $J_\parallel$ given by the Ampère's law $J_\parallel = -(c/4\pi)\nabla_\perp^2 A_\parallel$. It is introduced the divergence operator, also referred to as curvature operator, defined for a generic scalar f as

$$\mathcal{K}(f) = -\nabla \cdot \left(\frac{c\boldsymbol{B}}{B^2} \times \nabla f\right). \tag{3.52}$$

To close the system, a series of closure laws are required for $q_{e\parallel}, q_{i\parallel}, \Pi$ and R_{ei}. Only the last is here introduced

$$R_{ei} = 0.51\frac{m_e \nu_e}{e} J_\parallel - 0.71 n_e \nabla_\parallel T_e. \tag{3.53}$$

This is presented in [60], where also the *a posteriori* check involving the neglection of $\boldsymbol{A}_\perp$ is shown, that can be justified from ordering arguments.

3.2.3 Description and results of the DALF model

Low-frequency reduced fluid equations are used to treat a great variety of phenomena in magnetically confined plasmas. These include turbulence [63] as well as macroscopic modes [64]. In this section, the Drift-Alfvén model was presented, following the treatment that can be found in [60]. Describing the dynamics of a long, thin flux tube where, on the drift plane, plasma is dynamically incompressible, Alfvén dynamics is retained in the parallel direction with reference to the magnetic field. Under fluid drift dynamics (3.2.1), flows and fluxes in a magnetized plasma are given in terms of stream functions, which are scalar quantities among the dependent variables.

This model is widely used for three dimensional turbulence simulation in the tokamak edge, where the pressure gradient is the energy source for the instability to develop [60]. In particular, due to the inclusion of electromagnetic effects, the main result is that the turbulence arises from the drift Alfvén nonlinear instability, the electromagnetic version of the Drift Wave nonlinear instability (see Appendix C). The turbulent state develops spontaneously and its underlying cause is the nonlinear vorticity advection. The possibility to include electromagnetic effects in the overall dynamics is the first reason for the choice of this model in the treatment of this thesis, since the magnetic activity measured during the ELMs can in principle be reproduced.

Despite no simulation has ever recovered the L-H transition completely, with this model it is also possible to study the regime of the tokamak edge at the L-H transition with the appropriate parameter domain [65]. Indeed this is the second of the reasons why this model was chosen to provide the basis for the treatment presented in Chapter 4, since the I-phase is to be analyzed.

The study of sidebands dynamics has been made possible trough the introduction of a "zonal" average (the average over a flux surface). Such an operation allows to study zonal averaged variables. In this way, the coupling of small-scale microturbulence and system-scale zonal flows is enlightened and the tendency of driftwave turbulence to spontaneously generate of zonal flows is shown [66]. At the same time, other global plasma edge phenomena are reproduced, among which Geodesic Acoustic Modes (GAMs) and the Pfirsch-Schlüter current, allowing access to a more complete picture of the energy transfer mechanism for turbulence in a

plasma. The energy is transferred from the background gradient, acting as a source, to the dissipation via resistivity at small scale turbulence, acting as a sink. The inclusion of global sideband dynamics was the third motivation for the choice of this model, since ZFs in particular are one of the peculiarities of the I-phase.

There exist various versions of the Drift-Alfvén model. In particular, the DALF3 assumes constant temperature for ions and electrons, and due to its simplicity, is the version chosen to provide the base for the present treatment, as will be specfied in the next chapter. It is possible to show [67] that MHD and DALF3 models are nearly identical, despite the fact that in DALF3 model (and in general, in the fluid drift equations) the presence of the adiabatic coupling has a major role. This is the possibility to generate a potential fluctuation from a density perturbation with the mediation of $J_{\|}$, creating the path for the enegy transfer from the background pressure gradient to the microscopic eddies, the latter deriving from potential fluctuations. The adiabatic coupling, giving rise to the driftwave and its unstable state (see Appendix C), is not the only mechanism for turbulence seeding. Another main mechanism, considered in both DALF3 and MHD, is the interchange instability, in which a potential fluctuation arises from a density fluctuation due to the presence of a curvature in the magnetic field (see 2.3.3). In tokamak geometry, the interchange effect leads to a ballooning mode, since it results unstable only on the outer side of the torus. The possibility of DALF3 model to consider both instabilities, and in particular the prevailing of one depending on the resistivity only, is a further point for the choice of this model. Finally, the fact that MHD modes are actually contained in the DALF3 model is the final argument for the choice of this model, since the ELMs, as described in 2.5, are thought to be unstable MHD modes.

The dimensionless isothermal version of this set of equations (DALF3) is treated to reproduce the measured behavior of the plasma edge introduced in the previous Chapter 2. In Chapter 4 the reduction of DALF3 to a set of 0D equations is explained. A formal derivation of the equations describing the plasma dynamics is presented following a series of simplifying assumptions. In Chapter 5, a nonlinear analysis of the dynamics is performed on a minimum subset of the model. The expression of the obtained equations is compared to the models introduced in 3.1, underlining similarities and differences. Finally, the results of the simulation of the complete and minimum model and the comparison with the experimental results as well as with the numerical integration of the models introduced in this chapter is treated.

Chapter 4

Interchange model for the I-phase

The aim of this chapter is to present and discuss a reduced 0D dynamical model derived from the DALF equations, described in Sec. 3.2.2, able to reproduce the transition from quasi-sinusoidal LCOs at the onset of the I-phase and their transition to type-III ELMs like oscillations over time. The derivation of the 0D model is one of the results of this thesis, based on the models introduced in Chapter 3 and that will be used to justify the experimental observations presented in Sec.2.6.

In Sec. 4.1 the DALF3 model with constant ions and electrons temperatures is introduced as a dimensionless version of the Drift-Alfvén equations presented in Sec. 3.2.2. A series of preliminary remarks allows to compare the DALF3 model with the DALF equations. The former model is the theoretical base for the derivation presented in the following section.

In Sec. 4.2, the interchange model for the description of the instability dynamics in the context of a tokamak plasma edge is developed. The assumptions considered for the derivation of the model are presented and motivated. The various equations are obtained singularly from the DALF3 model. The necessity to add a dissipation term to the previously derived system of equations is discussed starting from an energy conservation approach. At the end of the Chapter, the complete interchange model is summarized.

4.1 DALF3 model introduction

The most basic electromagnetic model containing driftwave and interchange physics is a four field model in tokamak flux tube geometry, named DALF3 from three-dimensional drift-Alfvén turbulence. In this section, some simplification to the DALF model, derived in Sec. 3.2.1, are explained and the dimensionless equations are given as a basis for the derivation of the interchange model in Sec. 4.2.

4.1.1 Preliminary remarks

Before providing the full DALF3 model, it is useful to underline some characterizing features of this description of the plasma edge.

Constant temperature

In the DALF3 model, the assumption of constant temperature is introduced. Neglecting the temperature evolution does not exclude the physics of interest, since in principle the interchange instability, the fundamental underlying mechanism considered for ELMs, is still contained in the system, as it is shown in a comparison with DALFTI, with warm ions effects [67]. The temperature ratio at the edge is considered fixed, as in [66], which means

$$\tau_i = T_i/T_e = const.. \tag{4.1}$$

It is straightforward to derive therefore the new expression of the ion pressure, as a direct consequence of the quasineutrality (see Appendix A)

$$p_i = n_i T_i = n_e(\tau_i T_e) = \tau_i p_e. \tag{4.2}$$

Finally, the isothermal electrons assumption implies that the equation for the electron density can be treated to obtain an equation for the electron pressure (in the next subsection, Eq (4.17)). This allows to move from a six unknowns system to a four unknowns system, whose remaining variables are $p_e, \phi, u_\parallel$ and $A_\parallel$.

Vorticity

In the dimensionless version of the DALF equations, a vorticity term appears in the dimensionless charge conservation, which is here briefly described.

Assume a plasma with cylindrical geometry with a constant background magnetic field along a z direction such that $\boldsymbol{b} = \boldsymbol{e}_z$. In the dimensionless equation, due to Gyro-Bohm normalization [66], the divergence of the ion polarization velocity is given by

$$\nabla \cdot \boldsymbol{v}_{Pi} = -\nabla \cdot \frac{d_E}{dt} \nabla_\perp (\phi + p_i) = -\nabla \cdot \frac{d_E}{dt} \nabla_\perp W, \tag{4.3}$$

where it was introduced $W \equiv \phi + p_i$. The scalar field W is referred to as the dimensionless stream function for the ions since it satisfies

$$\boldsymbol{v}_{\perp i}^{(0)} = \boldsymbol{e}_z \times \nabla W = -\nabla \times W \boldsymbol{e}_z \qquad \nabla \cdot \boldsymbol{v}_{\perp i}^{(0)} = 0, \tag{4.4}$$

where the first is the definition of the perpendicular ion velocity from Eq (3.35) and the second is a consequence of vector calculus identities. This is the typical incompressible flow in the xy plane that can be considered only in absence of inhomogeneities of $\boldsymbol{B}$, as in the study of drift waves (Appendix C). Note that in this way, the perpendicular dimensionless $E \times B$ velocity can be written as

$$\boldsymbol{v}_E = \boldsymbol{e}_z \times \nabla \phi = \left(-\frac{\partial \phi}{\partial y}, \frac{\partial \phi}{\partial x}, 0 \right). \tag{4.5}$$

It is therefore useful to introduce the nonlinear contribution of the $E \times B$ advective derivative (e.g. $\boldsymbol{v}_E \cdot \nabla n_e$) with the aid of the bracket notation

$$\boldsymbol{v}_E \cdot \nabla n_e = [\phi, n_e] = \frac{\partial \phi}{\partial x} \frac{\partial n_e}{\partial y} - \frac{\partial \phi}{\partial y} \frac{\partial n_e}{\partial x} \tag{4.6}$$

that can be manipulated [68] to show the useful property

$$\nabla \cdot [f, \nabla_\perp g] = [\nabla_\perp f, \nabla_\perp g] + \left[f, \nabla_\perp^2 g \right]. \tag{4.7}$$

Consequently, the term containing the advective derivative of the ion stream function in the dimensionless charge conservation of DALF model Eq (3.49) can be written as

$$\nabla \cdot \frac{d_E}{dt} \nabla_\perp W = \nabla \cdot \frac{\partial}{\partial t} \nabla_\perp W + \nabla \cdot [\phi, \nabla_\perp W] \tag{4.8}$$

$$= \frac{\partial}{\partial t} \nabla_\perp^2 W + [\nabla_\perp \phi, \nabla_\perp W] + \left[\phi, \nabla_\perp^2 W \right] \tag{4.9}$$

$$= \frac{d_E}{dt} \nabla_\perp^2 W + [\nabla_\perp \phi, \nabla_\perp W] \tag{4.10}$$

$$= \frac{d_E}{dt} \nabla_\perp^2 W + [\nabla_\perp \phi, \nabla_\perp p_i] \tag{4.11}$$

where the last equivalence follows the fact that the brackets are antisymmetric.

The evaluation of the vorticity $\mathbf{\Omega}$ for a 2D flow leads to

$$\mathbf{\Omega} \equiv \nabla_\perp \times \boldsymbol{v}_{\perp i}^{(0)} = \nabla_\perp \times (-\nabla \times W\boldsymbol{e}_z) = \nabla_\perp^2 W\boldsymbol{e}_z \tag{4.12}$$

The charge conservation equation therefore becomes an evolution equation for the vorticity (in the next subsection Eq (4.16)). The last term in the RHS of Eq (4.11) is referred to as the gyroviscous correction.

4.1.2 DALF3 equations

The isothermal version of the drift Alfvén model is used in this study, as presented in [65]. Starting from the toroidal coordinates (r, θ, ϕ) the coordinate system is defined at a reference flux surface $r = a$ as $x = r - a$, $y = a/q_a[q(\theta - \theta_k) - \phi]$ and $s = \theta$ separately at every poloidal location θ_k with x and y normalized by the drift scale ρ_s (Eq (3.24)) and s defined in $[-\pi, \pi]$. The coordinates are respectively radial x, binormal y and parallel to the magnetic field line s. In this way, the drift plane is identified by the x and y coordinates and the perpendicular laplacian is given by

$$\nabla_\perp^2 = \partial^2/\partial x^2 + \partial^2/\partial y^2, \tag{4.13}$$

The equations are normalized with standard gyro-Bohm forms:

$$\frac{\partial}{\partial t} = \frac{L_\perp}{c_s}\left(\frac{\partial}{\partial t}\right)_{SI}, \quad \frac{\partial}{\partial x, y} = \rho_s\left(\frac{\partial}{\partial x, y}\right)_{SI}, \quad \frac{\partial}{\partial s} = qR\left(\frac{\partial}{\partial s}\right)_{SI}. \tag{4.14}$$

where $L_\perp$ is the perpendicular profile scale length, c_s is the sound speed and ρ_s is the drift scale. The variables are split in a background value and a fluctuating term as $x = \overline{x} + \widetilde{x}$, but nonlinearities in the advection leading to turbulence are maintained following drift ordering described in Sec. 3.2.1 that allows $\nabla_\perp \widetilde{x} \sim \nabla_\perp \overline{x}$ despite $\widetilde{x} \ll \overline{x}$. Due to the isothermal assumptions, the dependent variables are $p_e, \phi, u_\parallel$ and $A_\parallel$. The potential fluctuations are normalized to the background mean electron temperature T_{e0} and the electron charge e, the pressure fluctuation to a reference fixed background pressure p_{e0}, the velocities to the sound speed c_s and the magnetic fluctuations to the background B. Consequently to the drift ordering (see Eq (3.46)), the relative amplitude of the fluctuations is scaled with an additional factor of $\delta = \rho_s/L_\perp$ such that, as an example, for the potential fluctuations

$$\widetilde{\phi} = \frac{1}{\delta}\frac{e(\widetilde{\phi})_{SI}}{T_{e0}}. \tag{4.15}$$

The complete system of equations reads

$$\frac{d_E\widetilde{\Omega}}{dt} + \frac{\tau_i}{B^2}\left[\nabla_\perp\phi, \nabla_\perp\widetilde{p}_e\right] = B\nabla_\parallel\frac{\widetilde{J}_\parallel}{B} - (1+\tau_i)\mathcal{K}(\widetilde{p}_e), \tag{4.16}$$

$$\frac{d_E\widetilde{p}_e}{dt} + \boldsymbol{v}_E\cdot\nabla\overline{p_e} = B\nabla_\parallel\frac{\widetilde{J}_\parallel - \widetilde{u}_\parallel}{B} + \mathcal{K}(\widetilde{\phi} - \widetilde{p}_e), \tag{4.17}$$

$$\hat{\beta}\frac{\partial\widetilde{A}_\parallel}{\partial t} + \hat{\mu}\frac{d\widetilde{J}_\parallel}{dt} = \nabla_\parallel(\overline{p}_e + \widetilde{p}_e - \widetilde{\phi}) - C\widetilde{J}_\parallel, \tag{4.18}$$

$$\hat{\epsilon}\frac{d_E\widetilde{u}_\parallel}{dt} = -(1+\tau_i)\nabla_\parallel(p_e) + \mu_\parallel\nabla_\parallel^2\widetilde{u}_\parallel, \tag{4.19}$$

together with the Ampère's law and the vorticity definition as consistency relations

$$-\nabla_\perp^2\widetilde{A}_\parallel = \widetilde{J}_\parallel, \tag{4.20}$$

$$\widetilde{\Omega} = \nabla_\perp^2\widetilde{W} = \nabla_\perp^2(\widetilde{\phi} + \tau_i\widetilde{p_e}). \tag{4.21}$$

In this coordinates system, the curvature operator (Eq (3.52)) is written as

$$\mathcal{K} = \omega_B\left(\frac{\partial}{\partial x}\sin s + \frac{\partial}{\partial y}\cos s\right), \tag{4.22}$$

where $\omega_B = 2L_\perp/R$. A series of fixed parameters are introduced to close the system. They are

$$\hat{\beta} = \beta\left(\frac{L_\parallel}{L_\perp}\right)^2, \quad \hat{\mu} = \frac{m_e}{m_i}\left(\frac{L_\parallel}{L_\perp}\right)^2, \quad C = 0.51\frac{\nu_e}{c_s/L_\perp}\hat{\mu}, \quad \hat{\epsilon} = \left(\frac{L_\parallel}{L_\perp}\right)^2, \tag{4.23}$$

where $L_\parallel = qR$ is the parallel connection length. It is straightforward to notice that, if $\hat{\beta} > \hat{\mu}$, electromagnetic effects given by $\widetilde{A}_\parallel$ prevail upon electron dynamics given by the second term in the LHS of Eq (4.18). This is the so-called *resistive MHD* regime, that can be achieved in the edge of a toroidally confined plasma [69]. The term C is referred to as *collisionality* and is derived from the normalization of the isothermal version of Eq (3.53). The last term $\hat{\epsilon}$ controls the sound wave dynamics, which are damped by the parallel ion viscosity $\mu_\parallel$. The value of the interested parameters is discussed in Chapter 5 for the numerical integration.

Finally, the parallel derivative is given by

$$\nabla_\parallel = b_s\partial/\partial s + \widetilde{b}_x\partial/\partial x + \widetilde{b}_y\partial/\partial y, \tag{4.24}$$

where

$$\widetilde{b}_x = \hat{\beta}(\partial\widetilde{A}_\parallel/\partial y), \quad \widetilde{b}_y = -\hat{\beta}(\partial\widetilde{A}_\parallel/\partial x), \quad b_s = 1, \tag{4.25}$$

with normalized $B = 1$.

4.2 Derivation of the Interchange model for plasma edge instabilities

The derivation of the model for plasma edge instabilities is presented in this section. The assumptions considered for the reduction of the DALF3 model equations to a 0D dynamical system are introduced at the beginning and used during the subsequent derivation of the single equations. The interpretation of the model dynamics is left to Sec. 5.3 with the aid of numerical simulations.

4.2.1 Assumptions

Geometrical assumptions

The model presented in this thesis focuses on the physics phenomena localized at the plasma edge. The treatment is intended to provide a reduced model, that considers only the evolution in time of the amplitude of a set of variables without defining the evolution of their spatial profiles, but the geometry effects due to the torus-shaped plasma and the magnetic field must be taken into account. The considered variables are either zonal averaged quantities, i.e. evaluated over a whole flux surface, or fluctuations periodic around the torus (in poloidal and toroidal directions), evaluated in a single point.

The component of the wavevector parallel to the poloidal magnetic field $k_\theta = m/r$ and the one parallel to the toroidal magnetic field $k_\phi = -n/R$ are introduced such that any elementary mode can be expressed as

$$f(r, \theta, \phi) = |f(r)| \exp[i(k_\theta r\theta - k_\phi R\phi)], \tag{4.26}$$

in toroidal coordinates. Coherently with the coordinates system introduced for the DALF3 model, the 0d model considers the drift plane identified by the orthogonal coordinates x and y. The present analysis focuses on the evolution of modes localized at the edge where $r \approx a$ and $x \to 0$. Furthermore, for simplicity, the mode is considered periodic also in the drift plane, and the y component of the wavevector $\boldsymbol{k} = (k_x, k_y, k_s)$ of a mode is considered equivalent to the poloidal component such that

$$k_y \approx k_\theta = m/a. \tag{4.27}$$

As discussed in Sec. 2.6, the main objective of this treatment is to reproduce the transition measured in the magnetic pick up coils of ASDEX Upgrade during an L-H transition. The simulation is carried on the tokamak

midplane, since the $\dot{B}_r$ signal is measured in this location (Fig. 4.1(a)). Any point on the outer midplane is identified with a poloidal angle $\theta = 0$. This description is referred to as *slab geometry* [60], and in this assumption all the consequences of the finite aspect ratio are reduced to the presence of $\mathcal{K}$. Due to the fact that s can be considered the projection of the parallel direction onto the poloidal angle [66] as $s = \theta$, the curvature operator in the DALF3 model evaluated at the outer midplane of the torus becomes

$$\mathcal{K} = \omega_B(\sin s\frac{\partial}{\partial x} + \cos s\frac{\partial}{\partial y}) \rightarrow \omega_B\frac{\partial}{\partial y}. \tag{4.28}$$

.

E × B velocity

As a main consequence of the considered geometry, the $E \times B$ velocity $\boldsymbol{v}_E$ is analogous to the one described in Sec. 4.1.1, since the effects of the inhomogeneities of the magnetic field are contained in the term defined by $\mathcal{K}$. The velocity $\boldsymbol{v}_E$ is given by a background $E \times B$ contribution in the poloidal direction y plus a term due to potential fluctuations. The background contribution u^y, basing on recent experimental observations in H-mode [70], as well as in I-phase [46], is considered to be dominated by the neoclassical $E \times B$ flow, due to E_r^{neo} only. This is described by Eq (2.61) considering only the ∇p_i contribution, which in its dimensionless form reads $\boldsymbol{E}_r^{neo} = \nabla p_i$ and is directed in the direction $-\boldsymbol{e}_x$. Therefore it is possible to define an expression for the background $E \times B$ flow with normalized $B = 1$ at the edge as

$$\boldsymbol{u}^y = -E_r^{neo}\boldsymbol{e}_y = -\nabla p_i \boldsymbol{e}_y \tag{4.29}$$

And therefore the dimensionless $E \times B$ velocity is

$$\boldsymbol{v}_E = \left(-\frac{\partial\widetilde{\phi}}{\partial y} \ , \ u^y + \frac{\partial\widetilde{\phi}}{\partial x} \ , \ 0 \right) \tag{4.30}$$

Single mode analysis

The DALF3 model, developed to describe 3D turbulence in the plasma edge, is able to describe the plasma dynamics also in MHD scales, such as ELM events. For simplicity, in this analysis a single mode is considered to get unstable. Therefore a Fourier transform will be applied considering a *single dominating mode*, defined by its spatial scale. The dimensionless poloidal wavevector at the edge for a mode number m is $k_y = \rho_s(k_y)_{SI} =$

$\rho_s m/a$. Note that one of the main consequences of this approach is the modification of the nonlinear advection term for each of the considered scalar fluctuations

$$\boldsymbol{v}_E \cdot \nabla \widetilde{f} = \widetilde{v}_E^x \frac{\partial \widetilde{f}}{\partial x} + \widetilde{v}_E^y \frac{\partial \widetilde{f}}{\partial y} + u^y \frac{\partial \widetilde{f}}{\partial y}, \tag{4.31}$$

A single mode analysis of this expression leads to

$$\boldsymbol{v}_E \cdot \nabla \widetilde{f} \overset{F}{\rightarrow} k_y \widetilde{\phi} k_x \widetilde{f} - k_x \widetilde{\phi} k_y \widetilde{f} + i k_y u^y \widetilde{f} = i k_y u^y \widetilde{f}. \tag{4.32}$$

Consequently, this expression for the advection does not allow the energy cascade of the mode via the three-wave coupling with other modes, with the formation of turbulent structures, and therefore one of the main channel for energy dissipation is lost. This issue will be analyzed and a solution will be proposed in Sec. 4.2.3.

MHD ordering

The considered dominating MHD mode driven unstable during an ELM event is characterized by poloidal mode numbers m in the order of unity [47]. Therefore, the normalized wavevector $k_y = (k_y)_{SI}\rho_s \ll 1$ since ρ_s is close to the ion gyroradius while $(k_y)_{SI}$ is approximately of the order of the inverse of the system scale. Since turbulence, as explained in Sec. 3.2.1, is characterized by $k_{x,y} \sim 1$ [60], in this case the DALF model is treated in the so-called *MHD ordering* and small scale dynamics are not influent. This implies in particular that the ion stream function expression becomes $\widetilde{W} = \widetilde{\phi}$ and that the adiabatic dynamics driven by $\nabla_\parallel$ is reduced [68]. This is coherent with the present analysis for a pressure driven ballooning mode, for which the most unstable modes lie on the rational surfaces and $k_\parallel \rightarrow 0$.

Constant sound speed

Furthermore, for simplicity, in the present derivation a *constant sound speed* is considered, such that the dynamics is focused on the perpendicular drift plane

$$\widetilde{u}_\parallel = c_s = const. \ , \tag{4.33}$$

therefore reducing the number of dependent variables to $p_e, \phi, A_\parallel$ and their disturbances. This can be justified by the fact that, from numerical simulations in [66], the parallel ion velocity has a weak coupling with the rest of the system. In fact, focusing the study of a mode on a rational surface, $k_\parallel \rightarrow 0$ and Eq (4.19) lacks its main drive for the fluctuation.

Parallel dynamics and sheared slab approximation

Particular attention must be paid upon the expression of the parallel dynamics and the consequences of its evaluation for a single mode getting unstable at a rational surface.

Consider the definition of the parallel gradient as given by Eq (4.24) and reported here for convenience:

$$\nabla_{\parallel} = b_s \frac{\partial}{\partial s} + \widetilde{b}_x \frac{\partial}{\partial x} + \widetilde{b}_y \frac{\partial}{\partial y}. \tag{4.34}$$

By studying a single mode and substituting the definition of the magnetic fluctuation as a function of the parallel component of the vector potential Eq (4.25), one gets

$$\nabla_{\parallel} \xrightarrow{F} ik_{\parallel} = k_s + \hat{\beta} i k_y \widetilde{A}_{\parallel} i k_x - \hat{\beta} i k_x \widetilde{A}_{\parallel} i k_y = k_s. \tag{4.35}$$

Therefore, it is necessary to find an expression for k_s only, since the effect of the disturbances compensates.

The unperturbed component of the wavevector of a mode parallel to the magnetic field can be considered as

$$k_s = \boldsymbol{k} \cdot \frac{\boldsymbol{B}}{B} \approx \boldsymbol{k} \cdot \frac{\boldsymbol{B}}{B_t}, \tag{4.36}$$

where for a tokamak it is assumed $B_t \gg B_p$ and therefore $B \approx B_t$.

Due to the assumed elementary perturbation (Eq (4.26)), the component of the mode wavevector parallel to $\boldsymbol{B}$ reads

$$k_s = \frac{1}{B_t} \boldsymbol{k} \cdot \boldsymbol{B} = \frac{1}{B_t} \left(\frac{m}{r} B_p - \frac{n}{R} B_t \right) \tag{4.37}$$

$$= \frac{n}{r} \frac{B_p}{B_t} \left(\frac{m}{n} - \frac{B_t}{B_p} \frac{r}{R} \right) \tag{4.38}$$

$$= \frac{n}{r} \frac{B_p}{B_t} \left(\frac{m}{n} - q(r) \right). \tag{4.39}$$

Therefore, by a rational surface identified by r_0 such that $q(r_0) = m/n$ one gets $k_s = 0$. The most unstable modes are well localized around a rational surface, since the presence of a finite k_s has a stabilizing effect [29] by allowing the adiabatic response of the electrons. The interchange instability described in Sec. 2.3.3, where the parallel electron response to a potential perturbation is impeded by $k_s = 0$, is two dimensional. Taylor expanding $q(r)$ around a rational surface by r_0 one gets

$$q(r) = \frac{m}{n} + \frac{dq}{dr}(r - r_0), \tag{4.40}$$

that once substituted in the definition of k_s leads to

$$k_s = -\frac{n}{r}\frac{B_p}{B_t}\frac{dq}{dr}(r-r_0) = \frac{n}{qR}\frac{dq}{dr}(r-r_0) = -\frac{qn}{r}\frac{\hat{s}}{qR}(r-r_0). \tag{4.41}$$

In which it was introduced the *shear*, a standard way to describe how the safety factor variates with the minor radius r, defined as

$$\hat{s} = \frac{r}{q}\frac{dq}{dr} = \frac{d\ln q}{d\ln r} \tag{4.42}$$

Finally, the *shear length* is introduced

$$L_s = \frac{qR}{\hat{s}}. \tag{4.43}$$

Assuming that a rational surface can be found at the edge close to the separatrix, allows to consider $r_0 \approx a$. This can be motivated by the fact that $q(r)$ grows more than linearly with r and most of the unstable rational surfaces are concentrated in the edge region[1]. Recall also that $k_y \approx k_\theta = \rho_s m/a = \rho_s qn/a$ for a periodic perturbation in the poloidal direction at the edge. In this way, since $x = r - a$ one can relate the unperturbed parallel wavevector to the poloidal wavevector such as

$$k_s = -\frac{x}{L_s}k_y = -\epsilon\, k_y. \tag{4.44}$$

This is called *sheared slab approximation*. The term ϵ is a small factor when considering a mode by the edge ($x \to 0$ while $L_s \gg 1$). Note that the numerical value of ϵ will just limit the amplitude of the radial magnetic field fluctuation in the present analysis.

This treatment justifies the omission of the parallel derivative when it appears together with other driving terms for the dynamics of a variable.

4.2.2 Derivation of the equations

Following the previous assumptions, a derivation of the equations for the plasma edge dynamics is derived from the DALF3 equations.

Background pressure gradient evolution

The background pressure gradient evolution is obtained from Eq (4.17). From now on, for simplicity, the pedex e will be neglected and $p_e \equiv p$.

$$\frac{d_E\widetilde{p}}{dt} + \boldsymbol{v}_E \cdot \nabla\overline{p} = \mathcal{K}(\widetilde{\phi} - \widetilde{p}), \tag{4.45}$$

[1] in fact $q \to \infty$ at the separatrix of a diverted plasma

where the term due to the parallel gradient is already neglected following the assumption of $k_s \to 0$. In order to obtain an equation for the background value only, a zonal average is introduced as

$$\langle f \rangle = \oint \oint f \; ds \; dy. \tag{4.46}$$

Note that $\langle\rangle$ commutes with $\partial/\partial x$ and $\partial/\partial t$. In [66] it is shown that, applying the zonal average to one of the DALF3 equations, the term under partial time derivative can be considered as the background together with the fluctuation. Consequently, applying the zonal average, the equation becomes

$$\frac{\partial \langle \widetilde{p} \rangle}{\partial t} + \langle \boldsymbol{v}_E \cdot \nabla \widetilde{p} \rangle + \frac{\partial \langle \overline{p} \rangle}{\partial t} + \langle \boldsymbol{v}_E \cdot \nabla \overline{p} \rangle = \langle \mathcal{K}(\widetilde{\phi} - \widetilde{p}) \rangle, \tag{4.47}$$

In [66] it is also shown that the evaluation of $\langle \mathcal{K}(\widetilde{\phi} - \widetilde{p}) \rangle$, requiring to consider the complete form of $\mathcal{K}$ as in Eq (4.22) due to the average over the whole flux surface, allows to obtain a contribution from the Pfirsch-Schlüter transport, a high collisionality effect of neoclassical transport described in Sec. 2.2.2. On the opposite, the remaining linear periodic fluctuations disappear when the zonal average is applied. Developing the remaining nonlinear advection terms and splitting the average, one obtains

$$\frac{\partial \langle \overline{p} \rangle}{\partial t} + \langle \widetilde{v}_E^x \frac{\partial \widetilde{p}}{\partial x} \rangle + \langle \widetilde{v}_E^y \frac{\partial \widetilde{p}}{\partial y} \rangle + \langle u^y \frac{\partial \widetilde{p}}{\partial y} \rangle + \langle \widetilde{v}_E^x \frac{\partial \overline{p}}{\partial x} \rangle = C \frac{\omega_B^2}{2} \frac{\partial^2}{\partial x^2} \langle \overline{p} \rangle, \tag{4.48}$$

where by definition the background pressure is constant along the poloidal direction (i.e. on a flux surface) and therefore $\partial_y \overline{p} = 0$. Once more, the averaged terms containing only linear fluctuations disappear. Furthermore, the third term in the LHS of the equation is the poloidal advection of the pressure fluctuation, that is zero once averaged along the poloidal drift direction, leaving the evolution equation for the background pressure as

$$\frac{\partial \langle \overline{p} \rangle}{\partial t} = \langle \widetilde{v}_E^x \frac{\partial \widetilde{p}}{\partial x} \rangle + C \frac{\omega_B^2}{2} \frac{\partial^2}{\partial x^2} \langle \overline{p} \rangle. \tag{4.49}$$

In order to obtain the evolution equation for the background pressure gradient, contained in Eq (4.17), this equation is derived along the radial direction x. In the present study, the focus is on the description of the edge. During an ELM cycle, the pressure gradient at the pedestal regularly collapses. The considered system is therefore treated separately from the core, introducing the value of the pressure gradient in the edge, by the

considered rational surface, analogously to the systems described in 3.1.3, as

$$z = \langle -\frac{\partial \overline{p}}{\partial x} \rangle. \tag{4.50}$$

In this way, the characteristic radial wavelength during a single mode analysis of the edge system can be approximated with the pedestal width from now on referred to as Δ. Finally, the coupling with the core, in analogy with the models described in Sec. 3.1.3 and Sec. 3.1.1, is considered due to a energy flux incoming from the core plasma and reaching the edge. This factor, from now on called simply *heating power* will be indicated with h and treated as a control parameter, as it is considered proportional to the power introduced through external heating system (e.g. NBI or RF heating). Commuting the radial derivative with $\langle\rangle$, and focusing on a single MHD mode, thus performing a Fourier transform on the equation for a unique $\boldsymbol{k} = (k_x, k_y, k_s)$, one obtains

$$\frac{\partial z}{\partial t} = h - k_x^2 k_y |\widetilde{\phi}||\widetilde{p}| - C k_x^2 \frac{\omega_B^2}{2}\, z, \tag{4.51}$$

where the anomalous transport due to the fluctuation was treated following Eq (2.47) and assuming a crossphase between $\widetilde{\phi}$ and $\widetilde{p}$ of $\pi/2$ typical of interchange instability, justified in Sec. 4.2.3. The background gradient at the edge steepens following the energy flux from the core and is depleted due to anomalous and neoclassical transport.

Pressure fluctuation evolution

The pressure fluctuation evolution is obtained from equation Eq (4.17)

$$\frac{d_E \widetilde{p}}{dt} + \boldsymbol{v}_E \cdot \nabla \overline{p} = \mathcal{K}(\widetilde{\phi} - \widetilde{p}), \tag{4.52}$$

this time treated without any averaging and in which the parallel dynamics was neglected. As described in Sec. 4.2.1, neglecting the geodesic curvature (which is zero at the outboard midplane) leads to consider $\mathcal{K} = \omega_B \partial_y$. Furthermore, splitting the total $E \times B$ advective derivative leads to

$$\frac{\partial \widetilde{p}}{\partial t} = -\widetilde{v}_E^x \frac{\partial \widetilde{p}}{\partial x} - \widetilde{v}_E^y \frac{\partial \widetilde{p}}{\partial y} - u^y \frac{\partial \widetilde{p}}{\partial y} - \widetilde{v}_E^x \nabla_x \overline{p} + \omega_B \frac{\partial}{\partial y}(\widetilde{\phi} - \widetilde{p}). \tag{4.53}$$

Note that, in a single point at the outboard midplane by the considered rational surface, $-\nabla_x \overline{p} = \langle -\nabla_x \overline{p} \rangle = z$. This introduces a drive of the

fluctuation from the background pressure gradient. A single mode analysis of this equation requires to consider Eq (4.32). Consequently, one obtains

$$\frac{\partial \widetilde{p}}{\partial t} = -ik_y u^y \widetilde{p} - ik_y \widetilde{\phi} z + ik_y \omega_B (\widetilde{\phi} - \widetilde{p}), \tag{4.54}$$

or just settling the various terms for the subsequent analysis

$$\frac{\partial \widetilde{p}}{\partial t} = -ik_y \left(z - \omega_B\right) \widetilde{\phi} - ik_y \left(\omega_B + u^y\right) \widetilde{p}. \tag{4.55}$$

In this equations, it is underlined that the pressure gradient is the drive of the instability, while $\mathcal{K}$ acts both as an energy transfer mechanism to the potential fluctuations (see later Sec. 4.2.3), but also as a phase velocity of the mode together with u^y.

Potential fluctuation evolution

The potential fluctuation evolution is derived from Eq (4.16). The treatment of a macroscopic mode allows to assume MHD ordering [60], such that the expression of the ion stream function can be reduced to the potential contribution only and $W = \phi$. Following the fact that the Poisson bracket $[\cdot, \cdot]$ is antisymmetric, a single mode analysis of the equation makes the gyroviscous correction vanish. Finally, the parallel dynamics is neglected following the fact that $k_s \to 0$ by a rational surface and therefore

$$\frac{d_E \nabla_\perp \widetilde{\phi}}{dt} = -(1 + \tau_i)\mathcal{K}(\widetilde{p}). \tag{4.56}$$

The $E \times B$ advective derivative is split, the slab geometry is introduced as in the derivation of the pressure fluctuation evolution, such that the equation reads

$$\frac{\partial \nabla_\perp^2 \widetilde{\phi}}{\partial t} = -\widetilde{v}_E^x \frac{\partial \nabla_\perp^2 \widetilde{\phi}}{\partial x} - \widetilde{v}_E^y \frac{\partial \nabla_\perp^2 \widetilde{\phi}}{\partial y} - u^y \frac{\partial \nabla_\perp^2 \widetilde{\phi}}{\partial y} - (1 + \tau_i)\omega_B \frac{\partial \widetilde{p}}{\partial y}. \tag{4.57}$$

This simplified expression is treated for a single Fourier mode again considering Eq (4.32) and now introducing $k_\perp^2 = k_x^2 + k_y^2$. Therefore

$$-\frac{\partial k_\perp^2 \widetilde{\phi}}{\partial t} = -ik_y k_\perp^2 u^y \widetilde{\phi} - ik_y \omega_B (1 + \tau_i)\widetilde{p}. \tag{4.58}$$

The potential fluctuation is driven by the coupling with $\widetilde{p}$ through $\mathcal{K}$ while the advection contributes as a poloidal velocity with u^y.

Interlude

At this point, it is important to observe that equations Eq (4.51), Eq (4.55) and Eq (4.58) together form a closed set. This is mainly a consequence of the negligence of the parallel dynamics of $u_\parallel$ and the $\nabla_\parallel$ terms. The last is also referred to as the adiabatic coupling, giving rise to the driftwave dynamics (described in Appendix C). The model is therefore nothing else but reduced MHD, although it does not consider one very important effect: the energy cascade due to the nonlinear advection that disappears for a single mode. This will be clear in particular from Sec. 4.2.3, where a solution will be suggested for the necessary energy dissipation.

The model is not yet complete, since the interested dynamics to compare with the experimental results lies in the magnetics. It is also interesting to consider the evaluation of the zonal flow, despite in this model there is no back reaction of it onto the fluctuation (compare at the opposite the dynamics of the model presented in Sec. 3.1.1). This is done in order to identify the I-phase by the appearance of LCOs.

Zonal flow shear evolution

In the DALF3 model it is possible to obtain an evolution equation for the ZFs resembling Eq (2.62). This is done introducing, in an analogous fashion to what was made for the pressure gradient, a background value in the vorticity equation, and performing a zonal average that annihilates the linear fluctuation terms.

Coherently with their definition (see Sec. 2.4.1), ZFs must be poloidal flows, poloidally and toroidally homogeneous, varying in the radial direction only. Therefore, the potential defining them reads

$$\phi_{ZF} = \phi_{ZF}(x) \quad \Longrightarrow \quad v^y_{ZF} = \partial_x \phi_{ZF}. \tag{4.59}$$

Consequently, considering the contribution of the ZFs to the vorticity, in MHD ordering,

$$\overline{\Omega}_{ZF} = \nabla^2_\perp W_{ZF} = \nabla^2_\perp \phi_{ZF} = \frac{\partial^2 \phi_{ZF}(x)}{\partial x^2} = \nabla_x v^y_{ZF}. \tag{4.60}$$

In this way it is clear that the vorticity $\overline{\Omega}_{ZF}$ is exactly the zonal flow shear in the radial direction. Therefore it is possible to obtain an equation for the zonal flow shear from the averaged vorticity evolution with the addition of the background $\overline{\Omega}_{ZF}$ and neglecting the parallel dynamics

$$\frac{\partial \langle \overline{\Omega}_{ZF} \rangle}{\partial t} + \frac{\partial \langle \widetilde{\Omega} \rangle}{\partial t} + \langle \widetilde{v}^x_E \frac{\partial \widetilde{\Omega}}{\partial x} \rangle + \langle \widetilde{v}^y_E \frac{\partial \widetilde{\Omega}}{\partial y} \rangle + \langle u^y \frac{\partial \widetilde{\Omega}}{\partial y} \rangle = -\langle (1+\tau_i) \mathcal{K}(\widetilde{p}_e) \rangle. \tag{4.61}$$

The linear fluctuating terms disappear as well as the polodial averaged advection. The averaged interchange term given by $\mathcal{K}$, instead, gives rise, through the sideband dynamics [66], to a dissipating term explained by the rotation damping due to parallel viscosity. At this point, the equation reads

$$\frac{\partial \langle \nabla_x \, v^y_{ZF} \rangle}{\partial t} = -\langle \widetilde{v}^x_E \, \frac{\partial^2 \widetilde{v}^y_E}{\partial x^2} \rangle - \mu_\parallel \frac{\omega_B^2}{2} \langle \nabla_x \, v^y_{ZF} \rangle, \tag{4.62}$$

where it was substituted

$$\frac{\partial \widetilde{\Omega}}{\partial x} = \frac{\partial}{\partial x} \frac{\partial^2 \widetilde{\phi}}{\partial x^2} = \frac{\partial^2 \widetilde{v}^y_E}{\partial x^2}. \tag{4.63}$$

Consider that the $E \times B$ velocity appearing in the $E \times B$ advective derivative is divergence free (its finite divergence effect in this geometry are contained only in $\mathcal{K}(\phi)$). Therefore, commuting the radial derivative with the zonal average, it is obtained

$$\frac{\partial \langle \nabla_x \, v^y_{ZF} \rangle}{\partial t} = -\frac{\partial^2 \langle \widetilde{v}^x_E \, \widetilde{v}^y_E \rangle}{\partial x^2} - \mu_\parallel \frac{\omega_B^2}{2} \langle \nabla_x \, v^y_{ZF} \rangle. \tag{4.64}$$

Note that this equation is exactly Eq (2.62), derived along the radial direction, and the term $\langle \widetilde{v}^x_E \widetilde{v}^y_E \rangle$ is the Reynolds stress tensor. A single mode analysis is then performed. Note that, choosing values of k_x and k_y for a macroscopic MHD mode makes the ZF to get a drive arising not directly from microturbulence. This is an intrinsic limitation of this approach, but the contribution of the fluctuation to the ZFs is maintained anyways, in order to study the presence of LCOs and compare the results with the predator-prey fluctuations of the model presented in 3.1.2.

Performing finally a single mode analysis, it is possible to obtain an evolution equation for the zonal flow shear. The Reynolds stress term is expressed through Eq (2.47), where the crossphase between $\widetilde{\phi}$ and $\widetilde{v}^y_E$ is by definition $\pi/2$.

$$\frac{\partial \langle \nabla_x \, v^y_{ZF} \rangle}{\partial t} = k_y \, k_x^3 |\widetilde{\phi}|^2 - \mu_\parallel \frac{\omega_B^2}{2} \langle \nabla_x \, v^y_{ZF} \rangle. \tag{4.65}$$

Radial magnetic fluctuation

The magnetic fluctuation dynamics is obtained from Eq (4.18). Resistive MHD is assumed, such that the equation focus on the evolution of the parallel component of the vector potential is

$$\hat{\beta} \frac{\partial \widetilde{A}_\parallel}{\partial t} = \nabla_\parallel (\overline{p} + \widetilde{p} - \widetilde{\phi}) + C \nabla^2_\perp \widetilde{A}_\parallel, \tag{4.66}$$

where the Ampère's law was invoked in order to substitute the last term on the RHS.

Note that, in the case of magnetic fluctuations, the term related to $\nabla_\parallel$ is the only coupling with the remaining system. Therefore, it is necessary to find an expression for it and cannot be neglected as it was done in the previous cases.

At this point, it is possible to focus on the radial component of the magnetic field. The measurements performed in [1] are based on Mirnov coils located at the midplane of the tokamak (see Fig. 2.10(b)). Therefore, the actual geometry for the magnetic field is consistent.

Type-III ELMs precursors are dominantly seen in the radial magnetic field fluctuations. In order to derive the equation for the radial fluctuations, Ohm's law Eq (4.66) is derived along the y direction (note that $\partial_y \overline{p} = 0$) and the definition of $\widetilde{b}_x$ is introduced as in Eq (4.25) to get

$$\frac{\partial \widetilde{b}_x}{\partial t} = \frac{\partial}{\partial y}\nabla_\parallel(\widetilde{p} - \widetilde{\phi}) + \frac{C}{\hat{\beta}}\nabla_\perp^2 \widetilde{b}_x. \tag{4.67}$$

Therefore, proceeding with the analysis for a single Fourier mode and inserting the expression for k_s ofEq (4.44), it is possible to obtain the evolution equation for the radial magnetic field perturbation

$$\frac{\partial \widetilde{b}_x}{\partial t} = \epsilon k_y^2(\widetilde{p} - \widetilde{\phi}) - \frac{C}{\hat{\beta}}k_\perp^2 \widetilde{b}_x. \tag{4.68}$$

Poloidal magnetic fluctuation

While for the radial magnetic field fluctuations the measurement diagnostics were located almost on the midplane of the torus, the poloidal magnetic field fluctuation is measured in different positions around the tokamak. The most intense signal, as the one of Fig. 2.10(a), is measured in the coils by the lower divertor [1]. Such a feature can be motivated by the fact that $\widetilde{B}_\theta$ is strongly correlated to the divertor shunt current and the D_α signal indicating an increased transport of plasma out of the LCFS and towards the divertor plates [72]. The disposition of the pick-up coils in different sites of ASDEX Upgrade around the poloidal cross section (see Fig. 4.1(a) and Fig. 4.1(b)) allowed to obtain a global picture of the poloidal mode structure. The cross correlation between multiple displaced Mirnov coils was evaluated during the I-phase, showing a pronounced up-down asymmetry as can be seen in Fig. 4.2.

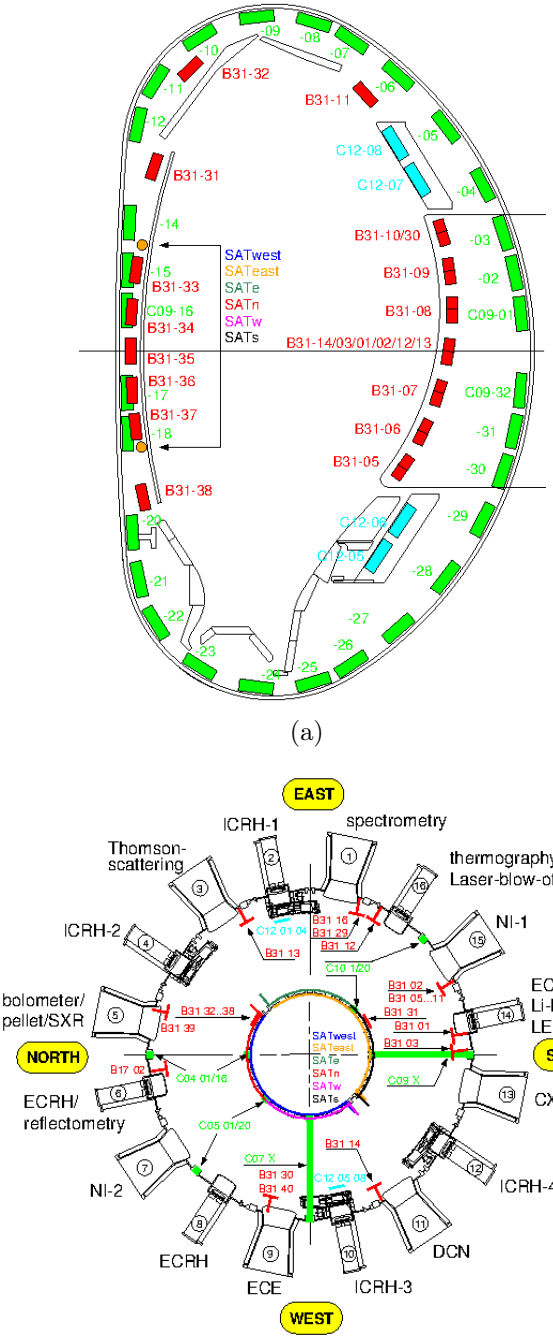

(a)

(b)

Figure 4.1: The Mirnov coils in ASDEX Upgrade evidenced. (a) a poloidal cross section. In green, one set of 30 coils measuring B_θ; in red, the coils by the midplane measuring B_r. (b) A toroidal cross section. The two complete set of poloidal coils are indicated with a green straight line. Around the torus, six other single poloidal coils are mounted on the midplane ([71]).

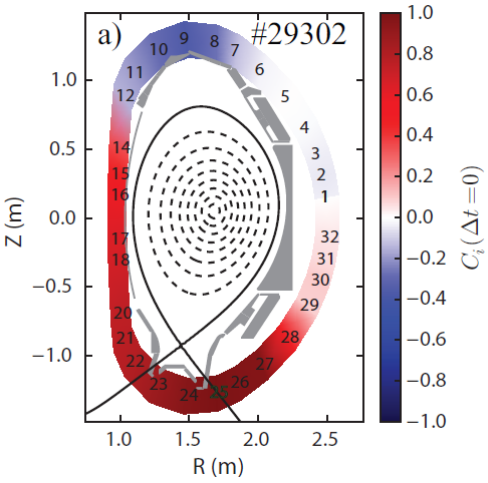

Figure 4.2: Poloidal mode structure of the $\dot{B}_\theta$ signal from cross-correlation analysis with reference probe 25 (Fig. 8(a) [1])

Consider, for the averaged dynamics, the coordinates system of the DALF3 model. In this case, the evaluation of a zonal average multiplied by the asymmetry function $\sin s$ allows to obtain the evolution equation for the poloidal magnetic fluctuation. Usually, in fact, a linear periodic fluctuation averaged over the flux surface is null. In this case, instead, due to the same up-down asymmetry of $\widetilde{b}_y$ and $\sin s$ it is possible to obtain $\langle \widetilde{b}_y \sin s \rangle \neq 0$. Take Eq (4.66), multiplied by $\sin s$ and averaged over the flux surface, considering already a resistive MHD assumption and the fact that, as it was derived, for a single mode analysis $\nabla_\parallel \to \partial/\partial s$.

$$\frac{\partial \langle \hat{\beta} \widetilde{A}_\parallel \sin s \rangle}{\partial t} = \langle \frac{\partial}{\partial s} (\overline{p} + \widetilde{p} - \widetilde{\phi}) \sin s \rangle + C \langle \nabla_\perp^2 \widetilde{A}_\parallel \sin s \rangle, \tag{4.69}$$

Consider that $\langle \partial_s(f) \ \sin s \rangle = \langle \partial_s(f \ \sin s) \rangle - \langle f \ \partial_s(\sin s) \rangle = -\langle f \ \cos s \rangle$, since the parallel derivative vanishes [72]. By deriving the whole equation along the radial direction x, it is possible to obtain $\widetilde{b}_y$ from its definition of Eq (4.25). The other linear fluctuations that do not show the same asymmetry, disappear once averaged. In the case of $\widetilde{\phi}$ and $\widetilde{p}$, the asymmetry is more like the one typical for ballooning modes of Fig. 2.4(b) (the fact that in this model is treated an interchange instability will be clear in Sec. 4.2.3). The zonal average multiplied by the $\cos s$ periodic function makes it vanish. The remaining terms read

$$\frac{\partial \langle \widetilde{b}_y \sin s \rangle}{\partial t} = \langle -\frac{\partial \overline{p}}{\partial x} \cos s \rangle + C \langle \nabla_\perp^2 \widetilde{b}_y \sin s \rangle, \tag{4.70}$$

At this point, to close the equation, Eq (4.70) is derived once more in time leading to

$$\frac{\partial^2 \langle \widetilde{b}_y \sin s \rangle}{\partial t^2} = \frac{\partial}{\partial t}\langle z \cos s \rangle + \frac{C}{\hat{\beta}} \nabla_\perp^2 \frac{\partial}{\partial t} \langle \widetilde{b}_y \sin s \rangle, \tag{4.71}$$

where $\nabla_\perp^2$ commuted with the average. It is now useful to evaluate the averaged dynamics for the background pressure gradient, multiplying it by $\cos s$ and averaging over the flux surface. Considering this time the presence of the parallel derivative $\nabla_\parallel = \partial_s$, and the fact that $u_\parallel$ is constant, leads to

$$\frac{\partial}{\partial t}\langle z \cos s \rangle = \frac{\partial^2}{\partial x^2}\langle \widetilde{v}_E^x \widetilde{p} \cos s \rangle - \frac{\partial}{\partial x}\langle \widetilde{J}_\parallel \sin s \rangle + C \frac{\omega_B}{2} \langle \frac{\partial^2}{\partial x^2} z \cos s \rangle. \tag{4.72}$$

Considering $\langle \widetilde{v}_E^x \widetilde{p} \cos s \rangle \approx \langle \widetilde{v}_E^x \widetilde{p} \rangle$ is allowed, following the fact that ballooned transport is actually dominating on the midplane (see again Fig. 2.4(b)) where $\cos s = 1$. Neglecting the small role of the neoclassical transport, substituting Eq (4.72) in Eq (4.71) and finally introducing the definition of $\widetilde{B}_\theta = \langle \widetilde{b}_y \sin s \rangle$, the equation for the poloidal magnetic fluctuation with up-down asymmetry is obtained

$$\frac{\partial^2 \widetilde{B}_\theta}{\partial t^2} = \frac{\partial^2}{\partial x^2}\langle \widetilde{v}_E^x \widetilde{p} \rangle + \frac{1}{\hat{\beta}} \nabla_\perp^2 \widetilde{B}_\theta + \frac{C}{\hat{\beta}} \nabla_\perp^2 \frac{\partial \widetilde{B}_\theta}{\partial t}, \tag{4.73}$$

where once more Ampère's law was used to substitute $\widetilde{J}_\parallel = -\nabla_\perp^2 \widetilde{A}_\parallel$ and therefore $\partial_x J_\parallel = (\nabla_\perp^2 / \hat{\beta}) \widetilde{b}_y$. A single mode analysis leads to

$$\frac{\partial^2 \widetilde{B}_\theta}{\partial t^2} = -k_x^2 k_y |\widetilde{\phi}||\widetilde{p}| + \frac{k_x^2 + k_y^2}{\hat{\beta}} (\widetilde{B}_\theta + C \frac{\partial \widetilde{B}_\theta}{\partial t}) \tag{4.74}$$

The drive for the fluctuation is the ballooned transport $\langle \widetilde{v}_E^x \widetilde{p} \rangle$, while the remaining terms are responsible for damping and derive from parallel transport and resistive terms, both linked to the parallel current.

4.2.3 Energetics of the interchange instability

In the present subsection, a series of features of the first closed subset of the model are analyzed. In particular, it is underlined how the equations describe an interchange instability, that justify in particular the assumption of a crossphase of $\pi/2$ between pressure and potential fluctuation as well as the strong transport concentrated on the outer midplane of a toroidally confined plasma.

Consider Eq (4.52) and Eq (4.56), that describe the pressure and potential evolution neglecting the parallel dynamics.

$$\frac{d_E\widetilde{p}}{dt} + \boldsymbol{v}_E \cdot \nabla\overline{p} = \mathcal{K}(\widetilde{\phi} - \widetilde{p}), \tag{4.75}$$

$$\frac{d_E\nabla_\perp\widetilde{\phi}}{dt} = -(1+\tau_i)\mathcal{K}(\widetilde{p}_e). \tag{4.76}$$

For this treatment, consider $\overline{p}$ as fixed and known, as well as cold ions (τ_i=0). A linearization of the equations has the same effect of the single mode analysis as described in 4.2.1, neglecting the nonlinear advection but also the contribution from u^y. The resulting system reads

$$\frac{\partial\widetilde{p}}{\partial t} - \frac{\partial\phi}{\partial y}\nabla_x\overline{p} = \mathcal{K}(\widetilde{\phi} - \widetilde{p}), \tag{4.77}$$

$$\frac{\partial\nabla_\perp\widetilde{\phi}}{\partial t} = -\mathcal{K}(\widetilde{p}). \tag{4.78}$$

The coupling of the dynamics is given by the interchange operator $\mathcal{K}$, deriving from quasistatic compression due to the finite divergence of the motion in an inhomogeneous magnetic field. This compression mechanism conserves energy during the energy transfer between $\widetilde{p}$ (related to compressional energy) and $\widetilde{\phi}$ (related to kinetic energy of the $E\times B$ motion) in an analogous way as parallel sound waves. In a simplified picture, the presence of a curvature and therefore an inhomogeneity of the magnetic field, allows the formation of potential fluctuations following density (pressure) fluctuations, as it was illustrated considering single particle drifts in Sec. 2.3.3, forcing a spatial crossphase of $\pi/2$ that was assumed throughout the derivation. This is the interchange instability of a toroidally magnetized plasma, that leads to enhanced transport directed radially outwards when the density (pressure) gradient is aligned with the curvature vector of the magnetic field.

Focus now on an energetic approach. Multiplying Eq (4.77) by $\widetilde{p}$ and Eq (4.78) by $-\widetilde{\phi}$ and integrating over all space, the energy evolution of fluctuations is found. As performed in [60], the energy theorem for the total energy of this reduced system is therefore the sum of the two energy evolutions

$$\frac{\partial}{\partial t} = \int \frac{1}{2}\left(|\nabla_\perp\widetilde{\phi}|^2 + |\widetilde{p}|^2\right)\, d^2\boldsymbol{x} = -\int \nabla_x\overline{p}\frac{\partial\widetilde{\phi}}{\partial y}\,\widetilde{p}\, d^2\boldsymbol{x}. \tag{4.79}$$

Form the energetic point of view, the pressure gradient acts as an energy source for the fluctuation, while the interchange effects is dissipation free

and simplifies. The nonlinear advection, giving rise to the energy cascade, would become effective when the instabilities amplitude grow and the linearization is no more a valid assumption. But for a single mode this would never happen, since the turbulent cascade requires coupling between different modes.

The interchange instability can be studied as a linear instability [60], to underline the necessity of a dissipation term. A single Fourier component inserted in the linearized system shows

$$+i\omega k_\perp^2 \widetilde{\phi} = -ik_y \omega_B \widetilde{p}, \tag{4.80}$$

$$-i\omega \widetilde{p} = +i\nabla_x \overline{p} k_y \widetilde{\phi} - i\omega_B k_y (\widetilde{p} - \widetilde{\phi}). \tag{4.81}$$

Solving Eq (4.81) for $\widetilde{p}$

$$\widetilde{p} = -\frac{(\nabla_x \overline{p} + \omega_B) k_y}{\omega - \omega_B k_y} \widetilde{\phi} \tag{4.82}$$

inserting it into Eq (4.80) taking a large scale limit (i.e k_y,$k_\perp^2 \to 0$ but $k_y^2/k_\perp^2 \neq 0$) it is possible to obtain an expression for ω.

$$\omega^2 = -\frac{k_y^2}{k_\perp^2}\omega_B(-\nabla_x \overline{p} - \omega_B) = -\frac{k_y^2}{k_\perp^2}\omega_B(z - \omega_B). \tag{4.83}$$

This means that only growing ($z > \omega_B$) or oscillating ($z < \omega_B$) solutions are admitted.

The selected approach to solve this problem, that can be found in [60], is the introduction of a dissipating term $\gamma_D \widetilde{\phi}$ in the dynamics of $\widetilde{\phi}$ such that the equations now look appear

$$\frac{\partial \widetilde{p}}{\partial t} - \frac{\partial \phi}{\partial y}\nabla_x \overline{p} = \mathcal{K}(\widetilde{\phi} - \widetilde{p}), \tag{4.84}$$

$$\frac{\partial \nabla_\perp \widetilde{\phi}}{\partial t} = -\mathcal{K}(\widetilde{p}) - \gamma_D \, \widetilde{\phi}, \tag{4.85}$$

In this way, through a new single mode analysis, for sufficiently large γ_D, a new solution is possible with

$$\omega = -i\frac{\gamma_D}{k_\perp^2}, \tag{4.86}$$

therefore allowing for damped solutions. Computing again the energy theorem for the system, it is straightforward to see that an equilibrium can be reached due to the presence of γ_D

$$\frac{\partial}{\partial t} = \int \frac{1}{2}\left(|\nabla_\perp \widetilde{\phi}|^2 + |\widetilde{p}|^2\right) \, d^2\boldsymbol{x} = -\int \left(\nabla_x \overline{p} \frac{\partial \widetilde{\phi}}{\partial y} \, \widetilde{p} + \gamma_D \widetilde{\phi}^2 \right) d^2\boldsymbol{x}. \tag{4.87}$$

The dissipation term γ_D can be loosely motivated as follows. Still considering a single mode for the instability, the energy cascade via coupling between different modes does exist. The coupling through the advection term for the vorticity is considered for the single dominating mode $\widetilde{\phi}$ with all the other modes $\phi'(k'_x, k'_y)$, each defined by a wavevector $\boldsymbol{k}'$. The advective term can be written as

$$\boldsymbol{v}_E \cdot \nabla \nabla_\perp^2 \widetilde{\phi} = \sum_{k'_x, k'_y} \left(-\frac{\partial \phi'(k'_x, k'_y)}{\partial y} \frac{\partial \nabla_\perp^2 \widetilde{\phi}}{\partial x} + \frac{\partial \phi'(k'_x, k'_y)}{\partial x} \frac{\partial \nabla_\perp^2 \widetilde{\phi}}{\partial y} \right) \tag{4.88}$$

$$\overset{F}{\Rightarrow} \widetilde{\phi}\, k_\perp^2 \sum_{k'_x, k'_y} \left(+k'_y\, k_x \phi'(k'_x, k'_y) - k'_x\, k_y \phi'(k'_x, k'_y) \right), \tag{4.89}$$

where it is was possible to isolate

$$\gamma_D = k_\perp^2 \sum_{k'_x, k'_y} \left(+k'_y\, k_x \phi' - k'_x\, k_y \phi' \right) \tag{4.90}$$

which is however treated as a free parameter of the system, as well as h. Note that, in order to describe consistently the plasma turbulence, the Poisson bracket giving rise to the nonlinear advection that were introduced in Sec. 4.1.1, need to be solved in at least two spatial dimensions. This will of course not occur in the present 0D model.

At last, in order to show the possible extension of this simplified approach, the consideration of the effect of a full 3D geometry are briefly discussed, as a more general case to the actual 0D model derived from *slab geometry*. Considering the effect of a tokamak magnetic field, the interchange forcing $\mathcal{K}$ is found to be directed along the major radius R while the pressure gradient is always along the minor radius r. For the instability to develop, i.e. by driving the pressure, then potential fluctuation and therefore enhancing transport, they must align, and this happens only on the outboard of the torus. On the other side, when they are opposed, this has a stabilizing effect. Considering the effects of the magnetic shear, a linear analysis of the full 3D four-field model finds a threshold value for the pressure gradient required for the instability to develop. This turns out to be exactly the standard ballooning limit for the pressure gradient, as can be derived from MHD [21]. In conclusion, the interchange instability in slab geometry considered in this model is nothing else than the 2D version of the 3D ideal ballooning instability in a tokamak, considered to be one of the main underlying mechanism during the ELM cycle, as it was described in Sec. 2.5. The treatment of ELMs as MHD instabilities through this model is therefore justified.

4.2.4 Interchange model

The 0D dynamical model for the interchange dynamics at the outer midplane of a magnetically confined toroidal plasma, derived from fluid drift equations following the assumptions described in 4.2.1 is given by the following closed set of equations

$$-\frac{\partial k_\perp^2 \widetilde{\phi}}{\partial t} = -ik_y k_\perp^2 u^y \widetilde{\phi} - ik_y \omega_B (1+\tau_i)\widetilde{p} - \gamma_D \widetilde{\phi}, \tag{4.91}$$

$$\frac{\partial \widetilde{p}}{\partial t} = -ik_y\,(z-\omega_B)\,\widetilde{\phi} - ik_y\,(\omega_B + u^y)\,\widetilde{p}, \tag{4.92}$$

$$\frac{\partial z}{\partial t} = h - k_x^2 k_y |\widetilde{\phi}||\widetilde{p}| - C k_x^2 \frac{\omega_B^2}{2}\, z, \tag{4.93}$$

$$\frac{\partial \langle \nabla_x v^y_{ZF}\rangle}{\partial t} = k_y k_x^3 |\widetilde{\phi}|^2 - \mu_\parallel \frac{\omega_B^2}{2} \langle \nabla_x v^y_{ZF}\rangle, \tag{4.94}$$

$$\frac{\partial \widetilde{b}_x}{\partial t} = \epsilon k_y^2 (\widetilde{p} - \widetilde{\phi}) - \frac{C}{\hat{\beta}} k_\perp^2 \widetilde{b}_x, \tag{4.95}$$

$$\frac{\partial^2 \widetilde{B}_\theta}{\partial t^2} = -k_x^2 k_y |\widetilde{\phi}||\widetilde{p}| - \frac{k_x^2 + k_y^2}{\hat{\beta}} (\widetilde{B}_\theta + C \frac{\partial \widetilde{B}_\theta}{\partial t}). \tag{4.96}$$

where the parameters k_x, k_y and ω_B are fixed by the mode or geometry of the torus, $\hat{\beta}, \mu_\parallel, \tau_i$ and C depend on the plasma characteristics and ϵ is a smallness factor. The only free parameters are h, as the heating power, and γ_D, as the dissipation rate. Note that, coherently with [72], the magnetics does not influence the dynamics but it is just a derived quantity. The presence of the terms $z\,\widetilde{\phi}$, $|\widetilde{\phi}||\widetilde{p}|$ and $|\widetilde{\phi}|^2$ makes this system of equations nonlinear. For a better comprehension of the equations, consider that $\widetilde{p}$ and $\widetilde{\phi}$ as well as $\widetilde{b}_x$ are treated as periodic functions along y. Due to the forced crossphase of $\pi/2$ between pressure and potential fluctuations caused by the interchange mechanism, their spatial distribution will always be forced to be as the one pictured in Fig. 4.3(b): when $\widetilde{p}$ is maximum, $\widetilde{\phi}$ is zero and vice versa.

In this case, it is useful to consider potential and pressure fluctuations as rotating vectors in the complex plane, whose rotation velocity, as will emerge from the treatment, is given by the phase velocity already present in the equations. Substituting in the model

$$\widetilde{p} = \alpha + i\beta, \tag{4.97}$$

$$\widetilde{\phi} = \xi + i\delta, \tag{4.98}$$

$$|\widetilde{p}|^2 = (\alpha^2 + \beta^2), \tag{4.99}$$

$$|\widetilde{\phi}|^2 = (\delta^2 + \xi^2), \tag{4.100}$$

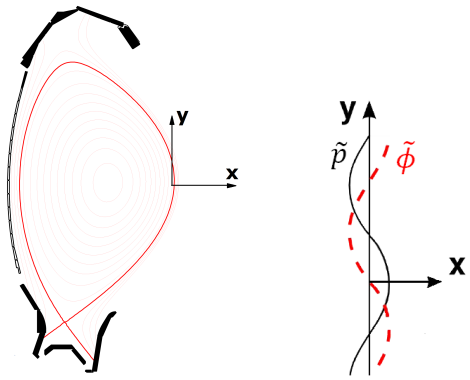

(a) (b)

Figure 4.3: (a) The considered point for the simulation of the intechange instability is the origin of the x, y, s reference frame for $\theta = 0$ and $r \approx a$, therefore at the outer midplane by a rational surface inside the pedestal. (b) A simplified picture of the potential and pressure fluctuation along the rational surface considered in this treatment. The crossphase of $\pi/2$ is due to the interchange forcing given by $\mathcal{K}$

it is possible to obtain

$$\frac{\partial \xi}{\partial t} = -(1+\tau_i)\frac{k_y\,\omega_B}{k_x^2+k_y^2}\,\beta - \gamma'_D\,\xi - k_y u^y \delta, \tag{4.101}$$

$$\frac{\partial \delta}{\partial t} = +(1+\tau_i)\frac{k_y\,\omega_B}{k_x^2+k_y^2}\,\alpha - \gamma'_D\,\delta + k_y u^y \xi, \tag{4.102}$$

$$\frac{\partial \alpha}{\partial t} = +k_y\,(z-\omega_B)\,\delta + k_y(\omega_B+u^y)\,\beta, \tag{4.103}$$

$$\frac{\partial \beta}{\partial t} = -k_y\,(z-\omega_B)\,\xi - k_y(\omega_B+u^y)\,\alpha, \tag{4.104}$$

$$\frac{\partial z}{\partial t} = h - k_x^2 k_y\,(\alpha^2+\beta^2)^{1/2}\,(\delta^2+\xi^2)^{1/2} - Ck_x^2(\omega_B^2/2)\,z, \tag{4.105}$$

$$\frac{\partial \langle \nabla_x v^y_{ZF}\rangle}{\partial t} = k_y k_x^3\,(\delta^2+\xi^2) - \mu_{\parallel}(\omega_B^2/2)\,\langle \nabla_x v^y_{ZF}\rangle, \tag{4.106}$$

$$\frac{\partial \widetilde{b}_x}{\partial t} = \epsilon k_y^2(\alpha-\xi) - \frac{C}{\hat{\beta}}k_\perp^2 \widetilde{b}_x, \tag{4.107}$$

$$\frac{\partial^2 \widetilde{B}_\theta}{\partial t^2} = -k_x^2 k_y(\alpha^2+\beta^2)^{1/2}\,(\delta^2+\xi^2)^{1/2} - \frac{k_x^2+k_y^2}{\hat{\beta}}\,(\widetilde{B}_\theta + C\frac{\partial \widetilde{B}_\theta}{\partial t}), \tag{4.108}$$

where $\gamma'_D = \gamma_D/k_\perp^2$ and in $\widetilde{b}_x$ only the real part of the fluctuation was

considered. This system of ordinary differential equations is particularly simple to integrate, as it will be shown in the next Chapter 5.

Note that the terms $k_y u^y$ and $k_y(\omega_B + u^y)$ in the potential and pressure fluctuation dynamics are nothing but phase velocities, that make the variables amplitude oscillate when simulated in the a chosen point of the torus.

In order to proceed with the analysis, a minimum set of equations able to summarize the overall dynamics is isolated from the interchange model in Chapter 5, where a physical explanation of the dynamics also is provided. This minimum model results particularly suited for a nonlinear analysis, showing the appearance of a limit cycle. Numerical simulations are required to study the temporal evolution of the system. Their main results will be presented, both for the reduced and the complete model, in the conclusive part of Chapter 5.

Chapter 5

Nonlinear analysis and numerical simulations

The aim of this chapter is to present and explain a minimum model able to summarize the dynamics of the interchange model introduced in Sec.4.2.4. Both the minimum and the complete model are then studied through numerical simulations.

In Sec. 5.1 a minimum subset of equations of the complete interchange model is isolated and its dynamics is discussed and compared to the models presented in Sec. 3.1. By means of nonlinear analysis, the presence of a limit cycle solution is explained as a consequence of the bifurcation of equilibria following the variation of a critical parameter.

In Sec. 5.2 a series of numerical integrations are performed on the minimum model. The bifurcation diagrams are drawn, in order to clearly separate the different dynamics and motivate the bifurcations. The stable limit cycle existing over a threshold of the critical parameter is presented. The numerical simulations are useful to actually understand the fundamental dynamics of the system and of the limit cycle in particular.

In Sec. 5.3, the results of the numerical integration of the complete 0D interchange model is introduced. Particular attention is made upon the choice of the parameters of the system, carefully chosen to simulate the physics of the plasma edge during the I-phase. The qualitative agreement with the experimental results introduced in Sec. 2.6 is discussed, motivating the cause-effect relationship between the variables that cannot be understood from the measurements only.

In Sec. 5.4, a final overview of the simulations is provided and an estimation for the quantitative comparison with the experimental results is presented and discussed as the end of this analysis.

5.1 Nonlinear analysis of a minimum model

To have a first comprehension of the dynamics of the full system, a nonlinear analysis of a minimum subset of its equations is performed. Here an analytical treatment is intended. As specified in Sec. 4.2.2, the dynamics of Eq (4.94), Eq (4.95) and Eq (4.96) does not have any feedback on the main dynamics dictated by the coupling between potential fluctuation (Eq (4.91)) pressure fluctuation (Eq (4.92)) and background pressure gradient (Eq (4.93)). The fluctuation induced by the phase velocity of the mode is neglected for the present treatment, and the study is focused in the origin of the reference frame of Fig. 4.3(b), where therefore $\xi(t) = \Re\left(\widetilde{\phi}(t)\right) = 0$ and $\beta(t) = \Im\left(\widetilde{p}(t)\right) = 0\ \forall t$.

5.1.1 Dynamics of the minimum model

The minimum nonlinear model isolated from the complete 0D interchange model reads

$$\dot{\delta} = a\ \alpha - b\delta \tag{5.1}$$

$$\dot{\alpha} = c\ (z - d)\ \delta \tag{5.2}$$

$$\dot{z} = h - e\ \alpha\ \delta - f\ z, \tag{5.3}$$

where $\alpha = \Re\ (\widetilde{p})$ and $\delta = \Im\ (\widetilde{\phi})$, which are positive at the origin of the reference frame of Fig. 4.3(b) for the considered mode while z is the dimensionless pressure gradient at the pedestal. In the equations, a, b, c, d, e and f can be easily obtained from the coefficients of the equations in Sec. 4.2.4 but their expression is not fundamenal for the subsequent nonlinear analysis. The heating power h is treated as a control parameter for the system and the solution depends on its value. The dynamics can be explained as follows. The variables are evaluated at the outer midplane of a toroidally confined plasma, in the pedestal region, coupled to the core plasma via h only. The heating power h in Eq (5.3) was inserted in the same way as in the models presented in Sec. 3.1. This is the flux of energy (particles) from the core determining the gradient steepening at the edge. The last term f on the RHS of Eq (5.3) is responsible for neoclassical Pfirsch-Schlüter transport. The pressure gradient dynamics equation has also an anomalous transport term ($e\ \alpha\ \delta$). This is effective only when the fluctuation level grows. The dynamics of the fluctuation is driven by the gradient, which is the source of free energy for a pressure-driven instability to develop when it overcomes the threshold value for the interchange

instability, the term $d \equiv \omega_B$ in Eq (5.2), which is purely a curvature effect. The free energy is transferred to the pressure fluctuation along the rational flux surface considered. The interchange mechanism, defined by $\mathcal{K} = \omega_B \partial_y$, drives a potential fluctuation (see Eq (5.1)) along the same flux surface as in Fig. 4.3(b). The growth of the amplitude must overcome the dissipation due to the turbulent cascade given by $b \equiv \gamma'_D$ to actually grow. Only at this point the transport due to the fluctuation can act strongly on the pressure gradient: the MHD activity of the mode causes the collapse of the edge pressure gradient. Eventually, the instability lacks its drive, while the dissipation induced by γ_D damps the fluctuation level to zero.

The analogies with the ELMs cycles presented in the models of [58] and [54] described in Sec. 3.1 are evident:

- All the models present a critical pressure gradient to overcome for the instability to develop.
- All the models feature a contribution from classical and anomalous transport in their equations for the pressure gradient.
- All the models treat the heating power h as a control parameter for different type of dynamics.

But at the same time:

- Differently from [58], the gradient collapses because of transport due to pressure-potential coupling and not magnetic fluctuation only.
- Differently from [54], there is no evolution of turbulence intensity (treated as fixed in γ_D) nor feedback of the zonal flows on the amplitude of the fluctuation in pressure and density.

This minimum set of equation can show interesting characteristics from the dynamics point of view.

Similarily to the the study of different models presented in 3.1, a nonlinear analysis of the stability of the fixed points of the nonlinear minimum system of Eq (5.1)-(5.3) is performed, to understand the fundamental dynamics.

5.1.2 Fixed points

The fixed point of an autonomous[1] dynamical system $\dot{\boldsymbol{x}} = f(\boldsymbol{x})$ are the points $\boldsymbol{x}_0$ such that $f(\boldsymbol{x}_0) = 0 \ \forall t \in \mathbb{R}$. To find the fixed point P :

[1] an autonomous dynamical system is a dynamical system $\dot{\boldsymbol{x}} = f(\boldsymbol{x})$ where f has no explicit dependence on time

$(\delta_0, \alpha_0, z_0)$ of the minimum subset, it is sufficient to solve

$$0 = a\alpha_0 \; - \; b\delta_0, \tag{5.4}$$
$$0 = c(z_0 - d)\; \delta_0, \tag{5.5}$$
$$0 = h - e\; \alpha_0\delta_0 - f\; z_0. \tag{5.6}$$

Three solutions are easily found

$$P_1 : (0, 0, h/f), \quad P_{2,3} : (\pm a/b\sqrt{(h - fd)b/ea}\;\; , \;\; \pm\sqrt{(h - fd)b/ea}\;\; , \;\; d) \tag{5.7}$$

where noticeably, $P_{2,3}$ exist as real solutions only for $h > fd$.

For the subsequent analysis, the coordinates system (δ, α, z) is moved in P_1 such that $z \to z + h/f$. The system becomes

$$\dot{\delta} = a\alpha \; - \; b\delta, \tag{5.8}$$
$$\dot{\alpha} = c(z + (h/f - d))\; \delta, \tag{5.9}$$
$$\dot{z} = -e\; \alpha\delta - f\; z. \tag{5.10}$$

and the origin $(0, 0, 0)$ is now a fixed point. It is interesting to notice that the system shows strong analogies to the Lorenz attractor [73] that presents a set of three quadratic ordinary differential equations representing e.g. three modes (x, y, z) of the Oberbeck-Boussinesq equations for fluid convection in a 2D layer heated from below. The Lorenz equations read

$$\dot{x} = \sigma(y - x), \tag{5.11}$$
$$\dot{y} = ((\rho + 1) - z)\; x - y, \tag{5.12}$$
$$\dot{z} = x\; y - \beta z, \tag{5.13}$$

where σ and β are positive constants while ρ is the control parameter of the system, with $\rho + 1$ representing the Rayleigh number. Summarizing the behavior of the solutions of the Lorenz system is interesting since one could expect an analogous dynamics of the presented minimum equations decribing the plasma edge. The Lorenz system has two fixed points P_1'=(0,0,0) and $P_{2,3}' = (\pm\sqrt{\beta\rho}\;, \; \pm\sqrt{\beta\rho}\;, \; \rho)$. By $\rho = 0$ the system undergoes a pitchfork bifurcation: $P_{2,3}'$ become real and are found to be stable, while the origin, a stable fixed point for $\rho < 0$, becomes unstable[2]. Over $\rho = \sigma(\sigma + \beta + 3)/(\sigma - \beta - 1) - 1$, the system undergoes a subcritical Hopf-Andronov bifurcation: an unstable limit cycle closes on P_2' and one

[2]definition of stability and bifurcation are given in detail in Sec. 5.1.4

closes on P_3' turning them unstable. The main feature of the system at this point is the appearance of a fully chaotic [42] behavior.

The difference in the minimum system lies in a series of different signs and in the absence of a term analogous to $-y$. This will change some features of dynamical behavior with respect to the Lorenz system. Nevertheless it is justified to expect some similarities in the bifurcations.

5.1.3 Stability analysis

The concept of Lyapunov stability for a fixed point $\boldsymbol{x}_0$ of a dynamical system $\dot{\boldsymbol{x}} = f(\boldsymbol{x})$ is now introduced.

Definition 5.1.1. Lyapunov stability
$\boldsymbol{x}_0$ is Lyapunov stable if $\forall t_0, \forall \epsilon > 0\ \exists \delta = \delta(t_0, \epsilon) > 0$ such that $\forall \boldsymbol{x}(t = 0)$with $|\boldsymbol{x}(t = 0) - \boldsymbol{x}_0| \leq \delta \Rightarrow |\boldsymbol{x}(t) - \boldsymbol{x}_0| \leq \epsilon, \forall t$

which is a general definition of stability. A fixed point of a linear system is instead considered stable simply when $\Re(\lambda_j) < 0\ \forall j$ where $j = 1 \dots n$ covers all the eigenvalues λ_j of the system. The stability analysis starts from the linearization of the system. Defining the linearized form of $\dot{\boldsymbol{x}} = f(\boldsymbol{x})$ by a generic point P as $\dot{\boldsymbol{x}} = Df(\boldsymbol{x})|_P\ \boldsymbol{x}$ it is possible to write for the considered system

$$Df(\boldsymbol{x}) = \begin{bmatrix} \partial\dot{\delta}/\partial\delta & \partial\dot{\delta}/\partial\alpha & \partial\dot{\delta}/\partial z \\ \partial\dot{\alpha}/\partial\delta & \partial\dot{\alpha}/\partial\alpha & \partial\dot{\alpha}/\partial z \\ \partial\dot{z}/\partial\delta & \partial\dot{z}/\partial\alpha & \partial\dot{z}/\partial z \end{bmatrix} = \begin{bmatrix} -b & a & 0 \\ c(z + h/f - d) & 0 & c\delta \\ -e\alpha & -e\delta & -f \end{bmatrix}. \tag{5.14}$$

Stability of P_1

In order to study the stability of P_1, the Jacobian matrix is evaluated as

$$Df(\boldsymbol{x})|_{P_1} = \begin{bmatrix} -b & a & 0 \\ c(h/f - d) & 0 & 0 \\ 0 & 0 & -f \end{bmatrix}, \tag{5.15}$$

and therefore the eigenvalues can be evaluated from $\chi(\lambda) = 0$ where $\chi(\lambda)$ is the *characteristic polynomial* of the matrix. The equation reads

$$\chi(\lambda) = \lambda^3 + \lambda^2(b + f) - \lambda(\eta a - fb) - f\eta a = 0, \tag{5.16}$$

where $\eta = c(h/f - d)$. In order to analyze the eigenvalues of the linearized matrix of the dynamical system to determine the stability, the Routh-Hurwitz criterion is introduced.

Theorem 5.1.1. Routh-Hurwitz criterion
Given a finite polynomial $p(\lambda) = a_n\lambda^n + a_{n-a}\lambda^{n-1} + \ldots + a_1\lambda^1 + a_0$, where a_j with $j = 0 \ldots n$ are real coefficients and $a_n > 0$, then the solutions λ_j of $p(\lambda) = 0$ have $\Re(\lambda_j) < 0 \ \forall j \iff R_j > 0 \ \forall j$ where the Routh determinant R_i is defined as

$$R_i = \begin{vmatrix} a_1 & a_0 & 0 & \ldots & & 0 \\ a_3 & a_2 & a_1 & \ldots & & 0 \\ a_5 & a_4 & a_3 & \ldots & & 0 \\ \vdots & & & \ddots & & \vdots \\ 0 & \ldots & 0 & a_i & a_{i-1} & a_{i-2} \\ 0 & \ldots & 0 & 0 & 0 & a_i \end{vmatrix}. \tag{5.17}$$

Corollary 5.1.1.1. If $\Re(\lambda_j) < 0 \ \forall j \Rightarrow a_j > 0 \ \forall j$.

whose proof can be found in [74]. This criterion, from now on referred to as the *RH criterion*, allows to define the sign of the eigenvectors of the characteristic polynomial, without solving directly $\chi(\lambda) = 0$ for λ, allowing to treat it as a necessary and sufficient condition to determine the linear stability of a fixed point. Furthermore, the corollary provides a sufficient condition to determine the lack of stability, whenever a coefficient is negative. When $\Re(\lambda_j) < 0 \ \forall j$ holds, the Hartman-Grobman theorem applies.

Theorem 5.1.2 (Hartman-Grobman theorem)**.** [42]
If $Df(\boldsymbol{x})|_{\boldsymbol{x}_0}$ has no zero or purely imaginary eigenvalues, then there is a homeomorphism h defined on some neighborhood U of $\boldsymbol{x}_0$ in $\mathbb{R}^n$ locally taking orbits of the nonlinear flow of $\dot{\boldsymbol{x}} = f(\boldsymbol{x})$ to those of the linear flow of $\dot{\boldsymbol{x}} = Df(\boldsymbol{x})|_{\boldsymbol{x}_0} \ \boldsymbol{x}$. The homeomorphism preserves the sense of orbits and can also be chosen to preserve parametrization by time.

This means, for the present purpose, that when $Df(\boldsymbol{x})|_{\boldsymbol{x}_0}$ has no eigenvalues with zero real part (in this case $\boldsymbol{x}_0$ is defined as an *hyperbolic* fixed point), then the stability of the solutions near to $\boldsymbol{x}_0$ is determined by the linearization also for the complete nonlinear system, i.e. the Lyapunov stability is determined. Therefore, when the RH criterion holds, the asymptotic stability of the fixed point is proven.

Applying this to the stability analysis of P_1 requires to define the Routh determinants R_i. These are, for a third order polynomial,

$$R_0 = a_0, \quad R_1 = a_1, \quad R_2 = a_1a_2 - a_0a_3, \quad R_3 = a_3R_2, \tag{5.18}$$

and therefore, since for $\chi(\lambda)$ there is $a_3 = 1$, the RH criterion is satisfied for

$$\begin{cases} a_0 > 0 \\ a_1 > 0 \\ a_1 a_2 - a_0 a_3 > 0 \end{cases} \Rightarrow \begin{cases} -f\eta a > 0 \\ fb - \eta a > 0 \\ fb^2 + f^2 b - \eta ab > 0. \end{cases} \tag{5.19}$$

The system 5.19 implies a condition on the sign of η, since all the other coefficients are assumed positive. When $\eta < 0$ the RH criterion is satisfied and P_1 is asymptotically stable. On the contrary, when $\eta > 0$, the fixed point P_1 becomes unstable.

Therefore, the marginal stability of P_1 is determined by a the condition $\eta = 0$, that turns out to be a condition on the heating power of the system h from the definition of η

$$P_1 \text{ is asymptotically stable } \iff h < fd \equiv h_{cr1}. \tag{5.20}$$

Stability of P_2

It is observed that, for $h > h_{cr1}$, then $P_{2,3} \in \mathbb{R}^3$ (see Eq (5.7)). The stability of P_2 is studied with the same approach. Only the positive P_2 needs to be explicitly studied, since the results are valid for symmetry arguments also for the negative P_3. The linearized matrix of the dynamical system evaluated in the positive solution P_2 reads

$$Df(\boldsymbol{x})|_{P_2} = \begin{bmatrix} -b & a & 0 \\ 0 & 0 & (ac/b)\ \alpha_0 \\ -e\ \alpha_0 & -(ea/b)\ \alpha_0 & -f \end{bmatrix}, \tag{5.21}$$

where the evaluation of P_2 leads to $\alpha_0 = \sqrt{(fb/ea)\eta}$. The corresponding characteristic polynomial is

$$\chi(\lambda) = \lambda^3 + \lambda^2(b+f) + \lambda\left[bf + (a^2ec/b^2)\alpha_0\right] + 2(a^2ec/b)\alpha_0^2. \tag{5.22}$$

Therefore, testing the RH condition, considering again that $a_3 = 1$, a condition for the asymptotic stability is found such that

$$\begin{cases} a_0 > 0 \\ a_1 > 0 \\ a_1 a_2 - a_0 a_3 > 0 \end{cases} \Rightarrow \begin{cases} \text{(always true)} \\ \text{(always true)} \\ -\alpha_0^2 \frac{eca^2}{b}\left(1 - \frac{f}{b}\right) + b^2 f + bf^2 > 0 \end{cases}, \tag{5.23}$$

where, substituting the computed value of α_0, a condition on the heating power h is found:

$$P_2 \text{ is asympt. stable } \iff h < fd + \frac{bf^2 + b^2 f}{ac(1 - f/b)} \equiv h_{cr2}. \tag{5.24}$$

5.1.4 Bifurcation of equilibria

As the parameters of the minimum system Eq (5.1)-(5.3) are varied, changes occur in the qualitative structure of the solutions, i.e. the fixed points of the system change their stability characteristics. These changes are called *bifurcations* and the parameters value determining the appearance of these bifurcations are called *critical* or *bifurcation values*. Since the equilibrium is studied close to the fixed point, the bifurcations presented here are local. The term "bifurcation" was originally used by Poincaré [42] to describe the "splitting" of equilibrium solutions in a family of differential equations $\dot{\boldsymbol{x}} = f_\mu(\boldsymbol{x})$, where the pedex μ is the bifurcation parameter that, once varied, determines the appearance of the bifurcation. It is shown that the equilibria are described by smooth functions of μ close to the point where μ_{cr} implies the presence of a zero eigenvalue. The change of the eigenvalue of the system from $\Re(\lambda_j) < 0$ to $\Re(\lambda_j) > 0$ is exactly what determines the change of the equilibria.

In this section, only a qualitative treatment is intended. The objective of this treatment is to identify the bifurcation type to justify the observed behavior of the system and therefore try to motivate the observed transition of LCOs into ELMs during the I-phase. In the numerical analysis in Sec. 5.2.2, the *bifurcation diagrams* will be drawn. These are the loci in the $(\boldsymbol{x}, \mu)$ product space of parts of the invariant set of the dynamical system $\dot{\boldsymbol{x}} = f_\mu(\boldsymbol{x})$. The different *branches* of equilibrium appearing in these graphs are not merely fixed points, but can also be *periodic orbits*. In particular, the definition of an stable periodic orbit, is given.

Definition 5.1.2. Stable periodic orbit
A closed curve $\mathcal{C}$ with no critical points is a stable periodic orbit for $\dot{\boldsymbol{x}} = f_\mu(\boldsymbol{x})$ in $\mathbb{R}^n$, if there exist an open set B containing $\mathcal{C}$ such that $\Phi^t(B) \subset B$ for $t > 0$ and $\cap_{t>0}\Phi^t(B) = \mathcal{C}$.

Here $\Phi^t(\boldsymbol{x})$ is the flow of $f(\boldsymbol{x}(0))$ that maps $\boldsymbol{x}(0)$ in the solution of $\dot{\boldsymbol{x}} = f(\boldsymbol{x})$ after a time t. The two bifurcations appearing at h_{cr1} and h_{cr2} are now briefly discussed.

Pitchfork bifurcation

The results of 5.1.3 show that the destabilization of P_1 at h_{cr1}, defined by the violation of the RH condition, comes together with the appearence of P_2. This, for $h_{cr1} < h < h_{cr2}$ is a stable fixed point, always from the RH condition. As it was anticipated, a complete treatment is not intended

here, but it is noticed that the projection of P_2 along α evolves as

$$\alpha_0 \sim \sqrt{h}. \tag{5.25}$$

This is exactly the expected behavior for a so-called pitchfork bifurcation.

Hopf-Andronov bifurcation

For $h > h_{cr2}$, P_2 becomes unstable. Determining what happens over this critical value is important to have a complete picture of the system dynamics. It is possible to observe that

- At $h = h_{cr2}$, the characteristic polynomial $\chi(\lambda)$ admits two purely imaginary zeros $\lambda_{1,2}$ and one real zero.

Proof. A third order polynomial always admits at least one real solution. The remaining two purely imaginary solutions of $\chi(\lambda) = 0$ can be found by substituting into the polynomial $\lambda_{1,2} = \pm i\omega$. This leads to

$$-i\omega^3 - a_2\omega^2 + i\omega a_1 + a_0 = 0, \tag{5.26}$$

that has as solution

$$\begin{cases} \omega^3 = \omega a_1 \\ \omega^2 a_2 = a_0 \end{cases} \quad \Rightarrow \ \omega = \sqrt{a_1} = \sqrt{\frac{a_0}{a_2}}. \tag{5.27}$$

The definition of ω implies that

$$a_1 a_2 = a_0, \tag{5.28}$$

Which is exactly the condition to have the Routh determinant $R_2 = 0$. This is already proven to be satisfied exactly by $h = h_{cr2}$ in Eq (5.23) for P_2. □

- At $h = h_{cr2}$, the eigenvalues $\lambda_{1,2} = \pm i\omega$ crossing the imaginary axis have $\partial_h \Re(\lambda_j) \neq 0$.

Proof. Due to the RH condition, there is at least one eigenvalue crossing the imaginary axis at $h = h_{cr2}$ since P_2 becomes unstable (the real part of this eigenvalue moves from negative to positive). Having the same expression for $\lambda_{1,2}$ grants that these are the interested eigenvalues. Assuming a continuous dependence on h, it is sufficient to prove that $\Re(\lambda_j)$ has a lower-than-cubic dependence on h to prove the previous statement. From the general formula for the roots of a third order polynomial, it is straightforward to check that the highest order dependence of λ on h is $\lambda \sim \sqrt{h}$. □

Whenever the previous two statements holds, the *Hopf bifurcation theorem* (whose complete form can be found in [42]), grants that a Hopf-Andronov bifurcation occurs at $h = h_{cr2}$. The main consequence is the presence of a limit cycle solution. The coefficients of the equations determine whether an unstable limit cycle, already present for $h < h_{cr2}$ shrinks and closes on P_2 at $h = h_{cr2}$ making it unstable (a subcritical Hopf bifurcation), or if a stable limit cycle appears for $h > h_{cr2}$ spreading its amplitude with increasing h (a supercritical Hopf bifurcation). In the Lorenz attractor, the bifurcation is subcritical and no other stable solutions exists for the system but a chaotic dynamics is triggered, with the appearance of a strange attractor. As an anticipation, just from the numerical simulations it will be shown that for the system $Eq(5.8) - (5.10)$, a stable limit cycle appears. This is what happens also for the model described in 3.1.3 as it was studied in [59], that shows the appearance of a stable limit cycle following the variation of the heating power over a threshold. The Hopf bifurcation has an important meaning for the system, since it clearly shows that the dependence on the heating power determines the change of behavior from damped to oscillatory. The presence of asymptotically stable fixed points implies that trajectories starting from any initial condition close to them, tend to reach the stable solution in a certain time. The presence of a stable limit cycle, instead, defines a stable oscillatory solution that is maintained over time. The interesting part for the scope of this thesis will be to show how an initial condition close to an unstable fixed point goes through a transitory period while reaching the attractive limit cycle. For this, numerical simulations are required.

5.2 Simulation of the minimum model

The aim of this section is to explain with the aid of numerical simulations the dynamics of the minimum model isolated in Sec. 5.1.

5.2.1 Parameters range

The choice of the parameters a, b, c, d, e and f is performed in order to enlighten the dynamics in the most clear way through the aid of simulations. These do not necessarily reflect typical plasma edge parameters, which will be discussed in Sec. 5.3.

One constrain derives from the fact that it is possible to obtain second order equations from the system, deriving Eq (5.1) in time and inserting

Eq (5.2) to obtain

$$\ddot{\delta} = a\ c(z-d)\delta\ -\ b\ \dot{\delta}, \tag{5.29}$$

which has exactly the same structure of Eq (3.15) for the plasma perturbation, although treating different quantities. For $z > d$ the solution is a growing exponential. For $z < d$, the equation is the classical damped harmonic oscillator described by

$$\ddot{x} = -\omega_0^2\ x\ -2\xi'\omega_0\dot{x}, \tag{5.30}$$

with ω_0 and ξ' real parameters. To be consistent with the models of [54] and [58], where the fluctuation are observed to decay, as they lack their drive, without oscillating around zero, the free parameter $b = \gamma'_D$ is chosen such that the system is an overdamped harmonic oscillator. Analytically, this simply means $\xi' > 1$. To be conservative, a maximum $z_{max} = 2d$ is fixed. Therefore, it is possible to obtain from the comparison of Eq (5.29) and Eq (5.30), a condition on the relative value of b as a function of the other parameters for the desired overdamped behavior.

$$\xi' = \frac{b}{2\sqrt{a\,c\,(z_{max}-d)}} > 1 \quad \Rightarrow \quad b > b_{cr} = 2\sqrt{a\,c\,d}. \tag{5.31}$$

The chosen parameters for the simulations performed in this section are $a = 2$, $c = 0.5$, $d = 1$, $e = 1$ and $f = 0.001$. This gives rise to $b_{cr} = 2$. Consequently, $b = 2.01 > b_{cr}$ is adopted. The evaluation of the critical heating power from Eq (5.20) and Eq (5.24) leads to $h_{cr1} = 0.001$ and $h_{cr2} \approx 0.005044$. The control parameter h is instead specified for the single simulations.

5.2.2 Classification of the dynamics

As it was derived analytically in Sec. 5.1, the stability of the fixed points variates with h. This can be summarized as follows.

The same information is contained in the bifurcation diagram obtained directly from the numerical simulations, whose results were plotted for $t \to \infty$ and different h, in Fig. 5.1(a). In this case it is possible to observe directly the Hopf bifurcation and the appearance of the stable limit cycle for $h > h_{cr2}$, which is evident in Fig. 5.1(b), and therefore the Hopf bifurcation is supercritical. The simulations perfectly agree with the analytical results of the nonlinear analysis performed in the previous Sec. 5.1. The initial condition for the simulations is $P(0) = (0.1, 0.1, 1)$.

The different behaviors are further described in the following table.

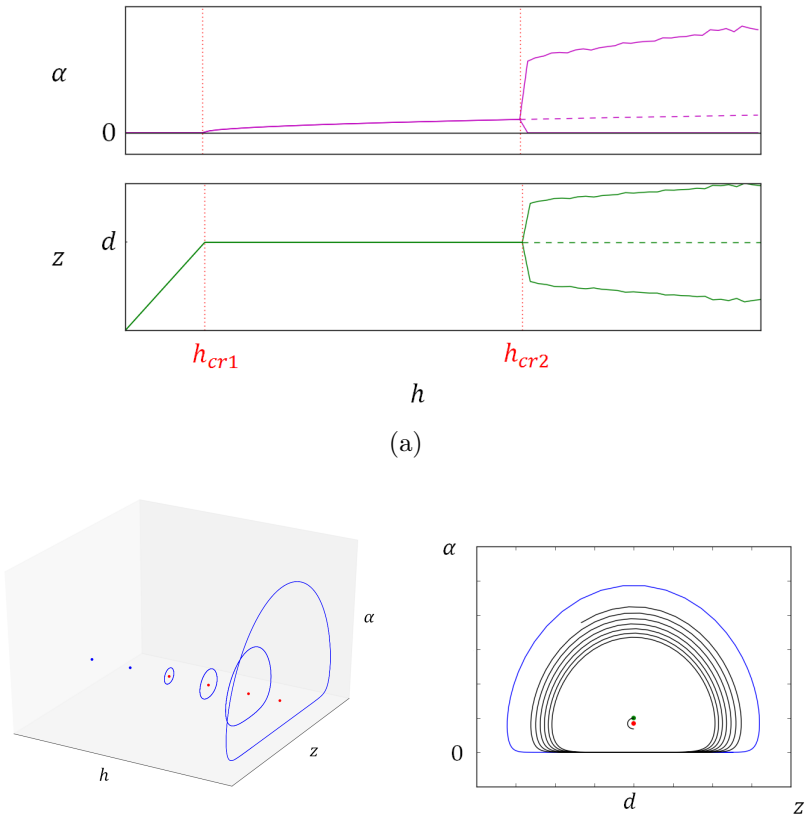

(a)

(b)

(c)

Figure 5.1: (a) Projection of the bifurcation diagram on the $h - \alpha$ subspace and $h - z$ subspace for $h \in [0, 0.008]$. Continuous lines are stable solutions and result from simulations. After the Hopf bifurcation in h_{cr2}, when a stable limit cycle appears, only maxima and minima of the limit cycle are plotted. Dashed line are the projections of the analytically derived P_2, unstable for $h > h_{cr2}$ (b) Numerical simulation of the Hopf bifurcation in the $h - z - \alpha$ space. Here $h \in [0.005039, 0.005046]$, therefore $h_{cr2} = 0.005044$ is included. Blue dots and lines are stable solutions, red dots are analytically derived unstable fixed points ($P_2 = P_2(h)$). The stable limit cycle is clearly distinguished and increases in amplitude with h. (c) The trajectory in the $z - \alpha$ phase space when $h = 0.008$ (same as in Fig. 5.2(c)). From the initial condition $P(0)$ (green dot), close to unstable P_2 (red dot), the trajectory spirals out in anticlockwise sense. For clarity, only part of the continuous trajectory is plotted. After a finite time, the trajectory reaches the limit cycle fixed for the given h (in blue).

	P_1	P_2
$0 < h < h_{cr1}$	stable	$\nexists$ real
$h_{cr1} < h < h_{cr2}$	unstable	stable
$h > h_{cr2}$	unstable	unstable

Table 5.1: Summary of the stability of the fixed points evaluated in Sec. 5.1. When both the fixed points become unstable, a stable limit cycle appears for $h > h_{cr2}$.

Stable P_1

As long as $h < h_{cr1}$, no fluctuation level is developed. All the energy introduced by h is expelled through neoclassical transport only. The stable fixed point $P_1 = (0, 0, h/f)$ is reached from any initial condition. An example can be seen in Fig. 5.2(a). This is analogous to what happens in the model described in Sec. 3.1.3 for $h < 1$, that features a subcritical Hopf bifurcation too. The stable pressure gradient $z_0 = h/f$ grows with h until it hits the critical value $d \equiv \omega_B$. Afterwards, a further increase in h allows the fluctuation level to grow and P_2 appears, characterized with constant $z_0 = d$.

Stable P_2

When $h_{cr1} < h < h_{cr1}$, the critical pressure gradient is reached and a fluctuation can develop. The fluctuation level grows monotonically with h, enhancing anomalous transport, that maintains the pressure gradient at $z_0 = \omega_B$ and does not allow it to grow with increasing h. The fixed point P_2 describes this equilibrium, which is stable and therefore reached for any initial condition close to it. The fixed point P_1 remains but it is unstable: as soon as the equilibrium is perturbed, it develops a finite level of fluctuation and the system moves oscillating to P_2 as can be seen in the example of Fig. 5.2(b).

Stable limit cycle

The most interesting state of the system for the present analysis is reached when $h \gtrsim h_{cr2}$. Both the fixed points get unstable and a stable limit cycle appears after the supercritical Hopf bifurcation. When the initial condition is taken close to P_2, the stable limit cycle is always reached after a finite time. The cyclic behavior follows the one described at the

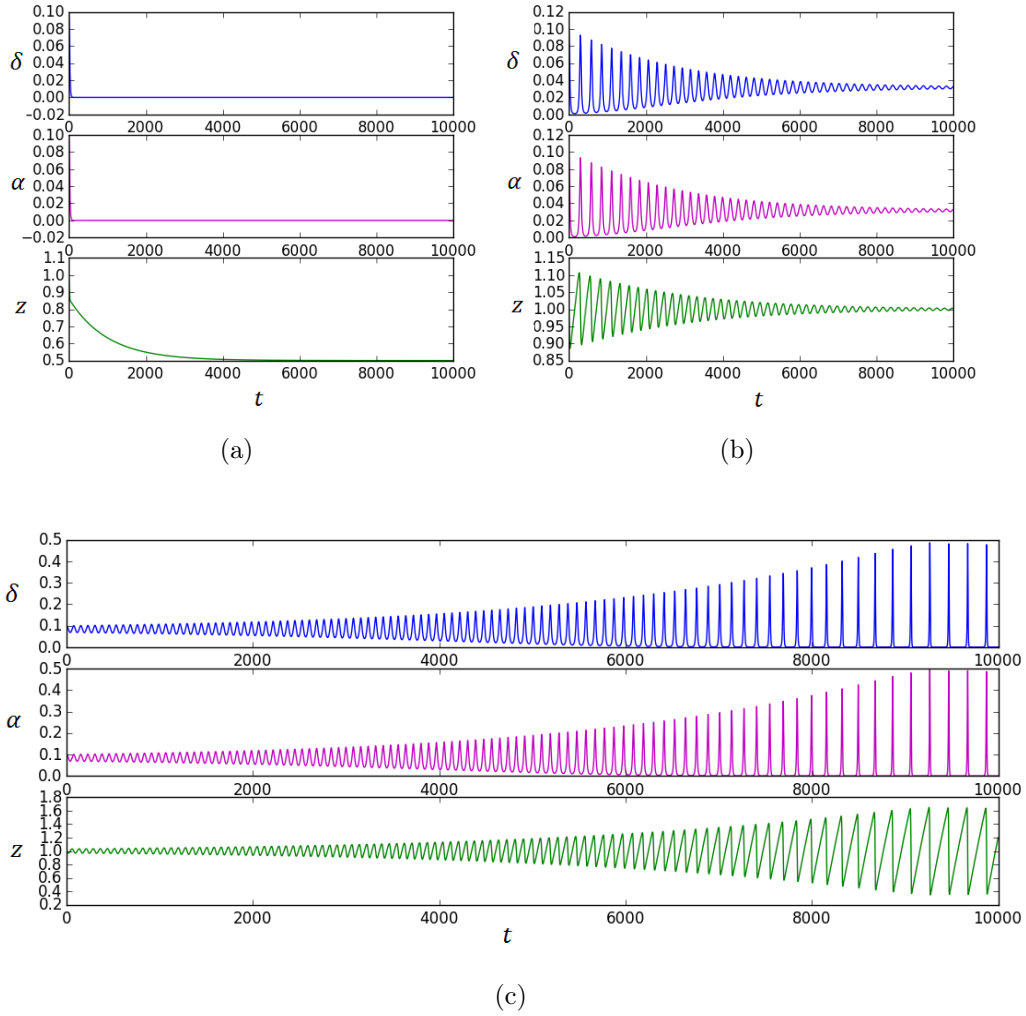

Figure 5.2: (a) The fixed point P_1, that is stable for $h < h_{cr1}$ is reached with an exponential decay. The simulation is run for $h = 0.0005$ and therefore $P_1 = (0, 0, 0.5)$. (b) The fixed point P_1 becomes unstable, while P_2 is stable for $h_{cr1} < h < h_{cr2}$. It is reached over time with a damped oscillation from the initial condition. Here $h = 0.002$ and therefore $P_2 \approx (0.0319, 0.0317, 1)$ (c) For $h > h_{cr2}$ the stable limit cycle appears. The simulation is run for $h = 0.008$. At the beginning, δ, α and z oscillate around P_2. Eventually, the behavior becomes clearly different with ELM-like spikes in δ and α while the gradient z alternates crashes and recoveries. After $t \approx 9000$ the limit cycle is reached and the amplitude of the oscillations does not grow anymore.

beginning of this section, with periodic growth of the pressure and its collapse due to an increase of MHD activity.

From the initial condition, the system follows a spiral trajectory in the phase space that can be observed in Fig. 5.1(c), while reaching the stable limit cycle. With higher h, the limit cycle is reached faster, i.e. with less oscillations, from the same initial condition. The solution is separately plot for the α, δ and z in Fig. 5.2(c). The initial small oscillations of all the variables, almost sinusoidal, pulse around the previous equilibrium and are always positive. Gradually, the MHD activity (indicated by α and δ) becomes characterized by single, isolated bursts of high intensity, separated by periods of zero level of fluctuation. The pressure gradient z, instead, alternates periods of slow growth and rapid crashes during the burst of MHD activity. During the whole simulation, the heating power h is maintained constant.

The initial, transitory period, shows features analogous to those characterizing the early I-phase as described in Sec. 2.4.2. Once the limit cycle is reached, the initial I-phase has performed a transition into ELM-like instabilities, and the oscillations do not increase in amplitude anymore. The analogies with the I-phase will be even more evident with the numerical analysis of the complete system performed in Sec. 5.3, showing the presence of LCOs. This simple, minimum 0D system of three equations Eq (5.1)-(5.3) seems to be able to reproduce the fundamental features of the dynamical transition observed in [1]. It is important to underline that, despite the control parameter defines the appearance of the limit cycle and the transition is extremely similar to the I-phase, h_{cr2} cannot be considered as the dimensionless heating power defining the transition from L- to H-mode, (called P_{LH} in Sec. 2.4). Turbulence evolution is in fact not described in this model, and its reduction at the tokamak edge inducing the transition is not covered as in the model described in Sec. 3.1.2. Furthermore, the gradient is able to steepen over the threshold defined by ω_B, but no discontinuity is defined before and after h_{cr2} in P_2: the transition is continuous, in the sense that all the equilibrium parameters are continuous function of h. A proper comparison with the experimental results is presented in Sec. 5.3 with the inclusion of the ZFs and the dynamics of the magnetic fluctuation, as well as the inclusion typical plasma parameters for the evaluation of the coefficients.

Chaotic oscillations

For $h \gg h_{cr2}$, the system starts to show chaotic nonperiodic behavior. Despite being interesting for the developed H-mode, in which the ELMs

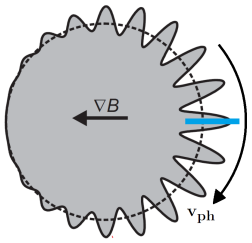

Figure 5.3: A simplified picture of a propagating ballooning mode over a flux surface. In this model, the propagation velocity of the mode contributes to the oscillations observed at the measurement point by the outer midplane, evidenced by the blue line. (adapted from [22])

cycle are characterized by a chaotic pattern in many measurement timelines, the fact that $z < 0$ for a wide range in the parameter range (among which the ones chosen for the simulations of Sec. 5.3) makes it physically not meaningful, and therefore is not further treated here.

5.3 Simulation of the complete model

In this section, selected simulations of the interchange model for the plasma described in Sec. 4.2.4 are presented and discussed. Realistic parameters are chosen for the evaluation of the coefficients, and the simulations are compared with the measured evolution of the plasma at ASDEX Upgrade during the I-phase. At the end of this section, quantitative comparison with the experimental data are suggested.

5.3.1 Dynamics of the interchange model

The introduction of the phase velocity in the interchange model requires to solve, together with the equations for the minimum model, the evolution of $\xi = \Re(\widetilde{\phi})$ (Eq (4.101)) and $\beta = \Im(\widetilde{p})$ (Eq (4.104)), since the mode now propagates along the y direction. Consequently, the vectors in the complex plane representing $\widetilde{p}$ $\widetilde{\phi}$ require to consider both the real and imaginary part. Interestingly, this does not modify the critical power that distinguishes the damped behavior and the stable limit cycle, which are still observed also for the complete model. The coupling of the remaining equations (the zonal flows Eq (4.106), the radial Eq (4.108) and poloidal Eq (4.107) magnetic fluctuations) has no effect on the fundamental dynamics and is in this sense passive. The system evolves following exactly the same behavior as the reduced system with some added features. In

a simplified but effective description, it is possible to consider the classic picture of the ballooning mode, propagating along the poloidal direction as in Fig. 5.3: when the local variables evolution is described at the outer midplane, they are observed oscillating sinusoidally. As the ELM regime is reached, oscillations due to the mode propagation are effectively observed only if the inverse of the instability growth rate is larger than the oscillation period due to the phase velocity.

5.3.2 Parameters range

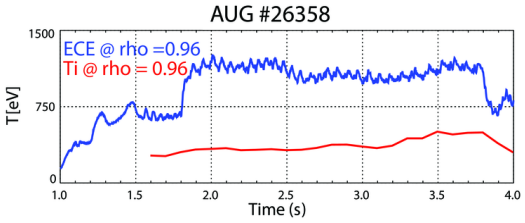

Figure 5.4: The time evolution of ions and electrons temperatures during a plasma discharge at ASDEX Upgrade at $\overline{n} \approx 1.5 \times 10^{-19} m^{-3}$. The temperature difference becomes less wide as the density increases ([75]).

The geometrical parameters of the ASDEX Upgrade tokamak [76] used in this analysis are the minor radius $a = 0.5\ m$ and the major radius $R = 1.65\ m$.

The plasma parameters chosen for the simulations are the ones typical for the plasma edge during an I-phase discharge at ASDEX Upgrade. As suggested in [66], the dimensionless resistivity is in the order of $C \approx 7.25$ and $\hat{\beta} = 2$. The damping parameter is usually small (in the mentioned paper is often set to zero), and for the present analysis is fixed to $\mu_{\parallel} = 7.7 \times 10^{-4}$. From the results of [1], the typical L-H transition are studied for a value of the line averaged density at the edge of $\overline{n} \approx 2.5 \times 10^{19} m^{-3}$. The averaged temperature at the pedestal can be estimated from the values measured with the aid of Electron Cyclotron Emission. For typical LCOs frequency f_{LCO} at the onset of the I-phase of $\approx 1kHz$ this was evaluated as $\overline{T}_e = (T_{e,100\%} + T_{e,95\%})/2 = (250 + 100)/2 = 175eV$. The toroidal field at the outer midplane by the edge is $B = 2T$. For the purpose of normalization, it is fundamental to evaluate the drift scale

$$\rho_s = \frac{(\overline{T}_e m_i)^{1/2}}{eB} = \frac{(175 \times \frac{2 \times 938 \times 10^6}{9 \times 10^{16}} \frac{eV^2}{m^2/s^2})^{1/2}}{2 \frac{eV\ s}{m^2}} \approx 10^{-3} m \tag{5.32}$$

where it was considered the conversion $1\ T = 1\ Vs/m$ and the deuterium mass $m_i = 2 \times 938 MeV/c^2$. The sound speed evaluated at the average electron temperature is

$$c_s = \sqrt{\overline{T}_e/m_i} = \sqrt{175/(2 \times 938)}\ 3 \times 10^4\ m/s \approx 10^5 m/s. \tag{5.33}$$

The experimental results that motivated this analysis are those presented in [1]. The precursors are observed to be characterized by $m \approx 15$. Consequently, this is the chosen poloidal mode number for the simulation. The corresponding dimensionless k_y can therefore be evaluated as

$$k_y = \rho_s \frac{m}{a} = 10^{-3} \frac{15}{0.5} = 0.03. \tag{5.34}$$

The characteristic length in the radial direction instead is considered to be the pedestal width Δ was evaluated as $\Delta = 0.05a$, coherently with the 1D model for the L-H transition of [43] that simulates the pedestal to expand inward from 0 to $0.1a$ during the transition. Therefore

$$k_x = \rho_s \frac{1}{0.05a} = 10^{-3} \frac{1}{0.05 \times 0.5} = 0.04. \tag{5.35}$$

At low densities, it is observed a decoupling of plasma electrons and ions temperature , such that

$$\tau_i = T_i/T_e \approx 0.3, \tag{5.36}$$

as can be observed from the timeline of Fig. 5.4. The different temperatures from those considered above are due to the fact that line averaged density is lower than the one measured in [1], but the ratio can still be considered valid. Finally, the dimensionless curvature parameter reads

$$\omega_B = \frac{a}{R} = \frac{0.5}{1.65} \approx 0.3 \tag{5.37}$$

Correction to the neoclassical transport

The neoclassical Pfrisch-Schlüter transport term in Eq (4.105) has a main role in determining the critical heating power necessary for the stable limit cycle to develop. It is evaluated, with the use of the typical parameters of the plasma edge as

$$f = C k_x^2 (\omega_B^2/2) \approx 5 \times 10^{-4}. \tag{5.38}$$

A series of simulations of the complete interchange model were not able to reproduce the results of [1] with similar features. The main issues were

- the fact that the pressure gradient z moved to negative values.
- the change of sign of α and δ also in absence of the phase velocity.
- the impossibility to reproduce the precursors observed in $\widetilde{b}_x$ due to the extremely fast dynamics of the instability.

All of these issues were analytical consequences of the general dynamics regulated by the choice of the heating power h. The heating power, in order to allow the presence of the stable limit cycle, had to be higher than the critical heating power h_{cr2}, determined by f as can be seen from Eq (5.24), which results valid also for the complete system. To determine a slower and smoother dynamics, still conserving all the terms in the various equations, a lower h was required. To maintain the stable limit cycle and reproduce correctly the ELM dynamics, a lower h_{cr2} was consequently necessary. This, in turn, was obtained artificially reducing the coefficient of the neoclassical transport term to a fixed value γ_P evaluated as

$$f \equiv \gamma_P = 1 \times 10^{-6}, \tag{5.39}$$

It should be noted that the k_x^2 dependence of f results from the second derivative of the pressure gradient, a profile effect which is of course poorly approximated by a single mode approximation. Formally, $f \equiv \gamma_P$ corresponds to the introductions of an independent parameter for the neoclassical transport. The following simulations are performed with this value for the parameter γ_P.

Damping parameter and critical heating power

In the same way as Sec. 5.2.1, the damping γ'_D is fixed to reproduce the observed dynamics during ELMs. Consider that the pressure gradient z oscillates around the critical value $d = \omega_B = 0.3$. An a posteriori check of the simulations fixed the maximum dimensionless pressure gradient for a given h to $z_{max} \approx 0.315$. The effect of the phase velocity in Eq (4.101), Eq (4.102), Eq (4.103) and Eq (4.104) is neglected for this analysis, but this has no consequence on the complete dynamics. In order to have overdamped oscillations for $\widetilde{\phi}$ and $\widetilde{p}$, the overdamping condition Eq (5.31) has to be satisfied. For the considered parameters, this implies a minimum value of γ'_D evaluated from

$$\frac{\gamma'_D}{2\sqrt{\frac{\omega_B\, k_y^2}{k_\perp^2}(z_{max} - \omega_B)}} > 1 \quad \Rightarrow \quad \gamma'_D > 0.09. \tag{5.40}$$

In a conservative approach, $\gamma'_D = 0.16$ is chosen.

Consequently, it is possible to evaluate the critical heating power h_{cr2} for the appearance of the stable limit cycle, assuming that it exists also for the complete model, which is confirmed by the numerical simulations. Its expression is considered the same as the one derived for the reduced model in Eq (5.24), although the parameters b, c, d, f are now taken from the complete interchange model. It is evaluated as

$$h_{cr2} = \gamma_P \omega_B + \frac{\gamma_P^2 \gamma'_D + \gamma_P \gamma'^2_D}{(1+\tau_i)\frac{\omega_B k_y^2}{k_\perp^2}(1-\gamma_P/\gamma_D)'} \approx 4.8 \times 10^{-7}. \tag{5.41}$$

Consequently, it is possible to evaluate P_2, the fixed point of the reduced system getting unstable for $h > h_{cr2}$. This point does not have the same meaning of a fixed point also for the complete system since, due to the presence of the phase velocity in the equations for $\widetilde{p}$ and $\widetilde{\phi}$, no fixed point can be found for the system. However, the initial condition chosen for all the following simulations for $\widetilde{p}$, $\widetilde{\phi}$ and z is a perturbation of P_2. Such a choice is motivated by the fact that the integration shows the slowest evolution of the trajectory in the phase space up to the stable limit cycle. This feature will allow to observe the transition from LCOs to ELMs. All the variables at the initial $t = 0$, not evaluated in P_2, are simply set close to zero at 10^{-6}. Finally, the heating power for the selected simulations is $h = 15 \times 10^{-7}$, implying the presence of the stable limit cycle.

Corrections to the poloidal magnetic field dynamics

The dynamics of the poloidal magnetic field fluctuation is described by Eq (4.108) that reads

$$\frac{\partial^2 \widetilde{B}_\theta}{\partial t^2} = -k_x^2 k_y (\alpha^2+\beta^2)^{1/2} (\delta^2+\xi^2)^{1/2} - \frac{k_x^2+k_y^2}{\hat{\beta}} (\widetilde{B}_\theta + C\frac{\partial \widetilde{B}_\theta}{\partial t}). \tag{5.42}$$

This equation is a forced damped harmonic oscillator. It is clear at this point that the forcing term is almost impulsive and due to the ballooned transport that causes the collapse of the edge pressure gradient. The dissipation due to the remaining terms can be considered to define either an underdamped or overdamped evolution. Comparing the homogeneous version of Eq (5.42) with the damped harmonic oscillator of Eq (5.30) it is possible to determine the behavior evaluating ξ' with the parameters described in Sec. 5.3.2, obtaining

$$\xi' = (C/2)\sqrt{(k_x^2+k_y^2)/\hat{\beta}} \approx 0.13 < 1. \tag{5.43}$$

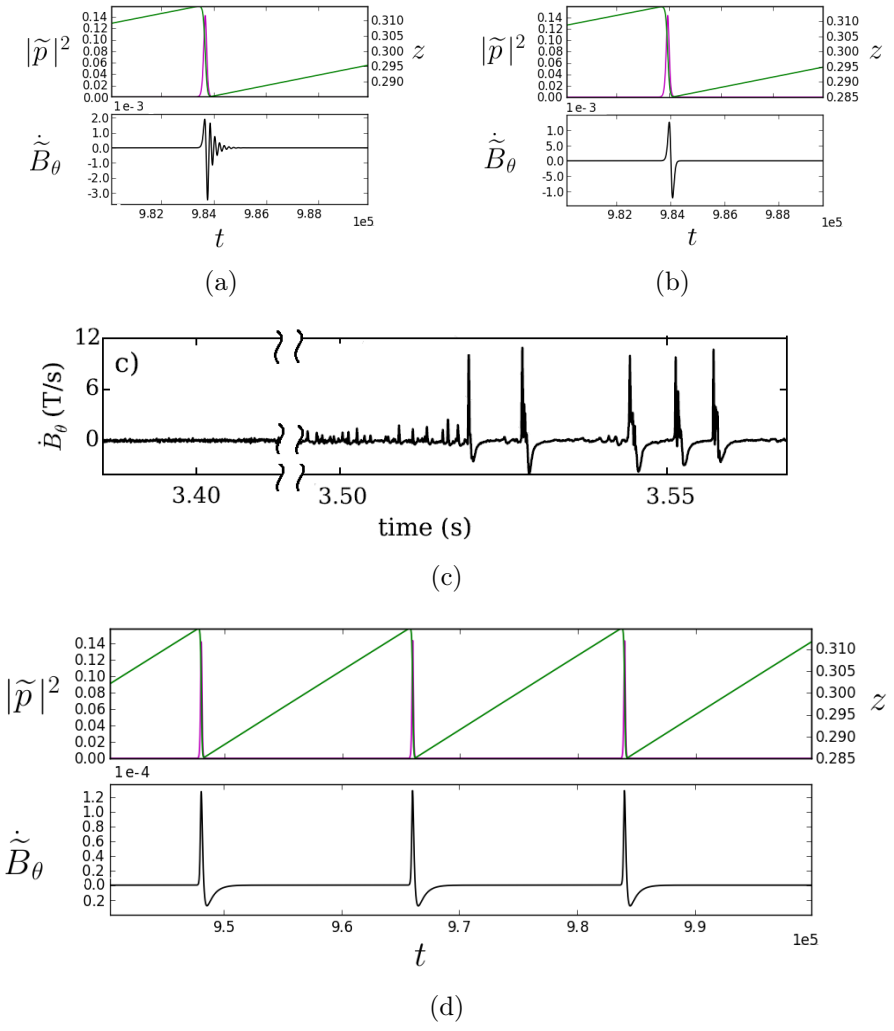

Figure 5.5: Different evolutions of $\dot{\widetilde{B}}_\theta$ following an ELM event when the stable limit cycle is already reached and there is no evolution in amplitude. The simulations are run for $h = 20 \times 10^{-7} > h_{cr2}$ considering the previously introduced parameters. (a) The simulation of the ELM event shows a drop of z (green) due to an increased MHD activity. Here the squared amplitude of $\widetilde{p}$ is plotted (purple). Following the impulsive drive due to transport, the underdamped evolution of $\widetilde{B}_\theta$ is evident from the evolution of its time derivative $\dot{\widetilde{B}}_\theta$ (black). (b) Simulation of an overdamped evolution with increased $C = 100$. The simulated behavior of $\dot{\widetilde{B}}_\theta$ is almost symmetric in the amplitude of the fluctuation above and below zero. (c) Experimental magnetic signature of the type-I ELMs (taken from Fig. 3 [1]) after the I-phase. (d) The characteristic asymmetry of the fluctuation can be reproduced assuming a weaker coupling of the $\widetilde{B}_\theta$ dynamics with the pressure gradient z dynamics, here fixing $K = 100$.

The oscillator is underdamped. This can be clearly seen in Fig. 5.5(a). No qualitative agreement is found with a comparison to the experimental results of [1], shown in Fig. 5.5(c), that, assuming that can be modeled by Eq (5.42), clearly show an overdamped behavior of the poloidal magnetic field fluctuation. Two approaches were proposed order to correct this issue.

The first approach is based on varying C. Considering a higher resistivity, it is in fact possible to obtain an overdamped oscillator for $C > 2\,(\hat{\beta}/(k_x^2 + k_y^2))^{1/2} = 56$. This still shows no qualitative agreement with the experimental results, as can be seen in Fig. 5.5(b). Furthermore, an higher C implies an increase of the Pfirsch-Schlüter transport (see Eq (5.38)) and would make the assumption of $f = \gamma_P$ less justified.

The second approach is based on considering a weaker drive of the magnetic field fluctuation from the background pressure gradient dynamics than it was evaluated during the derivation, while still considering the desired $C = 7.25$. This is obtained multiplying by a constant value $1/K$ the coupling with the background dynamics in the equation for the evolution of the poloidal magnetic fluctuation (Eq (4.71)) to get

$$\frac{\partial^2 \langle \widetilde{b}_y \sin s \rangle}{\partial t^2} = \frac{1}{K}\,\frac{\partial}{\partial t}\langle z \cos s \rangle + \frac{C}{\hat{\beta}} \nabla_\perp^2 \frac{\partial}{\partial t} \langle \widetilde{b}_y \sin s \rangle. \tag{5.44}$$

Consequently, the new equation for the poloidal magnetic fluctuation reads

$$\frac{\partial^2 \widetilde{B}_\theta}{\partial t^2} = -\frac{1}{K}\, k_x^2 k_y (\alpha^2 + \beta^2)^{1/2}\, (\delta^2 + \xi^2)^{1/2} - \frac{k_x^2 + k_y^2}{\hat{\beta}} \left(\frac{1}{K}\, \widetilde{B}_\theta \; + \; C \frac{\partial \widetilde{B}_\theta}{\partial t} \right), \tag{5.45}$$

and it was possible to force an overdamped evolution by evaluating the condition for $\xi' > 1$ leading to

$$K > \frac{4\,\hat{\beta}}{(k_x^2 + k_y^2)\, C^2} \approx 60. \tag{5.46}$$

This approach has the advantage to reproduce results that are in much better qualitative agreement with the experimental measurements, as can be seen from a comparison of Fig. 5.5(c) and Fig. 5.5(d), but the weaker coupling is not motivated physically. In the subsequent simulations, the second approach was used, fixing $K = 1000$.

In the table 5.2, the parameters considered for the subsequent results of the simulations are summarized.

h	15×10^{-7}	C	7.25
$\hat{\beta}$	2	$\mu_{\parallel}$	7.7×10^{-4}
k_y	0.03	k_x	0.04
τ_i	0.3	ω_B	0.3
γ_P	1×10^{-6}	γ'_D	0.16
K	1000.00	ϵ	0.01

Table 5.2: Summary of the parameters values used for the numerical simulation of the interchange model presented in this thesis.

5.3.3 Simulation results

The complete interchange system is solved numerically in Python, through a standard ODE solver (dopri5) that was regulated for a self-adaptive time step integration. The results of the numerical simulations are plotted for $h = 15 \times 10^{-7}$, higher than the critical $h_{cr2} \approx 4.8 \times 10^{-7}$, therefore determining the presence of the stable limit cycle.

The evolution from the initial condition of $\widetilde{\phi}$, $\widetilde{p}$ and z slowly moves from a quasi sinusoidal behavior to ELM-like oscillations. This is exactly the dynamics of the reduced model, but for the oscillations induced due to the phase velocity. Note that the dynamics of z, depending on the amplitude of the fluctuations, is not influenced by the propagation of the mode. Substituting the expression for $u^y = -\nabla p_i = \tau_i\, z$, the integrated equations are

$$\frac{\partial \xi}{\partial t} = -(1+\tau_i)\frac{k_y\,\omega_B}{k_x^2+k_y^2}\,\beta - \gamma'_D\,\xi - k_y\,\tau_i\,z\,\delta, \tag{5.47}$$

$$\frac{\partial \delta}{\partial t} = +(1+\tau_i)\frac{k_y\,\omega_B}{k_x^2+k_y^2}\,\alpha - \gamma'_D\,\delta + k_y\,\tau_i\,z\,\xi, \tag{5.48}$$

$$\frac{\partial \alpha}{\partial t} = +k_y\,(z-\omega_B)\,\delta + k_y(\omega_B\,+\,\tau_i\,z)\,\beta, \tag{5.49}$$

$$\frac{\partial \beta}{\partial t} = -k_y\,(z-\omega_B)\,\xi - k_y(\omega_B\,+\,\tau_i\,z)\,\alpha, \tag{5.50}$$

$$\frac{\partial z}{\partial t} = h - k_x^2 k_y\,(\alpha^2+\beta^2)^{1/2}\,(\delta^2+\xi^2)^{1/2} - \gamma_P\,z. \tag{5.51}$$

In the subsequent simulations, it will be often plotted $|p|^2 = \alpha^2 + \beta^2$ to describe the amplitude of the MHD activity. The zonal flow shear, included in the integration, is driven by the potential fluctuation and is damped following its dynamics.

$$\frac{\partial \langle \nabla_x v^y_{ZF}\rangle}{\partial t} = k_y k_x^3\,(\delta^2+\xi^2) - \mu_{\parallel}(\omega_B^2/2)\,\langle \nabla_x v^y_{ZF}\rangle. \tag{5.52}$$

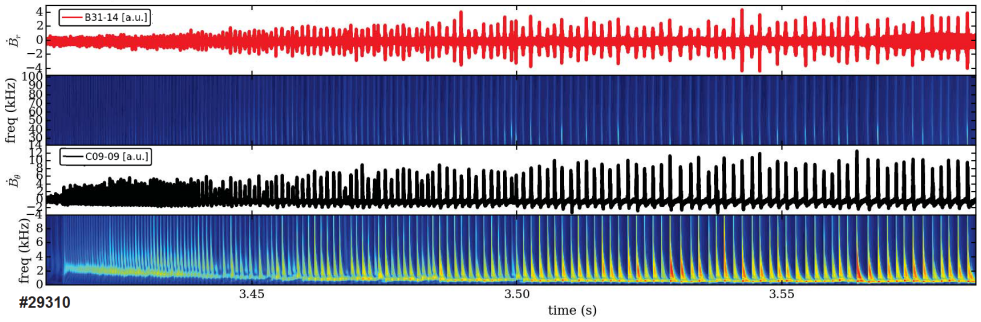

(a)

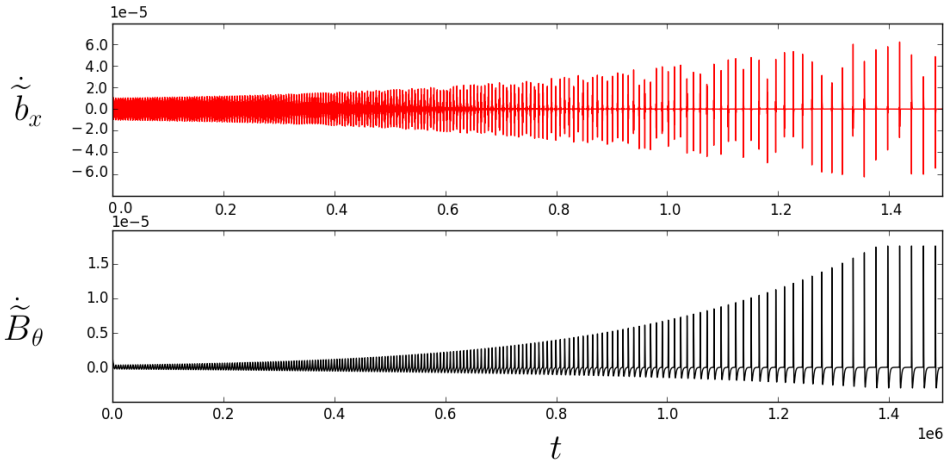

(b)

Figure 5.6: (a) The evolution of magnetic pick-up coils signal during the I-phase for shot #29310 at ASDEX Upgrade. The $\dot{B}_\theta$ signal is measured at the top of the tokamak, while the $\dot{B}_r$ signal is measured at the outer midplane [77]. (b) The smooth transition to lager spikes at lower frequency can be reproduced with good qualitative agreement for the introduced parameters with the interchange model. The fluctuations are induced following the dynamics of the reduced model described in Sec. 5.2, therefore grow until the stable limit cycle is reached. The various phases of the evolution towards the limit cycle, showing different features, are studied from this simulation.

The second order ODE for the poloidal magnetic field is split in two first order ODEs, one for $\dot{\widetilde{B}}_\theta$ and one for $\widetilde{B}_\theta$. Its drive comes from the ballooned transport.

$$\frac{\partial \widetilde{B}_\theta}{\partial t} = \dot{\widetilde{B}}_\theta, \tag{5.53}$$

$$\frac{\partial \dot{\widetilde{B}}_\theta}{\partial t} = -\frac{1}{K} k_x^2 k_y (\alpha^2+\beta^2)^{1/2} \, (\delta^2+\xi^2)^{1/2} - \frac{k_x^2+k_y^2}{\hat{\beta}} \left(\frac{1}{K} \widetilde{B}_\theta \; + \; C \dot{\widetilde{B}}_\theta \right). \tag{5.54}$$

The evaluation of $\dot{\widetilde{b}}_x$ can be calculated directly from Eq (4.107) that anyhow requires to know the expression for $\widetilde{b}_x$ and therefore to be integrated. It is straightforward to notice that its evolution results induced to the pressure and potential dynamics. The smallness term for the coupling is fixed at $\epsilon = 1/100$ but not justified formally.

$$\frac{\partial \widetilde{b}_x}{\partial t} = \epsilon k_y^2 (\alpha - \xi) - \frac{C}{\hat{\beta}} k_\perp^2 \widetilde{b}_x. \tag{5.55}$$

The result of the complete integration is now explained. The solution is evaluated from an initial condition close to P_2 for $\widetilde{p}, \widetilde{\phi}$ and z, while the other variables are set to 1×10^{-6}. The evolution of the magnetic fluctuations, shown in Fig. 5.6(b), feature an interesting qualitative agreement with the measurements of the magnetics performed in [77] and shown in Fig. 5.6(a). This is discussed in the following, evidencing three characteristic phases of the evolution towards the stable limit cycle.

Phase 1: Predator-prey like LCOs

The initial evolution of the system is plotted in Fig. 5.7(c). It is possible to observe that the squared amplitude of the pressure fluctuation oscillates around the initial value. Considering the energy cascade, this can be considered to imply a continuous, pulsating turbulence at the edge. At the same time, the ZF shear is observed to evolve following a growing, oscillating behavior. Assume that these fluctuations are periodic for a low number of cycles (the evolution to the limit cycle requires a high number of cycles). In the plot, it is evidenced how the two oscillations are characterized in this initial phase by a characteristic shift in their periodic behavior, evidenced by the dashed lines. Comparing it to the classic predator-prey model (see Fig. 5.7(a)), it is possible to observe the same feature: it seems that the ZF shear $\nabla_x \langle v^y_{ZF} \rangle$ acts like a predator for the prey $|\widetilde{p}|^2$. Note that in the model presented in Sec. 3.1.2 there is a direct cause-effect relationship between the density perturbation dynamics, representing the turbulence, and the zonal flows. In the interchange model, instead, the ZFs are driven by the potential fluctuation (see Eq (5.52)), and in turn have no feedback on the MHD dynamics. Therefore, despite the appearance, the predator prey dynamics is not involved in the interchange model presented here. Nevertheless, the presence of the characteristic delay of the ZFs allowed to associate this initial pulsing phase with the early I-phase, characterized by LCOs described in Sec. 2.4.2, that shows exactly this behavior.

Focus now on the magnetics. As described in [1] and summarized in Sec. 2.6, during the initial I-phase, oscillations at the LCOs frequency are observed in the poloidal magnetics. The radial magnetic signal, instead, shows a continuous level of fluctuation in which no clear precursor can be distinguished (Fig. 5.7(b)). The same feature can be reproduced in the initial pulses of $\dot{\widetilde{B}}_\theta$ and $\dot{\widetilde{b}}_x$. In the first, pulses with the frequency of LCOs are distinguished clearly, allowing to compare this initial phase to the experimental early I-phase.

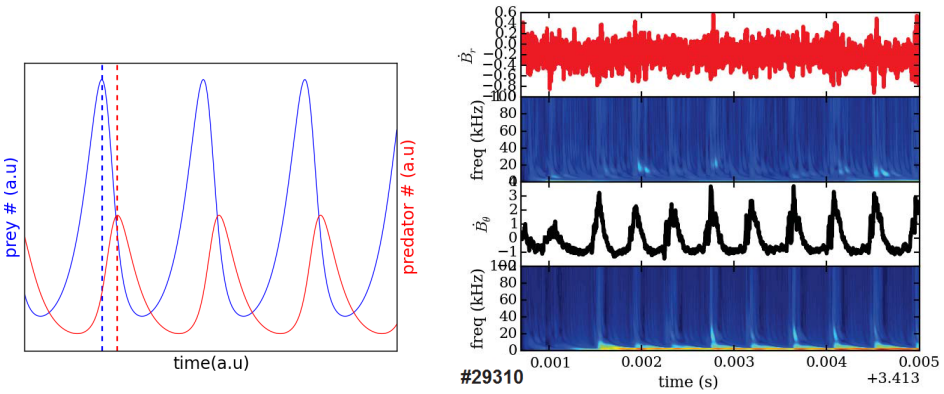

(a) (b)

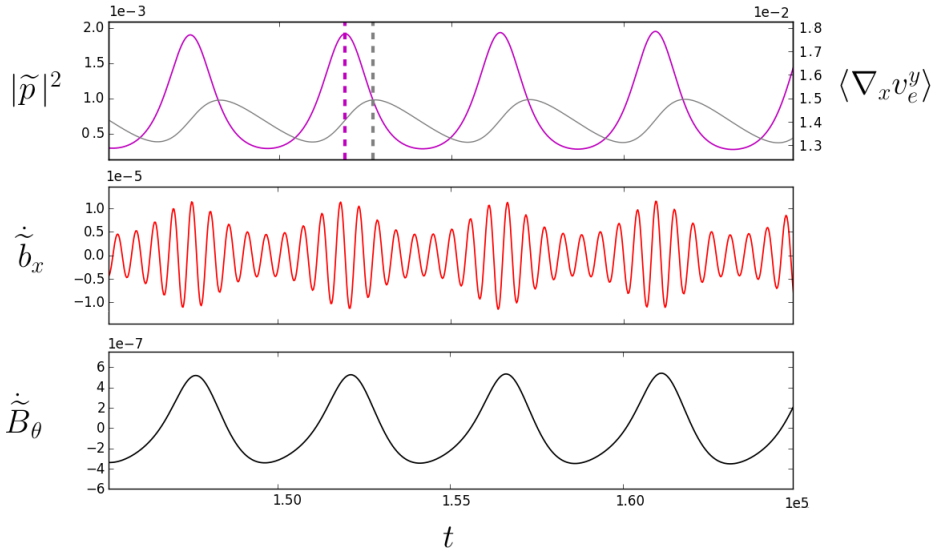

(c)

Figure 5.7: (a) The simulated predator-prey model already discussed in Fig. 3.2 is considered to reproduce the measured nonsinusioidal oscillations of the early I-phase between turbulence (prey) and zonal flow shear (predator). (b) The very first LCOs of shot #29310. No precursors are distinguished at the beginning in $\dot{B}_r$, while low amplitude oscillations are already observed in $\dot{B}_\theta$ that show most clearly the LCOs [77]. (c) In the early stage of the simulations at low $t \approx 150k$, the same characteristic shift of predator-prey models can be found in the pressure fluctuation amplitude $|\widetilde{p}|^2$ (purple) and zonal flow shear $\langle \nabla_x v_e^y \rangle$ (gray), despite predator-prey equations are not involved in the model. This identifies the LCOs. The radial magnetics $\dot{\widetilde{b}}_x$ (red), shows a continuous level of fluctuation, while the poloidal magnetics $\dot{\widetilde{B}}_\theta$ (black) already features regular oscillations at LCO frequency.

Phase 2: Type-III ELMs

During the simulation of the evolution towards the stable limit cycle, the system smoothly moves from LCOs-like to ELM-like oscillations. Pressure $\widetilde{p}$ and potential $\widetilde{\phi}$ fluctuations become characterized by single, isolated bursts of increasing amplitude and decreasing frequency that are able to induce a crash of the pressure gradient z, which then steepens again due to the energy flux from the core h. This smooth evolution is typically observed in I-phase discharges [1].

The MHD dynamics is accompanied by electromagnetic activity, in which the magnetic signature of the $\dot{B}_r$ differs significantly from the $\dot{B}_\theta$ signal. During this phase, the unstable growth and fall of the mode amplitude is slow enough to allow many oscillations due to the mode propagation to take place. These oscillations of the variables evaluated at the outer midplane are induced in the radial magnetics $\dot{\widetilde{b}}_x$ through the Ohm's law. This makes the radial magnetics characterized by an evolution in time that closely resembles the precursor activity observed in [1], which appears following the early LCO phase. The precursor is a mode getting unstable prior to the ELM crash and disappears when the pulse in the experimental $\dot{B}_\theta$ signal has reached its maximum. The simulated poloidal magnetics $\dot{\widetilde{B}}_\theta$, instead, moves from an oscillating phase to a series of growing, isolated pulses following the clearly separated ballooned transport bursts. It is therefore possible to reproduce also this feature of the I-phase as can be seen from the comparison of Fig. 5.8(a) and Fig. 5.8(b).

This dynamics of the instability is in agreement with the definition of Type-III ELMs provided in Sec. 2.5.1, since it features a precursor mode propagating in the poloidal direction and furthermore is smaller in amplitude than the ELMs observed in the later phase. Type-III ELMs in this model appear only as a transitory phase to larger ELMs. However, the instabilities studied with this model are based on the interchange mechanism that does not consider any resistive contribution, typical of Type-III ELMs. This point will be treated at the end of the present chapter. This smooth transition of LCOs into ELM-like plasma edge oscillations points to the same conclusion of [1], suggesting a common nature of the two phenomena, that can be described with the same underlying physical mechanism in this model.

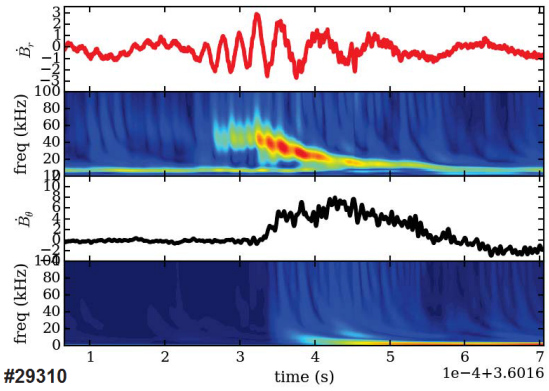

(a)

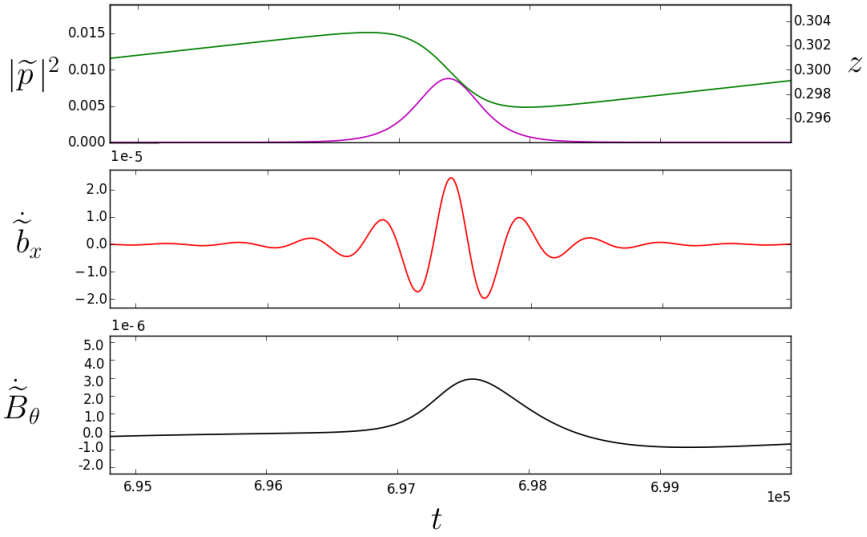

(b)

Figure 5.8: (a) A zoom into a single pulse during the I-phase of shot #29310. In the late I-phase, it is possible to clearly identify a precursor mode in $\dot{B}_r$ growing unstable prior to the $\dot{B}_\theta$ pulse indicating enhanced transport out of the LCFS. This allows to identify Type-III ELMs [77]. (b) This feature of the measurements is observed also in the simulation, during the transitory phase ($t \approx 750k$). The MHD activity, here represented by $|\widetilde{p}|^2$ (purple), becomes characterized by single, isolated bursts clearly separated that cause the collapse of the edge pressure gradient z (green). The radial magnetic fluctuation $\dot{\widetilde{b}}_r$ (red) shows a precursor mode that stops growing and disappears as the poloidal magnetics $\dot{\widetilde{B}}_\theta$ peaks following the ballooned transport.

Phase 3: Late ELMs

Once the stable limit cycle is reached, the system has moved to a stable periodic behavior (see Fig. 5.9(b)). The amplitude of the fluctuations reaches a limit and does not grow anymore. The ELM cycle is maintained: the pressure gradient z alternates long phase of growth and fast collapses due to the induced MHD activity of $\widetilde{p}$ and $\widetilde{\phi}$. The oscillations are now characterized by the highest amplitude and lowest frequency, compared to the previous phases. The electromagnetic activity induced by the instability shows interesting characteristics. The poloidal magnetic fluctuation $\dot{\widetilde{B}}_\theta$ was already shown during the previous discussion, and features a good qualitative agreement with the experimental measurements of [1] that show Type-I ELMs at the end of the I-phase. In the radial magnetic field fluctuation, no clear precursor activity can be distinguished smoothly growing and decaying. This point also agrees with the definition of Type-I ELMs. This fact is mostly due to the impulsive dynamics of the bursty crash of the ELM event. The fast growth and decay of the MHD activity, compared to the propagation velocity of the mode, do not allow many oscillations to take place during a single ELM crash. The radial magnetics is characterized by peaks during the pressure gradient collapse.

Furthermore, observing the ZF shear evolution, it is not possible anymore to distinguish clearly a predator-prey-like dynamics, with delayed oscillations in the density (pressure) amplitude and the zonal flow shear amplitude. This disappearance of the predator prey dynamics is covered also in the model described in [43], where however it moves from $\pi/2$ to π.

A feature that is not covered in this model is the irregular (chaotic) appearance of the Type-I ELMs, that characterizes the H-mode (see Fig. 5.9(a)). In particular, the ELM-free H-mode phase observed in [1] cannot be reproduced. The ELMs appear periodically at a frequency determined by h in the simulation, but fixed in amplitude as observed for the Type-I ELMs.

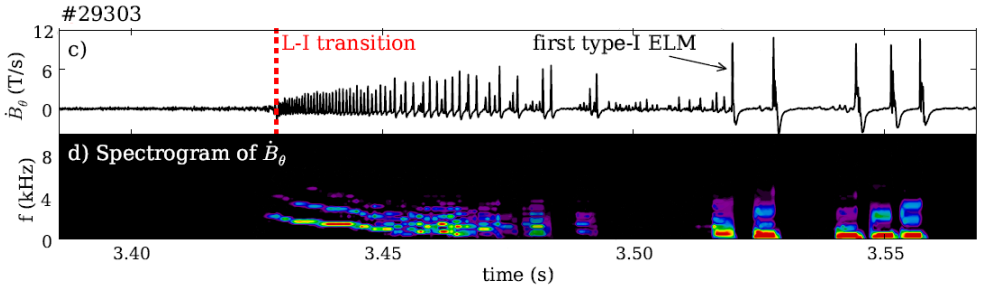

(a)

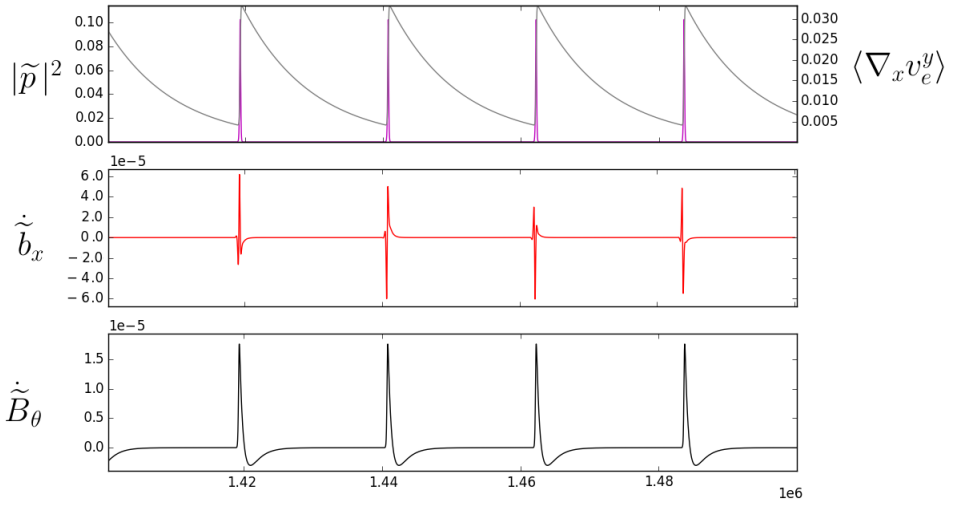

(b)

Figure 5.9: (a) The evolution of the $\dot{B}_\theta$ signal during the complete L-H transition of shot #29303 at ASDEX Upgrade. After the onset of the I-phase, LCOs smoothly move to ELM-like oscillations. The spectrogram is also plotted, showing the decreasing frequency of the oscillations more clearly. These harmonics are a unique characteristic of the I-phase that allow to identify the LCOs. The Type-I ELMs after the ELM-free H mode feature irregular bursts of fixed amplitude. (taken from Fig.3 [1]) (b) In the simulations, once the stable limit cycle is reached, the ELMs appear with fixed frequency at the maximum not growing amplitude in the poloidal magnetics $\dot{\widetilde{B}}_\theta$ (black). The radial magnetic signal does not feature a clear precursor mode in $\dot{\widetilde{b}}_x$ (red), coherently with the definition of Type-I ELMs. The intermittent appearance of the Type-I ELMs is not reproduced.

5.4 Final considerations

The presented 0D interchange model for the plasma edge dynamics during the I-phase shows good qualitative agreement with the results of the experimental measurements presented in [1]. With the right value of the heating power, the model features a transition of sinusoidal oscillations to spiked oscillations with the appearance of precursors during the evolution of the system from an unstable fixed point to a stable limit cycle. The amplitude of the fluctuations steadily increases, while the frequency decreases and the system moves from a continuous fluctuation at the edge analogous to the early I-phase to a ELM-like behavior with crashes and recoveries of the edge pressure gradient. This suggests the possibility to give a common explanation to the two phenomena, that up to now were treated separately. The fundamental mechanism appears to be the destabilization of a stable state of the plasma and the smooth transition to a new state described by a limit cycle characterized by ELM like oscillations driven by an interchange mechanism. The LCOs are intrinsic in the transition from the first to the second state.

Quantitative comparison can be performed following a complete renormalization of the DALF equations, which is not treated in this thesis. Some simple considerations are suggested in the following.

The poloidal mode number of $m \approx 15$ fits the measurements of a dominant poloidal modulation of the density with $k_\perp \approx 0.28 cm^{-1}$. In fact, in the model, $(k_y)_{SI} = m/a = 15/0.5 m^{-1} = 0.3 cm^{-1}$. The poloidal velocity can be evaluated as

$$(u^y)_{SI} = c_s \, u^y = c_s \, \tau_i \, z = 10^5 m/s \times 0.3 \times 0.3 = 9 \, km/s, \tag{5.56}$$

which results comparable with the measured $u^y \approx 12 \, km/s$ of [1]. It is possible in this way to determine the frequency of the precursors for this mode propagating along the poloidal direction with u^y, as it would be observed with the measurement in a single point. It results

$$f_{prec} = m \frac{(u^y)_{SI}}{2\pi a} = 15 \frac{9 km/s}{2\pi \times 0.5 \, m} \approx 43 kHz, \tag{5.57}$$

which agrees with the measured range for the observed precursors of the type-III ELMs that lies between 40 to $90 kHz$ in [1].

A rough evaluation for the LCOs frequency during the early simulated I-phase can be performed from Fig. 5.7(c). Here it is possible to observe that in the initial periodical phase, the frequency of the fluctuation in the radial magnetics is around 10 times higher than the frequency of the

simulated poloidal magnetics that defines the LCOs. Therefore $f_{LCOs} \approx 4kHz$, which is in the same order of magnitude of the modulation of the early LCOs of 0.5 to $5kHz$ observed at ASDEX Upgrade, as described in [1]. Note that the determination of the LCO frequency cannot be performed quantitatively from the nonlinear reduced model of Sec. 5.1, since it is not possible to determine analitically the frequency of the first cycles of the transitory behavior plotted in Fig. 5.1(c).

The model also agrees with the experimental observation of [1] that at higher heating power, less LCOs are found in the experimental measurements. In fact, with increasing h over h_{cr2}, the stable limit cycle is reached faster and with less oscillations.

The model, of course, has however a series of limitations that are briefly discussed here. Despite showing an ELM-like oscillations as the limit cycle is reached, the underlying physical mechanism relies on the interchange instability only. This means that the complete ELM cycle based on the coupled peeling-ballooning mode getting unstable as described in Sec. 2.5 is covered just for the ballooning part. This is due to the lack of any parallel dynamics that could include the evolution of the parallel current required for the peeling dynamics. This makes the model more suitable to describe Type-I ELMs than Type-III ELMs, as it does not consider resistive current driven instabilities. Finally it is possible to observe that $\partial f_{ELMs}/\partial h > 0$ for this model, that does not agree with the definition of Type-III ELMs. Furthermore, the description of the precursors is not complete also qualitatively, since it is observed a drop in the frequency of the precursor after the crash of the pressure gradient. In the present treatment, instead, the frequency of the fluctuations induced by the mode propagation stays almost constant along the whole simulation and the frequency drop of the precursors is not found. Finally, the model, despite being integrated for typical I-phase plasma parameters, does not aim to explain the L-H transition triggering, since it does not include any treatment for the edge plasma turbulence as the ones presented in Sec. 3.1.1 and Sec. 3.1.2. This does not allow to treat the critical heating power h_{cr2} as the critical heating power for the L-H transition P_{LH}.

In the next Chapter 6, a series of conclusions are made about the presented model. The predictive capability is discussed and possible integrations addressed to future works are considered.

Chapter 6

Conclusions

The aim of this final chapter is to draw the conclusions of the presented thesis and to suggest a series of issues for future works.

The H-mode of operation of a toroidally confined plasma is the candidate regime to realize a steady-state of operation in ITER, due to its improved confinement properties, with the purpose of showing the possibility to obtain a net gain of energy from thermonuclear fusion reactions.

Despite its paramount importance for fusion research, the comprehension of this mode of operation is nowadays still an open issue in plasma physics. In particular, the evolution of the L-mode to the H-mode is not yet fully understood (Sec. 2.7). During the I-phase the intermediate state between L- and H-mode, a series of periodical oscillations at the plasma edge are observed [1] to evolve from a low amplitude pulsating state, the limit cycle oscillations (LCOs), to macroscopic instabilities called edge localized modes (ELMs), able to degrade the confinement but also to expel impurities.

The 0D interchange model for the plasma edge oscillations presented in this thesis (Sec. 4.2.4) aims to provide a simplified analysis of this transition observed in various tokamaks, that was not covered up to now. The model was derived following a series of assumptions (Sec. 4.2.1) from the Drift-Alfvén equations (Sec. 3.2.2), therefore being based on first principles. Its numerical integration (Sec. 5.3.3) shows a good qualitative agreement with a series experimental results obtained at ASDEX Upgrade, being able to reproduce the evolution from an oscillating, transitory state resembling the LCOs to a stable state characterized by ELM-like oscillations. This is a consequence of the nonlinear structure of the equations of the model (Sec. 5.1 and 5.2), that allows this kind of transition with the destabilization of an MHD mode at the plasma edge, following the variation of the parameter representing the external heating power, and in

this sense agrees with a series of existing heuristic models for the plasma edge (Sec. 3.1). The results of the simulations of the model, performed with realistic parameters for the plasma edge in a tokamak, suggests that the LCOs and the ELMs can be in principle be explained from the same fundamental physical mechanism.

From the results of this analysis, further developments of the presented model are suggested for future works.

In the presented simulations, only a periodic evolution of the system is considered. The model, however, can also show a chaotic state, due to the nonlinear structure of its equations. This could allow to suggest an explanation also for the irregular intermittent appearance of ELMs during the H-mode, but requires a careful choice of the parameters to avoid unrealistic evolution of the considered variables.

A complete quantitative comparison with the experimental results is in principle possible, since the system is derived from fundamental equations. This would require a renormalization of the dimensionless variables that was not performed in the presented work.

The model does not include a description of turbulence evolution at the edge, despite it has a leading role in the instability dynamics. This is due to the fact that only the evolution of a single mode is considered. The turbulence is observed to be suppressed at the L-H transition and therefore its implementation, also in a 0D model, could provide a more complete explanation for the transition itself, considering in particular the feedback of turbulence driven zonal flows, possibly introducing a predator-prey dynamics. Furthermore, the inclusion of this feature would have a direct influence on the anomalous transport, in the model considered only due to MHD modes.

Finally, the model, being zero-dimensional, in intrinsically simple and cannot provide a complete physical description of the phenomena of interest. The implementation of a 1D model is in principle possible, since it is derived from the DALF equations. This would allow to include profile effects in the description, due to the evolution of the pressure profile at the edge. In particular, the bootstrap current could be included. This toroidal plasma current at the edge is a phenomenon arising from neoclassical effects, due to collisional exchange of momentum between trapped and passing particles, and it is observed to be related to the edge pressure profile. Its implementation in the model would allow to include a current driven mode to the overall dynamics, introducing resistive effects. This would induce a self-consistent peeling-ballooning instability, coherent to the current picture of ELMs. However, this requires to include neoclassical effects not considered in the DALF equations.

Appendix A

Quasineutrality

The widely used assumption of quasineutrality is derived as in [29]. A background density n_0 in a single charged plasma is assumed, and a perturbation $\delta n = \delta n_i + \delta n_e$ to it is considered such that Boltzmann relation holds

$$\frac{\delta n}{n_0} = \frac{e\phi}{T}, \tag{A.1}$$

Where T is

$$T = \frac{T_i T_e}{T_i + T_e} \tag{A.2}$$

The Poisson equation is written as

$$\Delta\phi = \frac{e}{\epsilon_0}(n_e - n_i). \tag{A.3}$$

Fourier transforming the equation underlines the role of the gradient scale

$$-k^2\phi = \frac{e}{\epsilon_0}(n_e - n_i), \tag{A.4}$$

$$\frac{n_i - n_e}{n_0} = \frac{\epsilon_0 T}{n_0 e^2} k^2 \frac{e\phi}{T} \tag{A.5}$$

For ions and electrons perturbations fulfilling $n_\alpha = n_0 + \delta n_\alpha$ and substituting Eq (A.1)

$$\frac{\delta n_i - \delta n_e}{\delta n} = \frac{k^2}{k_D^2} \tag{A.6}$$

where

$$k_D = \left(\frac{\epsilon_0 T}{n_0 e^2}\right)^{-1/2} \tag{A.7}$$

Therefore obtaining that, for the large scales such that $k \ll k_D$, perturbation in ions and electrons density are comparable and quasineutrality holds.

$$\delta n_i \approx \delta n_e \tag{A.8}$$

Quasineutrality is a consequence of a scale restriction and a frequency restriction at the same time. The product of the Debye length with the thermal speed $V_{T\alpha}$ gives the plasma frequency for the component. A characteristic time can be considered $\tau = L/V_{T\alpha}$, where L is a characteristic dimension of the plasma. The condition for quasineutrality can be summarized in

$$L \gg \lambda_D \qquad \tau \gg \omega_{pi}^{-1} \tag{A.9}$$

Where the lowest plasma frequency in a single component is usually given by ions. When the considered frequencies are above this threshold, ions are no more able to keep up with electron motion and quasineutrality is violated.

Multiplying ion and electron continuity equation (Eq (2.1)) by the particle charges and adding them together, the charge conservation equation is obtained

$$\frac{\partial \rho_{ch}}{\partial t} = -\nabla \cdot (n_i e \boldsymbol{v_i} - n_e e \boldsymbol{v_e}) = -\nabla \cdot \boldsymbol{J}. \tag{A.10}$$

As a consequence of quasineutrality,

$$\nabla \cdot \boldsymbol{J} = 0. \tag{A.11}$$

Appendix B

Collisional transport in plasmas

B.1 Random walk model

The basic idea of the random walk model is to show how a particle diffuses away from its initial position due to a series of collisions. A particle moves due to its autonomous motion in the system, until it undergoes a collision. At this point, there is an abrupt random change in the direction of its motion. After a series of N collisions, each characterized by a displacement of $\Delta \boldsymbol{x}_j$ from the previous position, the particle moved of

$$\Delta \boldsymbol{x} = \sum_{j=1}^{N} \Delta \boldsymbol{x}_j. \tag{B.1}$$

For an ensemble of particles it is shown that, performing the ensemble average $\langle\ \rangle$,

$$\langle \Delta \boldsymbol{x} \rangle = 0, \tag{B.2}$$

$$\langle (\Delta x)^2 \rangle = \langle \sum_{i,j} \Delta \boldsymbol{x}_i \cdot \Delta \boldsymbol{x}_j \rangle \neq 0. \tag{B.3}$$

The interpretation is that a particle has no preferential direction in a random motion ($\langle \Delta \boldsymbol{x} \rangle = 0$) but tends to move away from its initial position due to collisions ($\langle (\Delta x)^2 \rangle \neq 0$). This allows to define the magnitude of the average steps between collisions L as

$$L^2 = \langle (\Delta x)^2 \rangle / N. \tag{B.4}$$

Finally, by assuming that the average time between collisions is τ, the time required for N collisions is obviously

$$\Delta t = N\tau, \tag{B.5}$$

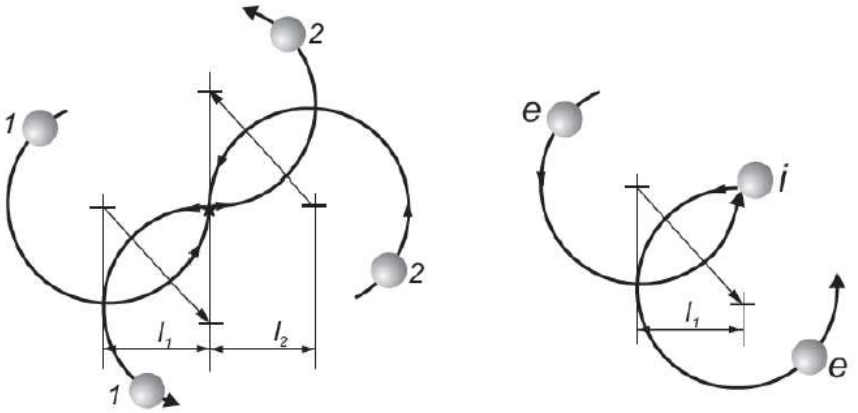

Figure B.1: The displacement of the centre of mass for like and unlike particles, used for the evaluation of the particles diffusion coefficient. Note that the net displacement of the ion in the second case is negligible (fig.1.2 [22])

and is possible to eliminate N, leading to the diffusive behavior

$$\langle (\Delta x)^2 \rangle = D\Delta t. \tag{B.6}$$

Where D is the *diffusion coefficient* that defines the diffusive motion for an ensemble of particles that evolve through random collisions

$$D = \frac{L}{\tau} \tag{B.7}$$

B.2 Classical Transport

The problem of defining the confinement time therefore reduces to derive correctly L and τ for the particles in a plasma in order to define the thermal diffusivity and estimate $\tau_E = a^2\chi$. In a fusion plasma, the most interesting diffusion is the one perpendicular to B, since in a closed field line configuration, it is the one responsible of energy losses towards the environment, by generating a flux directed outwards the LCFS.

In a magnetized plasma, after a Coulomb collision, two particles are assumed to be randomly scattered at an arbitrary angle, and once again they assume their gyro-motion. This difference, with respect to neutral particles diffusion, requires to include the motion of both particles in the derivation of the step size. The displacement is therefore evaluated as the difference in the center of mass position before and after the collision. Remarkably, as can be seen in Fig. B.1, collisions between identical particles

do not lead to particle diffusion, since the overall center of mass remains unchanged. On the contrary, unlike particle as electrons and ions do lead to a net change of the center of mass and therefore to diffusion. It is straightforward to adopt the average time between ion-electron collision at a given T (local thermodynamic equilibrium is assumed) as time step $\tau = \overline{\tau_{ei}} = 1/\overline{\nu_{ei}}$. The derivation of the average step length requires to evaluate the squared displacement of the centre of mass for any collision and scattering angle, leading to

$$L^2 \approx 2\frac{\mathrm{V}_{Te}^2}{\omega_{ce}^2} = 2r_{Le}^2. \tag{B.8}$$

The diffusion coefficient for particles is therefore obtained as in Eq (1.8) and Eq (2.33)

$$D_n = \frac{L^2}{\tau} = \frac{2r_{Le}^2}{\overline{\tau_{ei}}} \sim \frac{2nT\eta_\perp}{B_0^2}. \tag{B.9}$$

The evaluation of the diffusion coefficient includes parameters related to both ions and electrons. The diffusion is characterized by *ambipolarity*, as the two species diffuse together. Physically, if one of the two population diffuses faster, a charge imbalance is created. This induces an electric field that attracts the species to each other causing them to diffuse at the same rate.

The evaluation of the thermal diffusivity follows the same approach, but the main difference lies in the fact that like particles do lead to heat conduction. This can be formally derived. Instead of the centre of mass it is in fact necessary to refer to the "centre of energy" (i.e. the energy centroid) and its change before and after the collision. This leads to the evaluation of a step size, a time step and consequently a diffusivity for every population

$$\chi_i \sim \frac{r_{Li}^2}{\overline{\tau_{ii}}} \qquad \chi_e \sim \frac{r_{Le}^2}{\overline{\tau_{ee}}}.$$

Differently from particle diffusion, the major role is now played by ion-ion collisions. After a short calculation in fact $\chi_i \sim (m_i/m_e)^{1/2}\chi_e$ and therefore $\chi \approx \chi_i$.

B.3 Neoclassical transport

In a toroidal reference frame, vertical drifts of charged particles $\mathbf{v_D} = \mathbf{v}_{\nabla B} + \mathbf{v}_\kappa$ due to radial inhomogeneities of the toroidal field, move the trajectories radially away from flux surfaces. This can drive the particle in

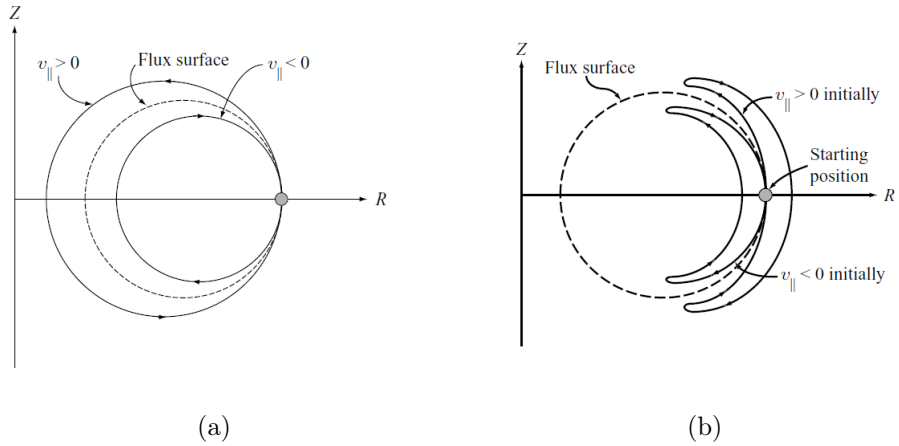

(a) (b)

Figure B.2: (a) Poloidal projections of the guiding centre orbits for two passing particles (Fig. 14.9 [9]); (b) Banana orbits of two particles starting at the same point but with equal and opposite $v_\parallel$ (Fig. 14.14 [9]). Note that in both cases tokamak geometry is considered and the $v_\parallel > 0$ particle drifts outwards, while the $v_\parallel < 0$ particle drifts inward w.r.t the flux suface.

a zone where the magnetic field is more intense, where they can be mirror reflected following the conservation of energy and magnetic moment. If B is not sufficient to induce reflection, the particle can complete a rotation in the poloidal plane and is called a "passing" particle (see Fig. B.2(a)). If B is high enough to induce reflection, the particle is called "trapped" and follows a *banana orbit* as can be seen in Fig. B.2(b) where the overall trajectory is projected on a unique poloidal cross section. The fraction of trapped particles can be evaluated for a Maxwellian distribution function as $f \sim \epsilon^{1/2}$ when $\epsilon \ll 1$, noticeably only a function of geometry.

The main contribution to neoclassical transport is due to trapped particles. A trapped particle completes the banana orbit with a bounce period $\tau_b = 4\pi R_0 q / v_{\parallel max}$, which is longer than a passing particle transit time due to the fact that at the reflection point it has $v_\parallel = 0$, therefore trapped particle have globally lower $v_\parallel$ than passing ones. Intuitively, a trapped particle is subject for a longer time to a drift in the same vertical direction, and therefore this increases the maximum distance from the original flux surface compared to a passing particle. This fact increases the displacement for banana particles following a collision. If a trapped particle undergoes a collision that inverts its parallel velocity as $v_\parallel \rightarrow -v_\parallel$, the trajectory changes to another banana orbit. The center of the distorted orbit is moved by twice the distance that a particle drifts off the original flux surface during a normal bounce period. This leads to the evaluation

of the average square step length of

$$L^2 \approx 2\left(q^2\frac{R_0}{r}\right)r_{Le}^2. \tag{B.10}$$

To induce such collision, a much shorter time than the average time between collisions for passing particles is required. This is mainly due to the fact that, in order to become "de-trapped", a banana particle needs to scatter over a much smaller angle. The effective collision time for trapped electron-ion collision is determined as $\tau_{eff} \sim \epsilon\overline{\tau}_{ei}$. Finally, evaluating the effect of trapped particles only, the diffusion coefficient is derived as

$$D_n^{NC} = f\frac{L^2}{\tau_{eff}} = 2.2\,q^2\,\epsilon^{-3/2}\,D_n^{CL}, \tag{B.11}$$

where the prefactor 2.2 is taken from a self-consistent kinetic theory of neoclassical transport. The thermal diffusivity for neoclassical transport is obtained, always considering that energy transport is due to like particle collisions and that ambipolarity still holds

$$\chi^{NC} \approx \chi_i^{NC} = 6.8\times10^{-22}\,q\,\epsilon^{-3/2}\,\frac{n}{B_0^2T^{1/2}}\,\frac{m^2}{s}. \tag{B.12}$$

The combination of a longer step length and a shorter time between collision, with reference to those which should be used for neoclassical transport due to passing particles, compensate the fact that, in large aspect ratio tokamaks, the fraction of trapped particles is reduced.

Appendix C

Driftwave and driftwave instability

The first linear instability considered is the driftwave, often referred to as "universal instability". The basic mechanism for its formation is the destabilization of drift waves in a plasma.

Drift waves are collective modes characteristic of magnetized plasmas in presence of a density and/or temperature gradients propagating in the electron diamagnetic direction [22]. The feature of this modes is a finite parallel and perpendicular wavenumber $k_\perp \neq 0$ and $k_\parallel \neq 0$ with $k_\perp \gg k_\parallel$ where parallel and perpendicular directions are referred to $\boldsymbol{B}$. For this simplified treatment, the driftwave is studied in a slab geometry, thus replacing the coordinate ϕ with z, r with x and θ with y. The plasma is strongly magnetized with $\boldsymbol{B} = B_0 \boldsymbol{e}_z$.

The description of the driftwave (that follows the one that can be found in [22]) requires the two-fluids model for ions and electrons, where isotropic pressure and noncollisional plasma is assumed. Furthermore, for simplicity, cold ions ($T_i = 0$) and isothermal electrons ($T_e = const.$) are considered. For this simplified treatment, the driftwave is studied in a slab geometry, thus replacing the coordinate ϕ with z, r with x and θ with y. The plasma is strongly magnetized with $\boldsymbol{B} = B_0 \boldsymbol{e}_z$.

Due to the asymptotic approximation for low frequency phenomena ($\omega \ll \omega_{pe}$), electrons flow freely along the parallel direction, instantaneously establishing a parallel equilibrium with an electrostatic field, deduced from the parallel equation of motion for electrons

$$0 = n_e e \frac{\partial \phi}{\partial z} - T_e \frac{\partial n_e}{\partial z}, \tag{C.1}$$

which integrated considering an equilibrium constant value n_0 leads to the

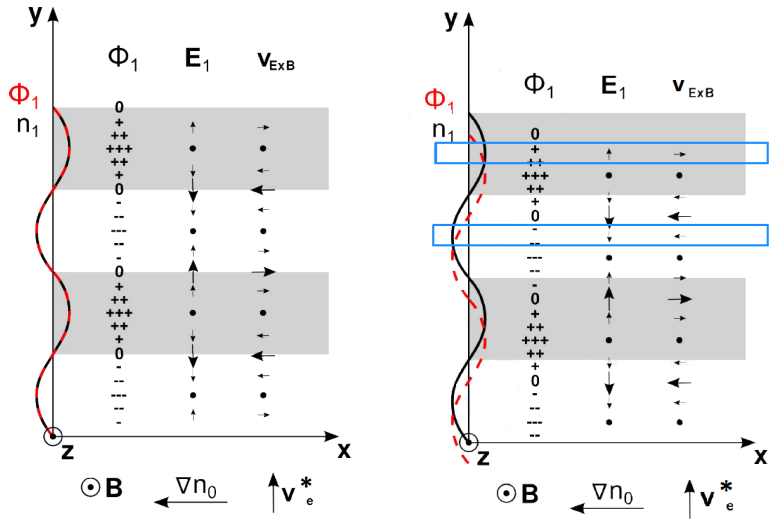

Figure C.1: The mechanism of drift waves. The black line indicates the density perturbation, the red doted line the potential perturbation, following from Boltzmann relationship; both are designed positive in the positive x direction. (a) the adiabatic response of electron implies a phase shift of density perturbation and $E \times B$ velocity such that the perturbation propagates in the positive y direction with electron diamagnetic velocity (b) a phase shift between density and potential perturbation causes the $E \times B$ velocity to generate net transport and undergo a transition into turbulence ([22]).

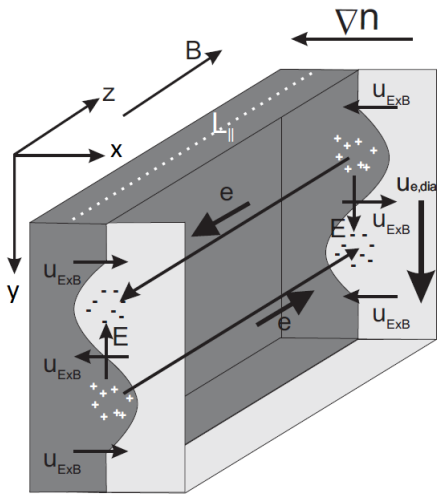

Figure C.2: The drift wave mechanism in a slab geometry. All three spatial directions are illustrated, such that electron parallel behavior due to a density perturbation can be evidenced ([22])

Boltzmann relation

$$\frac{n_e}{n_0} = e^{\frac{e\phi}{T_e}}. \tag{C.2}$$

An initial density harmonic perturbation is assumed as

$$\widetilde{n} = n_0\, exp[i(k_y y + k_z z - \omega t)], \tag{C.3}$$

and the instantaneous response of the electrons is derived from the linearized form of Eq (C.2) where $n_e = n_0 + \widetilde{n}_e$

$$\frac{\widetilde{n_e}}{n_0} = \frac{e\widetilde{\phi}}{T_e} \tag{C.4}$$

This *adiabatic* behavior of the electrons in z direction, implies that no phase difference is possible between density and potential perturbations. Due to the density perturbation of Eq (C.3), a positive potential fluctuation is generated in zones with increased density and vice versa. As a consequence, an electrostatic field $\widetilde{\boldsymbol{E}} = -\nabla\widetilde{\phi}$ is generated also in the drift plane directed in along the y direction (see Fig. C.2). It is possible to isolate the fluid velocity perpendicular to the magnetic field by vector multiplying the stationary momentum equation for the populations with

$\boldsymbol{B}$ to obtain

$$\boldsymbol{v}_\alpha = \frac{\widetilde{\boldsymbol{E}} \times \boldsymbol{B}}{B_0^2} - \frac{\nabla p_\alpha \times \boldsymbol{B}}{n_\alpha q_\alpha B_0^2} + \frac{m_\alpha}{q_\alpha B_0^2}\frac{\partial \widetilde{\boldsymbol{E}}}{\partial t} = \widetilde{\boldsymbol{v}_E} + \boldsymbol{v}_\alpha^* + \widetilde{\boldsymbol{v}}_{pol,\alpha}, \tag{C.5}$$

which are purely *fluid* drifts: note in particular that no particle drift analogous to $\boldsymbol{v}_\alpha^*$ was derived in 2.1. The $E \times B$ velocity, being the same for ions and electrons, it is able to advect the plasma as a whole. The second term is the diamagnetic drift and the third is the polarization drift, both driving ions and electrons in opposite directions due to their charge dependance. Considering the plasma incompressible, an usual approximation at low frequencies, the ion continuity equation for the ions reads

$$\frac{\partial n_i}{\partial t} + v_{ix}\frac{\partial n_i}{\partial x} = 0, \tag{C.6}$$

where a density gradient in the negative x direction was assumed. For cold ions, neglecting the polarization drift

$$\boldsymbol{v}_{ix} = \widetilde{\boldsymbol{v}_E} = -\frac{1}{B_0}\frac{\partial \widetilde{\phi}}{\partial y}\boldsymbol{e}_x \tag{C.7}$$

Dividing the continuity equation by n_0 and linearizing its perturbation

$$\frac{1}{n_0}\frac{\partial \widetilde{n_i}}{\partial t} + \frac{\kappa_n}{B_0}\frac{\partial \widetilde{\phi}}{\partial y} = 0. \tag{C.8}$$

where $\kappa_n = \nabla_x n_0/n_0$. Finally, applying quasineutrality and after short algebraic steps

$$\frac{\partial \widetilde{\phi}}{\partial t} + v_e^*\frac{\partial \widetilde{\phi}}{\partial y} = 0 \tag{C.9}$$

Where the electron diamagnetic drift velocity $v_e^* = \kappa_n T_e/(e\,B_0)$ was isolated. A Fourier transform makes now possible to identify a dispersion relationship for the drift wave

$$\omega = v_e^* k_y. \tag{C.10}$$

where $v_e^* = \kappa_n T_e/(e\,B_0)$ is the the electron diamagnetic drift velocity.

A more complete derivation, considering the effects of finite ion inertia for the parallel dynamics and polarisation drift leads to a dispersion relationship

$$\omega^2(1 + k_y^2\rho_s^2) - \omega\, k_y v_e^* - k_\parallel^2\, c_s = 0, \tag{C.11}$$

with $\rho_s = c_s/\omega_{ci}$ and $c_s^2 = T_e/m_i$.

Note that $v_e^* = \rho_s c_s \kappa_n$. The so-called *dispersion* or *drift scale* ρ_s has an important role in the Drift-Alfvén turbulence that is illustrated in 3.2.

Due to $\delta_{n,\phi} = 0$ no net transport is induced radially. This can be seen also from Fig. C.1(a). The $E \times B$ velocity is maximum only where the density perturbation is zero. As a consequence, the only effect of the plasma advection is the stable propagation of the perturbation.

Drift wave can be driven unstable by various mechanisms. These are generally based on limiting the free movement of the electrons, for example electron-ion collisionality, Landau damping and finite Larmor radius effect. As a consequence, the parallel momentum equation for electrons is modified and the linearized Boltzmann relation is changed with the introduction of a non zero crossphase

$$\frac{\widetilde{n_e}}{n_0} = \frac{e\widetilde{\phi}}{T_e}(1 - i\delta). \tag{C.12}$$

This, of course, influences the structure of the dispersion relationship, since the adiabatic response is not instantaneous anymore. In example, the simple linear dispersion relationship obtained above is modified as

$$\omega = \frac{v_e^* k_y}{(1 - i\delta)} \approx v_e^* k_y (1 + i\delta). \tag{C.13}$$

The introduction of a complex value in a dispersion relationship causes the growth of the mode. To illustrate one of the physical mechanisms, the destabilization due to electrons-ions collisions is explained. If the electrons cannot be considered adiabatic due to the presence of collision that slow theme down, their response to a density perturbation $\widetilde{n}$ is no more instantaneous. The potential $\widetilde{\phi}$ will require a certain time to follow the density perturbation that meanwhile propagated in the y direction. The consequent shift of the maximum radial $E \times B$ velocity of the plasma is therefore able to generate a net transport advecting more dense plasma outwards and less dense plasma inward, as can be seen in Fig. C.1(b). The radial transport due to the linear instability can therefore grow until linear theory is no longer valid and eventually turbulence is able to develop.

Appendix D

Further reduced models for plasma edge

Two further reduced models that were analyzed during the development of the thesis, but not essential for an initial comprehension of the interchange model, are included in this Appendix. The main difference is the absence of a critical heating power for the onset of the oscillations.

D.0.1 Itoh et al.

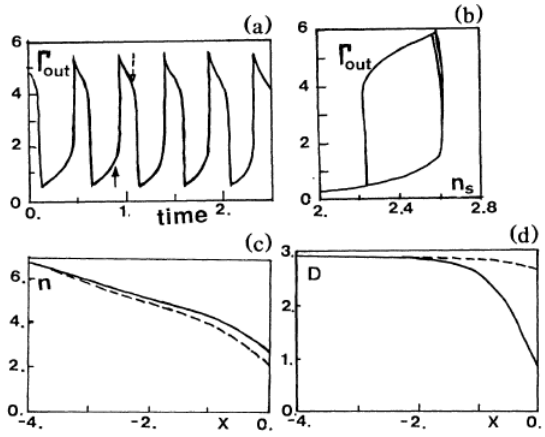

Figure D.1: (a) temporal evolution of Γ_{out} and Lissajous figure of $n(x=0)$ and Γ_{out}. Spatial profiles of (c) density and (d) diffusivity. The chosen parameters allow a limit cycle solution. Solid and dashed line are for before and after the burst, as pointed in the arrows of (a) (fig 3 [78])

The model presented in [78] was one of the first proposed models in-

troducing the theory of dynamical systems for the description of ELMs.

It presents a limit cycle solution to a time dependent system:

$$\frac{\partial n}{\partial t} = \frac{\partial}{\partial x} D(Z) \frac{\partial n}{\partial x}, \tag{D.1}$$

$$\epsilon \frac{\partial Z}{\partial t} = -N(Z, g) + \mu \frac{\partial^2 n}{\partial x^2}, \tag{D.2}$$

where n is the density and Z is the normalized radial electric field inducing the $E \times B$ sheared flow. Here ϵ is a smallness factor, while μ is a transport coefficient whose magnitude is assumed to be comparable with D. N represents the local non-ambipolar particle flux (i.e. the difference between the radial currents of ions and electrons) and it is modeled as an S-curve,

$$N = g - g_0 + \beta(Z^3 - \alpha Z), \tag{D.3}$$

where α β and g_0 are fixed parameters, while the variable $g \sim \nabla n/n$ is defined a "gradient parameter". This makes Eq (D.2) become a Ginzburg-Landau equation, allowing the presence of a supercritical bifurcation for small ϵ.

Furthermore the density diffusivity D, is a smooth function of Z

$$D(Z) = (D_{max} + D_{min})/2 + \tanh Z (D_{max} + D_{min})/2, \tag{D.4}$$

where D_{max} and D_{min} are fixed parameters. Following local theory in which $N(Z, g) = 0$, it is possible to obtain a curve for the effective diffusivity $D = D(g)$ that simulates an hysteresis at the L-H transition. Here g_m, g_M, D_m and D_M are functions of α, β and g_0.

The numerical integration is performed for a one-dimensional system, representing the slab region near the plasma edge for $-L < x < 0$. Considering a fixed particle flux from the core Γ_{in} at $x = -L$ and a fixed $\lambda_S = -n/\nabla n$ at the edge, the particle flux leaving the edge Γ_{out} is computed and compared to the dynamical evolution of the density at $x = 0$. In this way, two stable solutions (i.e. fixed point not evolving in time) are found, one with steep gradient and reduced D, associated to the H-mode for $\Gamma_{in}\lambda_S^2 < D_m/g_m$, the other with lower gradient and higher D for $\Gamma_{in}\lambda_S^2 > D_M/g_M$, comparable to a L-mode. A cyclic solution is found for a limited range of parameters, for $D_m/g_m < \Gamma_{in}\lambda_S^2 < D_M/g_M$ which exists only if $D_M/g_M > D_m/g_m$. In this case, a periodic oscillation of the particle flux Γ_{out} and the density is observed, resembling the ELM behavior, here defined also *dithering cycles*, with a series of bursts of plasma loss at the outer edge. It is possible to observe the delay in the density increase and the development of the transport burst in Fig. D.1 . In summary, the

most interesting features of the considered model, with reference to the goal of this thesis are

- The possibility to introduce a stable L-mode and H-mode and oscillating solutions at the border between the two.
- The control parameter given by fueling of particles from the core Γ_{in}, which is coherent with the critical P_{LH}, since defines the state of the system.
- The formation of the transport barrier localized at the edge due to the steepening gradient.

But at the same time the drawbacks are

- The heuristic models for many functions (e.g. D and N) used to reproduce the desired dynamical behavior but loosely justified.
- The absence of MHD activity.
- The treatment of transport with a diffusive approach, thus neglecting turbulence effects.

D.0.2 Pogutse et al.

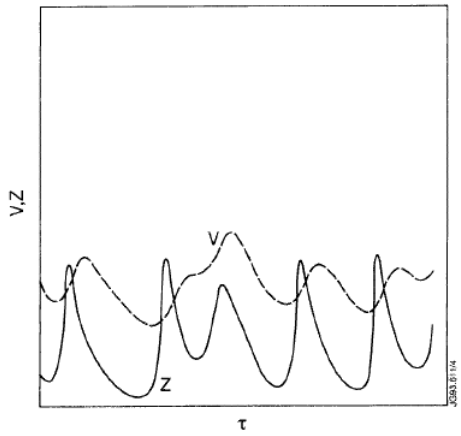

Figure D.2: Typical temporal evolution of the amplitude of the poloidal shear velocity, V, and of the desity, Z, for an unstable case where $\gamma_g > \gamma_{g2}$ for the model with a reduced number of harmonics (Fig. 6(b) [79])

In [79] a model is presented to describe self-consistently the generation of the poloidal flow and the onset of ELMs in the SOL of a tokamak. The dissipative flute-like resistive interchange instability at the plasma edge is considered to explain these phenomena.

The full model involves the equations for continuity, vorticity, temperature and Ohm's law. In the treatment, isothermal electron and ions at constant temperature are assumed, while magnetic perturbations are neglected since an electrostatic limit is considered. All the variables are decomposed in a background value and a fluctuating term as $x = x_0 + \widetilde{x}$. The remaining simplified equations are:

$$\frac{\partial \nabla_\perp^2 \phi}{\partial t} + [\nabla\phi \times \nabla\nabla_\perp^2\phi]_z + g_B \frac{\partial \widetilde{n}}{\partial y} - \sigma_1 \cdot [\phi - \widetilde{n}] = \nabla_\perp^2 \mu_\perp \nabla_\perp^2 \phi, \tag{D.5}$$

$$\frac{\partial \widetilde{n}}{\partial t} + [\nabla\phi \times \nabla\widetilde{n}]_z + g_n \frac{\partial \phi}{\partial y} = \frac{1}{\tau_\parallel} \cdot \widetilde{n} + \nabla_\perp D_\perp \nabla_\perp \widetilde{n}. \tag{D.6}$$

Here ϕ is the potential while $\widetilde{n}$ is the density pertubation. Furthermore $g_n = -\partial n_0/\partial x$ is equivalent to the background pressure gradient in this isothermal assumption. Another crucial term is $g_B \sim 1/R$, representing the curvature effects. These two parameters determine the maximum growth rate of the instability. This is obtained following a linear stability analysis to compute the dispersion relationship for the interchange mode. Other terms are not explained, but the equations are introduced in order to compare those derived in Sec. 4.2. The system is numerically integrated on a two dimensional grid, since in the SOL this description is sufficient, showing the spontaneous generation of strong sheared flows. These are able to suppress the fluctuation, as well as to reproduce quasiperiodical bursts of edge flux indicated as ELMs.

The most interesting analysis for the present thesis lies however in the subsequent derivation of simplified models of the full set of equations. The first proposed approach treats the fully developed interchange turbulence. The application of quasilinear theory leads to define an ordinary differential equation for the turbulence intensity I, one for the characteristic velocity of the sheared flow U, with the addition of an extra equation for the density/pressure gradient N dynamics, not derived from the original

set:

$$\frac{\partial I}{\partial t} = -\left(\gamma_0(1-U^2) - \frac{1}{\tau_1} - DI\right) I, \tag{D.7}$$

$$\frac{\partial U}{\partial t} = -\left(\frac{1}{\tau_{0u}} + \frac{1}{\tau_{1u}}\right) U + \beta IUN, \tag{D.8}$$

$$\frac{\partial N}{\partial t} = -\frac{N}{\tau_{0N}} + \frac{I}{\tau_{1N}}(N - N_0), \tag{D.9}$$

where τ_i, γ_0, β and D are derived from dimensional analysis from the terms of the previous system. This structure is typical in the treatment of 0-D turbulence models and will be discussed in particular in 3.1.1 and 3.1.2.

The second simplifying approach to the original set of equations is based on the observation that, in the full 2-D simulation, only a small number (5-8) of the harmonics in which ϕ and $\widetilde{n}$ are decomposed are effectively dominant. In this way, a minimal model is obtained from Eq (D.5) and Eq (D.6) for the dimensionless amplitude of the five dominating modes. The first three are:

$$\dot{X} = a\,X + \gamma_g\,Y - V\,W, \tag{D.10}$$

$$\dot{Y} = -b\,Y + \gamma_g\,X + X\,Z, \tag{D.11}$$

$$\dot{Z} = -c\,Z - X\,Y, \tag{D.12}$$

where $a, b, c > 0$ are fixed coefficients, dependent on the model parameters of Eq (D.5) and Eq (D.6), and $\gamma_g^2 = g_B g_n k_y^2/k_\perp^2$. The further adding of two new equation for the flow V generation and the vortex correction W, not derived from the original set but heuristically introduced, allows to close the system. The equations for the last two mode amplitudes are:

$$\dot{V} = -d\,V + X\,W, \tag{D.13}$$

$$\dot{W} = -e\,W + f\,X\,W,. \tag{D.14}$$

Here a term analogous to Reynolds stresses XW is inserted. The non-linear analysis of the 0D system is performed, finding different equilibria fixed point by setting the time derivatives to zero. The stability of such fixed points is determined by a critical value for γ_g. In particular, for $\gamma_g > \gamma_{g2}$, the system moves to an ELM regime, reaching a limit cycle. The evolution of X and V that resembles a Lotka-Volterra dynamics (see 3.1.2), having a characteristic delay in the fluctuations as can be seen in Fig. D.2. The fact that γ_B is a function of T implies that the system dynamical behavior is set by resistivity effects. This is in agreement with

the definition of Type-III ELMs as resistive phenomena, but in [79] the occurring instabilities are referred to as ELMs in general. Since the minimal model reproduces the generation of the sheared flow, the appearance ELM cycles and an improvement of the confinement over a critical value of a control parameter $\gamma_{g1} < \gamma_{g2}$, it is considered to describe an L-H transition. The simplified model is shown to reproduce in a close way the full numerical simulation results, therefore being able to summarize the overall dynamics in a minimal 0D model. The most interesting feature of the model are therefore:

- The complete treatment of fundamental equation for the plasma edge and the reduction to a minimum subset able to reproduce closely the complete dynamics.
- The induction of resistive ELMs cycle with features analogous to Type-III ELMs.
- The presence of a zonal flow activity that resembles predator-prey dinamics.

While some drawbacks with reference to the scope of the thesis are:

- The absence of a critical threshold of the heating power to induce the L-H transition.
- The various coefficients obtained from dimensional analysis that limit the predictive capability of the model.
- The electrostatic assumption, that neglects magnetic perturbations.

Appendix E

Derivation of the DALF equations

The derivation of the fluid drift equations for low frequency phenomena in a magnetized plasma (see the assumptions in Sec. 3.2.1) is presented. This starts from the two-fluids equations of Sec. 2.1.

Density evolution

The density equation for a single component, singly ionized plasma is derived from the electron continuity, chosen for the possibility to neglect the polarization drift due to $m_e \ll m_i$.

$$\frac{\partial n_e}{\partial t} + \nabla \cdot (n_e \boldsymbol{v}_e) = 0. \tag{E.1}$$

Splitting the velocity in its parallel and perpendicular components, and furthermore splitting the last in $E \times B$ and diamagnetic velocity, the equation can be written as

$$\frac{\partial n_e}{\partial t} + \boldsymbol{v}_E \cdot \nabla n_e + n_e \nabla \cdot \boldsymbol{v}_E + \nabla \cdot (n_e \boldsymbol{v}_e^*) + B \nabla_\parallel \frac{n_e v_{e\parallel}}{B} = 0. \tag{E.2}$$

Note that, for the parallel velocity, it was made use of $\nabla \cdot \boldsymbol{B} = 0$ in

$$\nabla \cdot (f\boldsymbol{b}) = \nabla \cdot (f\boldsymbol{B}/B) = \boldsymbol{B} \cdot \nabla(f/B) = B \nabla_\parallel (f/B), \tag{E.3}$$

where f is a generic scalar function.

It is now introduced a divergence operator, also referred to as curvature operator, defined for a generic scalar f as

$$\mathcal{K}(f) = -\nabla \cdot \left(\frac{c\boldsymbol{B}}{B^2} \times \nabla f \right). \tag{E.4}$$

In this way, it is possible to write the divergences as

$$\nabla \cdot \boldsymbol{v_E} = \nabla \cdot \frac{c}{B^2}\boldsymbol{B} \times \nabla\phi = -\mathcal{K}(\phi), \tag{E.5}$$

$$\nabla \cdot (n_e \boldsymbol{v}_e^*) = -\nabla \cdot \frac{1}{e}\frac{c}{B^2}\boldsymbol{B} \times \nabla p_e = \frac{1}{e}\mathcal{K}(p_e). \tag{E.6}$$

Note that, despite the motion across the field is treated as dynamically incompressible, quasistatic compression enters in the dynamics through the inhomogeneities of B giving rise to a non-zero divergence of the velocity field.

Furthermore, the parallel current is inserted in the equation from its definition

$$J_\parallel = n_e e(u_\parallel - v_{e\parallel}). \tag{E.7}$$

In conclusion, neglecting the parallel advection (Eq (3.45)) and isolating the $E \times B$ advective derivative (Eq (3.40)) the final form is

$$\frac{d_E\, n_e}{dt} = \frac{B}{e}\nabla_\parallel \frac{J_\parallel}{B} - n_e B \nabla_\parallel \frac{u_\parallel}{B} - \frac{1}{e}\mathcal{K}(p_e) + n_e \mathcal{K}(\phi). \tag{E.8}$$

The instability drive from the background gradients is contained in this equation, as will be shown in the next chapter.

Charge conservation

Consider that, for $c_A \ll c$, it is given $\rho_s \gg \lambda_D$ and therefore quasineutrality holds (see Appendex A). As a consequence the charge conservation equation reads

$$\nabla \cdot \boldsymbol{J} = \nabla \cdot \boldsymbol{J}_\perp + B\nabla_\parallel \frac{J_\parallel}{B} = 0. \tag{E.9}$$

Since $E \times B$ drift does not contribute to the perpendicular current (see Sec. 2.1), the only remaining contributions to the perpendicular current density divergence at order zero are polarization and diamagnetic drifts

$$\nabla \cdot n_i e \boldsymbol{v}_{Pi} + \nabla \cdot (n_i e \boldsymbol{v}_i^* - n_e e \boldsymbol{v}_e^*) + B\nabla_\parallel \frac{J_\parallel}{B} = 0. \tag{E.10}$$

Neglecting high order corrections of $O(\delta^2)$, $\boldsymbol{B}$ commutes with d_E/dt. Therefore, inserting the derived expressions for v_{Pi} and v_α^* under divergence, the final form of the charge conservation reads

$$\nabla \cdot \frac{n_i m_i c^2}{B^2}\frac{d_E}{dt}\left(\nabla_\perp \phi + \frac{\nabla_\perp p_i}{n_e e}\right) = B\nabla_\parallel \frac{J_\parallel}{B} + \mathcal{K}(p_e + p_i), \tag{E.11}$$

where from now on $\nabla_\perp = -\boldsymbol{b} \times (\boldsymbol{b} \times \nabla)$.

The equivalence of this equation with the vorticity conservation is described in the next chapter.

Parallel velocity evolution

The evaluation of the parallel component of the velocity is required in addition to the perpendicular $u_\perp$. The two fluids momentum equation is projected along the parallel direction through the scalar product $\boldsymbol{B}$, and the two evolution equations for ions and electrons parallel velocities are obtained. In the second, the electron mass is now considered. Again, gyroviscous (diamagnetic) cancellation is invoked to consider the $E \times B$ advective derivative only. Finally, the the magnetic field can commute with the total time derivative and operates on $\boldsymbol{v}$ only.

$$n_i m_i \frac{d_E}{dt} u_\parallel = -\nabla_\parallel p_i - B\nabla_\parallel(\Pi_{i\parallel}/B) + n_e e E_\parallel - R_{ei}, \tag{E.12}$$

$$n_e m_e \frac{d_E}{dt} v_{\parallel e} = -\nabla_\parallel p_e - B\nabla_\parallel(\Pi_{e\parallel}/B) - n_e e E_\parallel + R_{ei}. \tag{E.13}$$

While only the first is required for the model, the second is used in the following derivation

Ohm's law

An evolution equation for $u_\parallel$ can be obtained summing Eq (E.12) and Eq (E.13) and neglecting Π_e

$$n_i m_i \frac{d_E}{dt} u_\parallel = -\nabla_\parallel(p_e - p_i) - \nabla_\parallel(\Pi/B), \tag{E.14}$$

where from now on $\Pi = \Pi_{i\parallel}$ for simplicity. Multiplying this equation by μ_e and subtracting Eq (E.13), the evolution of the relative parallel drift velocity $u_\parallel - v_{\parallel e}$,isolating terms of order $\mu_e = m_e/m_i$, reads

$$n_e m_e \frac{d_E}{dt}(u_\parallel - v_{\parallel e}) = \nabla_\parallel p_e + n_e e E_\parallel - R_{ei} + O(\mu_e). \tag{E.15}$$

Invoking Faraday's law (Eq (3.33)) for $E_\parallel$ leads to

$$\frac{n_e e}{c}\frac{\partial A_\parallel}{\partial t} + n_e m_e \frac{d_E}{dt}(u_\parallel - v_{\parallel e}) = \nabla_\parallel p_e - n_e e \nabla_\parallel \phi - R_{ei} + O(\mu_e). \tag{E.16}$$

Commuting n_e and the $E \times B$ advective derivative is allowed in drift ordering when neglecting $O(\delta)$ corrections. This allows to express the parallel current $J_\parallel$. Dropping also the $O(\mu_e)$ terms, lets the Ohm's law

$$\frac{n_e e}{c}\frac{\partial A_\parallel}{\partial t} + \frac{m_e}{e}\frac{d_E}{dt} J_\parallel = \nabla_\parallel p_e - n_e e \nabla_\parallel \phi - R_{ei}. \tag{E.17}$$

Energy evolution

The energy evolution equations are introduced for the sake of completeness but not derived formally, since the model presented in this thesis is assumed to be at constant ion and electron temperature. Their expression is derived from the two fluid equation energy conservation Eq (2.3) and leads, for the electron temperature, to

$$\frac{3}{2}n_e\frac{d_E T_e}{dt} = \frac{T_e B}{e}\nabla_\parallel\frac{J_\parallel}{B} - p_e B\nabla_\parallel\frac{u_\parallel}{B} - B\nabla_\parallel\frac{q_{e\parallel}}{B} - \frac{5}{2}\frac{p_e}{e}\mathcal{K}(T_e) - \frac{T_e}{e}\mathcal{K}(p_e) + p_e\mathcal{K}(\phi). \tag{E.18}$$

For the ion temperature the divergence of the polarization drift appears and the equation reads

$$\frac{3}{2}n_i\frac{d_E T_i}{dt} = \frac{T_i B}{e}\nabla_\parallel\frac{J_\parallel}{B} - p_i B\nabla_\parallel\frac{u_\parallel}{B} - B\nabla_\parallel\frac{q_{i\parallel}}{B} + \frac{5}{2}\frac{p_i}{e}\mathcal{K}(T_i) - \frac{T_i}{e}\mathcal{K}(p_e) + p_i\mathcal{K}(\phi). \tag{E.19}$$

Bibliography

[1] Birkenmeier et al. "Magnetic Structure and frequency scaling of limit-cycle oscillations close to L- to H-mode transitions". Submitted to: Nuclear Fusion. 2015.

[2] Conway et al. "Mean and Oscillating Plasma Flows and Turbulence Interactions across the L-H Confinement Transition". In: *Phys. Rev. Lett.* 106.6 (2011), p. 065001.

[3] Kenneth S. Krane. *Introductory Nuclear Physics*. John Wiley & Sons., 1987.

[4] Irving Langmuir. "Oscillations in Ionized Gases". In: *PNAS, New York, NY* 106 (1928), p. 627.

[5] Kyōji. Nishikawa and Masashiro Wakatani. *Plasma Physics - Basic Theory with Fusion Applications*. Springer, 1990.

[6] *History of Max Planck Society*. URL: `http://www.mpg.de/history_mpg`.

[7] Dale Meade. "50 years of fusion research". In: *Nuclear Fusion* 50.1 (2010), p. 014004.

[8] Adelberger et al. "Solar fusion cross sections". In: *Rev. of Mod. Phys.* 70.4 (1998), p. 1267.

[9] Jeffrey Freidberg. *Plasma Physics and Fusion Energy*. Cambridge University Press, 2007.

[10] C M Braams and P E Stott. *Nuclear Fusion: Half a Century of Magnetic Confinement Fusion Research*. CRC Press, 2002.

[11] John D. Lawson. "Some criteria for a useful thermonuclear reactor". In: *AERE* (1957).

[12] Roberto Piazza. *Note di Fisica Statistica (con qualche accordo)*. Springer Verlag, 2011.

[13] Robin Herman. *Fusion: the Search for Endless Energy*. Cambridge University Press, 1990.

[14] R.J. Goldston. "Energy confinement scaling in Tokamaks: some implications of recent experiments with Ohmic and strong auxiliary heating". In: *Plasma Physics and Controlled Fusion* 26.1A (1984), p. 87.

[15] Fritz Wagner. "Regime of Improved Confinement and High Beta in Neutral-Beam-Heated Divertor Discharges of the ASDEX Tokamak". In: *Phys. Rev. Lett.* 49.19 (1982), p. 1408.

[16] Troyon et al. "MHD-Limits to Plasma Confinement". In: *Plasma Physics and Controlled Fusion* 26.1A (1984), p. 209.

[17] *Summary of the ITER Final Design Report*. URL: `http://www-pub.iaea.org/MTCD/publications/PDF/ITER-EDA-DS-22.pdf`.

[18] Harmut Zohm. "Recent ASDEX Upgrade research in support of ITER and DEMO". In: *Nuclear Fusion* 55.10 (2015), p. 104010.

[19] *Introduction: The ASDEX Upgrade tokamak*. URL: `http://www.ipp.mpg.de/16208/einfuehrung`.

[20] Köppendörfer et al. "The ASDEX Upgrade toroidal field magnet and poloidal divertor field coil system adapted to reactor requirements". In: *Nuclear Engineering and Design. Fusion* 3.3 (1986), p. 265.

[21] Jeffrey Freidberg. *Ideal MHD*. Plenum Press, 1987.

[22] Ulrich Stroth. *Plasmaphysik: Phänomene, Grundlagen, Anwendungen*. Vieweg+Teubner Verlag, 2011.

[23] Paradisi et al. "A Generalized Fick's Law to Describe Non-Local Transport Effects". In: *Phys. Chem. Earth (B)* 26.4 (2001), p. 275.

[24] Dif-Pradalier et al. "On the validity of the local diffusive paradigm in turbulent plasma transport". In: *Phys. Rev. E* 82.2 (2010), p. 025401.

[25] Alexander Kendl. "Two dimensional turbulence in magnetised plasmas". In: *European Journal of Physics* 29.5 (2008), p. 911.

[26] A.N. Kolmogorov. "Dissipation of energy in the locally isotropic turbulence". Trans. by V. Levin. In: *Proc. R. Soc. Lond. A* 434.1890 (1991), p. 15.

[27] *File:False color image of the far field of a submerged turbulent jet.jpg*. URL: `https://upload.wikimedia.org/wikipedia/commons/b/b9/False_color_image_of_the_far_field_of_a_submerged_turbulent_jet.jpg`.

[28] Robert H. Kraichnan. "Inertial Ranges in Two-Dimensional Turbulence". In: *Physics of Fluids* 10.7 (1967), p. 1417.

[29] Jan Weiland. *Collective Modes in Inhomogeneous Plasma*. IoP Publishing Ltd, 2000.

[30] *Single (seeded) blob computed with a full-f 2-D gyrofluid model.* URL: `http://iopscience.iop.org/0741-3335/labtalk-article/62791`.

[31] Philip Adrian Schneider. "Characterization and scaling of the tokamak edge transport barrier". PhD Thesis. LMU, 2012.

[32] Schirmer et al. "The radial electric field and its associated shear in the ASDEX Upgrade tokamak". In: *Nuclear Fusion* 46.9 (2006), S780.

[33] Fritz Wagner. "A quarter-century of H-mode studies". In: *Plasma Physics and Controlled Fusion* 49.12B (2007), B1.

[34] Kurzan et al. "Measurement and scaling of the radial correlation lengths of turbulence at the plasma edge of ASDEX Upgrade". In: *Plasma Physics and Controlled Fusion* 42.3 (2000), p. 237.

[35] H Biglari, P.H. Diamond, and P.W. Terry. "Influence of sheared poloidal rotation on edge turbulence". In: *Physics of Fluids B* 2.1 (1990), p. 1.

[36] P.W. Terry. "Suppression of turbulence and transport by sheared flows". In: *Rev. Mod. Phys.* 72.1 (2000), p. 109.

[37] Keith H. Burrell. "Test of Causality: experimental evidence that sheared ExB flows alters turbulence and transport in tokamaks". In: *Physics of Plasmas* 6.12 (1999), p. 4418.

[38] Stroth et al. "On the interaction of turbulence and flows in toroidal plasmas". In: *Plasma Physics and Controlled Fusion* 53.2 (2011), p. 024006.

[39] Diamond et al. "Zonal flows in plasma - a review". In: *Plasma Physics and Controlled Fusion* 47.5 (2005), R35.

[40] Peter Manz. "Strukturentstehung in Driftwellenturbulenz toroidaler Plasmen". PhD thesis. Universität Stuttgart, 2009.

[41] Sanae-I. Itoh and Itoh Kimitaka. "Model of L to H-Mode Transition in Tokamak". In: *Phys. Rev. Lett.* 60.22 (1988), p. 2276.

[42] John Guckenheimer and Philip Holmes. *Nonlinear Oscillations, Dynamical Systems and Bifurcation of Vector Fields*. Springer-Verlag New York, 1983.

[43] Miki et al. “Spatio-temporal evolution of the L-I-H transition”. In: *Physics of Plasmas* 19.9 (2012), p. 092306.

[44] Kobayashi et al. “Spatiotemporal Structures of Edge Limit-Cycle Oscillation before L-to-H transition in the JFT-2M Tokamak”. In: *Phys. Rev. Lett.* 111.3 (2013), p. 035002.

[45] Cheng et al. “Low-Intermediate-High confinement transition in HL-2A tokamak plasmas”. In: *Nuclear Fusion* 54.11 (2014), p. 114004.

[46] Cavedon et al. “Unraveling the interplay between turbuence, neoclassical and zonal flows during the L-H transition at ASDEX Upgrade”. Submitted to: Phys. Rev. Lett. 2015.

[47] Hartmut Zohm. “Edge Localized Modes (ELMs)”. In: *Plasma Physics and Controlled Fusion* 38.2 (1996), p. 105.

[48] Hartmut Zohm. “The physics of edge localized modes (ELMs) and their role in power and particle exhaust”. In: *Plasma Physics and Controlled Fusion* 38.8 (1996), p. 1213.

[49] Snyder et al. “Edge localized modes at the pedestal: A model based on coupled peeling-ballooning modes”. In: *Physics of Plasmas* 9.5 (2002), p. 2037.

[50] Liang et al. “Overview of Edge localized modes Control in Tokamak Plasmas”. In: *Fusion Science and Technology* 59.3 (2011), p. 586.

[51] J W Connor. “Edge-localized modes-physics and theory”. In: *Plasma Physics and Controlled Fusion* 40.5 (1998), p. 531.

[52] Colchin et al. “Physics of slow L-H transitions in the DIII-D tokamak”. In: *Nuclear Fusion* 42.9 (2002), p. 1134.

[53] Colchin et al. “Slow L-H Transitions in DIII-D Plasmas”. In: *Phys. Rev. Lett.* 88.25 (2002), p. 255002.

[54] Lebedev et al. “A minimal dynamical model of edge localized mode phenomena”. In: *Physics of Plasmas* 2.9 (1995), p. 3345.

[55] Diamond et al. “Self-Regulating Shear Flow Turbulence: A Paradigm for the L to H Transition”. In: *Phys. Rev. Lett.* 72.16 (1994), p. 2565.

[56] Kim et al. “Zonal Flows and Transient Dynamics of the L- H Transition”. In: *Phys. Rev. Lett.* 90.18 (2003), p. 185006.

[57] V. Volterra. “Variazioni e fluttuazioni del numero d’individui in specie animali conviventi”. In: *Mem. Acad. Lincei Roma* 2 (1926), p. 31.

[58] Constantinescu et al. “A low-dimensional model system for quasi-periodic plasma perturbations”. In: *Physcis of Plasmas* 18.6 (2011), p. 62307.

[59] Constantinescu et al. “Bifurcations and fast-slow dynamics in a low-dimensional model for quasi-periodic plasma perturbations”. In: *Romanian Reports in Physics* 67.3 (2015), p. 1049.

[60] B. Scott. “Low Frequency Fluid Drift Turbulence in Magnetized Plasmas”. Habilitation Thesis. Heinrich-Heine-Universität Düsseldorf, 2000.

[61] Tsai et al. “Thermal Conductivity and Low Frequency Waves in Collisional Plasmas”. In: *Physics of Fluids* 13.8 (1970), p. 2108.

[62] F. L. Hinton and C. W. Horton. “Amplitude Limitation of a Collisional Drift Wave Instability”. In: *Physics of Fluids* 14.1 (1971), p. 116.

[63] Masahiro Wakatani and Akira Hasegawa. “A collisional drift wave description of plasma edge turbulence”. In: *Physics of Fluids* 27.3 (1984), p. 611.

[64] D. A. Monticello and R. B. White. “Nonlinear drift tearing modes”. In: *Physics of Fluids* 23.2 (1980), p. 366.

[65] B. Scott. “Three-dimensional computation of drift Alfvén turbulence”. In: *Plasma Physics and Controlled Fusion* 39.10 (1997), p. 1635.

[66] B. Scott. “Energetics of the interaction between electromagnetic ExB turbulence and zonal flows”. In: *New Journal of Physics* 7.1 (2005), p. 92.

[67] B. Scott. “Drift wave versus interchange turbulence in tokamak geometry: Linear versus nonlinear mode structure”. In: *Physics of Plasmas* 12.6 (2005), p. 62314.

[68] B. Scott. “Nonlinear polarization and dissipative correspondence between low-frequency fluid and gyrofluid equations”. In: *Physics of Plasmas* 14.10 (2005), p. 102318.

[69] Militello et al. “Multi-machine comparison of drift fluid dimensionless parameters”. In: *Plasma Physics and Controlled Fusion* 53.9 (2011), p. 095002.

[70] Viezzer et al. “Collisionality dependence of edge rotation and in–out impurity asymmetries in ASDEX Upgrade H-mode plasmas”. In: *Nuclear Fusion* 55.12 (2015), p. 123002.

[71] *The MIRNOV-Diagnostics (MTR).* URL: https://www.aug.ipp.mpg.de/aug/local/aug_only/magnetics/.

[72] Manz et al. "Poloidal asymmetric flow and current relaxation of ballooned transport with particular application to limit cycles during I-phase in ASDEX Upgrade". 2015. Submitted to: Physics of Plasmas.

[73] E. Lorenz. "Deterministic nonperiodic flow". In: *J. Atmos. Sci.* 20.2 (1963), p. 130.

[74] Gantmacher F.R. *Applications of the theory of Matrices.* Trans. by J.L. Brenner. Dover Pubns, 1959.

[75] E. Wolfrum. *Lecture on 'H-mode pedestal physics'.* PhD Network in Fusion Science and Engineering, Advanced Course. Max-Planck-Institut für Plasmaphysik, 2015.

[76] *Detailed description of ASDEX Upgrade.* URL: https://www.aug.ipp.mpg.de/wwwaug/documentation/physics/techdata.shtml.

[77] G. Birkenmeier. *H-mode Workshop 2015.* Contribution. Max-Planck-Institut für Plasmaphysik, 2015.

[78] Itoh et al. "Edge localized mode activity as a limit cycle in tokamak plasmas". In: *Phys. Rev. Lett.* 67.18 (1991), p. 2485.

[79] Pogutse et al. "The resistive interchange convection in the edge of tokamak plasmas". In: *Plasma Physics and Controlled Fusion* 36.12 (1994), p. 1963.

Ringraziamenti

Mi piace pensare che la tesi di laurea sia il lungo scatto finale al termine della maratona che è il percorso universitario. Tuttavia, mentre si ha una seppur vaga immagine di cosa sia il traguardo, non si ha idea di come sia il tragitto finchè non viene percorso, nè di quanto si possa imparare nel percorrerlo con e senza l'aiuto dei libri.

Voglio quindi ringraziare i miei genitori, Renzo e Liliana, senza i quali questa corsa non l'avrei neppure potuta iniziare, nè tantomeno finire. Il loro supporto è stato tanto importante quanto il loro esempio costante.

Grazie al Professor Matteo Passoni, che oltre ad avermi insegnato molto, non solo mi ha sempre appoggiato in questo lavoro, ma mi ha anche assistito con una professionalità eccezionale. E grazie a Peter, sia per le lunghe discussioni assieme, sia per le lunghe pause quando finivamo. Grazie anche al Professor Ulrich Stroth, che ha riposto fiducia in me, facendo in modo che questa esperienza fosse possibile.

Non serve spiegare come lungo questo percorso universitario abbia incontrato la gente più strana e imbarcato compagni di viaggio. Qualcuno è rimasto, qualcuno è andato e non s'è più sentito.

Ma mio pensiero va soprattutto a Giangi e Raffo che ci sono da prima dell'inizio, e a Damiano, Luca e Mattia che hanno contribuito a renderne la fine un'esperienza incredibile.

Un ringraziamento di cuore ad Alberto, Giacomo e Francesco perchè i loro Aspri consigli mi hanno accompagnato in tutti questi anni, e sono stati sempre preziosi e mai scontati.

Grazie ad Ambro, con cui ho viaggiato e che mi ha raggiunto ovunque nelle mie trasferte, perchè alla fine ha avuto la pazienza di leggere la mia versione della Storia.

Infine, una menzione particolare a Stoipiz, che deve ancora decidere se la tesi fosse su una spada laser o su un cannone al plasma.

This work has been carried out within the framework of the EUROfusion Consortium and has received funding from the European Union's Horizon 2020 research and innovation programme under grant agreement number 633053. The views and opinions expressed herein do not necessarily reflect those of the European Commission